2014

Tropospheric composition in the Southern Hemisphere, investigated with spectroscopic measurements and global models

Rebecca Rhiannon Buchholz
University of Wollongong

Tropospheric Composition in the Southern Hemisphere, Investigated with Spectroscopic Measurements and Global Models

Rebecca Rhiannon Buchholz
B.Sc. (Chemistry Hons.), B.A. (Mathematics)

A thesis submitted in partial fulfilment of the requirements for the award of the degree

Doctor of Philosophy
University of Wollongong, Australia
School of Chemistry

Supervisors:
Dr. Clare Murphy
Prof. David Griffith
Dr. Peter Hurley (CSIRO)

2014

Declaration by Candidate

The work presented in this thesis was undertaken at The University of Wollongong between the dates of 17 March 2010 and 29 July 2014. I, Rebecca Rhiannon Buchholz, declare that this thesis, submitted as partial fulfilment of the requirements for the award of Doctor of Philosophy, in the School of Chemistry, University of Wollongong, is original and has not been submitted for any other award or degree at this or any other institution. The material presented herein is entirely my own work unless otherwise referenced or acknowledged.

_____

Rebecca Buchholz

Acknowledgments

Firstly, I would like to express enormous gratitude to my principal supervisor, Clare Murphy, for her constant support and exceptional mentorship. I appreciate the advice, freedom and friendship I have received along my PhD journey. A huge thanks to my co-supervisor David Griffith, for his support and wisdom, and for knowing the questions to ask to stretch my own knowledge. I am also grateful to my co-supervisor, Peter Hurley (CSIRO), who ran the ACCESS model at CSIRO and guided my work with the Earth System model.

I would like to offer special thanks to David Edwards from the National Center for Atmospheric Research (NCAR), who was integral in discussing the contents of Chapter 5, and hosted my visiting trip to the Atmospheric Chemistry Division of NCAR in 2013; Guang Zeng who provided CO and C_2H_6 solar FTS measurement data for Lauder and gave advice on the UKCA model; David Salter, from the Office of Environment and Heritage, for providing in situ air quality data for Gipps St, Wollongong; and David Carslaw for creating the immensely useful OpenAir R package and for implementing HYSPLIT trajectories for the Wollongong site. I would also like to mention my appreciation to Peter Rayner from the University of Melbourne, who spent valuable time teaching me about inverse modelling and the CTM TM5, although this work did not end up in this Thesis.

I am thankful to have had the opportunity to be a member of the Centre for Atmospheric Chemistry (CAC) team at the University of Wollongong throughout my PhD. I have enjoyed the lengthy discussions on the most appropriate way to perform uncertainty analysis with Stephen Wilson; understanding solar FTS theory with Nicholas Jones; and learning about agricultural emissions from Frances Phillips. The unending skills of CAC technical staff Graham Kettlewell, Martin Riggenbach and Travis Naylor have been invaluable, as has their willingness to offer a hand and help explain something instrumental, laboratory or software related.

I would like to thank additional CAC researchers: Dagmar Kubistin, for teaching me all things in situ FTIR and helping me edit Chapter 3; Voltaire Velazco for discussion pertaining to FTS and other various scientific curiosities; Nick Deutscher for forging the way for so many areas in which I have continued to work. I am particularly grateful for the assistance given by Jenny Fisher, the local GEOS-Chem expert who is always willing to answer questions, and has helped to edit Chapters 6 and 7. Thanks go to past CAC members Christopher Miller for the introduction to GEOS-Chem and to Ronald

Macatangay who taught me how to operate the solar FTS.

I value both the friendship and professional support of my fellow graduate students in CAC: Chris Caldow for helping me with in situ FTIR; newcomer Max Desservettaz who took over the role as group meeting co-ordinator; Elise-Andrée Guérette for providing precious SIFT data on HCHO and isoprene (which makes an appearance in Chapter 6); Ruhi Humphries my fellow ERCA buddy and ideas-bouncer; and Xue Shi for our long discussions on mathematics and CO_2. Overall, I am proud to have been a part of such a coherent, supportive team of researchers in the Centre for Atmospheric Chemistry.

I wish to acknowledge various funding that has made my PhD possible. The Australian Postgraduate Award from the Australian Government; The CSIRO OCE Postgraduate Top-Up scholarship; and travel funding provided by The University of Wollongong (Australia), Harvard University (USA), and the University of Aveiro (Portugal).

Finally, I could not have completed this monumental task without my personal cheer-squad. I would like to thank my parents Judy and Ralph Buchholz for instilling an interest in science and discovery, always believing I could finish this, and for talking me down from numerous figurative ledges. Their proof-reading skills were also highly valued. My best friend Emma Reid, for her interest in my PhD, even when much more important things were happening in her own life. My utmost thanks go to my eternally patient and always encouraging partner Tim Holt.

To all I give my deepest and sincere thanks.

Rebecca

Strength and honour.

Research Communication

First author oral presentations:

Buchholz, R., Paton-Walsh, C., Hurley, P., Griffith, D., Jones, N., Australasian total column CO and H_2CO investigated with GEOS-Chem, FTIR measurements, and an Earth-System Model (ACCESS). *The 6th International GEOS–Chem Meeting*, Harvard, Boston, USA, May **2013**.

Buchholz, R., Paton-Walsh, C., Hurley, P., Griffith, D., Jones, N., Wollongong total column CO and HCHO investigated with FTIR measurements, a Chemical Transport Model and the Earth System Model ACCESS. *AMOS Postgraduate Symposium*, UNSW, Australia, July **2012**.

Buchholz, R., Paton-Walsh, C., Hurley, P., Griffith, D., Jones, N., Tropospheric pollution over Wollongong investigated with the Earth-System Model ACCESS. *CAWCR and Cape Grim Annual Science Meeting*, Melbourne, Australia, November **2011**.

Buchholz, R., Griffith, D., Jones, N., Paton-Walsh, C.: Modelling Precursors of tropospheric ozone over Australasia, invited presentation *The 5th International GEOS–Chem Meeting*, Harvard, Boston, USA, May **2011**.

Buchholz, R., Griffith, D., Jones, N., Paton-Walsh, C.: Modelling Precursors of tropospheric ozone over Australasia, *AMOS 18th Annual and MetSoc NZ Joint Conference: Extreme Weather*, Wellington, New Zealand, February, **2011**.

First author poster presentations:

Buchholz, R., Paton-Walsh, C., Hurley, P., Jones, N., Zeng, G., Griffith, D., Australasian total column CO and H_2CO investigated with FTIR measurements, a Chemical Transport Model (GEOS-Chem) and an Earth System Model (ACCESS). *Atmospheric Chemistry in the Anthropocene, IGAC Open Science Conference*, Beijing, China, September **2012**.

Buchholz, R., Paton-Walsh, C., Hurley, P., Jones, N., Griffith, D., Comparison of total column CO and H2CO FTIR measurements at Wollongong with a Chemical Transport Model (GEOS-Chem) and an Earth System Model (ACCESS). *European Research Course on Atmospheres*, Grenoble, France, January-February **2012**.

Research publications:

Publications expected to arise from work in this thesis are outlined below.

Chapter 3 & 4: **In situ FTIR**

Buchholz, R. R., Paton–Walsh, C., Kubistin, D., Caldow, C., Cameron, M., Macatangay, R. C., Kettlewell, G. and Griffith, D. W. T., Using in situ carbon monoxide, methane and carbon dioxide to investigate the Southern Hemisphere site: Wollongong, Australia, *Atmospheric Chemistry and Physics, in prep.*

Paton–Walsh, C., Guerétte, E-A., Humphries, R., Kubistin, D., Wilson, S., Griffith, D., Buchholz, R. *et* al., Overview of the instruments deployed during the MUMBA Campaign: Measurements of urban, marine and biogenic air., *Proceedings of the 21st International Clean Air and Environment Conference 2013, in press.*

Paton-Walsh, C., Guerétte, E-A., Humphries, R., Kubistin, D., Wilson, S., Griffith, D., Buchholz, R. *et* al., Overview of the MUMBA campaign: Measurements of Urban, Marine and Biogenic Air., *Atmosphere*, *in prep.*

Chapter 5: **Ground based solar FTS versus MOPITT**

Edwards, D. P., Emmons, L. K., Jones, N. B., Paton-Walsh, C., Deutscher, N. M., Buchholz R. R., and Griffith, D. W. T., Satellite and ground-based remote sensing of carbon monoxide over Australasia: Linking global and local scales., *in prep.*

Chapter 7: **GEOS-Chem versus ground based solar FTS**

Buchholz, R. R., Paton–Walsh, C., Hurley, P., Jones, N. B., Kettlewell, G., Griffith, D. W. T., Zeng, G. and Smale, D., Total column CO and HCHO measurements compared with the Global Chemical Transport Model GEOS-Chem in Australasia, *Atmospheric Chemistry and Physics, in prep.*

Velazco, V.A., Macatangay, R. C., Griffith, D. W. T., Deutscher, N. M., Jones, N. B., Paton-Walsh, C., Buchholz, R. R., Kettlewell, G. and Shi, X., Towards Pinpointing GHG & Pollution Hot Spots: Synergistic Use of High-Resolution Ground–Based Remote Sensing Measurements and a Lagrangian Transport Model, *in prep.*

Abstract

There remains much uncertainty in processes driving atmospheric composition, particularly in relation to the Southern Hemisphere. This thesis examines contemporary atmospheric composition in the poorly characterised Southern Hemisphere, focusing on the Australasian region. A combination of measurements and modelling has been used to investigate atmospheric composition over a range of time and spatial scales.

The first semi-continuous record of in situ measurements of CO, CO_2, CH_4, N_2O and $\delta^{13}C$ from the University of Wollongong (UOW), Australia, was developed using FTIR measurements from 2011 through to 2013. This record was used to understand the boundary layer atmospheric signature of the UOW site. Clean air was found to arrive at UOW in approximately 10% of air masses. Whilst the dataset represented a short record, preliminary trends were determined for background air for CO (-3.8 [95th: -4.76, -3.08] nmol mol^{-1} per year), CO_2 (2.05 [95th: 1.19, 2.66] μmol mol^{-1} per year) and CH_4 (3.5 [95th: 0.24, 5.34] nmol mol^{-1} per year). Annual cycles in background data reflect the widespread influence from Southern Hemispheric biomass burning during Austral spring. Daily cycles, cluster analysis and O_3-CO correlation analysis were performed, revealing an atmosphere strongly influenced by urban and industrial sources.

Total column CO measurements from the ground-based solar Fourier-Transform infrared Spectrometer (FTS) at UOW were compared with satellite-based measurements from the Measurements Of Pollution In The Troposphere (MOPITT) instrument. Direct comparison of vertical column amounts from these instruments allowed distinction between local and transported pollution to the site. Anomalous CO events were identified in the 2000-2010 record of each instrument and back trajectory analysis was used to identify likely contributing causes. High anomalous events in both instruments resulted from large-scale transported biomass burning sources from Africa, South America or northern Australia. Two large-scale biomass burning events within the east Australian region were also measured by both instruments, Sydney bushfires in December 2001-January 2002 and Canberra bushfires in January 2003. Anomalously low column amounts corresponded with transported air-masses from the northern latitudes surrounding Antarctica. Anomalies found only in the FTS measurements reflected urban outflow, local biomass burning, or local industrial activity and were accompanied by slow moving air masses.

Two global models have been used in this study, the Global Chemical Transport Model, GEOS-Chem and the Australian Community Climate Earth System Simulator (ACCESS). Differences between measurements and the GEOS-Chem model were investigated for CO, HCHO and C_2H_6. GEOS-Chem simulations of daily averaged trace gas amounts were compared with ground-based FTS measurements for three stations in the Australasian region: Wollongong (34.4°S, 150.9°E), Darwin (12.4°S, 130.9°E) and Lauder (45.0°S, 169.7°E). GEOS-Chem performed well in matching column measurements of CO and HCHO. Ethane was biased high in the model, which was later found to be due to emission inventory biases. Analysis of CO was extended to cover the entire region by comparing month averaged GEOS-Chem results with MOPITT measurements over Australasia, and was found to generally reproduce spatial patterns. However, a low bias in GEOS-Chem was found over the whole region during September to November, and was concluded to be due to underestimates of emissions in the GFED2 biomass burning inventory.

Evaluation was performed for one of the first simulations of the Earth System Model ACCESS, in Chapter 8. Average annual cycles of total column values from ACCESS were compared with both FTS measurements and the GEOS-Chem model. As a result of the ACCESS evaluation, several recommended improvements were made for the model. In particular, it was recommended to implement a more recent emission inventory due to annual cycle mis-matches in CO and C_2H_6. Also, inclusion of the updated isoprene chemical mechanism would improve the magnitude of HCHO and C_2H_6. Finally, NO_2 stratospheric boundary conditions corrections are required to accurately represent Southern Hemisphere atmospheric composition.

Contents

List of Figures

List of Tables

Part I

Background Information

Chapter 1

Tropospheric Chemistry

1.1 Why study atmospheric composition?

The atmosphere is imperative for life on the surface of this planet, both in terms of creating a habitable climate and for respiration. Atmospheric composition has a large potential to affect human health. Recently, the World Health Organisation estimated that in 2012, 3.7 million premature deaths occurred worldwide due to outdoor air pollution (World Health Organization, 2014). Outdoor air pollution is particularly an urban issue. With more than 50% of the world's population living in urban areas in 2013, and this percentage projected to rise to 70% by 2050 (United Nations, 2012; World Health Organization, 2013), outdoor air pollution is a globally important issue.

Along with directly affecting human health, atmospheric composition influences Earth's radiative balance (Arrhenius, 1896; Hartmann et al., 2013b). Affecting the energy balance of the atmosphere through altering atmospheric composition has implications for global dynamics. Altering Earth's meteorology will lead to a future shift in global climate, which may require human migration from newly inhospitable locations (Hartmann et al., 2013b). Therefore, changing atmospheric composition has the potential to affect the stability of habitats.

We have entered the era now defined as the Anthropocene, where humans have become a major geological force (Crutzen, 2002). Human activities are altering atmospheric composition at unprecedented rates to levels not seen for millenia (Hartmann et al., 2013b). In order to minimise the detrimental effects human activities have on the globe, we must study and analyse both natural and anthropogenic contributions to the

atmosphere, and implement solutions to diminish human impact.

This thesis is concerned with studying trace chemicals present in Earth's atmosphere. The main theme is to characterise atmospheric composition for the poorly studied Southern Hemisphere, over the Australasian region. This research is predominantly interested in changes in chemical composition over time, and uses a combination of measurements and modelling to investigate aspects of atmospheric composition.

1.2 Tropospheric trace gases

The majority of the atmosphere contains molecular nitrogen (N_2) with a dry-air molar ratio of approximately 0.78 mol N_2/mol air (i.e. 78%), oxygen (O_2) approximately 0.21 mol/mol (21%) and argon (Ar) ∼0.0093 mol/mol (∼0.93%) (Jacob, 1999). The remaining ∼0.07% of the atmosphere consists of other gases in trace amounts (Crutzen & Lelieveld, 2001; Jacob, 1999). While present at low concentrations, many trace gases are highly reactive, meaning that a concentration perturbation may result in a significant effect on the atmosphere (Crutzen & Lelieveld, 2001). In order to quantify atmospheric perturbation effects, it is important to study sources and variability of these trace gases.

The atmosphere of Earth consists of several layers as shown in Figure 1.2.1. Different layers are defined by atmospheric properties, and mainly by the temperature profile with altitude. Approximately 99.9% of all atmospheric mass lies within the lowest two layers, the stratosphere and troposphere. The lowest layer, the troposphere, stretches from the Earth's surface to the tropopause at an average altitude of 14 km, and is characterised by decreasing temperature with height. Chemistry within the troposphere is of particular interest as it is the region that humans interact with every day. Being in contact with Earth's surface, the troposphere is directly affected by surface emissions. Both anthropogenic and natural emissions of trace gases from the surface may alter atmospheric composition (Marshall & Plumb, 2008; Wayne, 2000). Trace gases may affect Earth's atmosphere in two ways: alteration of chemical reactivity and/or change in radiative balance. The former may affect air quality, while the latter influences climate (Brune, 2007; Crutzen & Lelieveld, 2001).

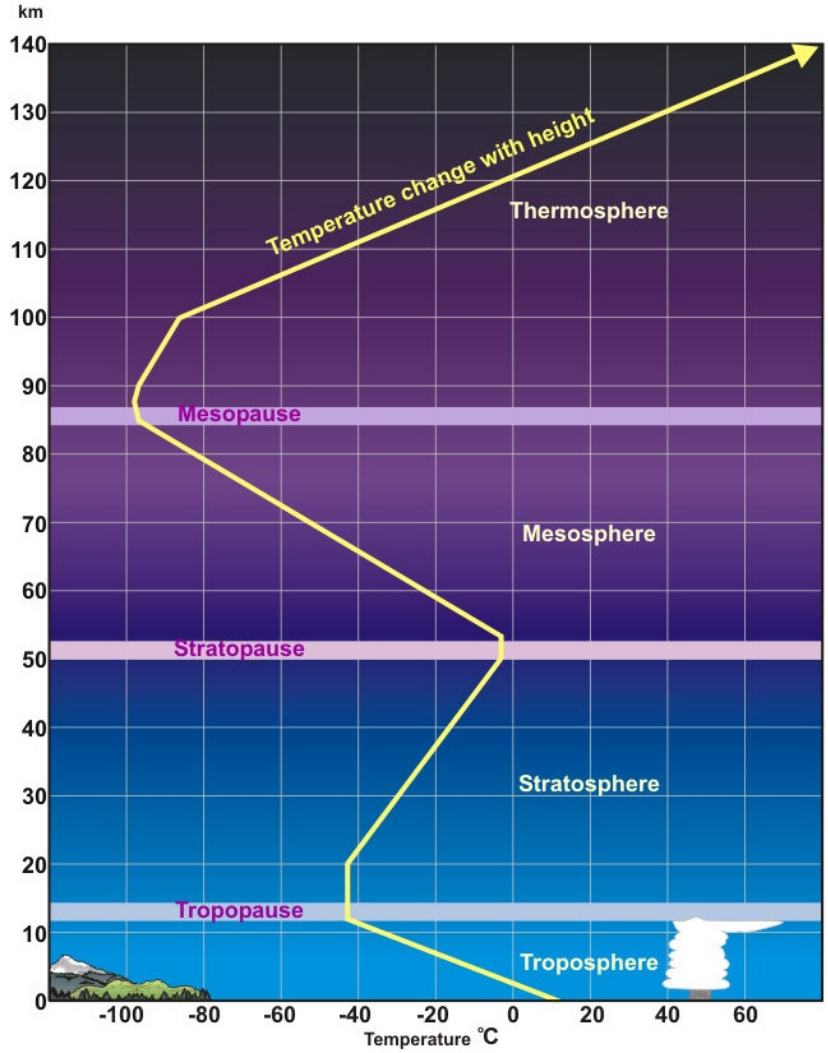

Figure 1.2.1: Temperature profile of the atmosphere showing atmospheric layers. Sourced from NOAA: http://www.noaa.gov/

1.2.1 Chemistry

The most important photochemically active trace gases in the troposphere are ozone (O_3), nitrogen oxides (NO_X), carbon monoxide (CO) and volatile organic compounds (VOCs) (Wayne, 2000). The photochemical pathways of these gases provide the major source of the highly reactive OH radicals, the species primarily responsible for removing pollutants from the atmosphere (Crutzen & Lelieveld, 2001). Thus, O_3, NO_X, CO and VOCs are important due to their influence on the oxidising, or "self-cleaning", capacity of the atmosphere. The production of O_3 is also of interest due to the detrimental health impacts of tropospheric O_3 (Atkinson, 2000; Crutzen & Lelieveld, 2001).

Major atmospheric photochemical pathways of nitrogen oxides, CO and volatile organic compounds involved in tropospheric ozone production have been extensively studied and are well understood (Atkinson, 2000, and references therein). Figure 1.2.2 presents an overview of major reactions occurring in the troposphere associated with O_X–NO_X–VOC chemistry. Tropospheric ozone production, nitrogen dioxide cycling and a general VOC oxidation mechanism are shown.

The main driver of tropospheric chemistry is the hydroxyl (OH) radical, which is predominantly sourced from photochemical destruction of O_3 to the $O(^1D)$ intermediate followed by reaction with atmospheric water vapour (Levy, 1971, 1972; Jacob, 2000), shown on the left of Figure 1.2.2. In areas of low pollution, tropospheric O_3 mainly originates from the stratosphere via turbulent exchange with the troposphere. However, in regions where NO_X (NO_2 + NO) is present, NO_2 is photolytically cleaved to NO, producing $O(^3P)$, which under ambient conditions combines with O_2 to form tropospheric ozone. In the absence of VOCs, a photochemical equilibrium exists between O_3 production from NO_2 photolysis and O_3 destruction via reaction with NO (Equation 1.2.1, Atkinson, 2000).

$$O_3 + NO \longrightarrow O_2 + NO_2 \tag{1.2.1}$$

In the presence of VOCs, the NO preferentially reacts with VOC-peroxy radicals, which recycles NO to NO_2. The NO_2 recycling enhances production of O_3 (Atkinson, 2000). This NO_X cycling is presented in the light-red region of Figure 1.2.2. The VOC molecule is represented as a generic hydrocarbon, RCH_3 (R= aliphatic or aromatic region), at the top of Figure 1.2.2. Alternatively, NO_2 may be regenerated from NO via the reaction with HO_2 (Equation 1.2.2, Atkinson, 2000, Seinfeld & Pandis, 2006a), which additionally regenerates atmospheric OH. Oxidation of VOCs produces HO_2 species, therefore for every one VOC molecule, assuming there is sufficient NO_X, two additional O_3 molecules can be produced via the NO_X cycle.

$$NO + HO_2 \longrightarrow NO_2 + OH \tag{1.2.2}$$

Most of the OH radical produced from O_3 photolysis is used in the oxidation of VOCs. About 30% is used to initiate the VOC oxidation and 70% converts CO to CO_2. The right pathway of Figure 1.2.2 presents the oxidation of a VOC, represented as a generic hydrocarbon RCH_3. The top of the figure indicates VOC degradation initiated by

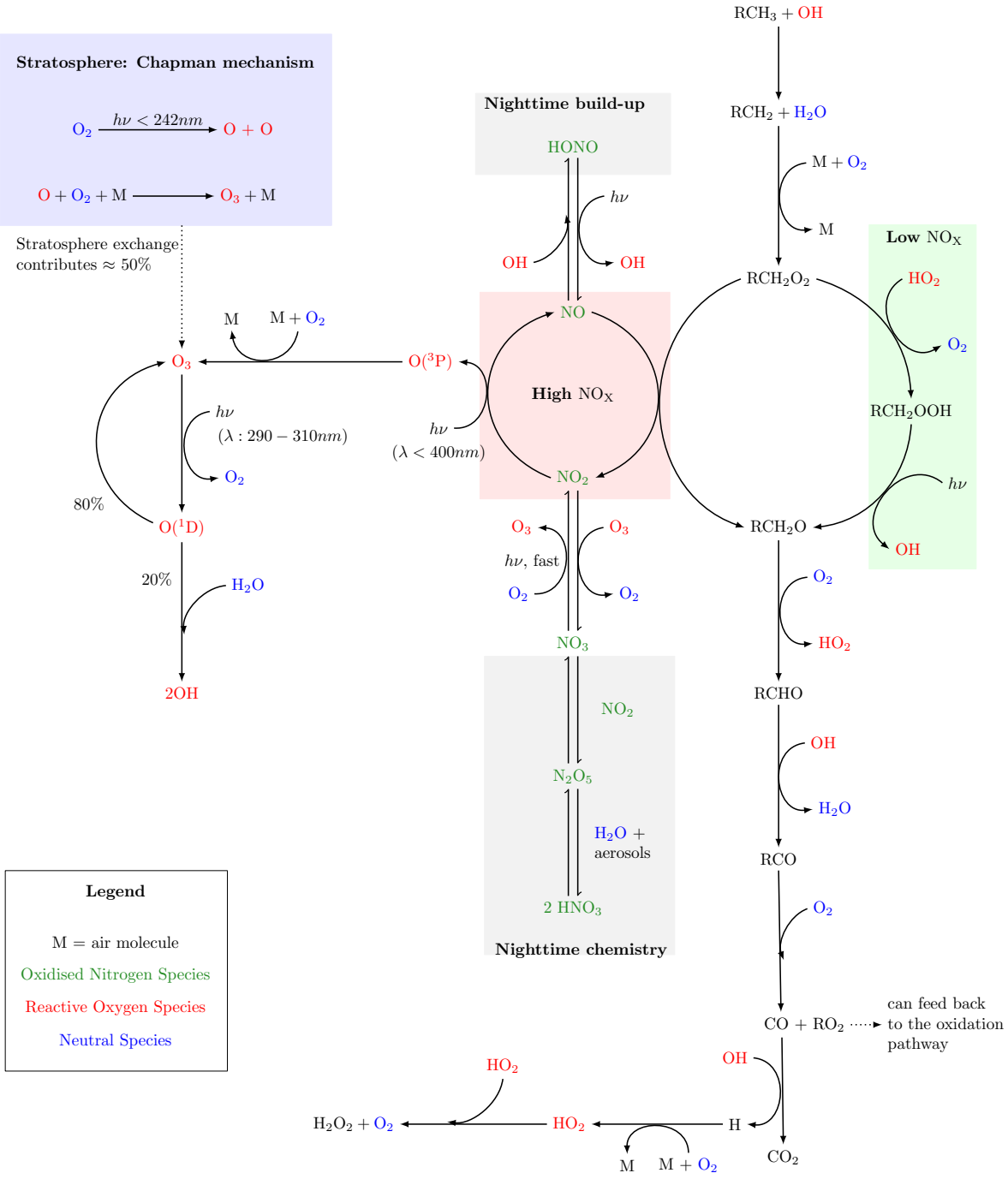

Figure 1.2.2: Major tropospheric reactions in the hydrocarbon oxidation pathway and tropospheric ozone precursor chemistry. Diagram is developed from (Atkinson, 2000; Seinfeld & Pandis, 2006a; Seco et al., 2007; Wayne, 2000).

reaction with OH radical to produce a VOC radical and water. Subsequent reaction of the VOC radical with O_2 gives a VOC peroxy radical, RCH_2O_2.

The peroxy radical may follow several reaction pathways depending upon the atmospheric environment. In high-NO_X environments, the peroxy radical reacts with NO to close the NO_X cycle and produce an alkoxy radical, RCH_2O (left pathway). Alternatively, in remote areas where atmospheric availability of NO_X may be limited and VOCs are still present, a pathway is taken whereby peroxy radicals react first with the atmospheric oxidant HO_2 and then OH, to arrive at the alkoxy radical. This alternative pathway is indicated by the green box on the right hand side of Figure 1.2.2.

From the alkoxy radical, the pathway follows a series of oxidation reactions through an aldehyde to produce CO. Alternate pathways exist from the aldehyde oxidation step, which are of importance during the day (Equations 1.2.3 and 1.2.4).

$$RCHO + h\nu \longrightarrow RCO + H \tag{1.2.3}$$

$$RCHO + h\nu \longrightarrow RH + CO \tag{1.2.4}$$

Any shorter-chain VOCs produced may be fed back into the oxidation pathway.

The final steps of VOC oxidation involves converting CO to CO_2, producing HO_2. The CO species may be either chemically produced at the end of the VOC oxidation pathway, or directly emitted from sources. Combination of two HO_2 molecules forms H_2O_2, which may either be a temporary reservoir of HO_X, or alternatively is very soluble and may be lost via wet deposition. The H_2O_2 species can therefore cause a loss of atmospheric oxidant species, terminating the oxidation chain rather than regenerating oxidants.

Another terminating reaction may result when forming the soluble atmospheric trace gas HNO_3, which when scavenged by wet deposition forms acid rain, providing a removal mechanism for both HO_X and NO_X. The HNO_3 species is produced by reaction of NO_2 with O_3 to form NO_3. Subsequently, another molecule of NO_2 reacts with NO_3 to give N_2O_5 which then reacts with atmospheric water to give two HNO_3 molecules (the complete reaction sequence is shown in the lower grey box of Figure 1.2.2). Alternatively, HNO_3 may be produced via the reaction of NO_2 with OH (Equation 1.2.5). Photolytic decomposition of HNO_3 to NO_2 is fast during the day, and HNO_3 tends to

build up at night (Atkinson, 2000).

$$NO_2 + OH \underset{h\nu,\ \text{fast}}{\rightleftharpoons} HNO_3 \tag{1.2.5}$$

Another important night process is the build-up of HONO through the reaction of OH with NO (top grey box of Figure 1.2.2). This acts as a reservoir of NO_X and leads to a morning spike of NO_2 when the sun rises, drastically affecting atmospheric chemical reactivity (Atkinson, 2000).

As has been discussed here, the major chemical reactions occurring in the atmosphere are complex. Different pathways dominate depending upon the trace gas proportions, thereby affecting the balance of intermediate trace gases. For example VOC oxidation follows different routes depending upon low or high NO_X regimes. Additionally, there are many minor pathways and alternate routes, which have not been discussed here and may become important under certain conditions, such as for remote environments. Determining precisely how changes to the mixture of trace gases in the atmosphere will evolve is a complicated task and requires the use of sophisticated computational modelling.

1.2.2 Sources and lifetimes of targeted trace gases

One driver of chemical reactivity in the atmosphere is the amount of trace gases available, for example as discussed in the previous section with respect to high and low NO_X environments. The amount of any particular trace gas in the atmosphere depends on the amount being sourced, combined with how much, or how fast, the trace gas is being removed. In the troposphere, sources of trace gases may be either direct emissions or the result of photochemical or other chemical reactions. Tropospheric loss processes for a trace gas may be due to chemistry, transport into the stratosphere, or physical deposition. Physical removal includes both dry and wet deposition, that is, direct transfer to the Earth's surface or loss during precipitation.

If we take an Eulerian view, the chemical composition of the troposphere as a whole is affected by mass transfer in (emissions) and out (stratospheric transport), as well as sources (chemical production) and sinks (chemical loss and physical deposition). Overall, the change in total tropospheric burden (or abundance) of a trace gas over time (dQ/dt) depends upon the sum of source product terms minus the sum of loss

terms, described by:

$$\frac{dQ}{dt} = P_n + P_a + P_c - (k_d + k_w + k_c + k_t)Q \tag{1.2.6}$$

where P_n are natural emissions, P_a are anthropogenic emissions and P_c are chemical sources; and k_d, k_w, k_c, k_t are rates of loss via dry deposition, wet deposition, chemical loss and stratospheric transport, respectively. Rates of removal are generally assumed to be first order with respect to the total quantity of trace gas Q (Seinfeld & Pandis, 2006c).

The lifetime of a trace gas indicates how long, on average, a substance remains in the atmosphere before being removed. Under steady-state conditions it is assumed the total tropospheric burden is constant ($dQ/dt = 0$), therefore sources of a trace gas are in balance with sinks. During steady-state, Equation 1.2.6 may be used to determine the lifetime based on loss terms via Equation 1.2.7, or based on product terms via Equation 1.2.8.

$$\tau = \frac{1}{k_d + k_w + k_c + k_t} \tag{1.2.7}$$

$$\tau = \frac{Q}{P_n + P_a + P_c} \tag{1.2.8}$$

Using these equations, calculations of the average expected lifetimes of trace gases in the troposphere have been determined (Warneck & Williams, 2012). The burden of a trace gas, Q, is estimated from an average atmospheric mole fraction, multiplied by the total molar amount of air in the atmosphere. Actual lifetimes may differ considerably from average lifetimes when looking at smaller specific regions of the troposphere, due to non-steady-state processes.

The trace gases studied in this thesis are targeted from a range of locations in the ozone production and VOC oxidation pathway, or selected due to their importance as greenhouse gases. A list of these trace gases, together with their corresponding abundance and lifetime values are presented in Table 1.2.1.

Table 1.2.1: Globally averaged tropospheric amounts and lifetime values of reactive trace gas species investigated in this thesis. Values are taken from Warneck & Williams, 2012, Wayne, 2000 and Seinfeld & Pandis, 2006c, Hartmann et al., 2013a. SH = Southern Hemisphere.

Trace Gas	**Formula**	**Average Amount (nmol mol^{-1})**	**Lifetime**	**Chapter Studied**
Carbon Monoxide	CO	50 (SH)	2 months	3, 4, 5, 6, 7, 8
Nitrous Oxide	N_2O	324	120/114† years	3, 4
Methane	CH_4	1800	8.4/12† years	3, 4
Carbon Dioxide	CO_2	400 (μmol/mol)	5 – 300 years‡	3, 4
Nitrogen Dioxide	NO_2	0.3 – 5 (land)	hours to 2 days (NO_X lower trop.) 19 days (NO_X upper trop.)	4, 8
Ozone	O_3	15 – 50	20 days (trop.)*	4, 8
Formaldehyde	HCHO	0.1 – 5	10 hours (average) 4 hours (hν) 1.5 days (OH)	6, 7, 8
Ethane	C_2H_6	0.4 (SH)	2 months	6, 7, 8
Isoprene	C_5H_8	2 – 5	2-5 hours (average) 1.7 hours (OH) 1.3 days (O_3)	6, 8

† Some species have perturbation lifetimes, that is a change in concentration alters species lifetimes due to feedback mechanisms. Perturbation lifetime (or adjustment time) is the amount of time required to decay back to the initial atmospheric state after an atmospheric pulse (Seinfeld & Pandis, 2006c).
‡ A single lifetime for CO_2 cannot be defined due to the non-steady-state nature of this trace gas in the atmosphere. Depending on the processes included in CO_2 lifetime calculations, the average time a molecule of CO_2 spends in the atmosphere ranges from 5 to over 300 years (Seinfeld & Pandis, 2006c).
*Latest estimates on mean global lifetime of tropospheric ozone (Stevenson et al., 2006; Young et al., 2013)

Carbon Monoxide

Carbon monoxide (CO) is the main trace gas targeted for study in this work and is investigated in each chapter. Tropospheric CO may be sourced from direct emissions or may alternatively result from the photochemical oxidation of higher order VOCs. Generally, direct emission sources of CO are from incomplete combustion, including biomass burning, biofuel burning and urban and industrial fossil fuel usage (Wayne, 2000; Seinfeld & Pandis, 2006c). A major source of CO occurs through the oxidation of methane, which contributes approximately 25% to overall atmospheric sources (Warneck & Williams, 2012). Oxidation of natural VOCs contributes a further ∼30%

to overall sources (Warneck & Williams, 2012). Small proportions of CO are directly emitted from vegetation and oceans. The main loss of CO is through chemical reaction with the hydroxyl radical (OH), with minor losses through uptake by soils or stratospheric exchange (Wayne, 2000; Warneck & Williams, 2012).

Tropospheric abundance of CO in the Southern Hemisphere is on average 50 nmol mol^{-1}, but may be substantially higher in urban environments. Carbon monoxide has a mean global lifetime of 2 months, which makes it an ideal trace gas for studying seasonality, interannual variability and transport of atmospheric pollution (Warneck & Williams, 2012). The lifetime of CO allows for sufficient atmospheric mixing, while being short enough to prevent a well mixed constant-atmospheric composition, allowing atmospheric patterns to be determined.

Formaldehyde

The mixing ratio of formaldehyde (HCHO) typically ranges from 0.3–5 nmol mol^{-1} in the troposphere and can reach values >150 nmol mol^{-1} at some surface locations. Direct sources of HCHO include soil microbial activity, vegetation, industry, vehicular exhaust and biomass burning (Levelt et al., 2006). A major source of HCHO is as an intermediate species in VOC oxidation cycles (in Figure 1.2.2 R=H for RCHO). Formaldehyde is produced as an oxidation product of many VOCs, for example from oxidation of isoprene, methanol and acetaldehyde. As such, HCHO is often used as a proxy for these short-lived and highly reactive species.

While plants contribute to atmospheric loss through uptake of HCHO, the extent of uptake is yet to be determined (Seco et al., 2007). Formaldehyde readily reacts with atmospheric OH, and also has direct photolytic losses. Formaldehyde has a lifetime of less than a day, which can drop to as low as 3–4 hours during daytime in summer. This short lifetime makes HCHO a good species for investigating daily cycles and fluxes over short timescales (Seco et al., 2007; Wayne, 2000).

Ethane

In the Southern Hemisphere, the majority of ethane is emitted from biomass burning. Globally, there is an equal source from co-emission in the transport and production of natural gas. Ethane is mainly lost via VOC oxidation. Over Southern Hemisphere marine environments C_2H_6 mole fraction is a low 0.4 nmol mol^{-1}. Ethane's lifetime of

2 months is the same order as CO, making it a good tracer to evaluate atmospheric transport (Wayne, 2000; Warneck & Williams, 2012).

Others

While CO, HCHO and C_2H_6 are extensively studied in this thesis, examination of additional trace gases has allowed insight into the atmospheric signature of measurement stations, or has helped understand the behaviour of CO, HCHO or C_2H_6.

Isoprene: The C_5H_8 trace gas is a strong indicator of biogenic activity, with emissions of isoprene being determined by biogenic cycles and driven by light and heat. The lifetime of isoprene is the shortest of the gases studied here (∼5 hours), and the main loss mechanism is through reaction with hydroxyl radical (Seinfeld & Pandis, 2006c).

Ozone: Tropospheric O_3 is of particular concern due to detrimental effects on human health (Atkinson, 2000; Crutzen & Lelieveld, 2001). Current concentration trends of tropospheric ozone and precursors differ, depending on location. However, the reason for these trends is still unknown, making tropospheric ozone and chemical precursors a priority area for research (Le Treut et al., 2007; Oltmans et al., 2006; van der A et al., 2008).

Globally, tropospheric ozone is mainly sourced from photochemical production, with a smaller portion transported down from the stratosphere (Seinfeld & Pandis, 2006a). However, up to 45% of surface O_3 can originate from the stratosphere in the Southern Hemisphere (Wayne, 2000). Equivalently, the main sink of O_3 is through photochemical means, with some loss via dry deposition (Seinfeld & Pandis, 2006a). The atmospheric lifetime of O_3 varies greatly depending upon season and location, from a few days in the tropics to a year in the upper troposphere. The current estimate of global mean lifetime is ∼20 days (Stevenson et al., 2006; Young et al., 2013; Warneck & Williams, 2012). Tropospheric ozone is mainly produced via photochemical means and is often found downwind of pollution sources. The relative abundance of O_3, compared with CO can be used as an indicator of ozone production environment in a pollution plume (Fishman & Seiler, 1983).

Nitrogen Oxides: The two nitrogen oxides investigated are nitrogen dioxide (NO_2) and nitrous oxide (N_2O). Nitrogen dioxide together with nitric oxide (NO) form the NO_X family. In the troposphere, cycling between NO_2 and NO occurs rapidly, so they are often combined in source and lifetime analyses. Anthropogenic origins of NO_X

include industry, fossil fuel usage, and biomass burning, while natural sources include lightning, forest fires and soil-based microbial activity (Atkinson, 2000; Levelt et al., 2006; Wayne, 2000). In photochemical reactions, NO_X forms part of a cyclic reaction between NO_2 and NO. The main method of removal is by conversion to HNO_3, followed by wet-deposition of HNO_3 (Warneck & Williams, 2012).

The NO_X family has a residence time of about a day (Leue et al., 2001; Wayne, 2000), making it a good species for investigating fluxes over a short timescale. The relatively short lifetime and associated emission source from anthropogenic origins, make the family a good indicator of urban influenced air. Southern Hemisphere NO_X emission is dominated by biomass burning whereas the majority of NO_X signal in the Northern Hemisphere originates anthropogenically (Penner et al., 1991).

Nitrous oxide has equal sources from oceans, soil microbial activity and anthropogenic origins. Anthropogenic origins include agriculture and industrial sources (Wayne, 2000; Warneck & Williams, 2012). In the troposphere, N_2O is non-reactive. The only loss mechanism is by transport into the stratosphere, where photolysis to N_2 occurs, or alternatively, reaction with stratospheric $O(^1D)$ provides a source of stratospheric NO. The low reactivity of N_2O results in a long lifetime for the trace gas of 120 years (Wayne, 2000). The average global abundance of atmospheric N_2O is 324 nmol mol^{-1} (Hartmann et al., 2013a). Nitrous oxide is also a strong absorber in the infrared, which when combined with its long lifetime makes N_2O of interest for climate studies (Hartmann et al., 2013b).

Carbon gases: Two other carbon gases, CH_4 and CO_2, are investigated briefly as components of in situ measurements in the planetary boundary layer at Wollongong (Chapters 3 & 4). Both are strong absorbers in the infrared, therefore are extensively studied in climate research. Average abundance of both these gases has been steadily increasing during the Anthropocene due to human activity (Hartmann et al., 2013b).

Currently, CH_4 abundance is approximately 1800 nmol mol^{-1} (Hartmann et al., 2013a), with sources from wetlands, agriculture biomass burning and fossil fuel use. The main loss mechanism is via reaction with OH. Stratospheric transport and soil uptake provide minor loss mechanisms. Methane has a lifetime of $\sim$8.4 years (Warneck & Williams, 2012).

Carbon dioxide recently exceeded 400 μmol mol^{-1} at Mauna Loa Observatory (Tans & Keeling, accessed June 2014), which measures well-mixed free-tropospheric air (Keeling et al., 1976; Keeling, 2008). Sources of CO_2 include complete combustion, from biomass

burning to biofuel and fossil fuel use. Also, it is the photochemical end point for oxidation of all atmospheric VOCs. Carbon dioxide is not photochemically active, and therefore is generally lost by physical deposition processes. Additionally, a strong sink process exists during vegetation growth, whereby atmospheric CO_2 is fixed during photosynthesis. Ocean uptake is also an important CO_2 sink (Seinfeld & Pandis, 2006c).

Due to the non-steady-state of CO_2 processes in the earth system, a single lifetime for atmospheric CO_2 cannot be defined. Depending upon the processes included in lifetime calculations, the lifetime can range from 5 to over 300 years. When lifetime calculations include achieving pre-industrial atmospheric abundance of CO_2, mixing with the deep ocean is included, and results in even longer lifetimes, on the order of millennia (Seinfeld & Pandis, 2006c; Ciais et al., 2013).

1.3 Southern Hemispheric atmospheric composition

Southern Hemispheric atmospheric composition is dominated by different processes compared to those of the Northern Hemisphere. Approximately 80.9% of the Southern Hemisphere is ocean and 19.1% is land, while in comparison 60.7% of the Northern Hemisphere is ocean and 39.3% is land (Sverdrup et al., 1942). Land based trace gas sources are diluted by mixing with air from the relatively clean atmospheric environments present over oceans. This dilution is greater in the Southern Hemisphere than in the Northern Hemisphere due to the relative amounts of land to ocean. Additionally, ∼90% of the world's human population live in the Northern Hemisphere, which is reflected by large anthropogenic sources of many trace gases, influencing atmospheric composition across the region. In contrast, anthropogenic emissions in the Southern Hemisphere tend to dominate atmospheric composition in small areas around urban environments. For these reasons, amounts of atmospheric trace gases tend to be lower in the Southern Hemisphere.

Although absolute magnitudes tend to be smaller in the Southern Hemisphere, the region presents a valuable opportunity for studying atmospheric composition due to there being limited complicating factors. For instance, identifying a source location in the Southern Hemisphere is less difficult due to fewer contributions from multiple possible source regions.

Well known major drivers of change in atmospheric composition for the Southern Hemisphere are mainly natural. Biomass burning is a dominant contributor, particularly for the trace gases CO and C_2H_6 (Edwards et al., 2006a,b; Xiao et al., 2008; Wayne, 2000). For those species which are not predominantly sourced from biomass burning, biogenic emissions become important. For example, biogenic emissions of isoprene are extremely important contributors to the magnitude and seasonality of HCHO, through isoprene oxidation (Pfister et al., 2008).

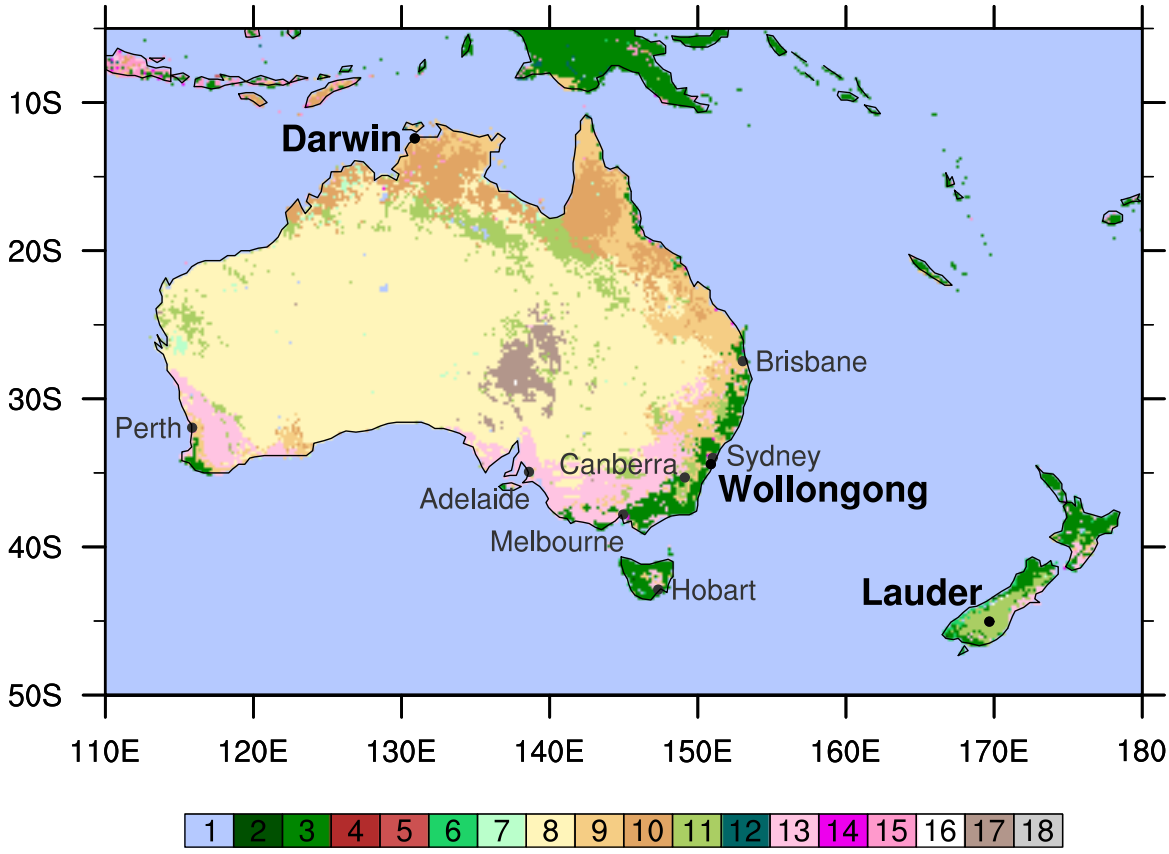

Figure 1.3.1: Location of major Australian cities (small font) and stations used in this study (bold font) overlaid on a MODIS Land-type map for 2001 (United States Geological Survey (USGS), 2014). Locations are shown as filled circles. Land types are classified according to the International Geosphere-Biosphere Programme (IGBP): **1**-water bodies, **2**-evergreen needleleaf, **3**-evergreen broadleaf, **4**-deciduous needleleaf, **5**-deciduous broadleaf, **6**-mixed forests, **7**-closed shrubland, **8**-open shrublands, **9**-woody savannas, **10**-savannas, **11**-grasslands, **12**-permanent wetlands, **13**-croplands, **14**-urban and built-up, **15**-cropland/natural mosaic, **16**-snow and ice, **17**-barren/sparsely vegetated, **18**-unclassified & fill values.

Currently, there remain uncertainties in our knowledge of atmospheric trace gases, particularly for the Southern Hemisphere. This project investigated spatial and temporal attributes for the targeted tropospheric trace gases, with particular focus on the Australasian region (10°S–50°S, 110°E–180°E). A plot of the Australasian region is displayed in Figure 1.3.1, and indicates different land types based on the International Geosphere-Biosphere Programme (IGBP) classifications. Data displayed is from the MODIS 0.05° resolution, yearly product for 2001 (MCD12C1, United States Geological Survey (USGS), 2014).

The East coast of Australia is the most populated area of the region, with major urban areas of Brisbane, Sydney and Melbourne. The main agricultural region is also located on the east of the Australian continent, stretching halfway into the Bight, near the city of Adelaide. Additional agricultural land is found in the southern region of Western Australia, close to Perth. Much of central Australia is dry, shrubland and desert. Northern Australia above 20°S is dominated by grassland and savanna land-types.

New Zealand is more temperate than the Australian continent and is dominated by grassland and evergreen forest regions. Due to the location of New Zealand at the boundary of two continental plates, volcanism is prevalent. Additionally, collision between these two plates has created the Southern Alps along the Alpine Fault, stretching the length of the South Island.

1.4 How do we study atmospheric composition?

Atmospheric composition may be studied directly through measurements or via theory using computational modelling. Models enable testing of our current understanding of the atmosphere. Research which includes a combination of models and measurements recognises the complementary nature of theory and observations. Relating model output to measurements quantifies model accuracy. Where models perform well, they can be used to predict and explain atmospheric composition, and where models underperform, they indicate that our understanding requires updating.

1.4.1 Measurements

Atmospheric measurements help assess the current state of the atmosphere by directly determining atmospheric composition. Techniques for measuring composition are many

and varied, ranging from in situ techniques to remotely sensed spectroscopic methods. Measurements are not perfect and their uncertainty parameters must be taken into account when analysing any results.

The majority of measurements used in this thesis are from instruments using spectroscopic methods exploiting the infrared (IR) region of the spectrum. Spectroscopic instruments take advantage of the property that many trace gas molecules absorb IR radiation, due to rotational-vibration transitions. Importantly, IR absorption magnitudes are directly related to the amount of trace gas, allowing trace gases to be quantitatively determined in the atmosphere. Also, each molecule has a unique IR spectral signature (Burrows et al., 2011). Spectroscopic methodology and details of instrumentation used to measure atmospheric composition for this research are fully described in Chapter 2.

Measurements covering a range of spatial and temporal resolutions has been employed in order to gain a broad understanding of atmospheric processes. Furthermore, different measurement techniques are appropriate for different aims. For example, satellite measurements, while temporally sparse, provide information about the spatial distribution of a trace gas. Spatial distribution can help elucidate transported sources. Also, satellites can obtain measurement in difficult areas, such as the Australian desert which has limited infrastructure. However, satellite instruments cannot be used to determine diurnal cycles, which is particularly important for trace gases with shorter lifetimes. Additionally, while spatial distribution may be determined, the satellite spatial resolution (e.g. 22 x 22 km) may be too coarse to investigate trace gases at a local level.

In contrast, remote sensing measurements taken at one location, such as from ground based solar Fourier Transform infrared Spectrometers (FTS), cannot directly impart information about spatial distribution of trace gases, but can give time evolution patterns of trace gases under higher resolution. This allows diurnal cycles to be better understood. FTS measurements also have much higher precision than satellite measurements and consequently are also helpful in determining local sources of trace gases, particularly shorter-lived species such as HCHO. Solar FTS measurements are heavily influenced by major transport events or large local sources, with small local sources being diluted in the total column. Since FTS uses the sun as an IR source, a shortfall of this method is that measurements may only be taken during the day in cloud-free conditions. Therefore, some information about the diurnal cycle and night-time conditions are missed.

In situ FTIR measurements cover the entire diel time period as opposed to solar FTS which can only measure during the day, or satellite measurements which overpass each site once or twice a day. Thus in situ FTIR have a more dense coverage of trace gas evolution throughout the day at a particular location. However, in situ measurements may be influenced by very local sources and the extent of atmospheric mixing, therefore the chosen location of the in situ instrument can influence the measurement results, and analysis procedures need to be quality controlled. In this case, the solar FTS vertically integrated measurements are superior because they are less influenced by the amount of vertical mixing and so are easier to interpret. Further detail about measurement methodology and analysis procedure can be found in Chapter 2.

1.4.2 Modelling

Atmospheric models are extensively used in atmospheric research, and are key in linking observations with theoretical knowledge. Computational models use our best current understanding of atmospheric chemical and physical processes to computationally reproduce atmospheric composition and properties. Comparison with observations identifies weaknesses in theoretical understanding, iteratively leading to improved models (Seinfeld & Pandis, 2006b; Dameris & Jöckel, 2013).

Many advantages arise from using models to study atmospheric composition. Measurements are often restricted in time or space, whereas models allow interpolation over a larger time or space domain. Models are also helpful in areas where measurements are sparse, difficult to obtain, or are simply unavailable. Another advantage is that contributions of model components to atmospheric state can tested. Such component testing is not possible in the real atmosphere. For example, one may wish to keep global emissions constant to determine the response of atmospheric composition due to chemistry or dynamics. Additionally, models may track components either forward or backward in time. Overall, models give a repeatable, and flexible method to study the atmosphere over a range of spatial and temporal scales.

Understanding the drivers of atmospheric composition increases our knowledge of variability and long term trends. With this knowledge we can hypothesise future changes in processes that consequently allows prediction of future atmospheric conditions. Short-term future simulations allow forecast of air quality to inform the public or plan measurement campaigns. Longer term simulations provide predictions of future atmospheres in a changing natural-anthropogenic influenced environment.

There are numerous atmospheric model types, which have advantages depending on the application. Models span 1-D box models, which are useful for investigating new chemical mechanisms; through 2-D column-models, which are used to understand global average atmospheric properties or a specific region; and finally to global 3-D models, which are used to study synoptic scale atmospheric properties (Seinfeld & Pandis, 2006b).

Modelling atmospheric composition requires consideration of several aspects, namely dynamics, emissions, chemistry and removal processes. These components may be either parameterised or fundamentally described. Advances in computational efficiency have allowed an increase in model complexity, which can be achieved in several ways. Models can move to higher resolution, which allows explicit representation of previously parameterised sub-grid dynamic processes. Additionally, increased chemicals and chemical reactions can be included in model algorithms. Feedback mechanisms may also be included. For example, chemistry-climate models are a subset of models where feedback from chemistry is directly included into the climate model. More complex models being developed are Earth-System Models, which aim to include a multitude of feedbacks (Dameris & Jöckel, 2013).

Ultimately, atmospheric models take our best current understanding of processes and simplify them into a workable model. Due to assumptions and simplifications, model output must be verified and uncertainties quantified, before simulations can be used confidently to probe atmospheric properties.

1.5 Thesis outline and aims

This thesis examines contemporary atmospheric composition in the poorly characterised Southern Hemisphere, focusing on the Australasian region. A combination of measurements and modelling has been used to investigate atmospheric composition over a range of time and spatial scales. Part I introduces background information necessary for interpreting this thesis. The majority of research carried out during this PhD can be divided into two categories: one category which analyses measurements to interpret atmospheric composition (Part II), and a second category which includes the use of global 3-D atmospheric model simulations (Part III).

Part II of this thesis presents research concerned solely with measurements at Wollongong, Australia. Chapter 3 develops the first semi-continuous record of in situ CO, CO_2, CH_4, N_2O and $\delta^{13}C$ at the University of Wollongong (UOW), Australia, using FTIR measurements from 2011 through to 2013. Calibration techniques, cross-sensitivity analysis, uncertainty analysis and quality control is presented. Subsequently, in Chapter 4 the ambient semi-continuous record is analysed to help understand the Wollongong atmospheric signature. Daily, weekly and annual cycles, cluster analysis and O_3-CO correlation analysis were performed to help understand contributions to atmospheric composition over Wollongong. Although influenced strongly by urban and industrial sources, clean air was found to arrive at UOW in approximately 10% of air masses. While the dataset represented a short record, preliminary trends were determined for background air for CO, CO_2 and CH_4. Trends were not computed for N_2O or $\delta^{13}C$ due to instabilities in their records. The UOW site was also investigated for how well it represented the Wollongong atmosphere by comparing measurements over a 9-week period with those from another site within the region.

In Chapter 5, Wollongong total column CO measurements are investigated from the ground-based solar Fourier-Transform Infrared Spectrophotometer (FTS). Ground-based measurements are compared with satellite-based measurements taken with the Measurements Of Pollution In The Troposphere (MOPITT) instrument. Direct comparison of vertical column amounts from these instruments, which have different viewing platforms, provided a distinction between local and transported pollution. Furthermore, anomalous CO events were identified in the 2000-2010 record and contributing causes were determined using back trajectory analysis.

Part III of this thesis uses global atmospheric modelling, with a focus on interpreting Australasian atmospheric composition. Two global 3-D Eulerian models have been used in this study, the Global Chemical Transport Model, GEOS-Chem and the Australian Community Climate Earth-System Simulator (ACCESS). These models are introduced in Chapter 6. Differences between model and measurements were investigated for CO, HCHO and C_2H_6. In Chapter 7, GEOS-Chem simulations of trace gases were compared with ground-based FTS measurements for three stations in the Australasian region: Wollongong, Darwin and Lauder. GEOS-Chem performed well in matching column measurements of CO and HCHO. Ethane was biased high in the model, and emission inventory inaccuracy was identified as the cause of this bias. Analysis of CO was extended to cover the entire region by comparing month averaged GEOS-Chem results with MOPITT measurements over Australasia.

Finally, an evaluation was performed for a first simulation of the Earth-System Model ACCESS, in Chapter 8. Average annual cycles of total column values from ACCESS were compared with both FTS measurements and the GEOS-Chem model. As a result of the ACCESS evaluation, several recommended improvements were made for the model. In particular, it was recommended to implement a more recent emission inventory to reduce annual cycle mis-matches in CO and C_2H_6; to include the updated isoprene chemical mechanism to improve the magnitude of HCHO and C_2H_6; and finally to correct NO_2 stratospheric boundary conditions to accurately represent Southern Hemisphere atmospheric composition.

Part IV, summarises the outcomes and discusses several future research directions.

An additional aim of the work performed in this PhD, was to familiarise the author with a variety of advanced techniques used in studying atmospheric composition, including both instrumental and computational techniques. Specifically, skills were developed in running of and interpreting output for spectroscopic instruments both for in situ and remotely sensed measurements. The modelling portion of the project required using computational techniques and packages associated with high-performance computing, and included creating programs to interpret large atmospheric datasets.

Part II

Measurements

Chapter 2

Spectroscopic measurements of trace gases in the atmosphere

2.1 Spectroscopic retrieval theory

The majority of measurements used in this thesis are from instruments using spectroscopic methods exploiting the infrared (IR) region of the spectrum. Trace gas molecules absorb IR radiation due to rotational-vibration transitions determined by intramolecular bond properties. Importantly, IR absorption magnitudes are directly related to the amount of trace gas, meaning trace gases can be quantitatively determined in the atmosphere. Vibrational energy levels within a molecule tend to have larger spacing than rotational states, therefore the position of an IR absorption peak is indicative of a vibrational mode, with spectroscopic fine structure due to rotational state energies. The combination of transitions available within a molecule gives rise to a unique IR spectral signature for each molecule (Burrows et al., 2011).

For example, the trace gas CO has one vibrational mode, a stretching along the triple bond axis. This vibration, combined with rotations, gives rise to a set of energy levels in the IR range (Burrows et al., 2011). Figure 2.1.1a shows some fundamental vibrational–rotational energy levels with example allowed transitions. An instrumental infrared spectrum of the fundamental CO transition is shown in Figure 2.1.1b, depicting wavenumbers corresponding to energy transitions. This pattern is known as a P–R spectrum, where the P–branch is at lower wavenumbers (i.e. lower energy) and indicates transitions to a higher vibrational mode with a lower rotational energy compared

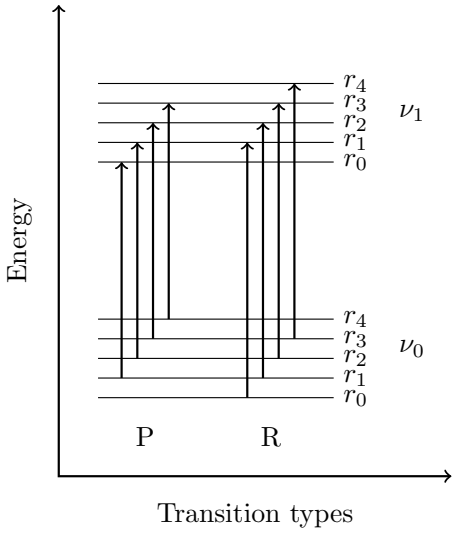

(a)

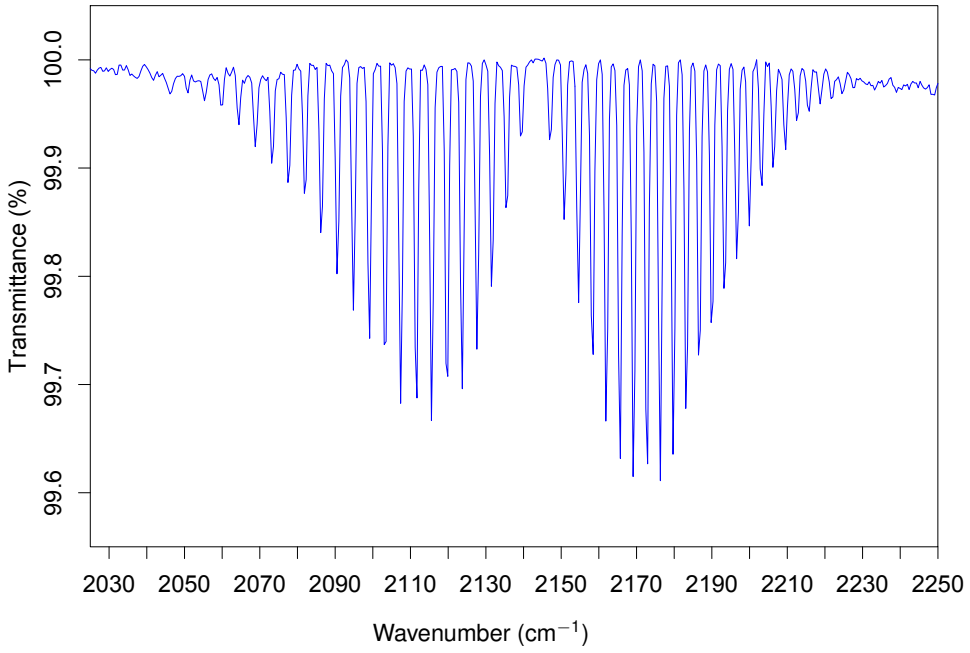

(b)

Figure 2.1.1: Fundamental vibrational-rotational transitions in CO. (a) Energy level diagram with example transitions in CO, showing rotational energy levels (r_i) within vibrational energy levels (ν_i). Example fundamental P and R transitions are shown between energy levels. (b) Example CO IR absorption (as transmittance) from the in situ FTIR analyser, measured in a sample of house N_2 gas on 2013-09-25. The characteristic P and R branches are seen, with P <2143 cm^{-1} and R >2143 cm^{-1}.

to the ground state. The R–branch indicates those transitions to a higher vibrational mode with a higher rotational energy (Banwell & McCash, 1994; Burrows et al., 2011). The fundamental transitions of CO are centred at 2143 cm^{-1} with the first overtone at 4260 cm^{-1} (Banwell & McCash, 1994; Rothman et al., 2013). Transitions above the first overtone are outside the IR region.

Molecules with a higher number of atoms and non-linear shapes have more complex IR spectra, but resulting IR absorption follow the same rules. Hetero-atomic diatomic and polyatomic molecules have the strongest absorption, as infrared absorption leads to a change in molecular dipole moments. Due to symmetry in the molecules, vibrations in O_2 and N_2 do not induce dipole moments, therefore these major atmospheric components are essentially transparent to IR, introducing the possibility of detecting atmospheric trace gases (Burrows et al., 2011). A record of IR absorption for trace gases at reference temperatures and pressures has been compiled in the HITRAN (HIgh resolution TRANsmission) database (Rothman et al., 2009, 2013). HITRAN data are derived by fitting measured spectra over a range of temperature and pressure conditions. The spectrum fitting calculations include parameters that may be either empirical, or determined by quantum-mechanics. For more fundamental discussions of vibrational and rotational transitions and IR radiation see Banwell & McCash, 1994 or Herzberg, 1950 .

A natural broadening in spectral peaks occurs due to uncertainty in the energy released by the excited molecule. Uncertainty in energy released is a result of the Heisenberg conjugate states, combination of the lifetime of an excited state with uncertainty in the energy of the excited state. All excited states within molecules have a natural lifetime due to intrinsic molecular properties, but this is usually very small, resulting in $\sim 10^{-6}$ cm^{-1} broadening. Pressure is the main form of uncertainty broadening in the atmosphere. In pressure broadening, collisions with other gas particles reduce the lifetime of the excited state, thereby broadening the line width. Line width is proportional to pressure, so that at high pressures line widths will be large and at low pressures, line widths will be small. The other major form of atmospheric line broadening is due to Doppler effects, which are dependent upon interaction between the velocity of the trace gas molecule, and the incoming IR. Infrared line shapes from atmospheric measurements are a combination of Lorentzian (pressure broadened) and Gaussian (Doppler broadened) shapes. The combination of these two modes of broadening is known as the Voigt line shape (Burrows et al., 2011).

Trace gas measurements from three main instruments are used in this thesis: a ground

based in situ Fourier Transform Infrared spectrometer (FTIR); a ground based solar Fourier Transform Infrared spectrometer (FTS); and a satellite based correlation radiometer. All three instruments use the properties of IR absorption by trace gases and record atmospheric IR spectra.

2.2 Michelson interferometer

Two of the instruments in this study use Fourier Transform Infrared (FTIR) methods to record atmospheric infrared spectra. The principle behind FTIR is that a complex wave can be decomposed into principal frequency components using the Fourier Transform method. The instruments use a Michelson interferometer (Figure 2.2.1) to recombine source radiation at different frequencies, producing an interferogram. A Fourier transform then converts the interferogram into a spectrum of intensity versus frequency (Davis et al., 2001; Griffiths & de Haseth, 2007).

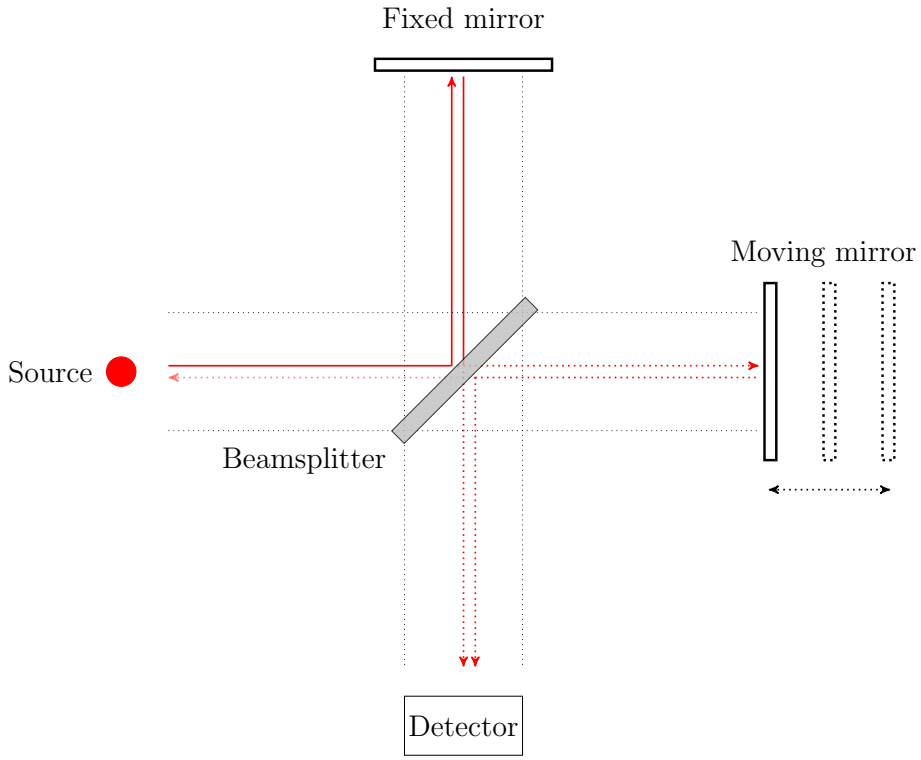

Figure 2.2.1: Diagram of components and workings of a Michelson interferometer. Red lines indicate path of radiation beam.

IR radiation entering the Michelson interferometer is partially reflected to a fixed mirror and partially transmitted to a moving mirror. The moving mirror introduces an optical path difference (OPD) to a recombined beam, allowing constructive and destructive interference depending on OPD relative to the wavelength of radiation (Davis et al., 2001; Griffiths & de Haseth, 2007). Collection of interferograms results in very complex combinations of frequencies being resolved at slower detector speeds. The infrared beam may be modulated either before being passed through the sample, as in the case of in situ FTIR, or after being passed through the sample, as is performed in solar FTS. Further instrument detail of these two FTIR-based instruments are discussed in the following sections.

2.3 In situ FTIR

The in situ FTIR instrument prototype was first developed at UOW by Esler and Griffith (Esler et al., 2000; Griffith, D. W. T. and Galle, B., 2000) and has been thoroughly described with specifications most recently in Griffith et al., 2012. Briefly, the in situ FTIR spectrometers used in this thesis are comprised of a low spectral resolution Bruker IR-Cube (1 cm^{-1}), combined with a White cell (White, 1942) and a thermoelectrically-cooled Mercury Cadmium Telluride (MCT) detector. The infrared source is a heated SLC globar and the IR beam is modulated by passing though a CaF_2 beamsplitter in a Michelson interferometer. The modulated beam is reflected through an atmospheric sample within the White cell to produce a folded path length of 24 metres.

The in situ FTIR instrument measures in the 1750–5500 cm^{-1} IR range, which covers the 2143 cm^{-1} region of CO, the main trace gas targeted in this thesis. Additionally, absorption ranges for CO_2, $^{13}CO_2$, CH_4, N_2O, and H_2O are covered, therefore these trace gases are concurrently measured. An example mid-infrared spectrum taken with the in situ FTIR is shown in Figure 2.3.1, with major spectral characteristics indicated. Spectra are collected over 3 minutes (104 co-added spectra). Recorded spectra are divided by a background spectrum, taken under vacuum conditions of the White cell. Dividing by the background spectrum ensures purely transmission spectra remain. An example of background correction is shown graphically in Figure 2.3.1. Once co-added spectra have been divided by the background spectra, they are ready to be analysed for trace gas constituents.

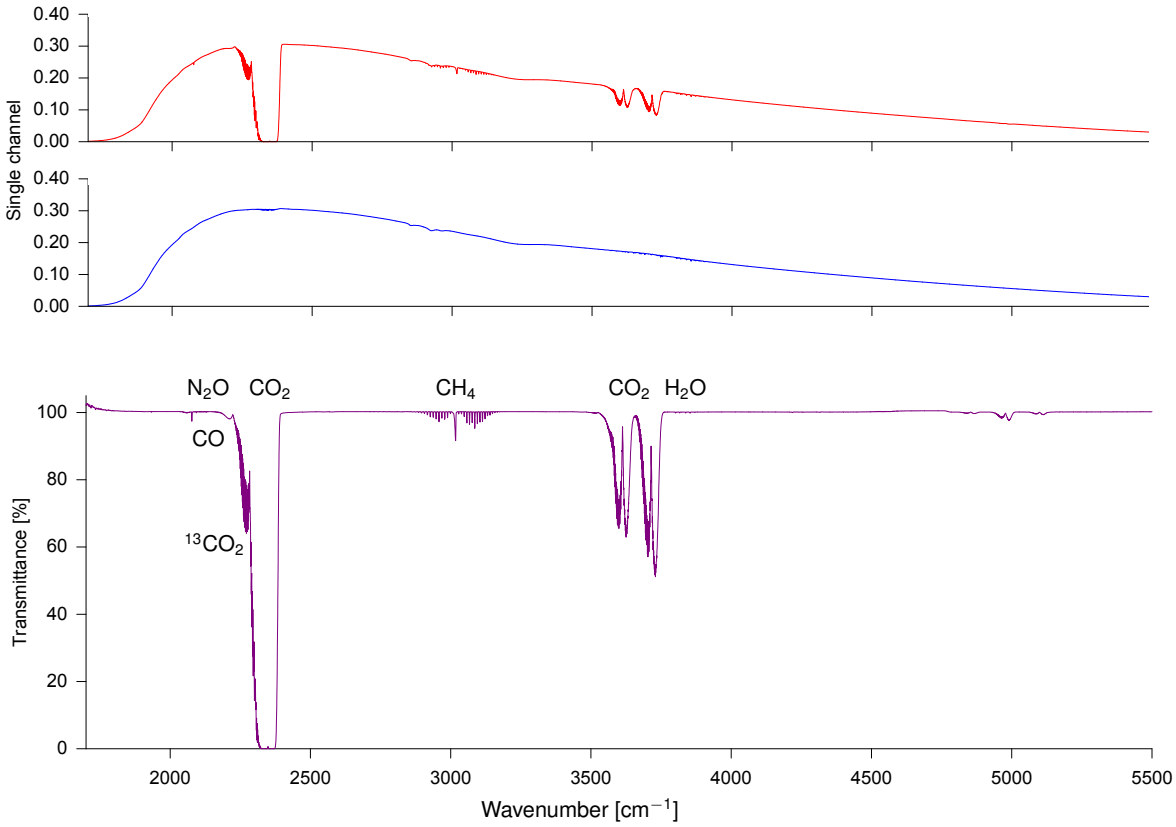

Figure 2.3.1: Example of a recorded spectrum (104 co-added scans) taken with the in situ FTIR instrument at UOW. The division of recorded spectrum (top, red) by background (middle, blue) results in a transmittance spectrum (bottom, purple). Spectral features associated with main trace gases are indicated on the transmittance spectrum.

2.3.1 Retrieval of trace gases using MALT

Retrieval of an amount of trace gas from an IR spectra requires the use of computational programs. In the case of the in situ FTIR instrument, spectra are analysed quantitatively using the non-linear least-squares program MALT (Multiple Atmospheric Layer Transmission) (Griffith, 1996; Griffith et al., 2012). MALT uses a forward model to produce a simulated transmittance spectrum, which is compared with the measured spectrum and iteratively improved until residuals reach a minimum.

After dividing by the background spectrum, transmittance spectra are simulated by including initial estimates of trace gas amounts of all absorbing gases in the spectral window, combined with reference lines from the HITRAN database, knowledge of the instrument line shape (ILS) and measured parameters such as temperature and pres-

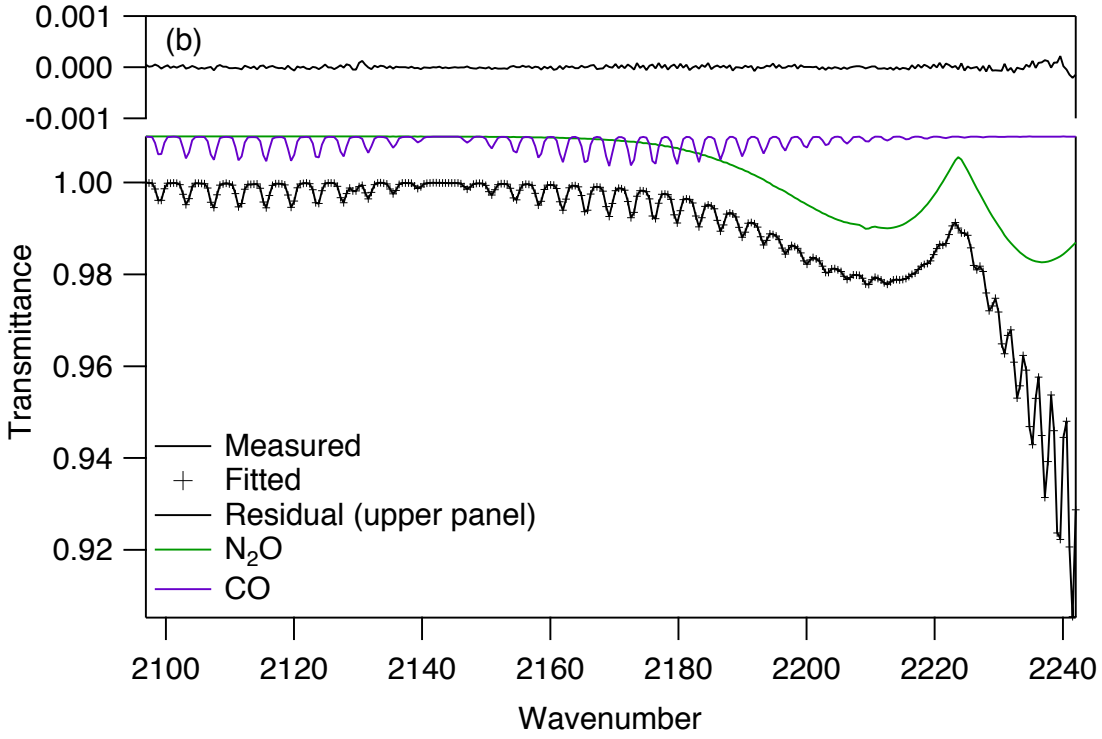

Figure 2.3.2: Example MALT fit of an in situ FTIR measurement in the 2097–2242 cm^{-1} window, taken from Figure 3.(b) Griffith et al., 2012. Modelled spectrum is shown as + and measured spectrum is shown as solid black line. Individual contributions from the trace gases CO (purple) and N_2O (green) are shown offset +0.02 to the measured spectrum. The residual between measured and modelled spectrum is plotted in the top panel.

sure. The ILS function accounts for instrument features such as instrument resolution, apodisation and divergence of infrared beam. The MALT software iteratively compares a simulated spectrum with measured spectrum, using the Levenberg–Marquardt algorithm (Press et al., 1992) to minimise the RMS residual. An example of the optimal simulated spectra is shown in Figure 2.3.2, plotted with the measured spectrum and each individual trace gas component. An advantage of using non-linear least squared analysis is that it allows interpretation of strong absorbing regions in addition to weak absorbing regions, which was not previously available in methods such as classic least squares.

Fitting is performed in broad regions of 100–200 cm^{-1}, which generally cover entire absorption bands of targeted trace gases. Four spectral windows are used to retrieve trace gas mole fraction values and are summarised in Table 2.3.1. All trace gases within a window are fitted, accounting for overlap between trace gas absorption profiles.

However, some cross sensitivities may remain, which are subsequently accounted for in a set of cross sensitivity experiments. Cross sensitivity analysis is discussed further in Chapter 3.

Table 2.3.1: Spectral windows used for in situ FTIR retrievals.

Window (cm^{-1})	**Trace gases retrieved**
2097–2242	CO, N_2O, CO_2
2150–2310	$^{13}CO_2$, $^{12}CO_2$, CO, N_2O, H_2O
3001–3150	CH_4, H_2O
3520–3775	CO_2, H_2O

Generally, trace gases are retrieved as above, resulting in mole fraction values. The procedure is extended in the case of $^{13}CO_2$ isotopologue, to determine the ratio with measured $^{12}CO_2$ and comparing with natural abundance to provide a $\delta^{13}CO_2$ value. Here, $\delta^{13}CO_2$ is defined as:

$$\delta^{13}\mathrm{C} = \left(\left(\frac{^{13}\mathrm{CO_2}}{^{12}\mathrm{CO_2}} \right)_{\text{retrieved}} - 1 \right) \times 1000 \text{ ‰} \tag{2.3.1}$$

Where MALT retrieved $^{X}CO_2$ implicitly takes into account the natural abundances using HITRAN, and therefore is implicitly comparing with natural abundance. Comparison with natural abundance allows for determination of air with depleted or enhanced $^{13}CO_2$, giving insight into sources and sinks.

Following trace gas retrieval, further improvements in accuracy may be made if we account for cross sensitivity between trace gases or to instrument parameters such as pressure or temperature. Additionally, while trace gas measurements with the in situ FTIR are very precise, the accuracy is affected by various systematic errors in the spectrometer, MALT or HITRAN database. Therefore calibration to a global scale is necessary in order to accurately compare between sites. Data preparation is extensively detailed in Chapter 3.

2.3.2 General running procedure

Evacuation or introduction of sample to the White cell is achieved with a four-stage oil-free diaphragm pump. The sample may be drawn into the instrument from four equivalent inlets, as shown on the instrument flow diagram in Figure 2.3.3, to fill the

3.5 litre capacity of the instrument, usually at a working pressure of 1100 hPa. Before entering the cell, the air passes through 2 drying filters and a 7 μm particle filter. Control of internal valves is automated by the UOW designed software Oscar, more recently ported to Spectronus™ (Ecotech P/L, Knoxfield, VIC, Australia). The recent addition of two mass flow control devices directly before and after the cell (Figure 2.3.3) has led to higher pressure and flow stability (Hammer et al., 2012). Previous to this, a manual needle valve and a flow meter was employed before the cell. Temperature of the cell is regulated with a PID controller. Dry nitrogen is flushed through the optics at 0.1–0.2 Lmin^{-1} to purge the optics system of interfering gases. Nitrogen cylinders often contain CO contamination, which may affect trace gas variability in the measurements.

Measurement variability of all gases is affected by cross-sensitivity to atmospheric H_2O, which varies greatly throughout the day. In order to minimise H_2O variability affecting other trace gases, the atmospheric sample is dried. Before entering the cell, the atmospheric sample passes first through a membranous Nafion® drier followed by a chemical dryer using magnesium perchlorate $Mg(ClO_4)_2$ (Figure 2.3.3). As a result, atmospheric amounts of H_2O are not studied in this work.

For the measurements described in this work, atmospheric sample is passed through the cell under continuous flow for ambient conditions. Ambient air operating procedures with corresponding instrument parameter ranges are discussed in detail in Chapter 3, Section 3.2. Briefly, atmospheric sample flows through the instrument at 1 Lmin^{-1}, for 23.5 hours, with the remaining half hour devoted to measuring target gas of constant composition. A background spectrum under cell vacuum conditions is collected once a month to identify any instrumental changes. It has been found that generally, instrument background remains stable unless major instrument changes or movement occurs. Thus, the spectrum used in background correction is only updated when major instrumental changes occur.

The UOW FTIR instruments are designed to be portable and are therefore often used in field campaigns, such as agricultural chamber experiments, train and ship voyages (Denmead et al., 2010; Deutscher et al., 2010; Ridder et al., 2012). Currently, there are four instruments devoted to the UOW Centre for Atmospheric Chemistry, which means at any one time there is likely to be an instrument remaining on campus. Identifying this as an opportunity, the author ensured instruments remaining at UOW were devoted to recording ambient measurements. However, the data record is near-continuous due to times when all instruments were either off-site or remaining instruments were being upgraded.

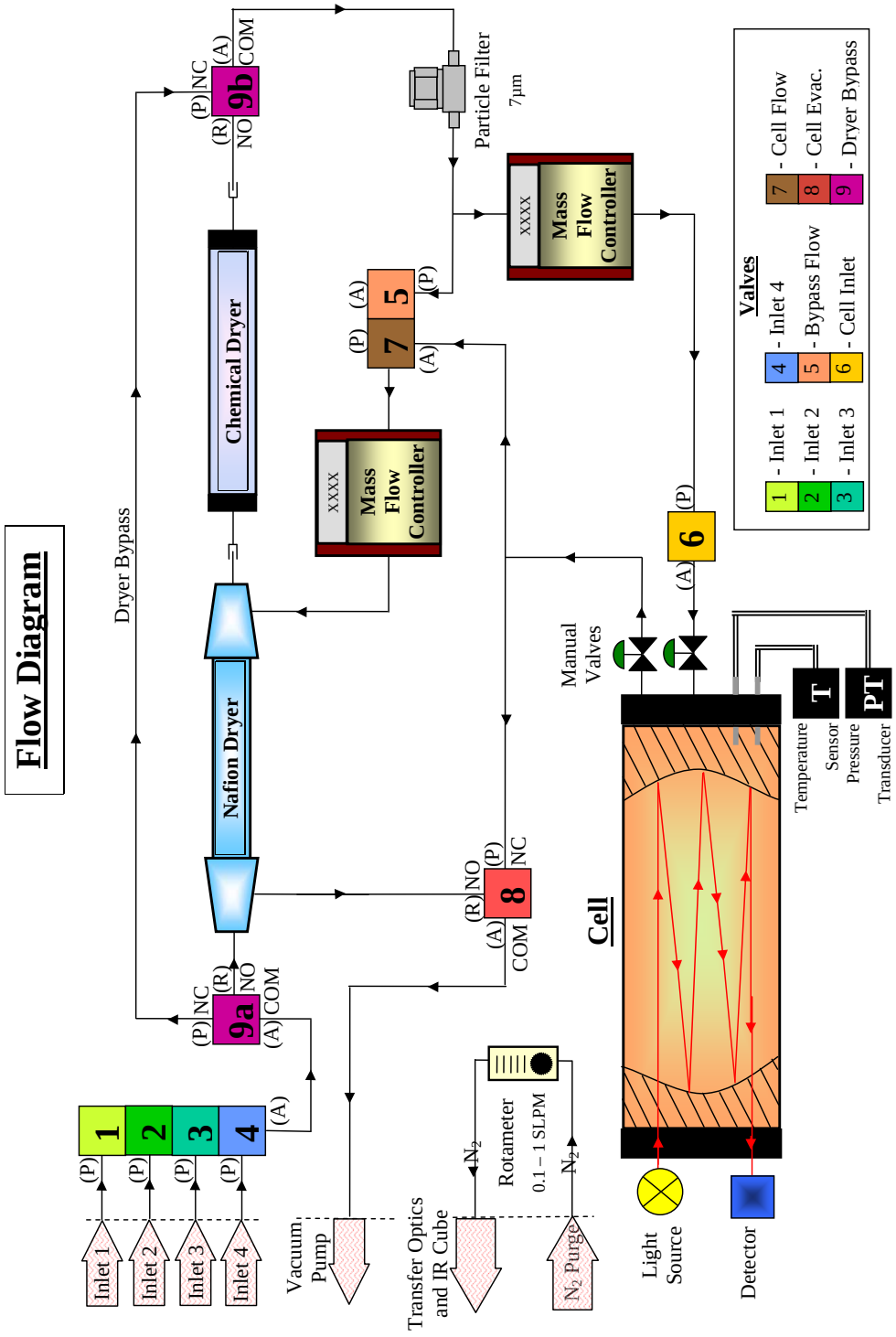

Figure 2.3.3: Flow diagram of the in situ FTIR instrument. Adapted from Deutscher, 2009, to include two MFCs.

Chapter 3 develops the combined near-continuous record from two in situ FTIR instruments at UOW, from 2011 to 2013. The two instruments were chosen for their design compatibility and temporal overlap, allowing for cross-platform comparison. While effort has been made to ensure consistent recording practices, changes in instrument operator, improved operating procedures, and instrument upgrades have led to data variability. These have all been acknowledged and dealt with in the quality control protocol, discussed in depth in Chapter 3.

2.4 Ground based solar Fourier Transform Infrared Spectrophotometer

Ground based solar Fourier Transform (Infrared) Spectroscopy (FTS) is similar to the in situ FTIR instrument in that it measures absorption of infrared radiation by trace gas molecules between the light source and the detector. However, in solar FTS the sun is the infrared source and the sample path is the entire atmosphere between the instrument and the sun. Solar FTS can measure spectra in the mid-infrared to near-infrared regions, over a range of 600 to 12000 cm^{-1}. Filters are used over different spectral regions to improve signal to noise. An example of spectra measured through various filters is shown in Figure 2.4.1.

As the position of the sun in the sky changes (i.e. solar zenith angle), the path length between the instrument and source changes, which must be accounted for in the trace gas retrieval algorithm. Unlike the in situ FTIR, the exact path length is not known and must be modelled.

Path length for the FTS is determined by a radiative transfer model, involving at least 30 and up to 70 atmospheric layers. The radiative transfer model takes into account atmospheric refraction (Meier et al., 2004). In addition to path length calculations, pressure, temperature and amounts of trace gases are dependent on altitude and must be modelled. The radiative transfer model is combined in a forward model with atmospheric and instrumental parameters, and with absorption line parameters from the HITRAN database (Rothman et al., 2013, 2009), to produce a simulated IR spectrum. Parameters such as trace gas amount or instrument line shape, are then iteratively adjusted to minimise the difference between simulated and measured spectra. The best match between synthetic and measured spectra indicates the most probable atmospheric amount of trace gas (Rodgers, 2000; Washenfelder et al., 2006; Pougatchev

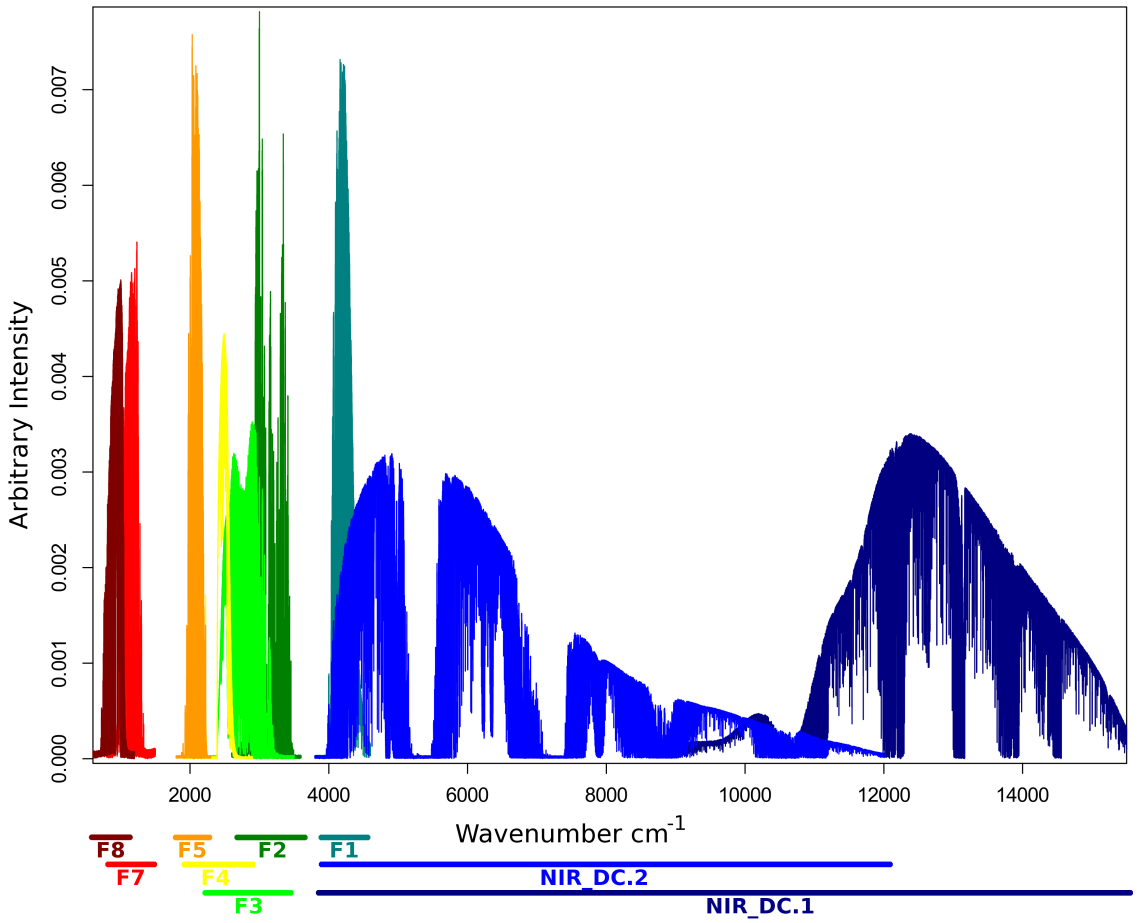

Figure 2.4.1: Example recorded spectra from the solar FTS, over the entire spectroscopic range. Spectra collected through different filters are shown. Filter ranges (in cm^{-1}): NIR_DC.1 3800–12000, NIR_DC.2 3800–15800, F1 3800–4600, F2 2600–3600, F3 2200–3500, F4 1900–2900, F5 1800–2300, F7 800–1500, F8 600–1200

et al., 1995).

The retrieval of trace gas amounts from atmospheric spectra is often a mathematically ill posed problem, with more unknowns than information content. The forward model therefore requires assumptions to be made in order to constrain results within a reasonably expected range.

2.4.1 Retrieving trace gases in solar FTS: GFIT and SFIT-2

One of two programs may be used to retrieve total column values from solar IR spectra: GFIT (Washenfelder et al., 2006) or SFIT-2 (Pougatchev et al., 1995; Rinsland et al., 1998). Previously measured or modelled profiles of trace gases in the atmosphere are used as initial approximations of the atmospheric state. These initial estimations are known as the a priori profiles, and are dependent upon season and latitude. For GFIT, a priori profiles combine MkIV balloon profile measurements and Atmospheric Chemistry Experiment (ACE-FTS) satellite measured profiles, between 2003 to 2007. SFIT-2 uses a priori profiles from model output from the Whole Atmosphere Community Climate Model (WACCM), interpolated to station locations. In either retrieval program, a priori profiles are used in the forward model, together with HITRAN database, and atmospheric and instrumental properties to produce synthetic spectra, which are then iteratively improved. The main difference between the two programs is the method of iterative improvements in the simulated spectra.

The GFIT program uses profile scaling to adjust the entire a priori profile equally by a constant factor. Adjustment is completed using the nonlinear least squares method, to best fit the calculated spectrum to the measured spectrum. An example of a best-fit synthetic spectrum determined by GFIT for CO is shown in Figure 2.4.2. Constant profile scaling means the a priori profile must be close to the true atmospheric shape. If a GFIT profile is vastly different from the truth, the fit between synthetic and measured spectra will be poor, reflected in a poor residual (R^2). Therefore, the R^2 value is important for quality checking both the fitting algorithm and the a priori approximation.

Due to constant profile scaling, the GFIT method does not produce vertical information about the distribution of trace gases, rather only a single column value is produced. However, some information about vertical location of the trace gas can be inferred from the shape of the IR lines. Altitude distribution may be achieved based on the predominant contributor to line shape. An infrared absorption line with a Voigt shape that is predominantly Lorentzian will be mainly pressure broadened and therefore have maximum contribution from trace gas in the troposphere. In comparison, a Voigt shape that is mainly Gaussian indicates a trace gas residing in the stratosphere.

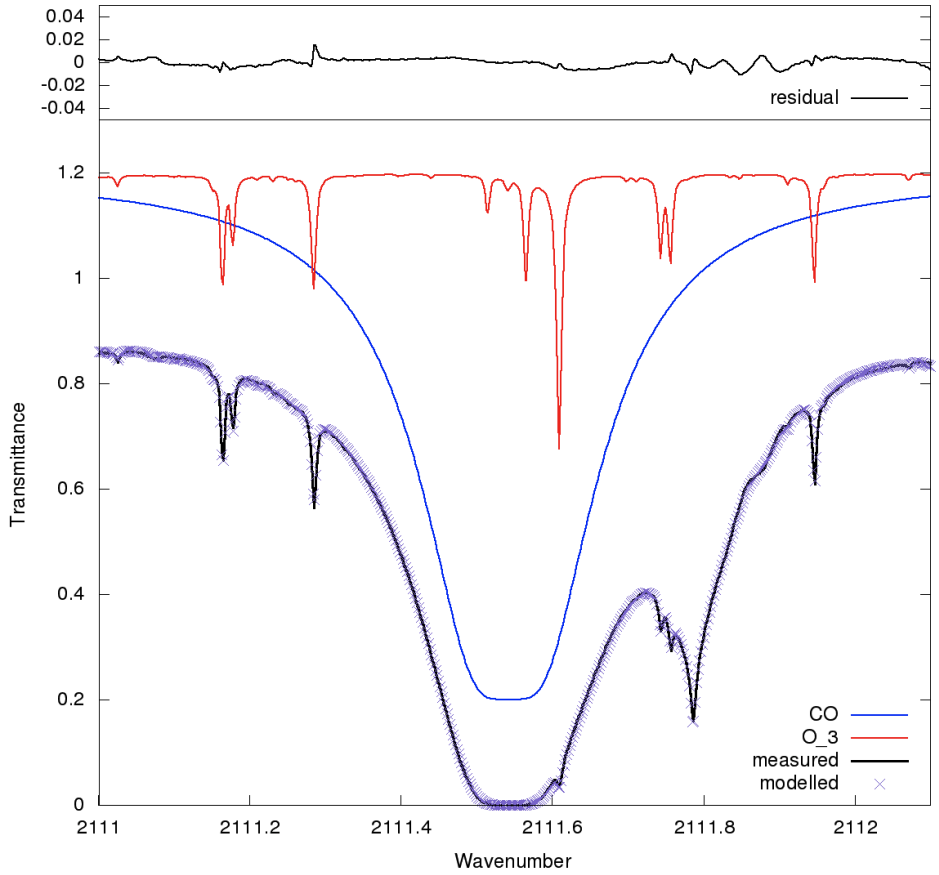

Figure 2.4.2: Spectral fit for CO from solar FTS measurements at Wollongong. Example results is from a GFIT retrieval of the microwindow centred on 2111.55 cm^{-1}, measured through Filter 5, on 25 Sept, 2008. Measured spectrum is in black, modelled is in purple crosses, modelled contributions from CO and the interfering species O_3 are shown in blue and red respectively and are offset +0.2 cm^{-1} for clarity. Residual between the modelled and measured spectrum is shown in the top panel. Retrieved CO column for this measurement was 1.469×10^{18} molec cm^{-2}.

SFIT-2 quantitatively uses these pressure broadening properties of the spectral lines to adjust each level of the a priori profile, incorporating Gaussian correlation between adjacent layers. SFIT-2 therefore alters the shape of the a priori profile in order to produce the lowest residual between simulated and measured spectra. Variable profile scaling is especially important for trace gases in which the vertical profile changes rapildly.

SFIT-2 uses optimal estimation techniques to determine trace gas mole fraction profiles (Rodgers, 2000). An a priori profile is still required for SFIT-2 retrievals because the inverse problem is ill posed, and requires weighting by initial approximation. This

method of optimal estimation only works well if the instrument line-shape (ILS) is accurately known. The ILS is determined using a set of measurements of low-pressure gas cells, with a program called Linefit (Hase et al., 1999).

Both GFIT and SFIT-2 retrieval algorithms produce slant column values, which depend upon solar zenith angle (SZA). Slant columns are normalised by dividing by the ratio of total air mass in the path length to vertical column. Normalised column amounts are known as total column values. Total column remains constant for a well-mixed atmosphere, regardless of SZA.

2.4.2 Comparison of GFIT and SFIT-2 CO retrievals

GFIT and SFIT-2 retrievals have been compared for CO at Wollongong 1996 to 2010 (Figures 2.4.3 and 2.4.4). Instruments are compared for daily average total column values. SFIT-2 processing can produce unstable retrievals that are rejected by automatic quality control procedures in the trace gas retrieval. Therefore, GFIT daily averages are likely to include retrievals from more spectra than SFIT-2 daily averages, and are the main reason differences may be seen between records.

Wollongong (-34.406°, 150.879°) is located approximately 80 km south of Sydney, Australia, and is at the intersection of marine, urban and biogenically influenced atmospheric conditions. The TCCON station was commissioned in 1996 at the University of Wollongong (Griffith, D. W. T. and Jones, N. B. and Mathews, W. A., 1998), and originally measured solar spectra with a solar-tracking FTS system using a Bomem Model DA8 spectrometer. In 2007, the spectrometer was upgraded to a Bruker IFS 125HR instrument, which continues measuring to the present day.

The Bomem instrument (1996–2007), having larger instrumental variability, showed minimal difference between GFIT and SFIT-2. Total column CO values were highly correlated between retrieval methods ($r = 0.91$). This means the uncertainty due to instrument fluctuations has greater influence on retrieved values than the variability introduced by either a biased a priori profile in GFIT, or rejection of some spectral retrievals by SFIT-2.

In contrast, the Bruker instrument, introduced in 2007, has a much lower instrument uncertainty, due to design improvements and the addition of corner-cube mirrors. SFIT-2 retrievals of total column CO for the Bruker are lower than GFIT retrievals, apparent in both the timeseries plot (Figure 2.4.3, region 2007 to 2010) and the correlation plot

(Figure 2.4.4b). Higher CO from GFIT suggests that either the a priori in GFIT is overestimating some part of the profile, or alternatively GFIT is including some high CO values that are being rejected by SFIT-2. The rejection of retrievals in SFIT-2 tends to occur with high CO values because scaling of the a priori is required to be larger and is consequently more likely to produce numerical instabilities.

Overall, there is no substantial bias between retrieval methods.

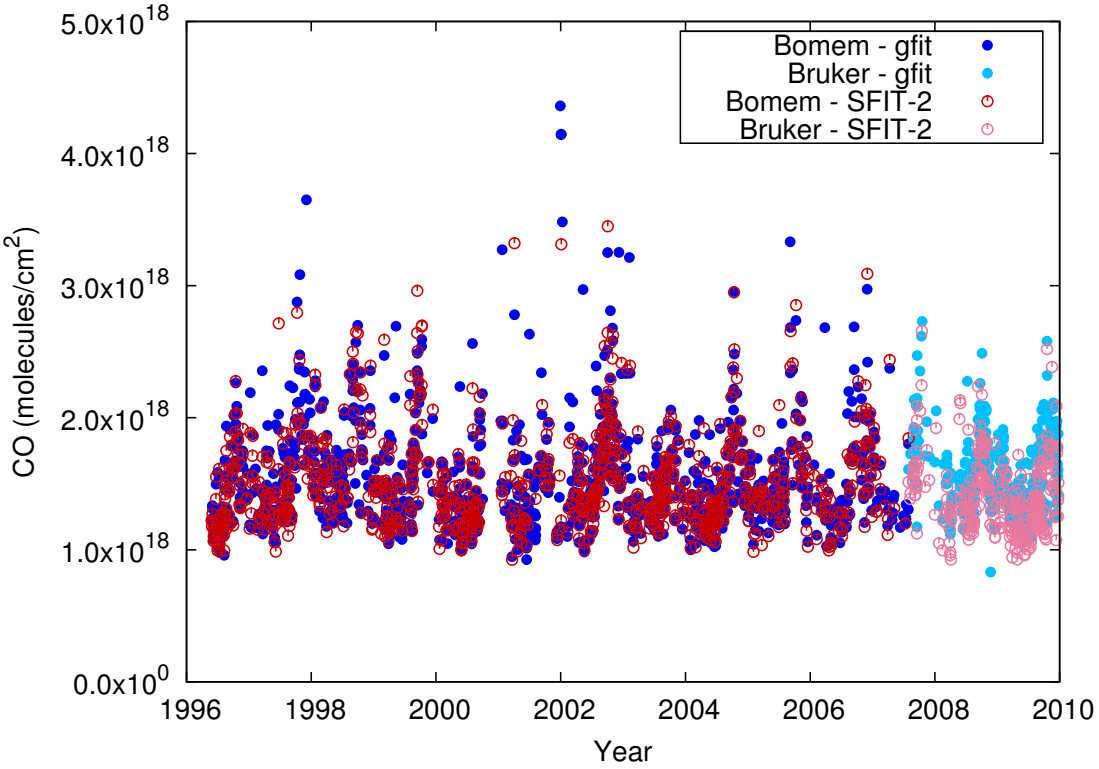

Figure 2.4.3: Daily averaged carbon monoxide at Wollongong retrieved with two separate retrieval programs GFIT (blue, light blue) and SFIT-2 (red, pink). The solar FTS changed from a Bomem instrument (blue and red) to a Bruker instrument (light blue and pink) in 2007.

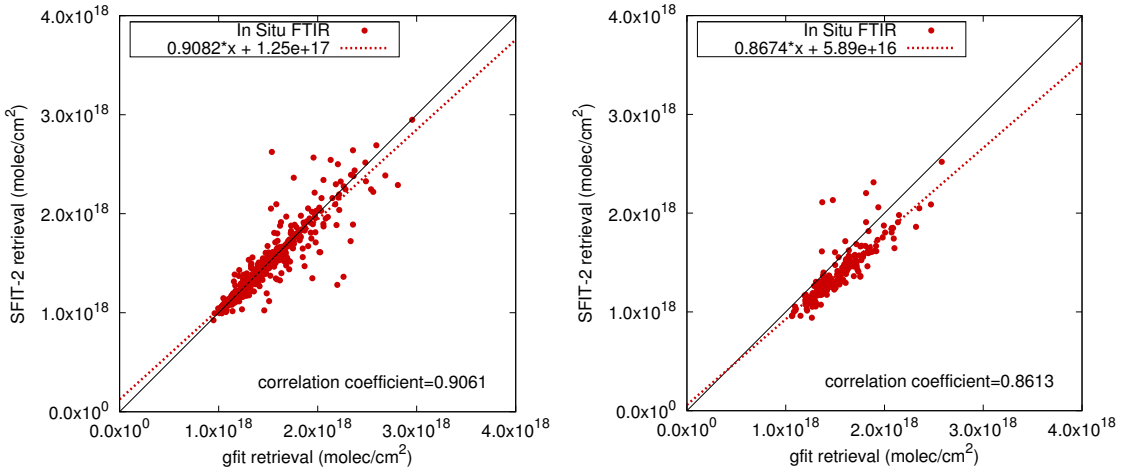

(a) Bomem instrument (b) Bruker instrument

Figure 2.4.4: Correlation comparison of GFIT and SFIT-2 retrievals of CO from solar spectra at Wollongong, for the (a) Bomem (1996–2007) and (b) Bruker (2007–2010) instruments. Red dotted line indicates line of best fit. The solid black 1:1 line is shown for comparison.

2.4.3 FTS instrument specifications

Solar FTS incorporates a Michelson interferometer (Section 2.2), and uses either a KBr or CaF_2 beamsplitter to partially reflect incoming radiation. Ground based solar spectrometers require a direct line of sight to the sun, and a solar tracker is therefore coupled with the spectrometer to track the location of the sun throughout the day. Solar FTS require clear-sky conditions and measure in the near-infrared and mid-infrared regions, 600 to 12000 cm^{-1} (Bacsik et al., 2004). Various filters are used to improve signal to noise in different spectral regions. Spectra are recorded with different detectors depending upon the filter (Figure 2.4.1). Filters 1 to 5 require liquid nitrogen cooled indium antimonide (InSb) or mercury cadmium telluride (MCT) detectors and filters 7 and 8 require the MCT detector. Filters in the NIR region use an un-cooled indium gallium arsenide (InGaAs) detector and silicon diode (Si).

Due to the higher resolution in solar FTS instruments, smaller spectral regions are used to retrieve trace gases, regions which often cover a single peak. These small spectral regions are known as microwindows. The use of microwindows further improves signal to noise by minimising the influence of interfering species. FTS retrievals used in this thesis are predominantly for CO, ethane (C_2H_6) and formaldehyde (HCHO). Microwindow retrieval regions for these three gases are given in Table 2.4.1, along with interfering gases that are also adjusted in the retrieval.

Table 2.4.1: Microwindows used in solar FTS retrievals. Filter ranges: NIR_DC.2: 3800–15800 , F1: 3800–4600 cm^{-1}, F2: 2600–3600 cm^{-1}, F3: 2200–3500 cm^{-1}, F4: 1900–2900 cm^{-1}, F5: 1800–2300 cm^{-1}.

Trace Gas	**Filters**	**Window Center (cm^{-1})**	**Window Width (cm^{-1})**	**Interfering species**
CO	F4, F5	2045.49†	0.78	OCS, O_3, CO_2, C_2H_4, H_2O
	F4, F5	2053.55†	4.8	OCS, O_3, CO_2, C_2H_4, H_2O
	F4, F5	2057.84	0.28	O_3, CO_2
	F4, F5	2069.64	0.19	O_3
	F4, F5	2111.55	1.1	O_3
	F4, F5	2158.25	1.8	H_2O, N_2O, O_3, CO_2
	F4, F5	2160	6	H_2O, N_2O, O_3
	F1, NIR_DC.2	4233.00	48.60	CH_4, H_2O, HDO
	F1, NIR_DC.2	4274.74	0.26	HDO
	F1, NIR_DC.2	4290.40	56.80	CH_4, H_2O, HDO
HCHO	F2, F3, F4	2760.9	0.6	CH_4, O_3, HDO, N_2O
	F2, F3, F4	2774.8	1.44	CH_4, O_3, HDO, N_2O
	F2, F3, F4	2778.4	1.04	CH_4, O_3, HDO, N_2O
	F2, F3, F4	2781.21	0.9	CH_4, O_3, N_2O
	F2, F3, F4	2798	2.25	CH_4, O_3, HDO, N_2O
	F2, F3, F4	2869.88	0.89	CH_4, O_3, HDO
	F2, F3	2914.5	0.6	CH_4, O_3, HDO, N_2O, H_2O
C_2H_6	F2, F3	2976.6	1	H_2O, CH_4
	F2, F3	2986.69	0.48	H_2O, O_3

† In these microwindows, CO is more of an interfering species and is not generally the major target.

Solar FTS were commissioned at the University of Wollongong (UOW, 34.4°S, 150.9°E) in 1996, Darwin (12.4°S, 130.9°E) in 2005 and Lauder (45.0°S, 169.7°E) in 1994. The UOW site originally measured solar spectra using a Bomem Model DA8 spectrometer. In 2007, the spectrometer was upgraded to a Bruker IFS 125HR instrument, which continues measuring to the present day. Darwin also measures spectra with a Bruker IFS 125HR. The Lauder site initially measured spectra with a Bruker 120M instrument, which was changed in September 2001 to a Bruker 120HR model.

Ground based FTS that are dedicated measuring carbon gases and N_2O from the NIR spectral region contribute to the Total Column Carbon Observing Network (TCCON, https://tccon-wiki.caltech.edu/). The Centre for Atmospheric Chemistry (CAC) at the University of Wollongong is responsible for two TCCON instruments, one in Darwin and one in Wollongong. Lauder is also a TCCON station. Other trace gases besides those defined for TCCON are often measured in the MIR region, and contribute

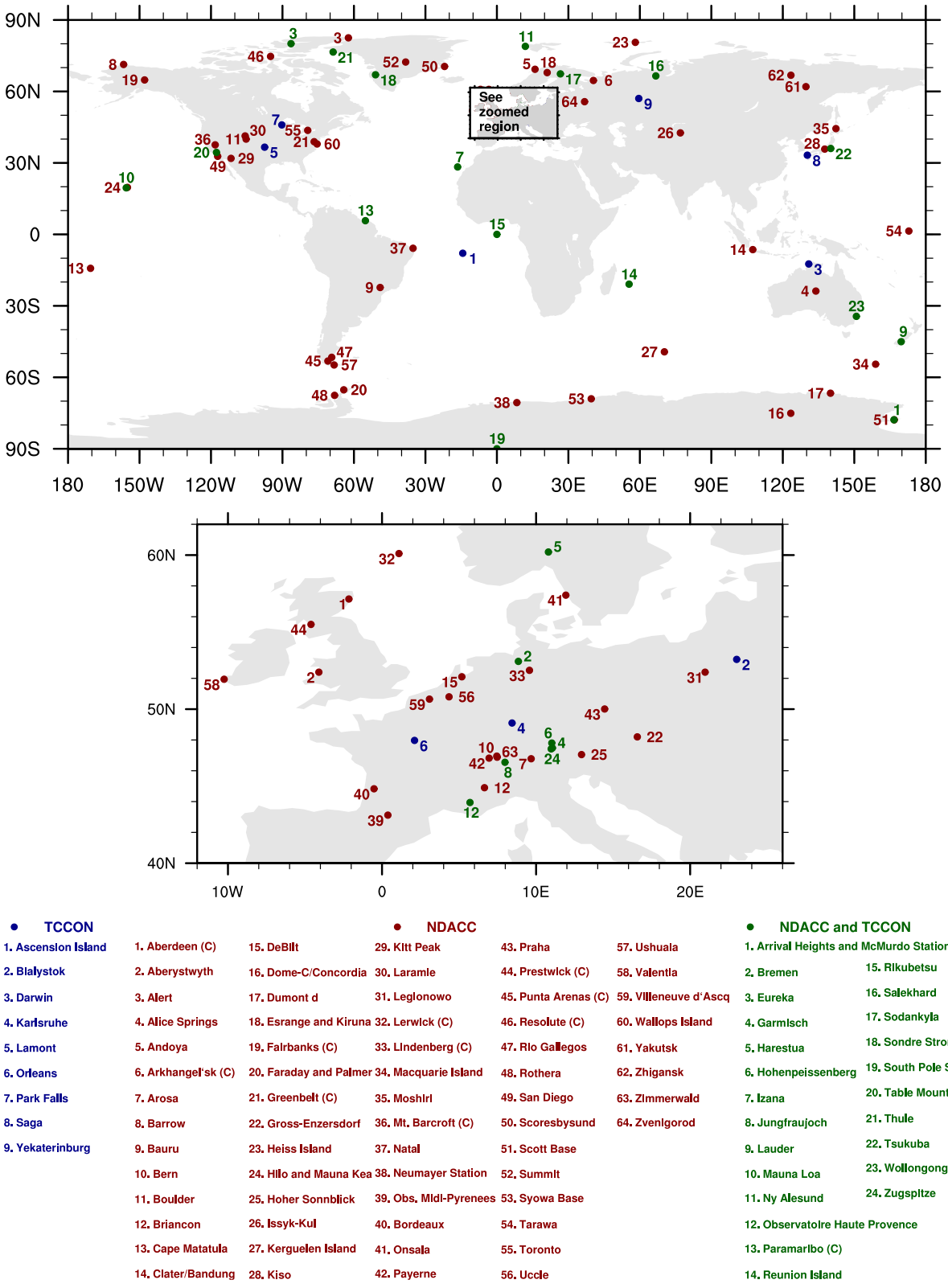

Figure 2.4.5: Location of TCCON and NDACC sites globally. Both long term and campaign sites (C) are shown.

to the Network for the Detection of Atmospheric Composition Change (NDACC, http://www.ndsc.ncep.noaa.gov/). Wollongong and Lauder are also NDACC stations, in addition to being TCCON stations. A map of worldwide NDACC and TCCON stations is shown in Figure 2.4.5.

2.4.4 General running procedure

Daily running of the solar FTS is carried out by a team of researchers who share operational responsibility. The assigned operator is required to ensure the FTS instrument begins measurements at sunrise. Weather is continuously monitored during the day and the solar tracker is parked during periods of rain, intense cloud, and overnight. Recently at UOW, sunrise, sunset and weather operation has been automated. However, correct instrumental operation remains the responsibility of the assigned operator.

At sites that measure both MIR and NIR spectral regions, daily operating procedures include ensuring that appropriate detectors (InSb and MCT) are cooled with liquid nitrogen. Also, operators are required to manually change beamsplitters, according to a schedule. This is due to some regions of the solar spectrum being blocked by the beamsplitter, which interferes with filter regions. Specifically, the CaF_2 beamsplitter may be used for NIR measurements and filters 1 to 5, while the KBr beamsplitter is used for filters 1 to 8. The recording of different filter regions follows a pre-defined schedule. At UOW, measurements of the NIR region are required to coincide with GOSAT (Greenhouse gases Observing SATellite) overpasses, as the UOW instrument is used in validation studies of the satellite instrument. Therefore, the schedule of filters to be used is based around GOSAT overpass times, which occur every three days.

End-of-day procedures include total column retrieval of standard gases from the days spectral record using GFIT. Coincident weather data from a Davis weather station is also downloaded and stored. Approximately once a week, data is transferred to a storage site, so that spectral information is available for future retrievals of gases. For example, an updated retrieval algorithm may need to be applied, or trace gases not included in the standard running procedures may be retrieved.

2.5 Satellite measurements: MOPITT

As an aspect of their Earth Observing System (EOS) project, NASA has implemented numerous satellite observatories aimed at investigating atmosphere, land, ocean and biosphere properties of earth. The flagship satellite of EOS is "Terra", which was launched on December 18, 1999. Terra completes ∼14 sun-synchronous polar orbits per day, flying at an altitude of 705 km and crossing the equator at ∼10:30 day–time and ∼22:30 night–time, local time. The main objectives of Terra are to determine how different components of the earth system are changing and ultimately improve our understanding of human impacts on the earth (Bordi et al., 1999; Liu et al., 2006).

MOPITT (Measurements Of Pollution In The Troposphere) is one of five instruments aboard Terra, and is devoted to measuring the atmospheric trace gas CO. CO measurements began in March 2000 (Drummond, 1992; Drummond & Mand, 1996; Deeter et al., 2003). MOPITT is one of a range of satellite-borne sensors currently measuring atmospheric CO from space (see Table 2.5.1). MOPITT was chosen for this study as it currently provides the longest continuously running measurements of CO. The extent of the MOPITT record provides optimal overlap with the Wollongong FTS station record.

MOPITT is nadir-viewing with a pixel size corresponding to 22 × 22 km ground resolution. MOPITT detectors are indium antimonide, which are cooled by a Stirling Cycle Cooler to 100 K. Each detector is a 4 × 1 array, resulting in an 88 × 22 km footprint. An improved ground coverage is achieved by cross–track scanning, resulting in a swath–width of 88 km × 612 km. The outcome is complete earth coverage in approximately 3 days (Drummond, 1992; Drummond & Mand, 1996; Deeter et al., 2003). A visualisation of the MOPITT swath is shown in Figure 2.5.1.

While MOPITT is interested in the IR region of atmospheric absorption, the instrument uses a different mechanism to FTIR. MOPITT uses correlation infrared radiometry, which employs a known sample of the same gas to be measured (i.e. CO) as a filter cell before the IR detector. Modulating cell pressure or length and subsequently determining spectral line differences gives information about the trace gas of interest. MOPITT measures the fundamental CO IR band (4.7 μm) from terrestrial (thermal–infrared, TIR) emission and the overtone band (2.3 μm) from reflected solar radiation (near–infrared, NIR), with 0.04 cm^{-1} spectral resolution. The fundamental band in the thermal region is used to retrieve vertical profiles (Drummond, 1992; Drummond & Mand, 1996; Deeter et al., 2003).

Table 2.5.1: Satellite instruments measuring CO. Viewing geometries: N = nadir, L = limb.

Instrument	**Satellite Platform**	**Meas. Period**	**View**	**Reference**
MOPITT Measurements of Pollution in The Troposphere	Terra (NASA)	2000–	N	(Drummond, 1992)
SCIAMACHY SCanning Imaging Absorption spectroMeter for Atmospheric CHartographY	Envisat (ESA)	2002–2012	N	(Burrows et al., 1995)
AIRS Atmospheric Infrared Sounder	Aqua (NASA)	2002–	N	(Aumann et al., 2003)
ACE-FTS Atmospheric Chemistry Experiment Fourier Transform Spectrometer	SCISAT-1 (CSA)	2003–	L	(Clerbaux et al., 2005)
TES Tropospheric Emission Spectrometer	Aura (NASA)	2004–	N/L	(Beer, 2006)
MLS Microwave Limb Sounder	Aura (NASA)	2004–	L	(Livesey et al., 2008)
IASI Infrared Atmospheric Sounding Interferometer	MetOp-A (ESA)	2006–	N	(Clerbaux et al., 2009)
CrIS Cross-track Infrared Sounder	Suomi NPP (NOAA/NASA)	2011–	N	npp.gsfc.nasa.gov/cris.html
CrIS Cross-track Infrared Sounder	JPSS-1 (NOAA/NASA)	2017 launch		

CSA - Canadian Space Agency
ESA - European Space Agency
NASA - National Aeronautics and Space Administration
NOAA - National Oceanic and Atmospheric Administration

Until recently, only the thermal–infrared (TIR, 4.7 μm) band has been used to retrieve CO values. From version 6 (V6), MOPITT products additionally include information from reflected solar radiation in the 2.2 μm near–infrared (NIR) region. Incorporation of near–infrared information provides enhanced information of surface concentrations. A limitation of the enhanced retrievals is that they are only available during the day, due to NIR originating from reflected solar radiation (Deeter et al., 2010).

The retrieval process for MOPITT follows maximum likelihood optimal estimation principles (Rodgers, 2000; Pan et al., 1998), which are combined with a fast radiative transport model of the atmosphere (Edwards et al., 1999) to invert the radiometric signals and retrieve trace gas values. Only scenes classified as cloud–free are used in retrievals (Warner et al., 2001). Retrievals combine a priori profiles with measurements to statis-

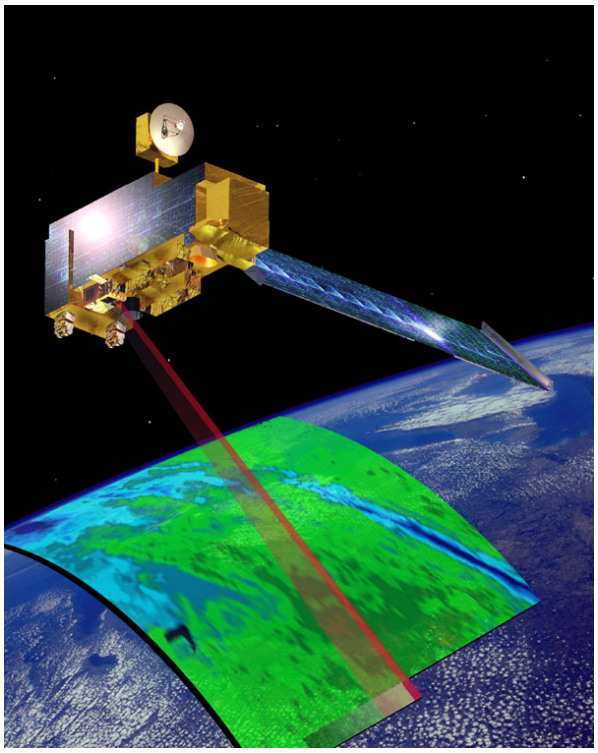

Figure 2.5.1: An artist's impression of the MOPITT instrument aboard Terra, showing instrument scanning and corresponding approximate swath–width of 88 km × 612 km. [Image: NASA].

tically determine a maximum a posteriori solution. Corresponding information about the sensitivity of retrieval with respect to the true state vector is described by the averaging kernel. Both discrete layer mole fraction profiles and total columns are retrieved (Deeter et al., 2003, 2010).

As retrieval algorithms have improved, new versions of MOPITT data are released to the public. In this thesis, both version 4 (V4) and version 6 (V6) products are used. The earlier V4 product is used in comparison with ground based FTS measurements in Chapter 5, drawing on differences in instrument sensitivity to distinguish transported and local sources. The V6 product is used in comparison with model output in Chapter 7, to help understand model biases.

Monthly varying a priori mole fraction profiles are used in MOPITT retrievals from V4 onwards. A priori profiles are gridded at one degree resolution and originate from model output. Prior to V6, the MOZART (Model for OZone And Related Tracers, Emmons et al., 2010) chemical transport model provided a priori profiles, based on a climatological average of model simulations 1997-2004 (Deeter et al., 2003, 2010).

From V6, a priori profiles are taken from a climatological 2000-2009 run of CAM–Chem (Lamarque et al., 2005). These CAM–Chem a priori profiles are more representative of the time period of MOPITT retrievals.

Volume mixing ratios are retrieved on vertical levels that include a floating surface pressure plus nine equally spaced pressure levels from 900 to 100 hPa (Deeter et al., 2010). Prior to V5, trace gas values were retrieved on level centres that were weighted tapering to zero at adjacent levels. From V5, retrievals are defined as level edges with uniform vertical weighting above that level (Deeter, 2011). Additionally, from the V4 product onwards, trace gas values are retrieved as log(VMR) (Deeter et al., 2003, 2010).

Prior to V6, meteorological parameters used in retrievals, such as water vapour and temperature profiles, were obtained from NCEP GDAS (Global Data Assimilation System) products (Deeter et al., 2003). From V6 onwards, the retrieval process uses MERRA (Modern–Era Retrospective analysis for Research Applications) reanalysis meteorological producst. MERRA is of higher time and spatial resolution than NCEP GDAS, resulting in superior MOPITT retrievals (Deeter, 2013).

Overall, MOPITT has been a key instrument contributing to our knowledge atmospheric chemistry for over a decade, and continues to be an important tool for investigating atmospheric CO.

2.6 Averaging kernels

2.6.1 Quantification of vertical sensitivity

Total column measurement retrievals have a depencence upon altitude. Specifically, the amount of trace gas retrieved at a particular altitude can depend on how much trace gas is present at other altitudes. This dependence can change according to trace gas of interest, time of day, and season, which in turn can influence the altitudes to which the instrument is sensitive. Averaging kernels (A_K) quantify the vertical sensitivity of an instrument by combining an a priori description of instrumental covariance, with parameters determined during the retrieval. Therefore, each measurement retrieval for a remote sensing instrument has an associated averaging kernel. The averaging kernel may be as a matrix form of sensitivities (for example in MOPITT), or can be a condensed vector form of sensitivities (solar FTS). Examples of both forms of averaging

kernels are plotted in Figure 2.6.1.

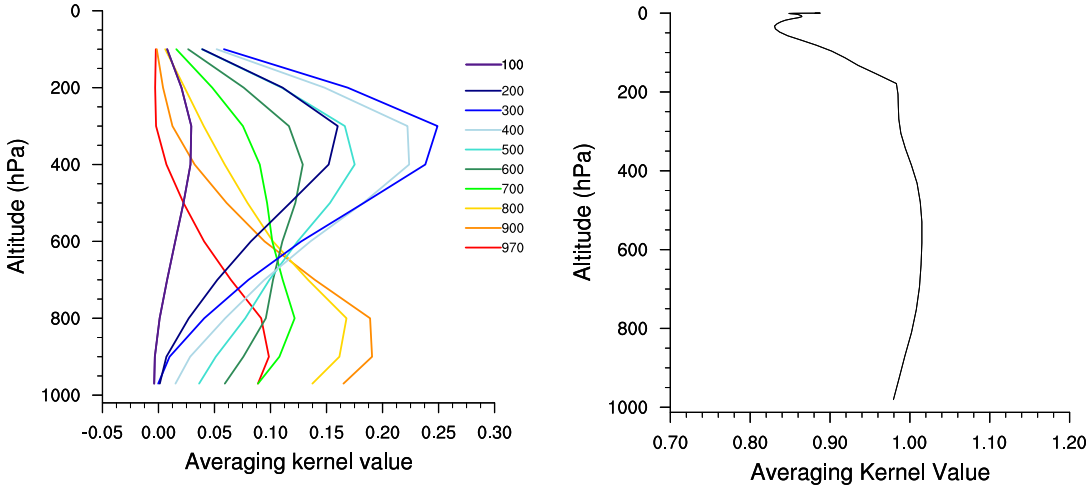

(a) Example of a MOPITT monthly averaged averaging kernel matrix for Wollongong CO, from V6 Level 3 product Jan 2008.

(b) Example of a total column vector averaging kernel for the solar FTS CO retrievals at Wollongong.

Figure 2.6.1: Example plots of both (a) matrix and (b) column averaging kernel types.

The row of an averaging kernel matrix (or vector) correspond to altitude levels. Values across the rows of an A_K matrix describe the sensitivity at a particular row index, to concentrations at other altitudes. An averaging kernel matrix is applied to profiles of mole fraction (e.g. nmol mol^{-1}), resulting in a smoothed profile. When described as a vector, an averaging kernel is applied to partial column profiles (molec cm^{-2}), resulting in a smoothed total column value.

The retrieved averaging kernel depends upon the instrument, retrieval algorithm, wavelengths in the retrieval window, location altitude, solar zenith angle and trace gas species. For example, GFIT uses profile scaling in retrievals, meaning the rows of the averaging kernel matrix all have the same shape, that is, the shape of the a priori. In comparison, SFIT-2 adjust parts of the profile differently and produces a normalised averaging kernel.

In addition to quantifying instrument altitude sensitivity, averaging kernels allow accurate comparison of model output with instrument measurements. The model result is smoothed by the instrument averaging kernel to determine the value that would have been retrieved by the instrument, assuming a model atmosphere. The method for convolving averaging kernels with model data follows the method of Rodgers, 2000, which

is described further in Chapter 7. The matrix form of A_K can be used to compare vertical profile values of trace gases. However, as the degrees of freedom for the instruments studied here is generally two or less, comparing total column values is more statistically valid.

2.7 Summary

Measurements from three main instruments are used in this research, with all three instruments employing infrared absorption properties of trace gas molecules to determine atmospheric composition.

The three instruments each have their own advantages and disadvantages. The in situ FTIR analyser has high temporal coverage, with measurements every three minutes allowing for the investigation of daily properties of trace gases. In situ FTIR can also be readily traceable to WMO (World Meteorological Organization) standards using calibration gases, and therefore has the highest accuracy. However the point–source nature of the instrument may result in long-distance transported sources being difficult to discern, due to the predominance of local signals in measurements. Additionally, height and stability of the boundary layer affect in situ measurements, with more stable PBL conditions resulting in less vertical mixing and therefore less dilution of surface sources. Therefore trace gas amounts in the PBL are strongly affected by a combination of sources and vertical mixing.

Alternatively, total column values from ground based solar FTS are able to determine transported concentrations more readily due to the inclusion of the free troposphere with the boundary layer in the measurements. The free troposphere captures uplifted trace gases from further afar. However, since the sun is the IR source for ground based measurements, only daylight hours can be investigated. Also, ground based total column values only give information for a few locations where instruments are located.

In contrast, total column measurements from satellite–based instruments provide increased spatial coverage and can give an excellent view of transported plumes. Using IR terrestrial thermal emission, satellite measurements can provide night-time values in addition to daytime coverage. The temporal coverage of satellite measurements is often more sparse than ground-based, for example the MOPITT instrument overpasses ground locations once every three days. Additionally, the larger spatial footprint of the satellite instrument can dilute the effect of local sources.

Here, measurements from these three spectroscopic instruments have been used to span different spatial and temporal scales, in order to gain insight into the atmosphere over Wollongong and ultimately, Australasia. The first part of this thesis studies atmospheric composition primarily using measurements. Chapter 3, develops a near-continuous ground based in situ FTIR measurement record, which is analysed in Chapter 4. The in situ record provides an overview of local and regional influences to boundary layer atmospheric composition at Wollongong. Following in situ investigations, total column values of CO are compared between ground based FTS and MOPITT satellite instrument at Wollongong, in Chapter 5. Total column values help understand the influence from regional and long–range transported sources. Total column measurements are further used to evaluate two models in Chapters 7 and 8. Comparison with models tests our current understanding of atmospheric processes.

Chapter 3

Preparation of in situ measurements at Wollongong

3.1 The in situ FTIR trace gas analyser

This Chapter describes the preparation of a combined timeseries from two ground based in situ FTIR trace gas analysers deployed at the University of Wollongong (UOW), from 2011 to 2013. A description of instrument design, optics, and spectroscopic retrieval theory was provided in the previous Chapter 2, Section 2.3. Here, a calibrated, quality controlled timeseries of trace gases is prepared. Subsequent data analysis is performed in Chapter 4.

The two FTIR trace gas analysers used in this study are referred to as "Eddy" (April 2011 to current) and "Sandpit" (December 2011 to current). For details on naming origin, see footnote[1]. The trace gas analysers were not always located at UOW during the time period of interest, often being deployed on field campaigns. However, when located at UOW and not undergoing instrumentation upgrades, the in situ FTIR were used for ambient air measurements. Combination of measurements from the two instruments provide a near-continuous ambient air record at UOW, spanning the years 2011 to 2013 and representing all seasons. A diagram of available raw data from each instrument is depicted in Figure 3.1.1. Centre for Atmospheric Chemistry researchers Christopher Caldow, Ronald Macatangay, Melanie Cameron and Dagmar Kubistin are

[1]Eddy was created originally for eddy cross-correlation experiments and Sandpit was built for instrumental research and development, and was playfully named.

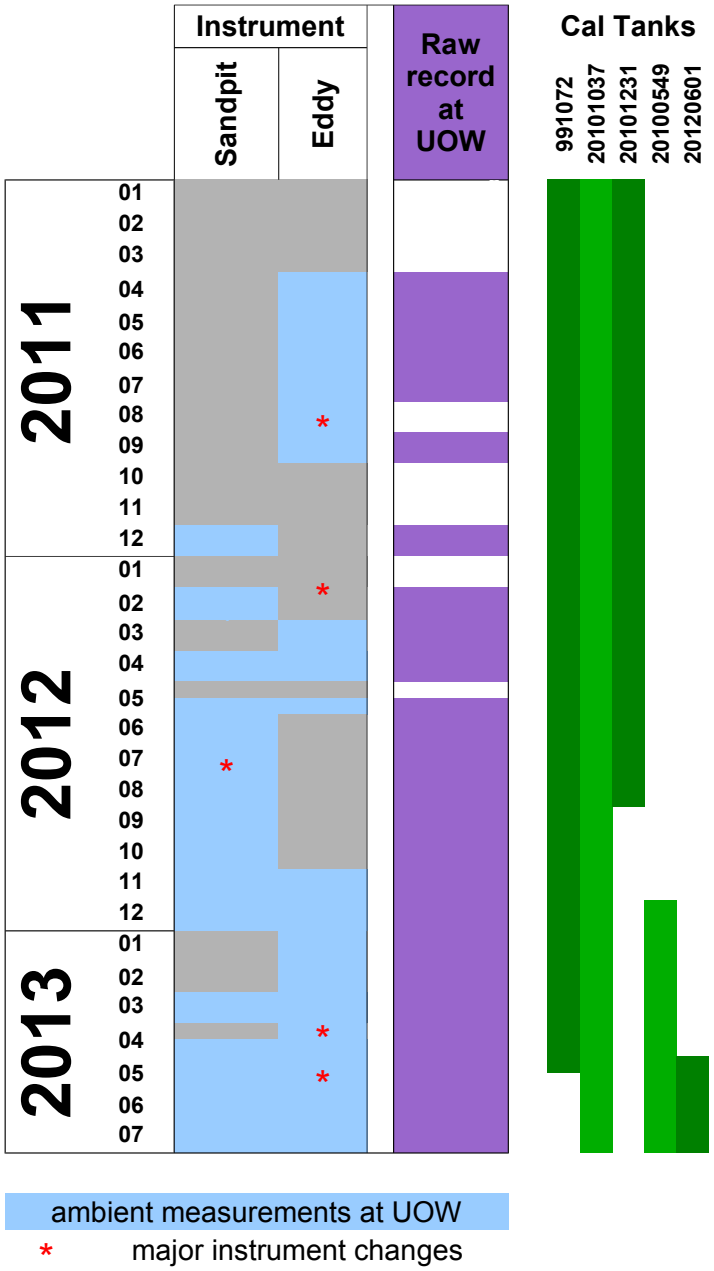

Figure 3.1.1: in situ FTIR trace gas analyser history at the University of Wollongong. Blue shaded areas indicate recording of ambient air at Wollongong. Grey shaded areas denote field trips or instrument upgrades, with no record of ambient air. Purple shaded area shows the extent of the combined raw record. Red stars flag major instrument changes, where care must be taken in ensuring record continuity. Green shaded areas show calibration tanks (UAN listed at the top) used at UOW.

acknowledged for their contribution to data collection, before 2012. The author was trained in instrument operation in 2010 and is responsible for the majority of UOW ambient measurement data collection using Eddy and Sandpit from mid-2011 onwards.

The instruments measure CO concurrently with CH_4, N_2O, CO_2 and isotopic $^{13}CO_2$ from which $\delta^{13}C$ is calculated. The main focus of this research is using in situ FTIR measurements to understand the atmospheric trace gas CO at Wollongong, with only preliminary study of the other atmospheric constituents. Datasets for all constituents are developed, and timeseries analysis performed for CO remains the most extensive, with only initial analysis performed for all other trace gases and $\delta^{13}C$ in this work.

Operational parameters, data preparation and quality control are outlined in this Chapter. Correction for cross-sensitivity, calibration to a World Meteorological Organisation–Global Atmosphere Watch (WMO–GAW) global scale, and quality control due to instrumental or environmental deviations are discussed in detail. Following preparation of the quality controlled dataset, detailed analysis was performed, which is presented in Chapter 4.

3.2 Operation and timeseries preparation

Operation of the in situ FTIR at UOW followed the same procedure for both Eddy and Sandpit instruments. Outside ambient air was continuously flushed through an inlet line at 5 L min^{-1}. From this inlet line, sample air was continuously drawn into the instrument at 1 L min^{-1}. Instrument parameters, such as flow, pressure and temperature, were monitored and maintained according to Table 3.2.1. These specified parameters were used to quality control the UOW ambient timeseries. Air was sampled under continuous flow through a White cell, in which the infrared beam was reflected through the sample multiple times to create a path length of 24 metres. Spectra were co-added over 3 minutes for both Sandpit and Eddy. Trace gas mole fractions were retrieved from the spectra using the non-linear least-squares program MALT (Multiple Atmospheric Layer Transmission, described earlier in Chapter 2) (Griffith, 1996; Griffith et al., 2012).

Ambient measurements were performed over 23.5 hours per day, with the remaining 30 minutes measuring constant composition air from a "target tank", an aluminium cylinder previously filled with ambient air. This target tank was recorded once a day usually at 11:30 pm, constrained to conditions in Table 3.2.1. The target tank allowed determination of instrument drift due to day-to-day instrument fluctuations. For example,

Table 3.2.1: Key instrument settings for the two in situ FTIR instruments at Wollongong. Parameters were maintained within the ranges indicated. Data collected outside these ranges is not included in final timeseries.

Variable	**Units**	**Instrument**	
		Sandpit Dec. 2011-current	**Eddy** Apr. 2011-current
Aperture	mm	3.0	1.5 except for: 3.0 Nov 2012 to Dec 2012
N_2 flow	L min^{-1}	0.15 ± 0.05	0.15 ± 0.05
Cell Temp	°C	31.2 ± 0.2, Nov. 2012 to 2013 31.0 ± 0.2, Apr. to Nov. 2012 30.8 ± 0.4, Feb. 2012 30.2 ± 0.2 in 2011	30.7 ± 0.2 in 2013 31.6 ± 0.3 in 2012 34.3 ± 0.2 in 2011
Cell Pressure	hPa	1100 ± 0.1, Apr. 2012 to 2013 1000 ± 0.5, Feb. 2012 1030 ± 0.5 in 2011	1100 ± 0.1 in 2012, 2013 1000 ± 10 in 2011
Flow	L min^{-1}	1.0 ± 0.2, Apr. 2012 to 2013 0.8 ± 0.4, Feb. 2012 1.2 ± 0.2 in 2011	1.0 ± 0.2 in 2012, 2013 0.5 ± 0.1 in 2011
H_2O	μmol mol^{-1}	$\leqslant$ 10	$\leqslant$ 10 $\leqslant$ 15 in 2011
Time co-adding	min	3	3 5 in 2011
# of spectra in co-additions		104 (single scan)	54 (reverse scan)

fluctuations in the N_2 purge flow surrounding the optics can affect retrievals, particularly for N_2O and CO. Target tank measurements were useful in determining when N_2 purge flow changed, allowing spurious data to be filtered out of the final dataset.

In addition to data filtering, there were further data processing steps used to prepare an accurate timeseries of the trace gases for UOW. These steps are listed below and discussed in further detail in the following sections.

- Firstly, retrieved mole fraction amounts for each trace gas are converted into dry-air mole fractions (Section 3.2.1).

- Secondly, corrections are applied for retrieval cross-sensitivity to physical parameters and other trace gases (Section 3.2.2).

- Finally, results are calibrated to a global calibration scale (Section 3.2.3).

3.2.1 Dry-air mole fraction

Mole fraction is defined as the molar amount trace gas of interest, divided by the total molar amount (i.e. the molar sum of all present species). Atmospheric water vapour varies greatly throughout the day, from season to season, at different altitudes, and between measurement sites. Water vapour variability is carried through to total molar amount variability. Therefore including water in mole fraction calculations means that variability of the target trace gas may be entirely due to variability of water vapour. Conversion to dry air mole fraction is described in Equation 3.2.1. Working with dry air mole fractions allows determination of the true variability of the trace gas of interest.

Conversion to dry-air mole fraction

$$\chi_{dry} = \frac{\chi_{raw}}{1 - \chi_{\mathrm{H_2O}}} \tag{3.2.1}$$

Where:

χ_{dry} = dry-air mole fraction (mol mol^{-1})

χ_{raw} = raw mole fraction determined by MALT (mol mol^{-1})

$\chi_{\mathrm{H_2O}}$ = retrieved mole fraction of H_2O using MALT (mol mol^{-1})

χ = CO_2, CH_4, CO, N_2O or $\delta^{13}CO_2$

The FTIR instruments used nafion® membrane followed by magnesium perchlorate ($Mg(ClO_4)_2$) to dry incoming air (instrument diagram in Chapter 2). However, residual water vapour remained in the cell, contributing to the retrieved mole fraction and requiring conversion to dry-air mole fraction. The remaining amount of water vapour in the dried ambient air sample is small (< 10 μmol mol^{-1}) compared with atmospheric amounts (typically $\sim$1%), therefore conversion to dry-air mole fraction generally introduces a small adjustment for χ_{dry} relative to χ_{raw}. For example, in a χ_{raw} for CO of 60 nmol mol^{-1}, a 10 μmol mol^{-1} water vapour concentration would induce a 0.0006 nmol mol^{-1} adjustment.

3.2.2 Cross-sensitivity quantification

Following the conversion to dry-air mole fraction, residual sensitivity to instrument and environmental parameters was accounted for. Cross sensitivity factors were quantified in a set of experiments and subsequently applied to the dry-air mole fraction values.

Trace gas retrievals show sensitivity to instrument and environmental parameters. In particular, spectroscopic retrieval of trace gases are sensitive to the pressure, flow, temperature, and the relative concentration of water or CO_2 (introduced in Chapter 2, Section 2.3). While instrument parameters are kept within a stable range for ambient measurement, small fluctuations can still affect the instrument response. The retrieval program MALT accounts for sample pressure and temperature, but small dependence on instrument lineshape and density may still occur due to errors in the HITRAN spectral database and the spectral model. Small fluctuations in parameters result in systematic errors of less that 1% of the final values. Cross-sensitivity to parameter fluctuations may be corrected through experimentation in order to reduce induced changes in the ambient record (Hammer et al., 2012).

Quantifying cross-sensitivity follows the same methodology for each instrument. Cross sensitivity was quantified separately relative to the parameters: pressure (P), flow (F), CO_2, water (Q) and temperature (T). Once determined, cross sensitivity factors were applied to the dry-air mole fraction values in linear combination according to Equation 3.2.2.

Correction for cross sensitivities

$$\chi_{cor} = \chi_{dry} - \frac{\partial\chi}{\partial P}(P-P_0) - \frac{\partial\chi}{\partial F}(F-F_0) - \frac{\partial\chi}{\partial Q}(Q-Q_0) - \frac{\partial\chi}{\partial CO_2}(\mathrm{CO_{2,dry}} - \mathrm{CO_{2,0}}) - \frac{\partial\chi}{\partial T}(T-T_0) \tag{3.2.2}$$

Where:

$\chi_{cor} =$ corrected dry-air mole fraction of χ (mol mol^{-1})
$\chi_{dry} =$ dry-air mole fraction of χ (mol mol^{-1}) determined in Equation 3.2.1
$\frac{\partial\chi}{\partial U} =$ (U = P, F, Q, T, CO_2) cross sensitivity factor to parameter U
$P - P_0 =$ pressure variation around $P_0 = 1100$ mbar
$F - F_0 =$ flow variation around $F_0 = 1.0$ (Lmin^{-1})
$Q - Q_0 =$ water vapour variation around $Q_0 = 0$ mol mol^{-1} (H_2O retrieved using MALT)
$\mathrm{CO_{2,dry}} - \mathrm{CO_{2,0}} =$ variation of dry-air mole fraction of CO_2 around $\mathrm{CO_{2,0}} = 400$ μmol mol^{-1}
$T - T_0 =$ temperature variation around 30.0 °C

Cross-sensitivity in each trace gas to each parameter was quantified in a set of separate experiments for both in situ FTIR instruments. Air of constant composition from a target tank was measured under continuous-flow conditions to analyse retrieval fluctuations relative to parameter changes. The parameter of interest was varied non-monotonically while holding all other parameters constant. The varied parameter was held constant at each new value for 30 minutes to minimise disequilibrium thermal fluctuations. The first 5 to 10 points were removed from each 30 minute time period to remove thermal and cell-memory effects, prior to calculating the cross sensitivity factor. Cross sensitivities were assumed to be linear and factors were calculated using Igor Pro software (WaveMetrics, 2012). Final cross-sensitivity factors are mean values of several experiments. A description of specific methodology for determining cross sensitivity to each parameter now follows.

Pressure and Flow

Pressure and flow parameters were adjusted using internal pressure and flow control of each instrument. Pressure was ranged between 900 and 1200 hPa in 40 hPa increments. Flow was ranged between 0.8 and 1.2 L min^{-1} in increments of 0.05 L min^{-1}. An example of pressure and flow cross-sensitivity is shown for Sandpit CO in Figures 3.2.1a and 3.2.1b. As indicated, Sandpit showed cross sensitivity of 0.0026 $\pm$ 0.0005 nmol mol^{-1} CO per hPa change in pressure, and -0.77 $\pm$ 0.24 nmol mol^{-1} CO per L min^{-1} change in flow rate. Typically, pressure varies by 0.5 hPa and flow by 0.2 L min^{-1}, which means variation induced by the cross sensitivity is smaller than the factors indicated.

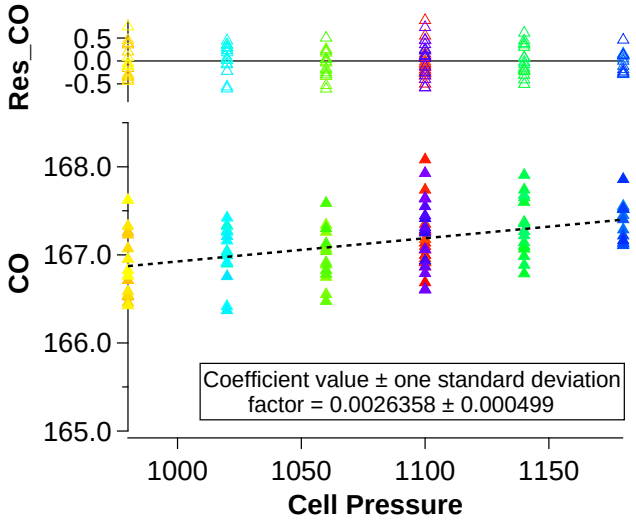

(a) CO versus Cell Pressure, 11 March, 2013

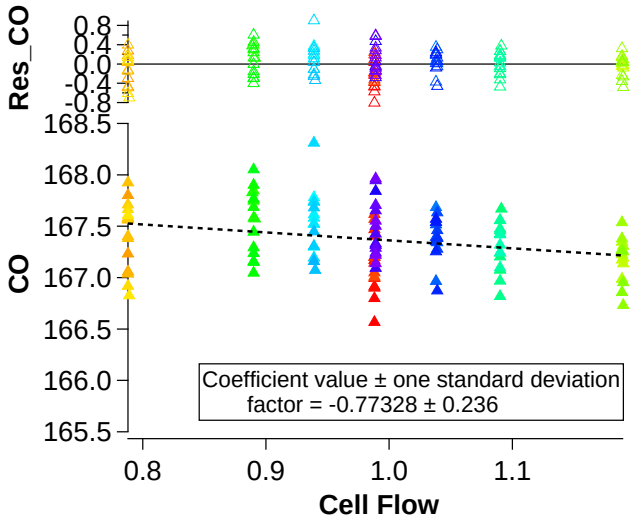

(b) CO versus Cell Flow, 11 March, 2013

Figure 3.2.1: Cross sensitivity experiments for CO on Sandpit with (a) Pressure, and (b) Flow. Dry air mole fractions of CO (nmol mol^{-1}) are plotted as filled triangles against parameter of interest. Colours represent time progression, red being the beginning of the experiment, through the rainbow to purple at the end of the experiment. Pressure and Flow include the last 15 points during each 30-minute time period where the parameter was held constant. Linear regression is indicated by the black dotted line and slope factor with 1σ standard deviations values are shown. Residuals are shown as open triangles in the upper panels and are the difference between the trace gas values and the line of best fit, calculated using Igor Pro (WaveMetrics, 2012).

CO_2

A target tank was spiked with high amount of CO_2 before filling with ambient air. Determination of CO_2 cross sensitivity required a custom-built mixing device in order to produce air of varying CO_2 composition, while remaining constant in all other species. Target tank air was sampled through a mixing device, which split the air into two streams, each controlled by a mass flow controller (MFC). One MFC sent air through ascarite®, removing CO_2 with the result known as "scrubbed' air. The other stream was unaffected. Scrubbed and unscrubbed air streams were recombined in a range of flow ratios. This ensured reproducible control over the amount of CO_2 within the air sample. The range of flow ratios were chosen to produce CO_2 values between 200 and 1000 μmol mol^{-1}, in increments of 50 to 100 μmol mol^{-1}. An example of CO_2 cross-sensitivity is shown for Sandpit CO in Figure 3.2.2. Cross sensitivity for CO is -0.00071 $\pm$ 0.00012 nmol mol^{-1} CO per μmol mol^{-1} of CO_2. Experimentally, CO_2 typically ranges around 100 μmol mol^{-1}, which typically induces a 0.07 nmol mol^{-1} change in CO.

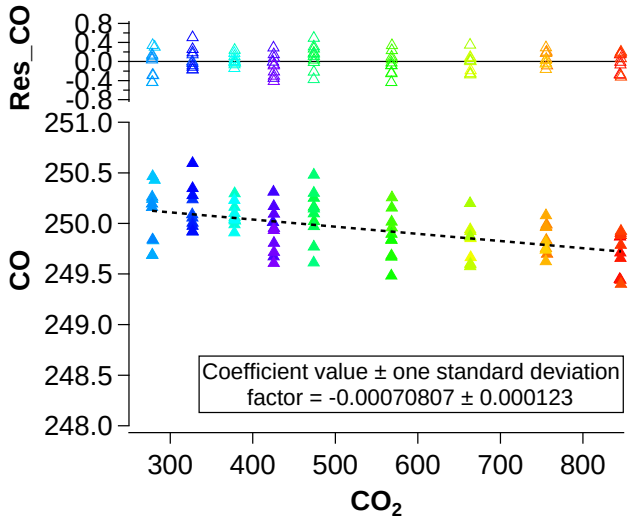

Figure 3.2.2: Cross sensitivity experiments for CO on Sandpit relative to CO_2. Dry air mole fractions of CO (nmol mol^{-1}) are plotted as filled triangles against CO_2 mole fraction. Colours represent time progression, red being the beginning of the experiment. The last 15 points during each 30-minute constant-parameter time period are plotted. The black dotted line indicates linear regression, and slope factor with 1σ standard deviation is shown. Open triangles indicate residuals between CO values and the line of best fit, calculated using Igor Pro (WaveMetrics, 2012).

Water Vapour

A mixing device similar to that used for CO_2 cross sensitivity experiments is usually used to determine water cross sensitivity. In water vapour cross-sensitivity experiments, $Mg(ClO_4)_2$ scrubs air of H_2O. However, water cross sensitivity is challenging due to a large hysteresis effect from fast changes in water content, the result of an equilibrium between water adsorption on the cell walls and atmospheric water content. Hysteresis response to water content makes cross sensitivity analysis difficult to reproduce and interpret using this method.

As an alternative, water cross sensitivity was determined by assessing target tank measurements during slow saturation of $Mg(ClO_4)_2$, at the end of the chemical dryer lifetime (over several days). Slow saturation of $Mg(ClO_4)_2$ resulted in a slow increase in cell water vapour content. In addition to the slow saturation experiment, measurements of a target tank are taken over the drying period of approximately a day, after replacement of the saturated $Mg(ClO_4)_2$. This method does not see hysteresis effects, resulting in more reproducible cross-sensitivity values compared with the mixing device method.

In addition to being reproducible, these saturation and drying experiments are more representative of water fluctuations in ambient measurements, as these slower processes are what is experienced by the ambient measurements. An example of H_2O cross-sensitivity is shown for Sandpit CO in Figure 3.2.3. Cross sensitivity for CO is -0.041 $\pm$ 0.0065 nmol mol^{-1} CO per μmol mol^{-1} of H_2O. In the ambient record, water vapour is kept below 10 μmol mol^{-1}, usually around 3 μmol mol^{-1}, therefore corrections to CO for water vapour are within -0.41 nmol mol^{-1} CO. Cross sensitivity parameters determined using this method are on the same order as Hammer et al., 2012, with the ability of producing robust results for CH_4 and CO.

Temperature

Temperature distribution of the sample within the cell may be affected by the set temperature of the cell enclosure, the flow rate and the temperature of the incoming sample. There are three main causes for temperature error: the difference between measured and true gas temperature, the overall mean set instrument temperature, and sensitivities due to rapid changes in temperature. Hammer et al., 2012 determined corrections for two of these temperature sensitivities, equilibrium or residual temperature sensitivity (RTS) and temperature disequilibrium sensitivity (TDS). The first accounted for sensitivity to equilibrium temperature and was found to be insignificant.

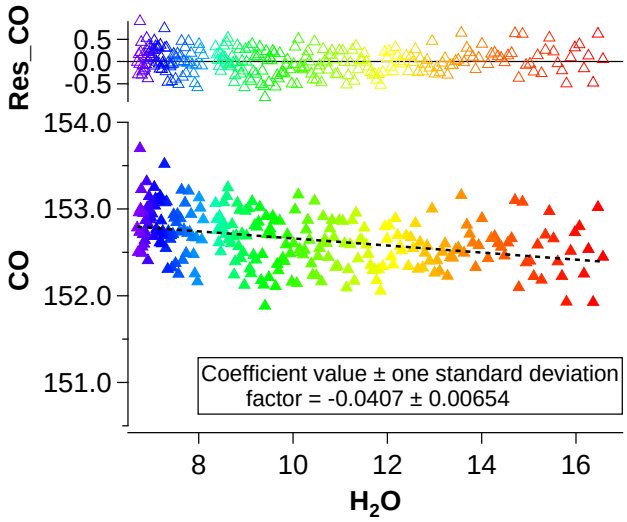

Figure 3.2.3: Cross sensitivity experiments for CO on Sandpit with H_2O. Dry air mole fractions of CO (nmol mol^{-1}) are plotted as filled triangles against H_2O mole fraction. Colours represent time progression, red being the beginning of the experiment. Cross sensitivity was recorded during slow drying of the cell environment after replacement saturated $Mg(ClO_4)_2$. All trace gas values measured below 17 μmol mol^{-1} H_2O are retained. The dotted black line indicates linear regression and slope factor with 1σ standard deviation is shown. Open triangles represent residuals between the trace gas values and the line of best fit, calculated using Igor Pro (WaveMetrics, 2012).

Temperature cross sensitivity was calculated using a different method to other cross sensitivity experiments, and differently to that used in Hammer et al., 2012. Since the cell is temperature controlled, the most likely temperature fluctuations affecting the ambient record are due to small fluctuations occurring between concurrent measurements, rather than fast and/or large temperature fluctuations. Residual non-random dependence of temperature was found after applying Pressure, Flow or H_2O cross sensitivity factors to their respective datasets. For this reason, temperature cross sensitivity values were calculated from the datasets of Pressure, Flow and H_2O cross sensitivity experiments, after other corrections were applied. No statistically significant temperature cross sensitivity could be determined for CO on Sandpit.

An example of CO temperature cross sensitivity is shown from Eddy, in Figure 3.2.4. Cross sensitivity for CO is 2.03 ± 0.79 nmol mol^{-1} CO per °C. Therefore, a typical experimental temperature variation of 0.2 °C induces a 0.4 nmol mol^{-1} change in CO. Temperature cross sensitivity values calculated here compare well with the temperature disequilibrium sensitivity (TDS) described in Hammer et al., 2012.

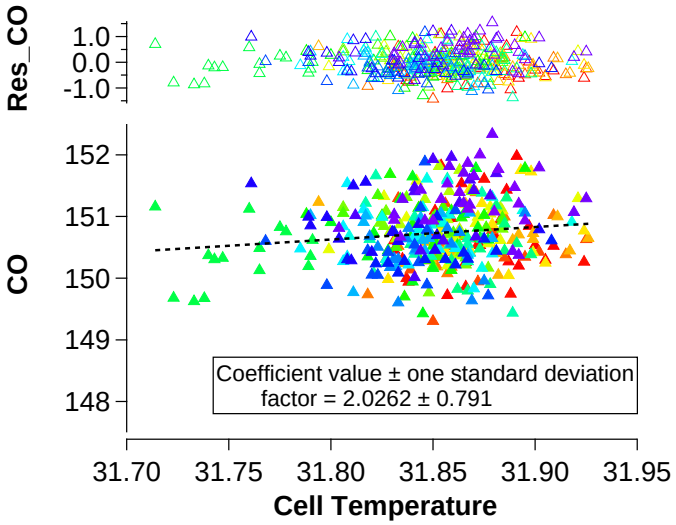

Figure 3.2.4: Example temperature cross-sensitivity experiment with respect to CO from Eddy, February, 2013. Temperature cross sensitivity was determined in target tank data, after water cross sensitivity was determined then applied. Colours represent time progression, red being the beginning of the experiment, through the rainbow to purple at the end of the experiment. Linear regression is indicated by the black dotted line and slope factor with 1σ standard deviations values are shown. Residuals are shown as open triangles and are the difference between the trace gas values and the line of best fit, calculated using Igor Pro (WaveMetrics, 2012).

This type of temperature correction does not account for step-changes in average cell temperature, only fluctuations about a mean temperature. Step changes in the mean temperature require alternate methods to account for effect on trace gas amounts. Here, temperature step changes are accounted for during the calibration procedure, described in the next section (3.2.3).

In the case of the ambient dataset, temperature cross sensitivity was determined using tank measurements and was applied to the entire ambient record. Systematic uncertainty may have been introduced into the ambient record by using this temperature cross-sensitivity. Ambient measurements may not undergo the same temperature processes experienced by tank air, for example gas expansion. Therefore, cross sensitivity determined using measurements of tank air may not be transferrable to ambient measurements. However, it is expected that there is some temperature cross sensitivity with the ambient measurements, but changes may be smaller than for tank measurements because the tank measurements require evacuation of the White cell beforehand, whilst ambient measurements use a continuous flow technique.

A representative ambient timeseries was analysed with and without applying temperature cross sensitivity and the mean absolute difference between resulting datasets calculated. Mean differences for trace gases with percentages relative to the dataset mean are: CO_2: 1.22 (0.32%), CO: 1.44 (2.4%), CH_4: 5.92 (0.056%), N_2O: 1.39 (0.43%), $\delta^{13}C$: 2.33 (23%). These values indicate a significantly altered dataset, between applying and not applying temperature cross sensitivity. Temperature bias is not considered further in this work, but it would be an advantage to further determine temperature effects on these instruments during ambient measurements, and determine whether the temperature cross sensitivity factor used here is representative.

All cross sensitivity correction factors are summarised for each trace gas relative to each parameter and are listed for Sandpit in Table 3.2.2 and Eddy in Table 3.2.3. Sandpit gave cross-sensitivity factors which were applied across the entire instrument record. Robust cross sensitivity in Sandpit for CO to temperature and $\delta^{13}C$ to water were unable to be determined. Eddy required application of different cross sensitivity factors in different time periods. This was due to Eddy undergoing more instrument changes than Sandpit, which subsequently produced different factors for some cross sensitivities. In particular, Pressure and Flow cross sensitivities are different in Eddy between 1.5 mm and 3.0 mm apertures. Additionally, CO_2 cross sensitivity is different before and after two mass flow controllers were introduced in 2013.

Tables 3.2.2 and 3.2.2 also indicate a typical induced change in trace gas amounts due to a typical experimental range of parameter of interest (listed below).

Typical parameter ranges:

$$\begin{aligned} \Delta P &= 0.5 \text{ hPa} \\ \Delta F &= 0.2 \text{ L min}^{-1} \\ \Delta Q &= 10 \ \mu\text{mol mol}^{-1} \\ \Delta T &= 0.2 \ ^\circ\text{C} \\ \Delta CO_2 &= 100 \ \mu\text{mol mol}^{-1} \end{aligned}$$

For example flow cross sensitivity in Sandpit induced a $6.3{\times}10^{-1} \times 0.2 = 0.13$ nmol mol^{-1} change in CO. When taking typical parameter ranges into account, the three cross sensitivities which contribute the most to systematic inaccuracies in trace gas retrievals are flow, water and temperature. Pressure cross sensitivity in both instruments induces a small change in all atmospheric amounts. This is due to a combination of low cross sensitivity factor with tight control over instrumental pressure.

Table 3.2.2: Summary of mean cross sensitivity correction factors for Sandpit with associated standard uncertainty (1 σ). χ represents trace gas that is cross sensitive to the parameter, to be replaced with columns headers. Parameters which have no significant cross-sensitivity are denoted with: $\sim$. Cross sensitivity corrections are shown relative to typical experimental variation in parameters (ΔU=U-U$_0$).

	CO $\pm\sigma$ (nmol mol^{-1})	**CO$_2$** $\pm\sigma$ (μmol mol^{-1})	**CH$_4$** $\pm\sigma$ (nmol mol^{-1})	**N$_2$O** $\pm\sigma$ (nmol mol^{-1})	δ^{13}**C** $\pm\sigma$ (‰)
$\frac{d\chi}{dP}$ (hPa^{-1})	2.36e-03 ±8.9e-04	1.312e-02 ±1.0e-04	4.486e-02 ±6.8e-04	8.848e-03 ±2.8e-04	8.07e-03 ±2.3e-04
Typical variation of ΔP= 0.5 hPa	0.0012 ±0.0004	0.007 ±0.003	0.0224 ±0.0003	0.0044 ±0.0001	0.0004 ±0.0001
$\frac{d\chi}{dF}$ (slpm^{-1})	-6.3e-01 ±1.5e-01	-5.31e-01 ±1.5e-02	-2.27 ±1.4e-01	-4.872e-01 ±6.3e-02	-1.087 ±4.2e-02
Typical variation of ΔF= 0.2 slpm	-0.13 ±0.03	-0.106 ±0.003	-0.45 ±0.03	-0.10 ±0.01	-0.217 ±0.008
$\frac{d\chi}{dQ}$ (μmol^{-1} mol)	-4.07e-02 ±6.5e-03	-7.9e-03 ±1.0e-03	-9.41e-02 ±6.3e-03	-1.05e-02 ±2.6e-03	$\sim$
Typical variation of ΔQ= 10 μmol mol^{-1}	-0.41 ±0.07	-0.08 ±0.01	-0.94±0.06	-0.11 ±0.03	$\sim$
$\frac{d\chi}{dT}$ (°C^{-1})	$\sim$	1.25 ±2.1e-01	5.41 ±8.3e-01	1.29 ±3.6e-01	2.27 ±4.6e-01
Typical variation of ΔT= 0.2 °C	$\sim$	0.25 ±0.04	1.1 ±0.2	0.26 ±0.07	0.45 ±0.09
$\frac{d\chi}{d\mathrm{CO_2}}$ (μmol^{-1} mol)	-3.9e-04 ±1.3e-04	N/A	-3.84e-03 ±1.3e-04	-7.43e-04 ±5.4e-05	2.79e-03 ±1.6e-04 -6.71e+02 ±3.5e+01
Typical variation of ΔCO$_2$= 100 μmol mol^{-1}	-0.04 ±0.01		-0.38 ±0.01	-0.074 ±0.005	0.28 ±0.02
total absolute adjustment	0.57 ±0.07	0.44 ±0.04	2.9 ±0.2	0.54 ±0.07	0.95 ±0.09

Table 3.2.3: Summary of mean cross sensitivity correction factors for Eddy with associated standard uncertainty (1 σ). χ represents trace gas that is cross sensitive to the parameter, to be replaced with columns headers. E = general values for Eddy cross sensitivity, to be replaced in some cases by E* = Eddy values for 3 mm aperture and E† = Eddy values prior to 2 MFC. Parameters which have no significant cross-sensitivity are denoted with: $\sim$. Cross sensitivity corrections (ΔU_X) are shown relative to typical experimental variation in parameters (ΔU).

		CO $\pm\sigma$ (nmol mol^{-1})	**CO$_2$** $\pm\sigma$ (μmol mol^{-1})	**CH$_4$** $\pm\sigma$ (nmol mol^{-1})	**N$_2$O** $\pm\sigma$ (nmol mol^{-1})	δ^{13}**C** $\pm\sigma$ (‰)
$\frac{d\chi}{dP}$ (hPa^{-1})	E	4.78e-03 ±4.1e-04	7.26e-03 ±2.7e-04	2.710e-02 ±5.7e-04	3.44e-03 ±2.3e-04	3.995e-02 ±5.0e-04
	E†	-8.53e-03 ±6.6e-04				-1.080e-02 ±4.3e-04
Typical variation	ΔP_{XE}	0.0024 ±0.0002	0.0036±0.0001	0.0135 ±0.0003	0.0017 ±0.0001	0.0200 ±0.0003
of ΔP= 0.5 hPa	$\Delta P_{XE^\dagger}$	-0.0043 ±0.0003				-0.0054 ±0.0002
$\frac{d\chi}{dF}$ (slpm^{-1})	E	-5.9e-01 ±1.1e-01	3.14e-01 ±7.6e-02	6.8e-01±1.8e-001	2.27e-01 ±9.0e-02	1.2e-01 ±1.5e-01
	E*		-6.0e-02 ±2.0e-02	-1.185 ±3.5e-02	-3.8e-02 ±1.1e-02	-4.53e-01±6.0e-02
Typical variation	ΔF_{XE}	-0.05 ±0.03	0.06±0.02	0.14 ±0.04	0.05 ±0.02	0.03 ±0.03
of ΔF= 0.2 slpm	ΔF_{XE^*}		-0.012±0.003	-0.237 ±0.007	-0.007 ±0.002	-0.091 ±0.004
$\frac{d\chi}{dQ}$ (μmol^{-1} mol)	E	-3.54e-02 ±2.0e-03	2.66e-02 ±1.8e-03	-1.78e-02 ±3.4e-03	-3.76e-03±5.4e-04	-6.16e-02 ±3.1e-03
Typical variation of ΔQ= 10 μmol mol^{-1}	ΔQ_{XE}	-0.35 ±0.02	0.26±0.02	-0.17 ±0.03	-0.03 ±0.01	-0.62 ±0.03
$\frac{d\chi}{dT}$ (°C^{-1})	E	1.65 ±8.3e-01	1.90 ±5.4e-01	7.06 ±1.1e-00	1.55 ±4.5e-01	2.19 ±9.8e-01
Typical variation of ΔT= 0.1 °C	ΔT_{XE}	-0.17 ±0.08	0.19±0.05	0.7 ±0.1	0.15 ±0.05	0.3 ±0.1
$\frac{d\chi}{dCO_2}$(μ mol^{-1} mol)	E	3.5e-04 ±1.9e-04	N/A		-1.12e-03 ±1.3e-04	-3.31e-02 ±1.8e-03
				-5.06e-03 ±4.3e-04		-1.051e+04 ±2.9e02
	E†	6.25e-03 ±8.5e-04	N/A		1.39e-03 ±3.2e-04	1.29e-02 ±1.3e-03
						-4.2e+02 ±2.7e+02
Typical variation of	ΔCO_{2XE}	-0.03 ±0.02		-0.51±0.04	-0.11 ±0.01	-3.3 ±0.2
ΔCO_2= 100 μmol mol^{-1}	$\Delta CO_{2XE^\dagger}$	0.62 ±0.09			0.14 ±0.03	1.3 ±0.1
total absolute adjustment	E	0.60 ±0.09	0.52 ±0.06	1.5 ±0.1	0.35 ±0.05	4.2 ±0.2
	E*		0.47 ±0.06	1.6 ±0.1	0.30 ±0.05	4.3 ±0.2
	E†	1.2 ±0.1			0.37 ±0.06	2.2 ±0.2

Total absolute adjustment is also noted in the summary tables to give an idea of the relative adjustment for each cross sensitivity. However, cross sensitivity corrections are often of alternating signs and end up cancelling. Cross sensitivity corrections are applied to the dry-air mole fraction amounts of trace gases, even if very small. Errors in these corrections are used in uncertainty analysis in Section 3.2.4.

3.2.3 Calibration quantification

Following correction for cross-sensitivity, in situ FTIR data preparation required calibration to World Meteorological Organisation – Global Atmosphere Watch (WMO–GAW) standards, traceable to a global reference scale. Calibration is necessary in order to account for systematic instrument biases. In addition to conforming results to a benchmark, calibrations may also alert the operator to any non-linear instrumental variations, indicated by a drift in calibration parameters.

Once determined, calibration values were applied to the corrected ambient record following Equation 3.2.3.

Calibration to a global scale

$$\chi_{cal} = \frac{\chi_{cor} - Cal_{off}}{Cal_{fac}} \tag{3.2.3}$$

Where:

χ_{cal} = calibrated (and corrected) dry-air mole fraction of χ (mol mol^{-1})
χ_{cor} = determined in Equation 3.2.2
Cal_{off} = intercept of calibration experiment
Cal_{fac} = slope of calibration experiment

Calibration experiments were performed using a set of reference gas tanks filled with air at different constant compositions which are independently verified. Reference tanks were provided by CSIRO Global Atmospheric Sampling Laboratory (GASLAB) with mole fractions measured on WMO–GAW scales, traceable to the relevant primary standards for all species (Griffith et al., 2011). Composition of the calibration tanks as was determined by GASLAB are shown in Table 3.2.4.

Calibration measurements with three tanks of differing composition were performed at least once a month. Hammer et al., 2012 found that monthly calibration was sufficient to determine any instrument drift. The target tank was measured at the same time as calibration measurements, to benchmark constant composition.

The general method and workup of calibration followed a set procedure. Each calibration tank was measured for 30 minutes in 1 minute co-added intervals, under flow conditions where tank air was continuously drawn through the instrument at 1 L min^{-1}. Experiments were performed at 1100, 1030, or 1000 hPa, according to Table 3.2.1. Other

Table 3.2.4: Primary standard values and associated uncertainty from gas cylinders with constant composition, used in calibration experiments. Composition measurements of primary standards were performed by the CSIRO-GASLAB.

UAN (Tank Code)	**CO** nmol mol^{-1}	**CO_2** μmol mol^{-1}	**CH_4** nmol mol^{-1}	**N_2O** nmol mol^{-1}	**$\delta^{13}C$** ‰
20120549 (CA1682)	163.33 ±0.44	447.03 ±0.15	1950.29 ±1.9	334.61 ±0.44	-13.08 ±0.02
20101231 (CA6845)	105.37 ±0.64	418.37 ±0.10	1842.18 ±2.33	345.71 ±0.42	-8.6
20101037 (CA4918)	53.82 ±0.31	385.23 ±0.08	1749.81 ±2.62	321.64 ±0.44	-8.3
991072 (CA1628)	62.46 ±0.37	365.29 ±0.07	1732.00 ±2.19	313.53 ±0.31	-8.02 ±0.05
Scale (Griffith et al., 2011)	CSIRO	WMOX2007	Tohoku University (gravimetric)	SIO-98	VPDB

instrument parameters also followed Table 3.2.1. The cell was evacuated for 2 minutes, filled to 300 hPa, and evacuated again for 2 minutes between each tank, before filling the cell to the specified pressure and initiating flow conditions. Only the last 15 points measured for each tank are retained for analysis to avoid influence from gas thermal expansion or memory effects within the cell, which may be present in the first several measurements.

Following measurement of three calibration tanks, calibration factors and offsets were calculated using linear least squares analysis of the measured values versus the CSIRO-GASLAB reference values. FTIR measurements have previously been shown to conform to linearity (Griffith et al., 2012). Linear regression was performed using the Igor Pro analysis software (WaveMetrics, 2012). Least squares fitting resulted in a scaling offset (Cal_{off}) and slope factor (Cal_{fac}) for each trace gas. An example of linear least squares analysis is shown for all gases using Sandpit on 27 February, 2013, in Figure 3.2.5. Calibration results in Figure 3.2.5 show CO has a scaling factor (Cal_{fac}) of 1.037 ± 0.004 and an offset (Cal_{off}) of 1.9 ± 0.2 nmol mol^{-1}. By applying these values, according to Equation 3.2.3, to a representative atmospheric CO value of 60 nmol mol^{-1}, this calibration would result in calibrated value of 56.03 nmol mol^{-1}, which has induced a 3.97 nmol mol^{-1} difference in CO. This indicates there was approximately a 7% systematic error in retrieved CO, relative to the global scale.

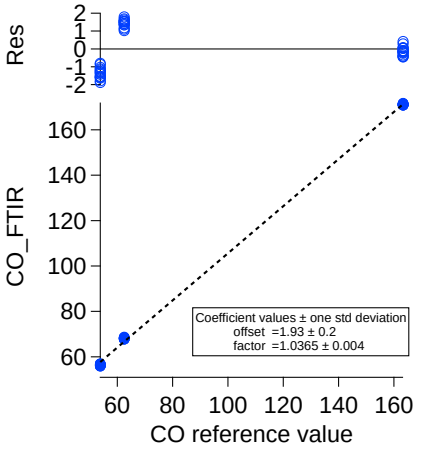

(a) Calibration for CO, 27 Feb., 2013.

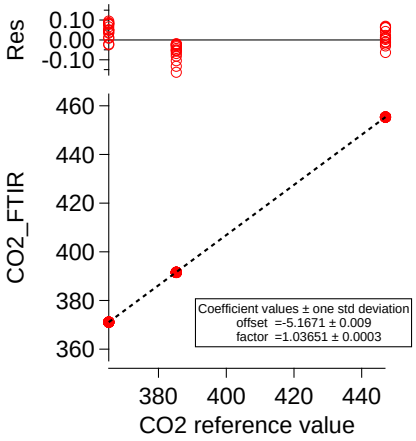

(b) Calibration for CO_2, 27 Feb., 2013.

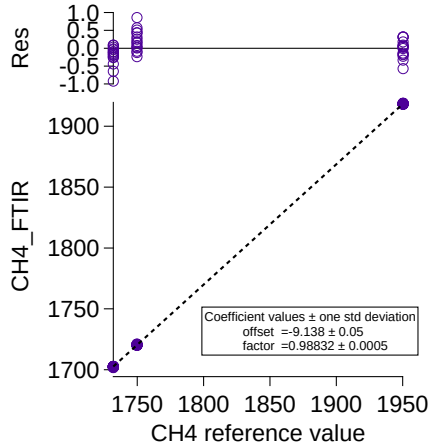

(c) Calibration for CH_4, 27 Feb., 2013.

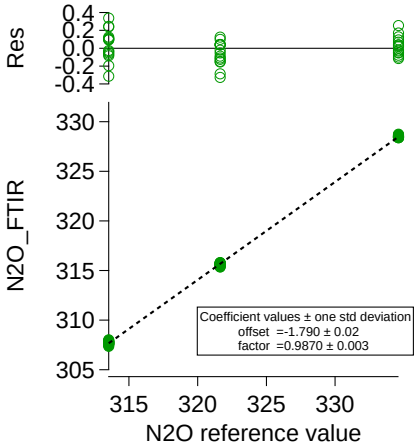

(d) Calibration for N_2O, 27 Feb., 2013.

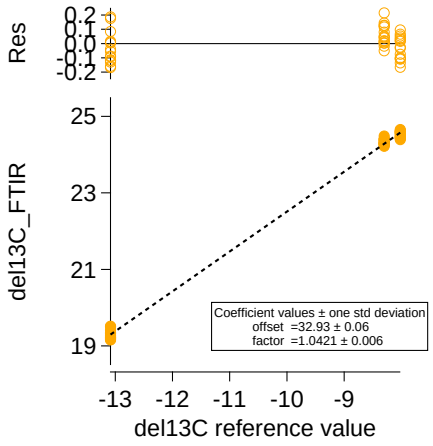

(e) Calibration for $\delta^{13}C$, 27 Feb., 2013.

Figure 3.2.5: Sandpit calibration results using three tanks of differing compositions, 27 February, 2013. Each tank was measured over 30 minutes and the last 15 points evaluated. Closed circles plot measured trace gas mole fractions against reference values, in nmol mol^{-1} (CO, CH_4 and N_2O), μmol mol^{-1} (CO_2), or ‰(del13). Slope factors and offsets are shown. Open circles represent residuals between measured values and the line of best fit, calculated using Igor (WaveMetrics, 2012).

Recorded standard uncertainties in slopes and intercepts are the uncorrelated uncertainties determined from least squares analysis, normalised by the mean of the reference values. For instance, Equation 3.2.3 can be thought of as:

$$\chi_{cal} = \frac{\chi_{cor} - b}{Cal_{fac}} + \bar{\chi_{ref}} \tag{3.2.4}$$

Where:

$\bar{\chi_{ref}} =$ mean reference value

$b = Cal_{off} - Cal_{fac} \times \bar{\chi_{ref}}$

The error in b of Equation 3.2.4 is then the uncorrelated error in the offset.

Monthly calibration experiments allowed determination of long-term instrument stability. Calibration results between months were compared by applying calibration values (Cal_{fac} and Cal_{off}) to representative trace gas values (according to Equation 3.2.3). Representative values of atmospheric trace gases were chosen as those most likely to be expected in the Wollongong atmosphere. In particular, CO_2 = 400 μmol mol^{-1}, CO = 60 nmol mol^{-1}, CH_4 = 1800 nmol mol^{-1}, N_2O = 320 nmol mol^{-1} and del^{13}C = -8 ‰. Timeseries of applied calibration values were produced from monthly calibration results. The timeseries of applied calibration values for all trace gases are shown for Sandpit in Figure 3.2.6, and cover the whole time period.

The timeseries of calibration values applied to representative trace gas amounts were subsequently used to determine the best way to apply calibration values to the ambient dataset. In months that the applied calibration results were stable, a mean of all calibration results was applied to the ambient data. For example, Sandpit displays two stable calibration regimes (Figure 3.2.6), with a step change in late 2012. This step change was determined to be due to a step change in mean instrument cell temperature, in November, 2012. This type of temperature effect was not accounted for in the temperature cross sensitivity, and is intrinsically accounted for during calibration. Sandpit therefore had two sets of calibration values determined from a mean before and after the change in cell temperature. Mean calibration values in the two Sandpit regimes are summarised in Table 3.2.5.

Two outliers of calibration values occurred in Sandpit for CO_2 in August, 2012. This was due to tank pressures being below 100 hPa. Measurements from tanks with low pressure are unreliable and therefore these calibrations were unreliable. Differences are not as pronounced for other trace gases in these calibrations.

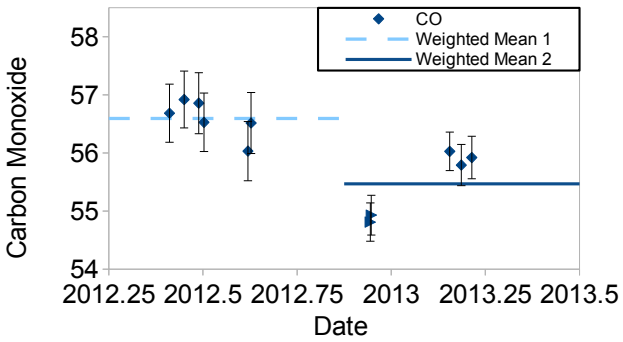

(a) Calibration factor and offsets applied to r.v 60 nmol mol^{-1} CO.

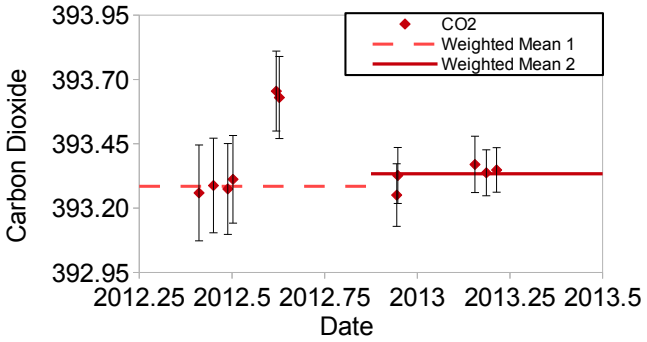

(b) Calibration factor and offsets applied to r.v. 400 μmol mol^{-1} CO_2

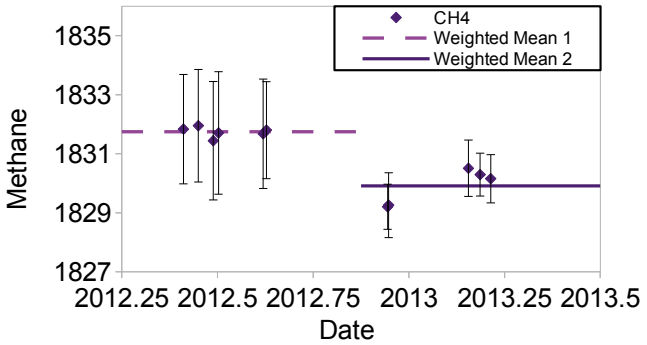

(c) Calibration factor and offsets applied to r.v. 1800 nmol mol^{-1} CH_4

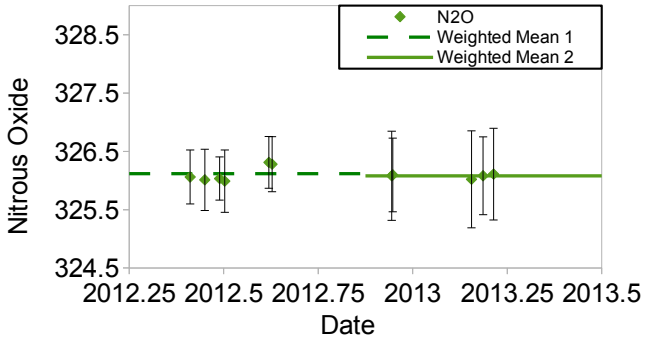

(d) Calibration factor and offsets applied to r.v. 320 nmol mol^{-1} N_2O

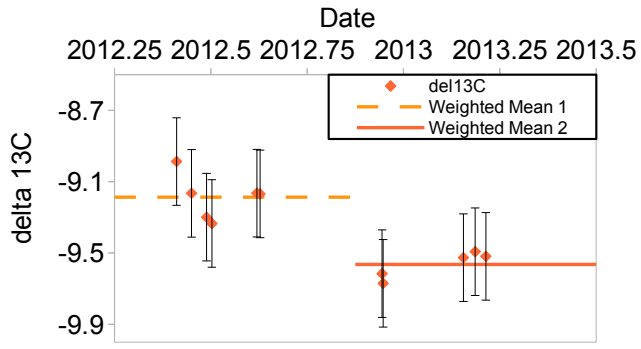

(e) Calibration factor and offsets applied to r.v. 40 ‰del^{13}C

Figure 3.2.6: Timeseries of different calibration experiment values applied to representative trace gas amounts for Sandpit. Representative values (r.v.) are CO = 60 nmol mol^{-1}, CO_2 = 400 μmol mol^{-1}, CH_4 = 1800 nmol mol^{-1}, N_2O = 320 nmol mol^{-1} and del^{13}C = -8 ‰. Error bars show standard error in calibration values, applied to representative values.

Of the two instruments, Sandpit is the most stable, due to it possessing a newer detector and having a more precise pressure, temperature and flow control. In contrast, Eddy was often used for research and development, meaning fundamental parameters of the instrument often changed. Eddy's major instrumental changes introduced three calibration regimes. The first step change occurred upon the introduction of two mass flow controllers in early 2012. The second step-change occurred when measurements moved from 3 mm aperture to 1.5 mm aperture. Mean calibration values for Eddy for the three regimes are summarised in Table 3.2.6.

Table 3.2.5: Calibration coefficients with associated standard uncertainty (1 σ) for Sandpit, which were applied to the ambient record. Sandpit has two calibration regimes: prior and post 16 November, 2012.

Trace Gas	Sandpit (prior to 16 Nov. 2012)				Sandpit (After 16 Nov. 2012)			
	Cal_{fac}		Cal_{off}		Cal_{fac}		Cal_{off}	
CO	1.0607	±8.1e-03	-0.03	±1.8e-01	1.0343	±3.9e-03	2.62	±1.9e-01
CO_2	1.02890	±4.3e-04	-4.7955	±9.5e-03	1.03052	±2.4e-04	-5.3367	±8.5e-03
CH_4	0.9900	±1.0e-03	-13.462	±4.9e-02	0.98886	±4.5e-04	-9.521	±4.5e-02
N_2O	0.9857	±1.4e-03	-1.480	±1.9e-02	0.9869	±2.2e-03	-1.814	±1.9e-02
$\delta^{13}C$	1.032490	±2.7e-05	32.49	±1.3e-01	1.03287	±1.4e-05	32.879	±7.8e-02

Table 3.2.6: Calibration coefficients with associated standard uncertainty (1 σ) for Eddy, which were applied to the ambient record. Eddy has three calibration regimes: 2011, 2012 prior to November and November 2012 through 2013.

Trace Gas	Eddy 1.5 mm aperture (2011)				Eddy 3 mm aperture (prior Nov 2012)			
	Cal_{fac}		Cal_{off}		Cal_{fac}		Cal_{off}	
CO	0.984	±2.4e-02	-7.91	±5.2e-01	1.0360	±6.6e-03	-1.91	±1.5e-01
CO_2	0.988	±1.6e-02	-11.89	±3.5e-01	1.0352	±1.6e-03	-7.886	±3.6e-02
CH_4	0.9567	±4.3e-03	-43.29	±2.1e-01	0.9816	±1.1e-03	-19.183	±5.2e-02
N_2O	0.9425	±8.9e-03	-7.35	±1.2e-01	0.9659	±1.2e-03	-2.574	±1.7e-02
$\delta^{13}C$	1.0178	±1.2e-03	15.0	±4.2e+00	1.049939	±6.8e-05	50.8	±1.4e+00

	Eddy 1.5 mm aperture (Nov 2012 onwards)			
	Cal_{fac}		Cal_{off}	
CO	0.9937	±4.0e-03	-1.92	±2.0e-01
CO_2	0.9914	±1.7e-03	-6.312	±5.8e-02
CH_4	0.9626	±1.1e-03	-21.74	±1.1e-01
N_2O	0.9501	±5.0e-03	-3.180	±4.3e-02
$\delta^{13}C$	1.05660	±1.4e-04	56.52	±4.9e-01

Application of calibration values to the ambient record produced a quality controlled timeseries, traceable to WMO–GAW standards.

3.2.4 Total dataset uncertainty

Before assessing the UOW ambient dataset for properties such as background values and seasonal cycles it was important to quantify dataset uncertainty in order to statistically interpret dataset properties. This section details uncertainty analysis for the ambient measurements recorded using the in situ FTIR. Uncertainties are calculated for the ensemble of ambient air record, rather than for each individual measurement, to give an estimate of the general uncertainty associated with the ambient dataset.

Total uncertainty in ambient measurements is a combination of instrument precision and uncertainties associated with the three dataset processing steps previously introduced in Section 3.2, namely: conversion to dry-air mole fraction; correction for cross-sensitivity; and calibration to a global scale. Uncertainties arising for each of these processing steps were not independent due to the steps being applied sequentially. Therefore, each processing step incorporates uncertainty from the previous step. Combination of all uncertainties is developed throughout this section.

Instrument precision is limited by random uncertainty. Random uncertainty for the in situ FTIR measurements was previously determined by a set of repeatability experiments in (Griffith et al., 2012) and (Hammer et al., 2012). Allan variance was used to show that in general, variance of uncorrected and uncalibrated dry-air mole fraction retrievals by the in situ FTIR is dominated by detector noise, up to at least 20 minutes. Random uncertainties in dry-air mole fractions are listed in table 3.2.7 and are within WMO-GAW repeatability requirements.

Table 3.2.7: Random uncertainty (Allan deviation) from 1 and 10 minute repeatability experiments (Griffith et al., 2012) and 2.5 and 10 minute repeatability experiments (Hammer et al., 2012).

Trace Gas	**Random Uncertainty**				**Units**
	(Griffith et al., 2012)		(Hammer et al., 2012)		
	1 min	10 min	2.5 min	10 min	
CO	0.2	0.08	0.2	0.1	nmolmol^{-1}
CO_2	0.02	0.01	0.018	0.012	μmolmol^{-1}
CH_4	0.2	0.06	0.2	0.1	nmolmol^{-1}
N_2O	0.1	0.03	0.07	0.04	nmolmol^{-1}
$\delta^{13}C$	0.07	0.01	0.05	0.03	‰

Instrument accuracy is limited by systematic error, such as errors in the MALT model or HITRAN database, instrument cross-sensitivity to parameters such as pressure and flow, or offset to a global standard scale. Systematic error is accounted for through cross sensitivity and calibration steps of data processing. However, while systematic errors may be minimised, correction for systematic error will leave residual uncertainty, which is further discussed in this section.

The first uncertainty to consider is associated with conversion to dry-air mole fraction. Equation 3.2.5 describes the combination of uncertainty contributing to the dry air mole fraction if we were to include the uncertainty in MALT retrievals. However, systematic error due to MALT retrieval errors are insignificant compared with random uncertainty, because results from the Allan Variance test show dry-air retrievals are dominated by random processes (Griffith et al., 2012). MALT fitting procedure is therefore driven predominantly by random differences between synthetic and measured spectra. That is, any systematic error introduced by MALT retrievals is much smaller than the random uncertainty, or instrument precision, and consequently are not considered here. Additionally, the sample water content is kept very low, so the error contribution from water correction is extremely small. Therefore, uncertainties for dry air mole fractions are taken to be random uncertainties determined from the 2.5 minute experiments from Hammer et al., 2012, listed in Table 3.2.7.

Fractional uncertainty associated with dry-air mole fraction

$$\frac{\delta\chi_{dry}}{\chi_{dry}} = \sqrt{\left(\frac{\delta\chi_{raw}}{\chi_{raw}}\right)^2 + \left(\frac{\delta \mathrm{H_2O}_{raw}}{1 - \mathrm{H_2O}_{raw}}\right)^2} \tag{3.2.5}$$

Where:

$\delta\chi_{dry} =$ uncertainty from MALT retrieval for χ (μ or nmol mol^{-1})
$\delta \mathrm{H_2O}_{raw} =$ uncertainty from MALT retrieval for $\mathrm{H_2O}$ (μmol mol^{-1})

Next, residual uncertainty associated with cross-sensitivity correction was determined. While the systematic error due to instrument cross sensitivity is minimised by applying cross sensitivity factors, some uncertainty remains. The remaining uncertainty contains uncertainty introduced during cross sensitivity studies from linear regression and from intrinsic uncertainties in the apparatus which measures the particular parameter during the ambient record. Remaining uncertainty after applying a single cross sensitivity parameter (U) can be described by equation 3.2.7.

Uncertainty in a single cross sensitivity correction

For the cross sensitivity correction to parameter U:

$$U_{Xsens} = \frac{\partial \chi}{\partial U}(U - U_0) \tag{3.2.6}$$

The associated uncertainty is:

$$\delta U_{Xsens} = U_{Xsens}\sqrt{\left(\frac{\delta_{\frac{\partial \chi}{\partial U}}}{\frac{\partial \chi}{\partial U}}\right)^2 + \left(\frac{\delta U}{U - U_0}\right)^2} \tag{3.2.7}$$

Where:

$U =$ P, F, Q, CO_2, T

$\frac{\partial \chi}{\partial U} =$ cross sensitivity factor for parameter U, determined in Section 3.2.2 and listed in Tables 3.2.2 & 3.2.3.

$\delta_{\frac{\partial \chi}{\partial U}} =$ uncertainty in cross sensitivity factor for parameter U listed in Tables 3.2.2 & 3.2.3.

$\delta U =$ uncertainty of measuring cross sensitivity parameter U listed in Table 3.2.8, note that $\delta U = \delta(U - U_0)$ as U_0 is a constant and therefore has no associated uncertainty

$U - U_0 =$ difference between measurement and ideal value of U_0

Uncertainty exists in the cross sensitivity due both to the uncertainty of the multiplicative slope correction factor and in the uncertainty of parameter measurement. For example there is intrinsic uncertainty in the manometers used to record pressure. Cross sensitivity factor uncertainties are listed in Tables 3.2.2 and 3.2.3, which were determined as standard error in the slope calculations. Parameter uncertainties are listed in Table 3.2.8, determined from manufacturing specifications. These two residual sources of uncertainty for one parameter (U) are combined in the way described by Equation 3.2.7. Combination of uncertainty from cross sensitivity corrections to all parameters is a quadrature sum, as the corrections are treated linearly independently.

In order to determine an upper-bound for uncertainty, the maximum $U - U_0$ (ΔU) was used in calculations (listed below), calculated from maximum experimental range. Accounting for the maximum optimal range produced an estimate of the maximum possible uncertainty introduced during the cross sensitivity correction. Maximum difference for CO_2 was calculated considering the ideal value of $CO_{2,0}$ of 400 μmol mol^{-1} with a range of ambient CO_2 spanning 300 to 500 μmol mol^{-1}.

Maximum parameter ranges:

$$\begin{aligned} \Delta P &= 0.5 \text{ hPa} \\ \Delta F &= 0.2 \text{ L min}^{-1} \\ \Delta Q &= 10 \ \mu\text{mol mol}^{-1} \\ \Delta T &= 0.2 \ ^{\circ}\text{C} \\ \Delta CO_2 &= 100 \ \mu\text{mol mol}^{-1} \end{aligned}$$

Table 3.2.8: Uncertainties associated with instrument parameter measurements. Uncertainties are taken from manufacturing specifications for parameter measurements, except in the case for CO_2 and H_2O, where uncertainty in the raw values are taken as random uncertainty determined in (Griffith et al., 2012)

Cross Sensitivity Parameter (U)	**Instrument uncertainty** (δU)		**units**
Pressure (P)	Piezo manometer	±0.66	hPa
Flow (F)	mass flow controller	±0.001	slpm
H_2O (Q)	raw in situ FTIR	±0.2	μmolmol^{-1}
CO_2	raw in situ FTIR	±0.018	μmolmol^{-1}
Temperature (T)	thermocouple	±0.003	°C

Total residual uncertainty in the ambient dataset following cross sensitivity application is then a quadrature addition of all the individual cross sensitivity uncertainties together with the previously calculated uncertainty in dry-air mole fraction (Equation 3.2.8).

Uncertainty due to correction for cross sensitivities

$$\delta\chi_{cor} = \sqrt{\delta\chi_{dry}{}^2 + \sum \delta U_{Xsens}{}^2} \tag{3.2.8}$$

Where:

$\delta\chi_{dry}$ = listed in Table 3.2.7

δU_{Xsens} = cross sensitivity uncertainty for each parameter U (= P, F, Q, CO_2, T)

Substituting Equation 3.2.7 into Equation 3.2.8 gives an equation describing the total combined error once cross sensitivity factors have been applied:

$$\delta\chi_{cor} = \sqrt{{\delta\chi_{dry}}^2 + \sum {U_{Xsens}}^2 \left[\left(\frac{\delta \frac{\partial \chi}{\partial U}}{\frac{\partial \chi}{\partial U}} \right)^2 + \left(\frac{\delta U}{U - U_0} \right)^2 \right]} \tag{3.2.9}$$

Finally, in dataset uncertainty analysis, residual systematic errors were determined with respect to calibration. As with cross sensitivities, correcting systematic error by calibration leaves residual uncertainty. In particular, there remain smaller systematic uncertainties due to the uncertainty in linear regression used to determine calibration factors and offsets (Tables 3.2.5 & 3.2.6). A total uncertainty for ambient measurements of each trace gas was determined by combining random uncertainties discussed so far, and residual uncertainty introduced by calibration corrections. Combination of uncertainties is demonstrated in Equation 3.2.10.

Uncertainty due to calibration to a global scale

$$\delta\chi_{cal} = \frac{\chi_{cor} - Cal_{off}}{Cal_{fac}} \sqrt{\left(\frac{\sqrt{{\delta\chi_{cor}}^2 + {\delta Cal_{off}}^2}}{\chi_{cor} - Cal_{off}} \right)^2 + \left(\frac{\delta \mathrm{Cal}_{fac}}{\mathrm{Cal}_{fac}} \right)^2} \tag{3.2.10}$$

Where:

$\delta\chi_{cal} =$	final combined uncertainty for ambient measurements
$\chi_{cor} =$	cross sensitivity corrected trace gas value
$\delta\chi_{cor} =$	determined in Equation 3.2.9
$\mathrm{Cal}_{\mathrm{off}}$, $\delta Cal_{off} =$	calibration offset and associated uncertainty, Tables 3.2.5 & 3.2.6
$\mathrm{Cal}_{\mathrm{fac}}$, $\delta \mathrm{Cal}_{fac} =$	calibration factor and associated uncertainty, Tables 3.2.5 & 3.2.6

To determine a representative total uncertainty for the ambient record at UOW, representative ambient values were used for each trace gas to substitute χ_{cor}. This produced an uncertainty centred around a representative ambient value. Dataset uncertainties for each instrument are tabulated in Table 3.2.9. These uncertainties may be used to compare different datasets with the in situ FTIR dataset, such as atmospheric models or column average mole fractions.

Table 3.2.9: Combined uncertainty for the ambient in situ FTIR record at UOW. Absolute values are given for representative values: CO_2 = 400 μmolmol^{-1}, CO = 60 ηmolmol^{-1}, CH_4 = 1800 ηmolmol^{-1}, N_2O = 320 ηmolmol^{-1}, $\delta^{13}C$ = 9‰. Relative error is shown as percentage. Uncertainty in the records follows several instrumental regimes (Sandpit: 2, Eddy: 3), introduced and described in Section 3.2.3. Blue values indicate those that meet GAW compatibility requirements (World Meteorological Organization, 2011).

Trace Gas (units)	**Total Dataset Uncertainty**						
	This Study					Hammerle et al., 2012	GAW
	Sandpit		Eddy				
	prior Dec. 2012	post Dec. 2012	1.5 mm 2011	3.0 mm 2012	1.5 mm post 2012		
CO (nmol mol^{-1})	0.51 (0.9%)	0.35 (0.6%)	1.8 (3%)	0.46 (0.8%)	0.39 (0.6%)	0.30	2.0
CO_2 (μmol mol^{-1})	0.17 (0.04%)	0.10 (0.03%)	6.8 (2%)	0.63 (0.2%)	0.69 (0.2%)	0.132	0.05 (S.H.)
CH_4 (nmol mol^{-1})	1.9 (0.1%)	0.88 (0.05%)	8.7 (0.5%)	2.0 (0.1%)	2.1 (0.1%)	0.25	2.0
N_2O (nmol mol^{-1})	0.47 (0.1%)	0.74 (0.2%)	3.3 (1%)	0.43 (0.1%)	1.8 (0.5%)	0.084	0.1
$\delta^{13}C$ (‰)	0.16 (0.6%)	0.13 (0.5%)	4.2 (18%)	1.3 (2%)	0.5 (0.8%)	0.07	0.01

3.3 Combination of datasets and quality analysis

Four main overlap periods between Sandpit and Eddy were used to determine consistency between instruments. Overlap periods were (a) Jan 2012 to May 2012; (b) Nov 2012 to Dec 2012; (c) Dec 2012 to Jan 2013; and (d) Jan 2013 to May 2013. Sandpit and Eddy records were compared by correlation analysis, as well as plotting the difference between Eddy and Sandpit, against Sandpit results. Figure 3.3.1 shows an example correlation comparison between Eddy and Sandpit for CO, including all overlapping time periods.

While Sandpit and Eddy sample nearby each other, with a separation of a few metres of inlet line, they do not measure the exact same air mass, therefore some scatter is expected, especially for air masses that rapidly change composition. Comparison between instruments was assessed for mean offsets to determine any biases between instruments.

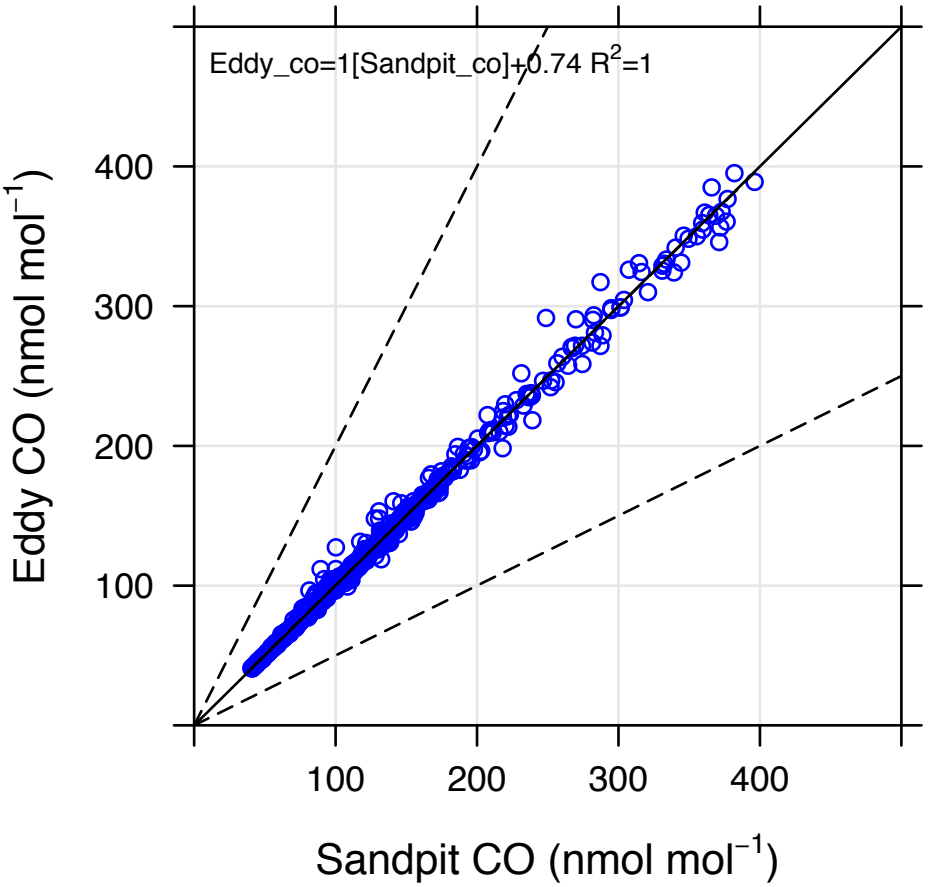

Figure 3.3.1: Correlation of Eddy and Sandpit CO for overlapping measurement periods during 2012 to July 2013. Linear model is presented in the dashed line and equation, with R^2 value in the top left. The 1:1 line is shown as a solid line and 1:2 and 1:0.5 lines are also shown as dashed lines for comparison.

Application of cross sensitivity factors and calibration to a global scale for both instruments produced records that generally matched well between instruments, particularly for dates when the instruments were well-characterised. However, between-instrument bias was present for some of the ambient record due to operational changes. Specifically, bias between instruments was seen in the first overlap period for CO_2, CH_4, N_2O and $\delta^{13}C$. The bias was outside calculated dataset error (Table 3.2.9). Correction offsets were determined from the 3-minute data for CO_2 CH_4, N_2O and $\delta^{13}C$ and were subsequently applied to datasets.

Bias between datasets during the first overlap is attributed to Eddy operation prior to November, 2012 being performed using 3 mm aperture. At this aperture, the detector is slightly saturated and spectra can include added constant interference. Therefore,

calibrations are likely not to be as accurate on this aperture as on 1.5 mm, and produce more variable calibration factors and offsets. Eddy was therefore corrected by a mean offset value to produce insignificant bias when compared with Sandpit.

Additional bias was found for N_2O during overlap periods b and c, and for $\delta^{13}C$ for overlaps b, c and d. The biases in these values were attributed to temperature control on Eddy being less accurate than on Sandpit. These two atmospheric constituents were found to be highly sensitive to temperature fluctuations. Therefore, these gases were likely to have systematic errors in Eddy calibrations. Eddy N_2O and $\delta^{13}C$ were therefore corrected to be in line with Sandpit values. N_2O and $\delta^{13}C$ absorbing features are also particularly sensitive to changes in background spectra, as well as instrument temperature. During instrument background measurements, even though the cell is evacuated to < 0.1 mbar, a small amount of atmosphere remains within the cell leaving residual absorption. Background stripping accounts for this, but depending on the amount and version of MALT used, background stripping may vary, particularly in the regions of N_2O and $\delta^{13}C$. Small variation in background stripping does not adversely affect the other trace gases, which have robust absorbing features. Additionally, uncertainty in the 2011 Eddy record of N_2O (1%) and $\delta^{13}C$ (18%) was deemed too great to use this part of the record reliably in analysis of ambient records. Therefore combined ambient records for N_2O and $\delta^{13}C$ extend from May 2012 onward.

Dataset offset and correlation coefficient values for each overlap period where significant offsets were determined are presented in Table 3.3.1. Due to no overlap between instruments during 2011, corrections were only applied back to January 2012. Final corrected correlation and offset values are presented in Table 3.3.1, indicating offset values are now within dataset error (Table 3.2.9). These datasets were subsequently combined to produce a UOW in situ FTIR record of ambient air measurements.

Following combination of datasets the quality controlled combined dataset was finalised and ready for further interpretation. A quality controlled, calibrated dataset of air quality data for CO, CO_2, CH_4, N_2O and $\delta^{13}C$ was developed combining the record from two in situ FTIR instruments. The record is traceable to the WMO-GAW atmospheric standard scale. The combined records from 2011 to 2013 are presented and further analysed in Chapter 4.

Table 3.3.1: Correlation values and corrections for Eddy in overlap periods a, b, c and d, calculated for 3-minute retrievals. All CO for time periods a-d, and CH_4 results and CO_2 for time periods b-d were within dataset error, therefore are not shown. Correlation results of the corrected dataset are also given in lower section.

Raw dataset			
		mean offset	r
CO_2	a	-3.29	1.000
CH_4	a	-3.53	1.000
N_2O	a	-1.07	0.989
	b	-0.419	0.896
	c	-0.149	0.656
$\delta^{13}C$	a	1.74	0.452
	b	0.887	0.813
	c	0.225	0.628
	d	0.411	0.768
Final complete dataset			
01 Jan. 2012 to 01 Aug. 2013			
CO		0.286	0.998
CO_2		0.137	0.999
CH_4		0.590	0.999
01 May 2012 to 10 Apr. 2013			
N_2O		0.187	0.940
$\delta^{13}C$		-1.92e-05	0.768

a = 01 Jan. 2012 to 01 Nov. 2012
b = 01 Nov. 2012 to 04 Dec. 2012
c = 04 Dec. 2012 to 01 Jan. 2013
d = 01 Jan. 2013 to 01 Aug. 2013

Chapter 4

Wollongong boundary layer atmospheric composition

The previous chapter developed a quality controlled in situ FTIR dataset at the University of Wollongong (UOW, 34.4°S, 150.9°E), 2011 to 2013. This chapter uses the in situ dataset to characterise the atmospheric signature of Wollongong. Wollongong is a complex site, with many possible local, regional, and long-distance sources of atmospheric trace gases, such as from agriculture, biomass burning, biogenic, urban and industrial sources. Figure 4.0.1 displays the Wollongong region, indicating some major contributors.

The complete in situ FTIR dataset is shown, and general statistical properties for trace gases at UOW are discussed. Two main investigations are then performed with the air quality dataset. Initially, background records are determined for CO, CO_2, CH_4, N_2O and $\delta^{13}C$ and compared with the Cape Grim clean air station. Annual cycles for CO, CO_2 and CH_4 background values are also shown. Background values are additionally used to determine preliminary trends for CO, CO_2 and CH_4 at Wollongong.

The second avenue of investigation involves understanding non-background conditions at Wollongong. Diurnal cycles help show local influence on elevated trace gases values. Furthermore, cluster analysis was performed on CO using wind direction and wind speed. Within-cluster enhancement ratios of O_3 to CO were investigated, allowing an estimation of ozone production environment. Trajectory analysis helped determine meteorological contributions to these conditions.

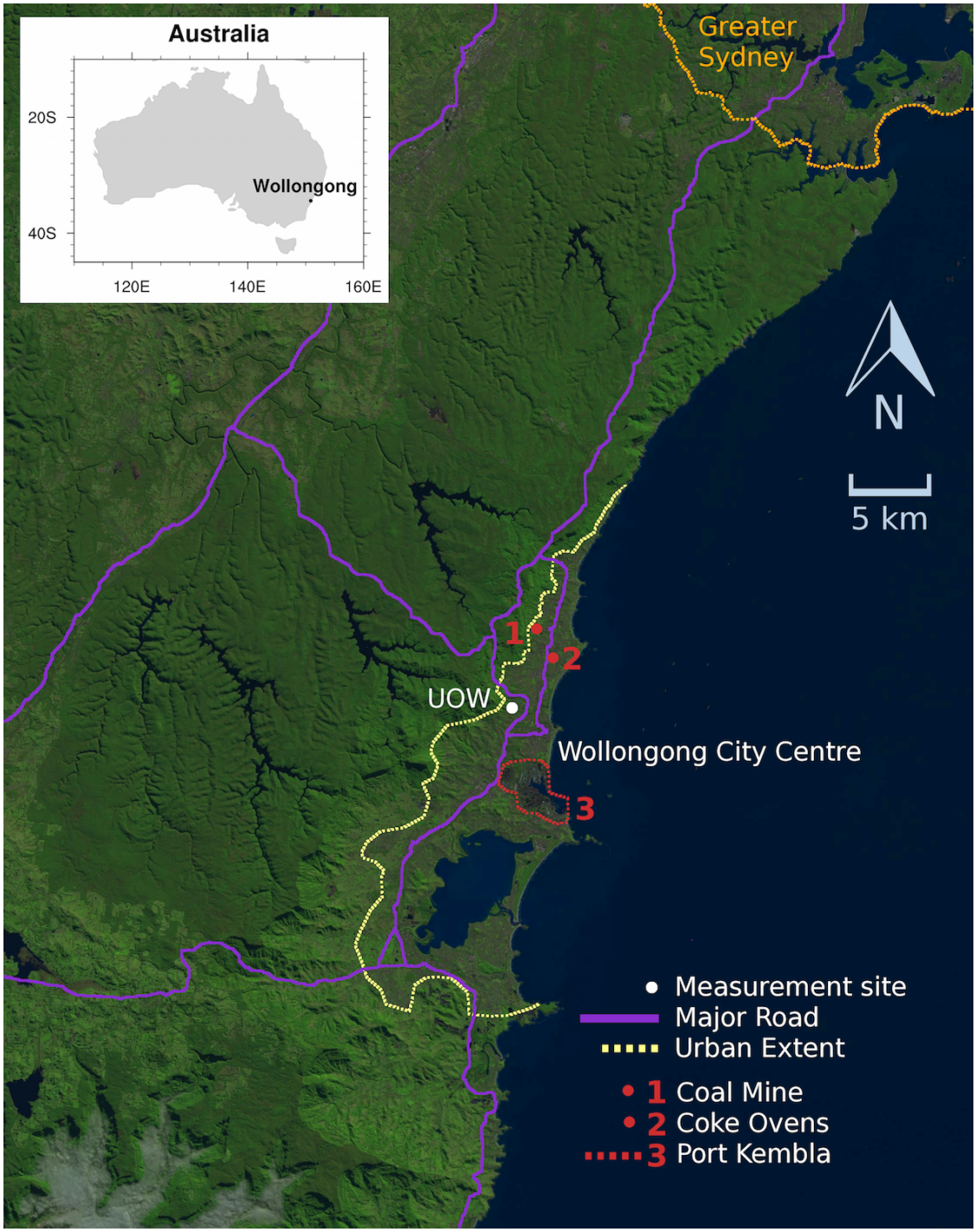

Figure 4.0.1: Map displaying the Wollongong region and surrounds, including major roadways, industrial locations and extent of the urban footprint. Industrial sites are numbered 1 to 3. Port Kembla (industrial site 3) is the location of the steelworks facility and is a major shipping hub. Background satellite image courtesy of United States Geological Survey (USGS), downloaded from http://landsatlook.usgs.gov/.

4.1 Complete timeseries

The complete records from 2011 to 2013 for CO, CO_2 and CH_4 at UOW are shown in Figure 4.1.1. Records extend from May 2012 to 10, April 2013 for N_2O and $\delta^{13}C$, and are shown in Figure 4.1.2. Reduced datasets for N_2O and $\delta^{13}C$ are due to dataset instability outside these times. Timeseries are plotted as 10-minute averages. All timeseries analysis is completed using the statistical programming language R (R Core Team, 2012), and the "OpenAir" package written in the R language (Carslaw & Ropkins, 2012).

Statistical analysis for all trace gases was performed to give an overview of the trace gas composition at Wollongong. Statistical results are summarised in Table 4.1.1. Mean values are larger (more negative in the case of $\delta^{13}C$) than median values, indicating a higher density of values at lower trace gas values (less negative values for $\delta^{13}C$). A "long tail" of enhanced values is supported by maximum values being substantially larger than the 95th percentile, as well as maximum and minimum values being unevenly placed relative to mean values. Values at the 95th percentile are CO: 317.2 nmol mol^{-1}, CO_2: 422.4 μmolmol^{-1}, CH_4: 2288.7 nmol mol^{-1}, N_2O: 326.8 nmol mol^{-1} and $\delta^{13}C$: -8.0 ‰.

Table 4.1.1: Statistical values for the 10-minute datasets of each trace gas. Means are given with one standard deviation.

		Statistical results					
	units	**min**	**1st Quar.**	**mean (σ)**	**median**	**max**	**95th**
CO	nmol mol^{-1}	38.31	71.11	127.56 (98.3)	95.08	1574.05	317.2
CO_2	μmolmol^{-1}	377.8	393.0	400.4 (10.7)	397.0	473.9	422.4
CH_4	nmol mol^{-1}	1746	1782	1887 (190)	1807	4249	2288.7
N_2O	nmol mol^{-1}	323.9	325.0	325.4 (0.72)	325.3	331.9	326.8
$\delta^{13}C$ †	‰	-12.23	-8.80	-8.58 (0.50)	-8.46	-6.26	-8.0

The median value of CO (95.08 nmol mol^{-1}) is substantially higher than average Southern Hemisphere CO (50 nmol mol^{-1}, Warneck & Williams, 2012), reflecting the abundance of local sources. In comparison, median values for longer lived trace gases CO_2 (397.0 μmol mol^{-1}), CH_4 (1807 nmol mol^{-1}) and N_2O (325.3 nmol mol^{-1}) are similar to global averages (CO_2: 400 μmol mol^{-1}, CH_4: 1800 nmol mol^{-1}, N_2O: 324 nmol mol^{-1}, Warneck & Williams, 2012), indicating these trace gases at Wollongong are often representative of globally averaged, well-mixed atmospheric amounts.

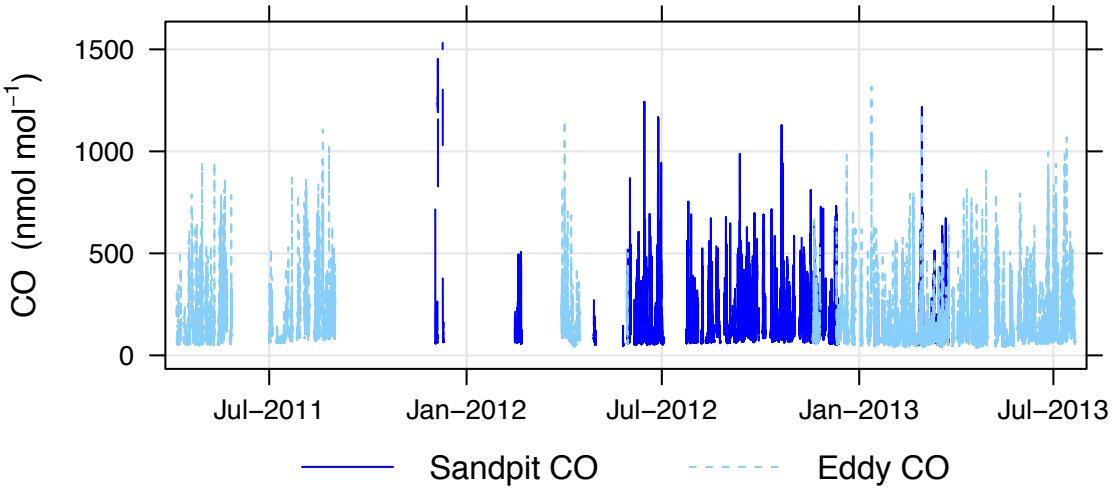

(a) CO timeseries

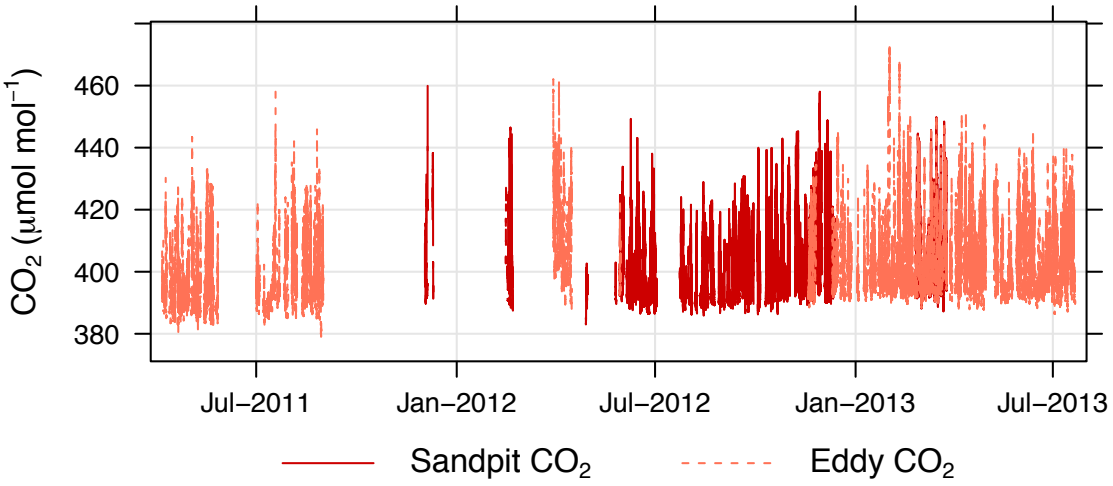

(b) CO_2 timeseries

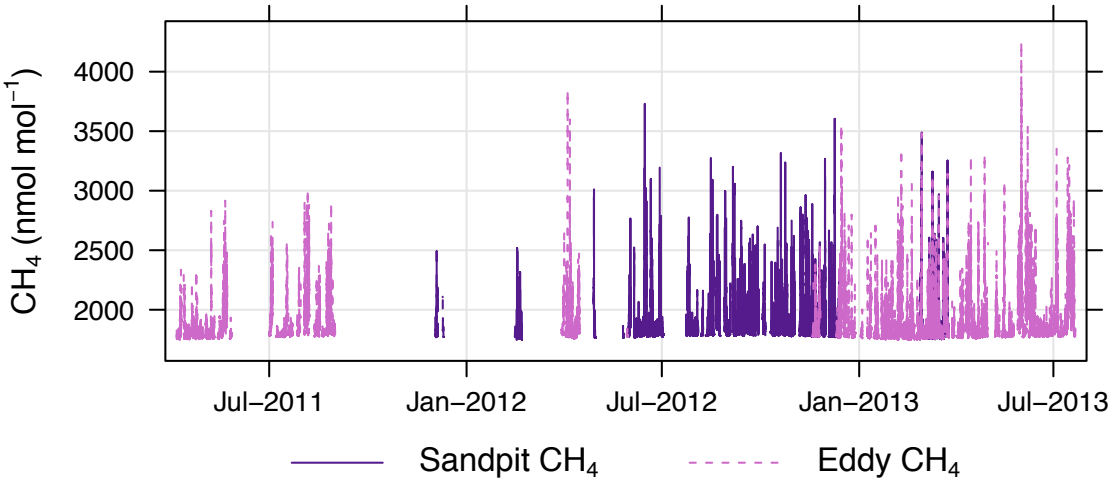

(c) CH_4 timeseries

Figure 4.1.1: Quality controlled 10-minute timeseries of (a) CO, (b) CO_2, and (c) CH_4 over the time period 2011 to 2013. Different instruments are plotted in different colours for clarity.

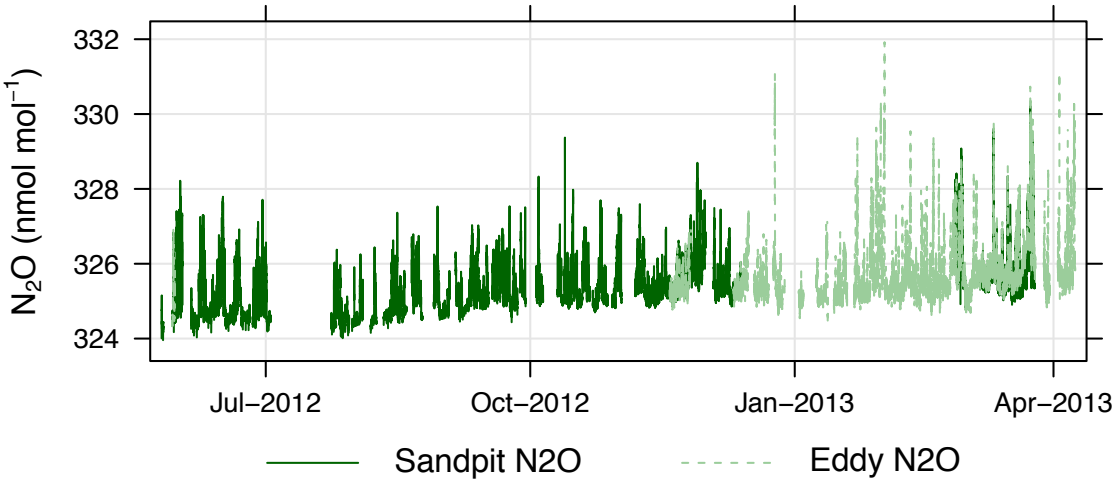

(a) N_2O timeseries

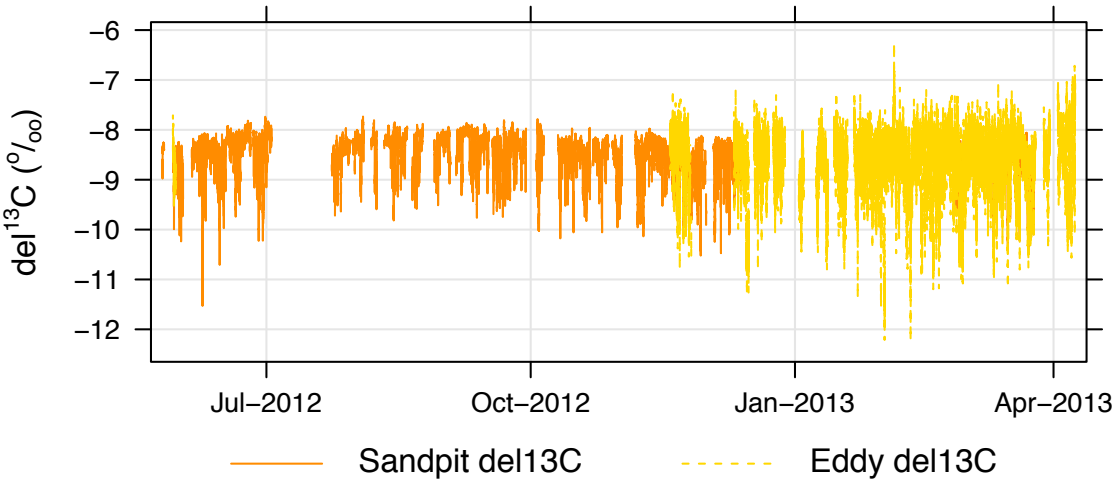

(b) del^{1}3C timeseries

Figure 4.1.2: Quality controlled 10-minute timeseries for (a) N_2O and (b) $\delta^{13}C$. Results from the different instruments are plotted in different colours for clarity.

Upon inspection of the complete timeseries plots (Figures 4.1.1 & 4.1.2) it becomes apparent that all trace gas timeseries show features of very large enhancements, which spike well above the baseline. The baseline values change depending upon time of year, so in order to quantify and interpret large enhancements, the general baseline at UOW must first be determined.

To assist in further analysis, the in situ FTIR dataset was combined with meteorological data recorded at UOW with a Davis weather station (Davis Wireless Vantage Pro2). Meteorological data were recorded as 10-minute average wind speed and 10-minute dominant wind direction. Meteorology was therefore directly combined with the 10-minute average in situ FTIR datasets.

4.2 Background values

Atmospheric background amounts of trace gases vary, depending on location and time of year. Here, a background value is defined as the concentration of well-mixed atmosphere, without extensive contribution from local sources. It is challenging to determine background atmospheric amounts of trace gases at the UOW site, due to numerous nearby pollution sources, such as a motorway directly to the north of the site and a steel-making factory to the south (see Figure 4.0.1). This section determines background values in two ways. The first method solely uses local regression to fit a baseline to the entire dataset, and the second more stringent method includes bounds on wind direction prior to fitting a baseline.

4.2.1 Background and clean air methodology

Local regression was used to determine a background envelope for each trace gas dataset. This background envelope threshold was determined using the local regression method named REBS (Robust Extraction of Baseline Signal) (Ruckstuhl et al., 2012). The REBS method is an extension of the robust baseline estimation (RBE) originally developed for applications to analytical chemistry (Ruckstuhl et al., 2001). REBS was found to produce similar baseline selection when compared with commonly used background extraction methods of "smooth curve fit" (Thoning et al., 1989; Novelli et al., 1998, 2003) and AGAGE (Advanced Global Atmospheric Gases Experiment, method described in O'Doherty et al., 2001). REBS is therefore a valid alternative method of calculating baseline values for air quality data (Ruckstuhl et al., 2012). An advantage of REBS over other methods is that it is freely available with the IDPmisc R package (Ruckstuhl et al., 2009).

The underlying principle of REBS assumes that long-term trends and seasonal contributions vary slowly relative to contributions from local pollution sources. Measurement

errors are also required to be random. The method uses least-squares regression on a "local neighbourhood" of data, smoothed with a tricube weighting function, in order to determine a background envelope. The width of the local neighbourhood is defined by the user and encompasses sufficient points to calculate a smooth background envelope, while remaining short enough to account for seasonal effects. All values below the background envelope are then classed as background values (Ruckstuhl et al., 2012). The in situ FTIR air quality dataset described here fulfils these method requirements, thus REBS is appropriate for use on the UOW dataset.

Background envelopes at UOW were calculated using REBS, separately for each 10-minute averaged trace gas timeseries, with a smoothing parameter set over 6000 points (approximately 6 weeks). Trace gas timeseries were subsequently split into a record of background measurements and polluted measurements. Values were determined from the entire in situ FTIR dataset, and are referred to as "Background".

A second record of baseline values were determined using a more stringent methodology. This more stringent method rejects a greater fraction of air as polluted, and it is differentiated from the first method by being defined as the "Clean Air" record. Prior to performing REBS, the Clean Air record restricts the UOW trace gas dataset by wind direction and wind speed.

Trace gas amounts at UOW have a dependence upon wind direction and wind speed. Figure 4.2.1a displays the UOW record for CO categorised by wind speed and coloured by wind direction. Enhanced CO conditions generally occur at low wind speeds, particularly less than 2 ms^{-1}. Enhanced trace gas values at low wind speeds are usually due to build up of local sources under atmospheric conditions of low turbulence. The colouring by wind direction indicates there are generally two air-types arriving at UOW, clarified in Figure 4.2.1b. High levels of CO originate from ∼150 to 250°, travelling from local urban areas, Port Kembla industrial area and rural/agricultural regions. Intermediate values of CO originate from ∼300°, through 0° to 50°, arriving from the north, and enhanced either due to sources from the adjacent motorway or alternatively due to Sydney outflow.

In order to determine Clean Air values at UOW, the trace gas dataset was restricted to wind directions which minimised sources of CO, namely directions originating from the ocean between 50° to 150°, and from non-polluted westerly directions 245° to 300°, including wind speeds greater than 0.4 ms^{-1}. These directions and wind speeds were chosen to ensure minimal sampling of ambient air influenced by local urban or industrial sources. After filtering for wind speed and wind direction, REBS was used with the smoothing parameter set over 600 points, to produce a UOW Clean Air dataset.

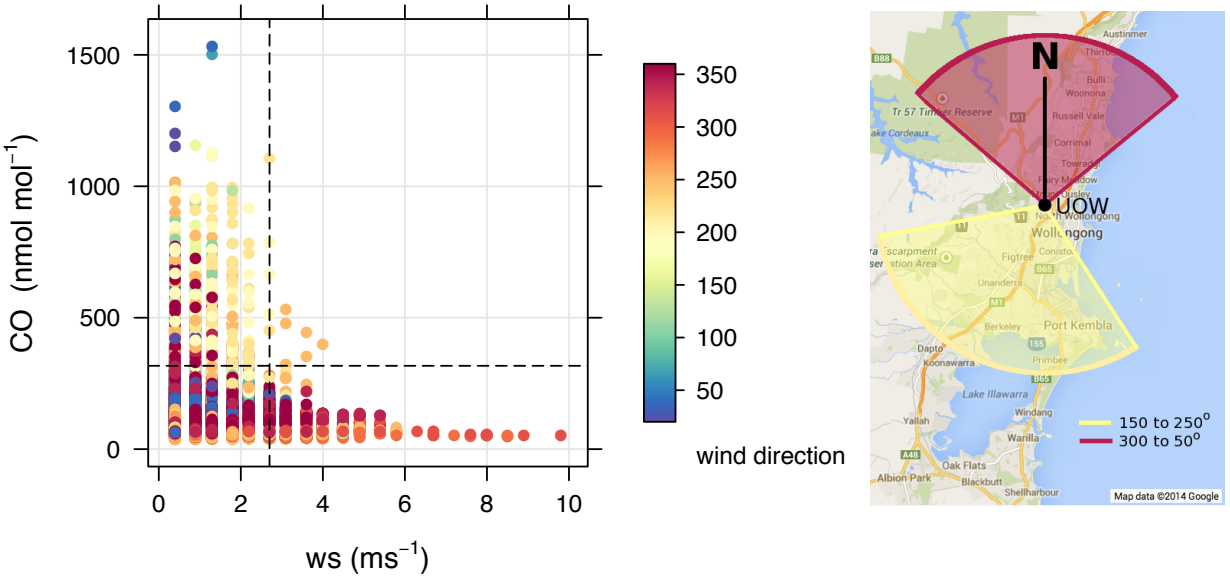

(a) CO timeseries (b) Wind directions at UOW

Figure 4.2.1: (a) CO timeseries plotted against wind speed and coloured by wind direction. Dashed horizontal line indicates the 95th percentile of CO (317 nmol mol^{-1}) and dashed vertical line indicates wind speed 95th percentile (2.7 ms^{-1}). (b) Wind directions wedges corresponding with the two apparent air-types in (a).

4.2.2 Results and comparison with Cape Grim

Approximately 50% of the in situ FTIR timeseries was determined to be Background record. In particular, percentages of background data relative to the complete 10–minute averaged dataset were CO: 47%, CO_2: 47%, CH_4: 45%, N_2O: 49%, and $\delta^{13}C$: 66%. In all cases, UOW Clean Air values are lower than Background values. A trade off for the Clean Air record is a reduction in the number of measurements.

Firstly, a challenge for the Clean Air record is that the UOW meteorological dataset is incomplete. Combining the FTIR dataset with wind speed and wind direction information resulted in a loss of approximately 25% of the air quality dataset. While this is not ideal, analysis of the combined FTIR and meteorological information datasets remains viable. The main discounting of data originates from the restriction of wind direction and wind speed. Following REBS analysis of the restricted dataset, the remaining percentages of Clean Air record relative to the original 10–minute averaged FTIR dataset are: CO: 13%, CO_2: 12%, CH_4: 13%, N_2O: 11%, and $\delta^{13}C$: 14%. In general, Clean Air arrives at UOW in approximately 10% of cases.

Examples of the two baseline CO records at UOW are shown for Background CO in Figure 4.2.2, and Clean Air CO in Figure 4.2.3. Similar plots resulted for the other trace gases (not shown).

Annual and seasonal means of Background and Clean Air values were subsequently determined for each trace gas and are presented in Table 4.2.1. Mean values were determined from one 12 month period encompassing the highest data density, June 2012 to May 2013. The UOW background records were compared with values from monthly flask data taken at the Cape Grim clean air baseline station (40.7°S, 144.7°E), which are also presented in Table 4.2.1 (CSIRO Marine and Atmospheric Research & the Australian Bureau of Meteorology, 2013a,b)[1]. The same time period was covered for Cape Grim CO_2, CH_4 and N_2O. However, the CO and $\delta^{13}C$ products were only available to December 2011, therefore Cape Grim 2011 values were used as comparison in these cases.

[1] "CSIRO and the Australian Bureau of Meteorology give no warranty regarding the accuracy, completeness, currency or suitability, for any particular purpose and accept no liability in respect of data."

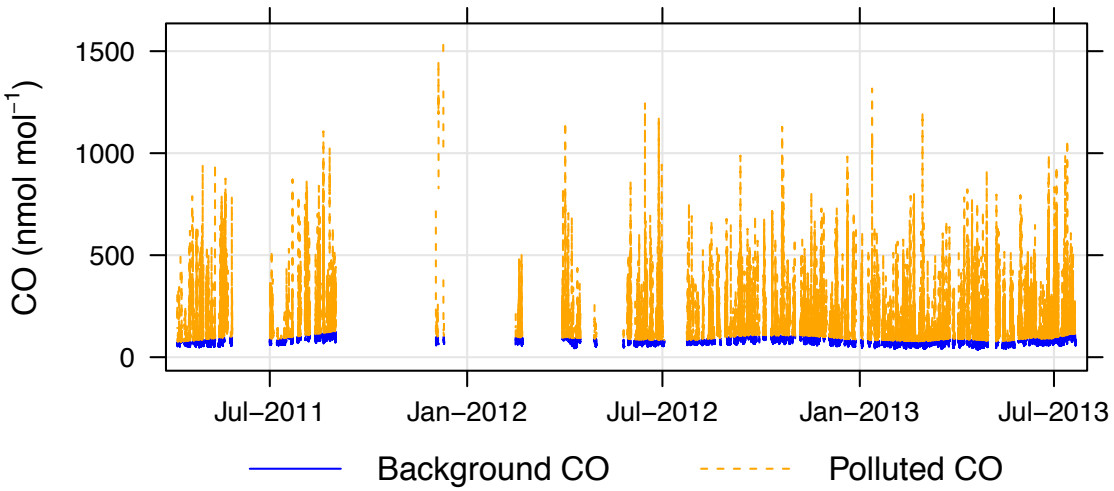

Figure 4.2.2: UOW CO in situ FTIR measurement record split into Background (blue) and polluted (orange), using the REBS method (Ruckstuhl et al., 2012).

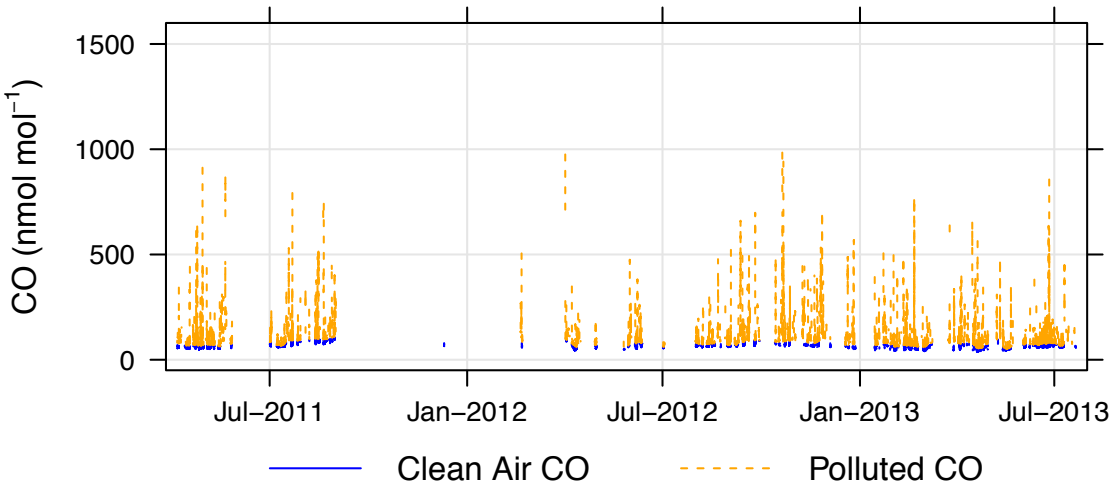

Figure 4.2.3: UOW CO in situ FTIR measurement record split into Clean Air (blue) and polluted (orange), by initially restricting the wind direction and wind speed, followed by applying the REBS method (Ruckstuhl et al., 2012).

All trace gas annual means in the Background record at UOW are higher than Clean Air annual means (Table 4.2.1), indicating Background values still include some contributions from local sources. The Clean Air record therefore is a better representation of well-mixed Southern Hemispheric air, with minimal regional influence. Clean Air values at UOW compare significantly better with the Cape Grim record than Background values compare with Cape Grim. In particular, Clean Air N_2O annual mean is not significantly different to Cape Grim, according to the Student's t-test ($p > 0.05$). This implies UOW can measure background values of this well-mixed, long-lived trace gas. The other trace gases, CO, CO_2 and CH_4, as well as $\delta^{13}C$, show annual means which are significantly different to the Cape Grim means, CO_2 significant below the 0.05 level, CH_4 below the 0.01 level, and CO and $\delta^{13}C$ below the 0.001 level.

Table 4.2.1: Annual and seasonal mean values of Background (UOW–BKD) and Clean Air (UOW–CA) at Wollongong, June 2012 to May 2013. Results are compared with Cape Grim clean air monitoring site (CSIRO Marine and Atmospheric Research & the Australian Bureau of Meteorology, 2013a,b). Bold values denote means which are not significantly different to Cape Grim means, determined using Student's t-test.

	Site	**Annual Mean (σ) June 2012 to May 2013**		**Seasonal mean Winter (JJA)**	**Spring (SON)**	**Summer (DJF)**	**Autumn (MAM)**
CO	UOW–BKD	70.01 (13)	***	68.70	82.86	66.12	62.94
(nmol mol^{-1})	UOW–CA	61.05 (11)	***	65.35	71.54	56.30	51.82
	‡Cape Grim	46.52 (7.2)		49.30	55.57	41.01	40.21
CO_2	UOW–BKD	393.2 (2.4)	***	391.6	392.6	394.1	394.5
(μmolmol^{-1})	UOW–CA	391.8 (1.8)	*	390.5	391.1	392.9	392.6
	Cape Grim	391.2 (0.73)		390.2	391.3	391.2	392.0
CH_4	UOW–BKD	1780 (14)	***	1787	1794	1768	1775
(nmol mol^{-1})	UOW–CA	1776 (12)	**	1783	1787	1762	1770
	Cape Grim	1764 (11)		1770	1776	1755	1755
N_2O†	UOW–BKD	325.0 (0.33)	*	324.5	325.0	325.2	325.4
(nmol mol^{-1})	UOW–CA	**324.9** (0.31)	+	324.5	324.9	325.1	325.5
	Cape Grim	324.7 (0.35)		324.2	324.8	325.0	324.7
$\delta^{13}C$†	UOW–BKD	-8.307 (0.47)	**	-8.228	-8.269	-8.330	-8.447
(‰)	UOW–CA	-8.167(0.22)	***	-8.137	-8.169	-8.171	-8.200
	‡Cape Grim	-8.287 (0.018)		-8.283	-8.296	-8.305	-8.265

Denoting level of significant difference to Cape Grim mean:
*** $p < 0.001$, ** $p < 0.01$, * $p < 0.05$, and + $p < 0.1$
†N_2O and $\delta^{13}C$ at UOW are only valid between May 2012 to April 8, 2013, therefore Autumn average is March, 2013 only.
‡Cape Grim CO and $\delta^{13}C$ were only available till December 2011

Differences are expected between Cape Grim and Wollongong for CO and CH_4, due to diffusion and lifetime induced latitudinal gradients for these two trace gases. The latitudinal difference between Wollongong and Cape Grim is 6.3°.

The Southern Hemisphere latitudinal gradient in CO is on the order of ∼0.5 nmol mol^{-1} per degree (Novelli et al., 1998; Yashiro et al., 2009) to 1.5 nmol mol^{-1} per degree (Notholt et al., 2000). These gradients would induce a 3.2 to 9.5 nmol mol^{-1} difference in CO between UOW and Cape Grim. The observed difference of 14.5 nmol mol^{-1} between Clean Air and Cape Grim annual means is of the correct magnitude to be described by latitudinal differences, but 5 nmol mol^{-1} above the upper end of determined literature trends. Differences between expected and observed latitudinal influence for CO is likely due to Notholt et al., 2000 and Yashiro et al., 2009 being determined from short time period campaign measurements of ship-borne measurements in the Atlantic Ocean and western Pacific Ocean respectively. Additionally, Novelli et al., 1998 addresses the time period 1992 to 1995, over 15 years earlier than the record investigated here. Atmospheric amounts and consequently latitudinal trends of the highly variable CO would not be expected to be identical between all time periods. Differences between CO records at the two sites may also be pronounced due to comparing with the Cape Grim record from 2011. Moving to the updated Cape Grim record is recommended as soon as more recent data becomes available.

A latitudinal gradient in CH_4 was determined by Deutscher et al., 2010 to be 1.2 ± 0.2 nmol mol^{-1} per degree, using train-borne transect measurements across remote regions of Australia. The latitudinal gradient in CH_4 would produce a 7.6 ± 1.3 nmol mol^{-1} difference in CH_4 between sites. The observed difference of 12 nmol mol^{-1} between Clean Air and Cape Grim annual mean values is about 4 nmol mol^{-1} higher than predicted by the Deutscher et al., 2010 gradient. The latitudinal trend found by Deutscher et al., 2010 was determined during a limited measurement period during 2008, therefore would not necessarily be expected to represent differences between sites for annual values. For example, Notholt et al., 2000 found differences of 2 ± 0.2 nmol mol^{-1} per degree for the Southern Hemisphere in a different campaign during 1996, based on ship-borne measurements in the Atlantic Ocean, using solar FTS. The Notholt et al., 2000 gradient would produce an expected 12.6 ± 1.3 nmol mol^{-1} difference between sites, closer to the observed difference here.

Differences in CO and CH_4 found here between UOW Clean Air and Cape Grim are generally consistent with currently published latitudinal gradients. However, calculation of latitudinal gradients for CO and CH_4 from satellite data which include greater

spatial and time coverage would help determine a more representative average difference expected between UOW and Cape Grim due to latitude difference.

Differences in CO_2 and $\delta^{13}C$ are not expected between sites for well-mixed background values of these trace gases. However, the results seen here indicate local or regional sources are still influencing these atmospheric constituents. Additionally, the $\delta^{13}C$ Cape Grim record only extends to 2011 and the UOW record for $\delta^{13}C$ ends in March due to dataset instabilities for this constituent during April and May, 2013. These two properties, combined with a trend in atmospheric $^{13}CO_2$, is most likely the main reason very significant differences between sites are seen for annual means of $\delta^{13}C$.

While absolute magnitudes differ, seasonal means for CO and CH_4 in both Background and Clean Air records at UOW follow the same seasonal variability found at Cape Grim. CO seasonal means for all records peak in spring and show a minimum in autumn. Similarly, CH_4 seasonal means peak in spring, but have a minimum in summer. Similarities in seasonal variability indicate the main drivers of atmospheric composition are similar between sites. Seasonal means at UOW for CO_2 differ to Cape Grim, with a peak in summer for Clean Air and autumn for Background and minimum values in winter. Cape Grim CO_2 also has minimum values in winter but peaks in autumn. CO, CO_2 and CH_4 seasonality are further discussed under annual cycles. Seasonal comparisons are not valid for N_2O and $\delta^{13}C$, due to records for these truncating at the end of March 2013.

Annual Cycles

Annual cycles for CO, CO_2 and CH_4 were determined for Background and Clean Air records for the 12 months from June 2012 to May 2013, and are presented in Figure 4.2.4. Cape Grim annual cycles are also shown for comparison. Monthly averaged data were fit with the OpenAir smoothTrend function. Due to the strong trend in atmospheric CO_2, the datasets for this trace gas were de-trended prior to smooth curve fitting, in order to unambiguously analyse seasonal variability. Annual cycles for N_2O and $\delta^{13}C$ were not determined, as the stable datasets for these trace gases do not cover an entire 12 month period.

In all cases, Clean Air annual cycles are lower than Background annual cycles, and generally, Cape Grim annual cycles are lower than both Background and Clean Air. Annual cycles for Clean Air and Background CO and CH_4 follow a similar pattern to

Cape Grim (Figures 4.2.4a and 4.2.4c). Larger magnitudes in the Clean Air cycle are due to latitudinal gradients as previously discussed. Differences seen in Background cycle are due to latitudinal gradients plus the less stringent filtering, which allows inclusion of influence from local land-based sources.

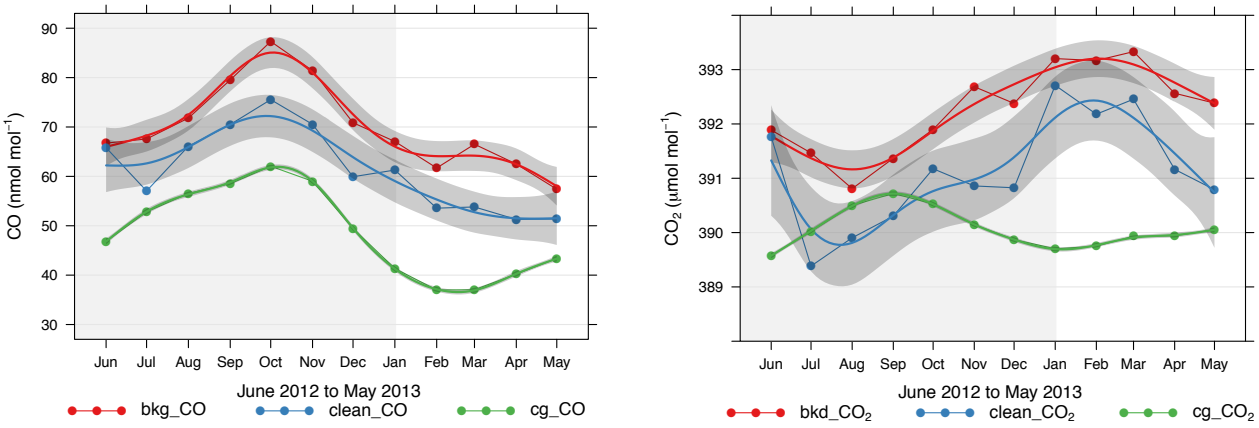

(a) CO

(b) Detrended CO_2

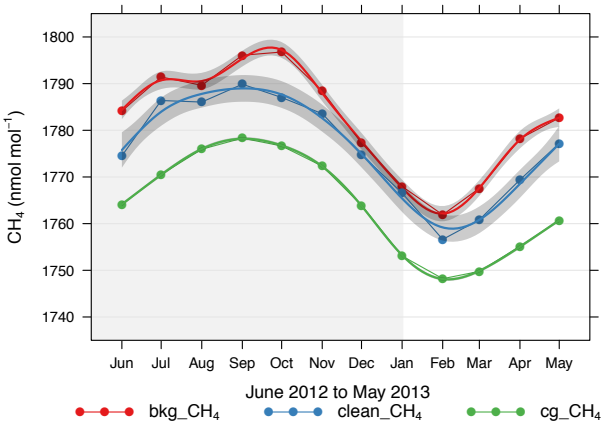

(c) CH_4

Figure 4.2.4: Annual cycles from June 2012 to May 2013, with smooth curve fits for (a) CO, (b) Detrended CO_2 and (c) CH_4. Curves for UOW Background (red) and Clean Air (blue) are shown, with Cape Grim (green) for comparison. Shaded areas indicate 95% confidence intervals of the smooth curve slopes, calculated using bootstrap simulations.

Annual cycles for CO display the characteristic spring maximum associated with peak Southern Hemisphere biomass burning season (Edwards et al., 2006b). CH_4 annual cycles also show a maximum in spring, coinciding with biomass burning season. At UOW, a second peak occurs for Background CH_4 in July, most likely reflecting a winter peak in fossil fuel use. Both UOW CH_4 records and Cape Grim CH_4 show summer

minimum in the annual cycles. The main loss mechanism for CH_4 is via reaction with photochemically produced OH radical. The production of OH maximises in summer, which when combined with reduced trace gas sources, results in a summer minimum.

Minimum CO in the Cape Grim record also occurs in summer, due to the main loss mechanism of this trace gas being through reaction with OH. The CO minimum in UOW records is less clearly summer, occurring between February and May, and indicating local sources may counteract the main loss mechanism. The CO annual cycle may also be convoluted by a trend, therefore analysis of a de-trended longer timeseries would be valuable to help determine contributions to the CO minimum at UOW.

Annual cycles for CO_2 are markedly different between sites (Figure 4.2.4b). Background and Clean Air UOW CO_2 annual cycles are anti-phase to the Cape Grim cycle. Clean Air CO_2 annual cycle is less certain, described by the large 95% confidence interval envelope. A longer timeseries may help to reduce this uncertainty. The annual cycle for atmospheric CO_2 is mainly influenced through biogenic uptake of CO_2 during photosynthesis. Uptake is greatest during the growing season, summer in each hemisphere, and induces a minimum in the CO_2 annual cycle. At Cape Grim, the minimum in CO_2 annual cycle coincides with Southern Hemispheric summer, indicating biogenic drawdown.

At UOW, CO_2 seasonality is more complex, due to a combination of sources. The peak for UOW CO_2 during Southern Hemisphere summer corresponds with Northern Hemisphere winter, therefore transported Northern Hemisphere CO_2 could be contributing to the annual cycle at UOW (Miyazaki et al., 2008). Wollongong (34.4° S) would be expected to be influenced by transported Northern Hemisphere CO_2 more than Cape Grim (40.6° S), due to being located closer to the equator, particularly as the Cape Grim record selects for air sourced from the Southern Ocean. Alternatively, or additionally, the peak in UOW CO_2 during summer may be due to photosynthesis being both light and water limited in the arid Australian climate (Eamus et al., 2001), meaning a drop in photosynthesis would occur during the dry season. Both these processes could counteract the expected minimum associated with Southern Hemisphere summer biogenic drawdown. Tagged tracer modelling would be required to quantitatively partition contributions to the CO_2 annual cycle at Wollongong.

4.2.3 Preliminary temporal trend analysis

Background analysis has determined well-mixed air arrives at the UOW site, which generally provides trace gas values representative of Southern Hemisphere background values. Measurement of background air presents the opportunity to gain a preliminary understanding of temporal trends in the trace gas values at Wollongong.

While it is understood that robust long-term trends cannot be determined from a semi-continuous 3 year record, trend analysis was employed to gain experience with the UOW dataset, and to provide a benchmark for comparison with future research. Trend analysis was performed on the UOW Background and Clean Air records. Initial trends were determined for trace gases CO, CO_2 and CH_4, which had datasets spanning 2011 to 2013. N_2O and $\delta^{13}C$ datasets were only stable over 9 months (see Section 3.3), therefore trend analysis was not performed at this time. It is highly recommended to revise atmospheric trace gas trends for UOW upon collation of additional data, in order to produce more robust trends. The results presented here should only be used as an initial guide for the region.

Trends were calculated using the "TheilSen" function, supplied in the OpenAir R package (Carslaw & Ropkins, 2012; Carslaw, 2013). Datasets were de-seasonalised and any missing months were interpolated during trend analysis. The TheilSen function applies bootstrap methods and uses non-parametric techniques based on Theil, 1950 and Sen, 1968 to computationally determine trends in timeseries data. The method essentially calculates slopes between all pairs of points in a dataset and the median of all these slopes is the Thiel-Sen estimate of the trend. The method also provides confidence intervals and an estimate of statistical significance. Calculations are performed using bootstrap-resampling techniques. An advantage of using this type of trend estimation is that it is robust to outliers and does not require data to be normally distributed.

Trends were calculated for both Background and Clean Air 10-minute datasets. Cape Grim baseline data trends were also calculated for comparison, using overlapping time period for CO_2 and CH_4. At the time of writing, only pre-2012 data were available for CO, so a trend was calculated from Cape Grim data from 2005 to 2011. Example of trend fitted plots are shown for UOW Clean Air records of CO, CO_2 and CH_4 in Figure 4.2.5. Calculated trend values and 95% confidence intervals for all datasets are collated in Table 4.2.2.

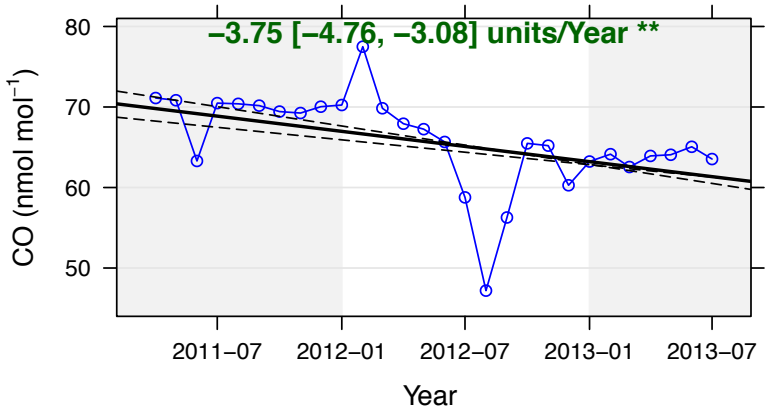

(a) CO Trend

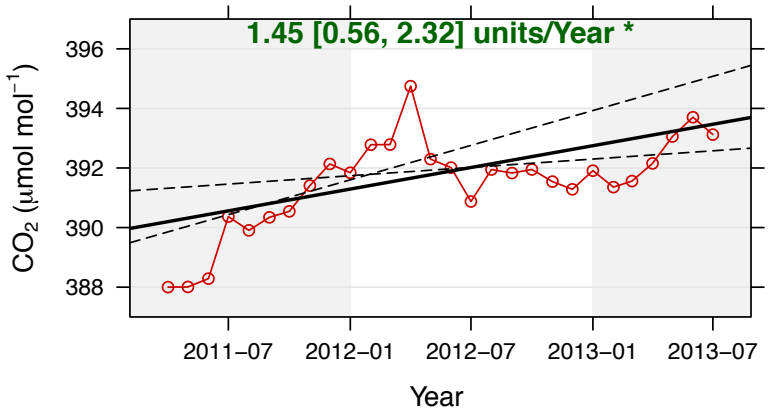

(b) CO_2 Trend

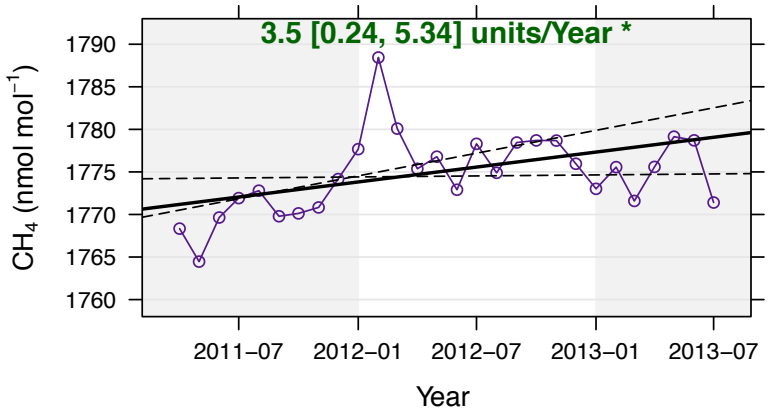

(c) CH_4 Trend

Figure 4.2.5: Trend in de-seasonalised Clean Air UOW for (a) CO, (b) CO_2, and (c) CH_4, from April 2011 to August 2013. The solid black line is the trend estimate and dashed black lines are the 95 % confidence intervals on the trend, calculated using bootstrap resampling methods. The stars indicate trend significance level, specifically ** denotes $p < 0.01$ and * denotes $p < 0.05$.

Table 4.2.2: Trends for UOW Background (UOW–BKD) and Clean Air (UOW–CA) datasets, calculated from April 2011 to August 2013.

	Trend per annum [95% confidence interval]		
	UOW–BKD	**UOW–CA**	**Cape Grim†**
CO (nmol mol^{-1}a^{-1})	-3.79 * [-7.21, -0.70]	-3.75 ** [-4.76, -3.08]	-0.51 *** [-0.74,-0.32]
CO_2 (μmolmol^{-1}a^{-1})	2.05 ** [1.19, 2.66]	1.45 * [0.56, 2.32]	2.26 *** [2.03,2.58]
CH_4 (nmol mol^{-1}a^{-1})	2.93 * [0.04, 6.25]	3.5 * [0.24, 5.34]	4.05 *** [3.66,4.43]

Denoting trend significance level:
*** $p < 0.001$, ** $p < 0.01$ and * $p < 0.05$

† Cape Grim trends were calculated from monthly flask measurements 2005 to 2011 for CO, and 2011 to June 2013 for CO_2 and CH_4 (CSIRO Marine and Atmospheric Research & the Australian Bureau of Meteorology, 2013a,b).

The Clean Air trend value for CO shows improved significance relative to the trend in the Background dataset. Clean Air CO showed trends significant to the 0.01 level while for Background, the significance was to the 0.05 level. Clean Air CH_4 showed no change in significance between datasets, significant to the 0.05 level. Clean Air CO_2 experienced a reduction in significance ($p < 0.05$) relative to the Background ($p < 0.01$). As the measurement dataset at UOW grows, the significance of trends found in the Background and Clean Air records is expected to increase. Calculated trends for Cape Grim data were all significant to the 0.001 level.

A negative trend was found for CO at both UOW and Cape Grim. The trend at UOW is -3.79 ± 3.4 nmol mol^{-1} per annum for Background and -3.75 ± 1.0 nmol mol^{-1} per annum for Clean Air. The UOW trends is approximately 6 times greater in magnitude than the Cape Grim trend. Langenfelds et al., 2011 found the trend in Cape Grim CO to be -0.2 nmol mol^{-1} per annum between 1984 to 2008 and -1.3 nmol mol^{-1} per annum between 2007 to 2008. The trend of -0.51 ±0.23 nmol mol^{-1} per annum between 2005 to 2011 found in this study lies between these two values. Using annual mean CO values presented in Table 4.2.1, percentage trends were determined. At UOW, the trend is -5.4 ± 4.9 % per annum (Background), -6.1 ±1.6 % per annum (Clean Air), and Cape Grim is -1.1 ±0.49 % per annum.

Other studies have estimated trends in Southern Hemispheric CO. Worden et al., 2013a, calculated the trend to be -0.88 ±0.52 % per annum, using satellite-based measurements with MOPITT from December 2000 to November 2011. Warner et al., 2013, calculated CO trends in the Southern Hemisphere using AIRS satellite CO at 500 hPa from 2003-2012, and found decreases of -0.14 to -0.28 nmol mol^{-1} per annum (-0.28 to 0.56 % per annum relative to 50 nmol mol^{-1}) over land and -0.62 to -0.85 nmol mol^{-1} per annum (1.2 to 1.7 % per annum relative to 50 nmol mol^{-1}) over ocean. Zeng et al., 2012, found the trend in CO at Lauder to be -0.94 ±0.47 % per annum, between 1997 and 2009, using ground based solar FTS records. These trends are closer to Cape Grim percentage trend than UOW Clean Air. However, both these literature trend calculations use column average measurements. Vertical dilution of CO and inclusion of upper tropospheric CO trends may influence the overall trends found in these studies. An earlier study by Novelli et al., 1998 used National Oceanic and Atmospheric Administration Climate Monitoring and Diagnostics Laboratory (NOAA/CMDL) surface measurements 1990 to 1995 to determine Southern Hemispheric trends. They found trends of -1.9 ±0.1 nmol mol^{-1} per annum, or -3% per annum relative to 1991 levels. This suggests surface trends are expected to be larger than column averaged or column integrated trends.

Additionally, a greater trend for CO at UOW is expected, compared with Cape Grim and average Southern Hemisphere surface trends. Trends averaged over the Southern Hemispheric region would spatially dilute atmospheric responses to changes in sources, due to larger areas of ocean and low population. Wollongong is closer to sources of CO than Cape Grim. This combined with the two-month lifetime of CO and the atmospheric mixing required to reach Cape Grim, would result in Wollongong being more readily able to detect changes in sources. The large negative trend in CO at Wollongong suggests substantial changes to the sources and/or sinks and may be due to improvements in vehicular or industrial emission standards. Zeng et al., 2012 used model simulations to suggest the main reason for the trend in Southern Hemispheric CO is due to a decline in CO industrial emissions. It will be interesting to see if the strong trend in CO at UOW is sustained in future years with a longer record.

Positive trends in CO_2 are found at both sites. The trends for UOW Background CO_2 (2.05 ±0.86 μmol mol^{-1} per annum) and Clean Air (1.45 ±0.89 μmol mol^{-1} per annum) encompass the Cape Grim trend (2.26 ±0.32 μmol mol^{-1} per annum) within their 95% confidence slopes. The Cape Grim trend determined here is consistent with previously determined trends (1984-2008: 1.7 μmol mol^{-1} per annum, 2007-2008: 2.0 μmol mol^{-1} per annum, Langenfelds et al., 2011), accounting for a trend which increases year-to-

year. The UOW and Cape Grim values are also consistent with the mean global trend in CO_2 of 2.0 $\pm$0.3 μmol mol^{-1} per annum since 2001, determined in the most recent IPCC study (Hartmann et al., 2013b). This indicates that UOW receives sufficient amounts of well-mixed background air in order to determine globally relevant trends in CO_2. Minor differences may be due to analysis of a short record at UOW, which has data gaps. As additional years are collated, it is expected that the CO_2 trend comparisons between Cape Grim and UOW will converge further.

The trend in CH_4 at both sites is also positive. The trends for UOW Background CH_4 (2.9 $\pm$3.3 nmol mol^{-1} per annum) and Clean Air (3.5 $\pm$3.3 nmol mol^{-1} per annum) cover the trend for Cape Grim (4.05 $\pm$0.39 nmol mol^{-1} per annum) within the 95% confidence slopes. Cape Grim baseline CH_4 trends were determined by Langenfelds et al., 2011 to be 6.2 nmol mol^{-1} per annum (1984-2008), and 6.8 nmol mol^{-1} per annum (2007-2008). Globally averaged growth rates for CH_4 are approximately 6 nmol mol^{-1} per annum between 2007 through 2011 (Hartmann et al., 2013b). These results suggest CH_4 at UOW can also be used to follow the trend in globally relevant, well-mixed background values.

4.3 Non-background conditions

Background atmospheric trace gas values are useful for determining large-scale drivers of atmospheric composition. However, contributions to changing air quality at UOW is also of interest. This section investigates non-background properties of the atmosphere over Wollongong.

4.3.1 Daily cycles

Average daily cycles were calculated for each trace gas and δ^{13}C over the entire time period 2011 to 2013. All trace gases show significant variable diel behaviour, presented in Figure 4.3.1. The daily cycles are influenced by a variation in turbulent mixing combined with with local sources.

The Wollongong region experiences frequent boundary layer inversions, which often occur during the night. The topography of the region includes a 500 metre escarpment, bounding the urban extent. This geological boundary is ideal for promoting the trapping of a layer of colder atmosphere underneath a warm layer, a feature of inversions.

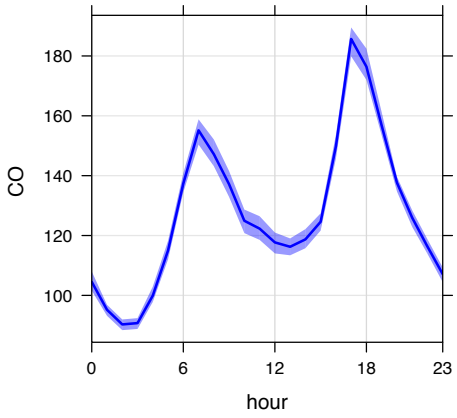

(a) CO (nmol mol^{-1})

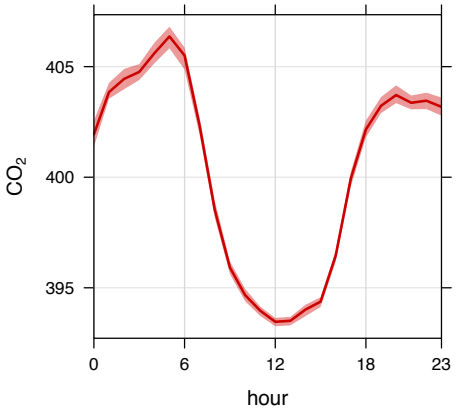

(b) CO_2 (μmol mol^{-1})

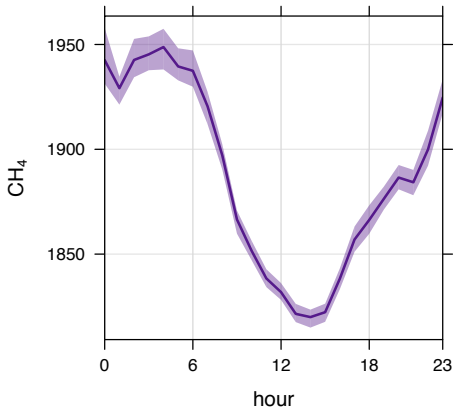

(c) CH_4 (nmol mol^{-1})

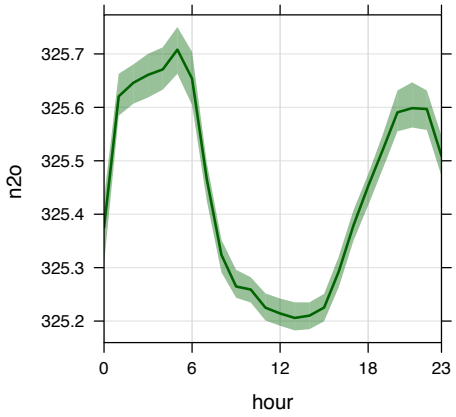

(d) N_2O (nmol mol^{-1})

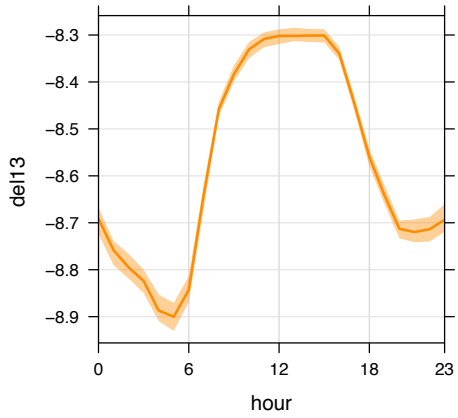

(e) δ^{13}C (‰)

Figure 4.3.1: Average daily cycles in the in situ FTIR measurements at UOW, 2011 to 2013. Shaded areas indicate 95% confidence intervals, calculated using bootstrap simulations.

Still conditions associated with inversions encourage a build up of trace gases from local sources, and are the main cause of the overnight build-ups seen in daily cycles.

At UOW, daily cycles of CO_2, CH_4, N_2O and $\delta^{13}C$ all show overnight build-up, which maximises just before sunrise. Additionally, all trace gases at UOW display the characteristic feature of a dip around midday associated with maximum boundary layer turbulence. During the day, atmospheric turbulence increases as a function of heating the earth's surface by incoming solar radiation, and reaches maximum mixing around midday. Increased mixing combines air influenced by local sources with air from the regional background. For all trace gases, regional background values are lower, so air of lower concentration is diluting the higher concentrations seen overnight. For $\delta^{13}C$, instead of a dip, a peak is seen, due to atmospheric sources being depleted in $\delta^{13}C$ relative to the free troposphere.

In addition to the turbulence influenced feature, the daily cycle plot for CO (Figure 4.3.1a) shows two sharp peaks enhanced by approximately 40 to 80 nmol mol^{-1} and attributed to vehicular activity. The first peak occurs between 6:00 and 9:00, when people are travelling to work, and the second peak occurs between 17:00 and 19:00 when people are travelling from work. The midday dip in CO is a combination of maximum turbulence and reduction in traffic conditions. An overnight build-up is not seen for CO, which may be due to the lack of vehicular sources, katabatic transport of air low in CO from the forested escarpment, or additionally, nighttime oxidation by species such as NO_3.

4.3.2 Cluster analysis: CO

CO by wind speed and wind direction

Atmospheric CO at UOW was plotted against wind speed and wind direction in a bivariate polar plot, using the OpenAir R package (Figure 4.3.2). Prior to determining the bivariate polar plot, the CO record was transformed into hour-averaged data. Data were subsequently filtered for wind speeds above 0.2 ms^{-1}. A disadvantage to surface measurements is the dependence on boundary layer mixing, as seen in the daily cycles of the previous section. Still conditions under a contracted boundary layer, often associated with an inversion layer, encourage build up of local sources. The record was therefore filtered against very low wind speed values in an effort to remove CO enhancements resulting from a build up of local sources during these still boundary

layer conditions. Removal of low wind speeds results in trace gas amounts being more likely to have been influenced by transported sources, or strong local sources.

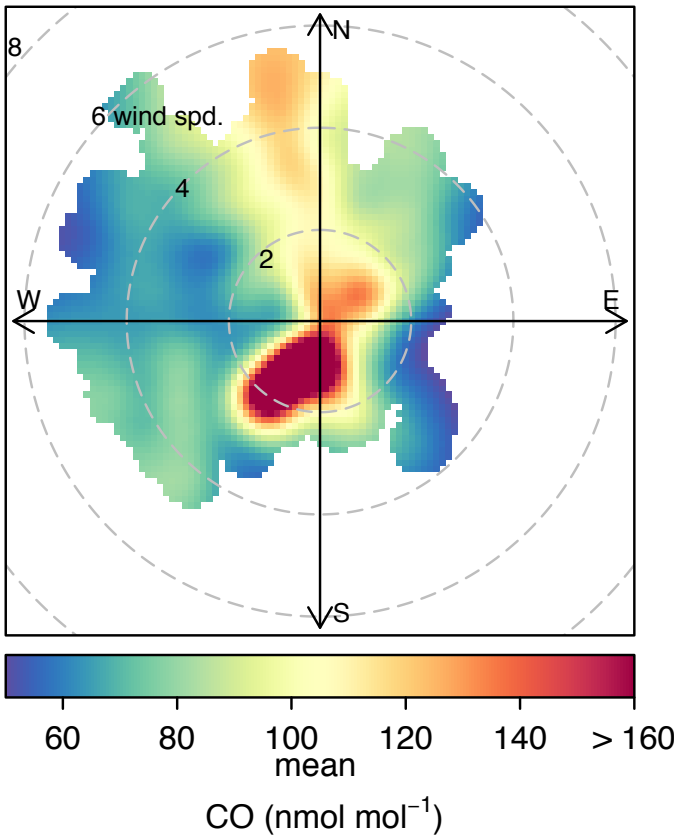

Figure 4.3.2: Bivariate polar plot of UOW atmospheric CO, filtered for wind speeds greater than 0.2 ms^{-1}. Plots show CO mole fraction as a function of wind direction and wind speed, relative to the centre which is positioned at UOW. Colours denote CO amount, concentric circles represent wind speed (in ms^{-1}), and compass directions equate to wind direction.

The bivariate polar plot of CO (Figure 4.3.2) shows that a high atmospheric amount of CO is measured at UOW when winds are from the south to southwest direction and wind speeds are low (<3 ms^{-1}). Sources from this direction are local urban pollution associated with the centre of Wollongong city and the steelworks at Port Kembla. Additionally in the bivariate polar plot, enhanced CO is associated with air originating from the north to northwest direction at wind speeds below and above 3 ms^{-1}. Enhanced CO from this direction at lower wind speeds is likely due to pollution from the adjacent motorway. Higher concentrations at faster wind speeds are unusual and can indicate downward transport from a lofted plume. The northern direction at UOW corresponds with Sydney urban districts, therefore this enhanced region of the bivariate plot is likely

due to transport of urban outflow from Sydney. In order to help understand features of the bivariate polar plot, cluster analysis was used.

Seasonal clustering methodology

The hour-averaged record of CO was split into seasons prior to performing cluster analysis. This was necessary because it was found that dominant wind directions at UOW change depending upon season, which consequently may affect plume diffusion and subsequent selection of clusters. Seasonal evolution of wind directions are shown in Figure 4.3.3. During spring and summer, the dominant wind direction is from the northeast, associated with a peak in sea-breeze occurrence, while autumn and winter display dominant wind from the southwest.

Cluster analysis was performed using the inbuilt clustering function of the OpenAir package. The clustering technique uses the wind speed, wind direction and concentration k-mean clustering methodology, as described in Carslaw & Beevers, 2013. An advantage of k-means analysis is that it is robust to outliers. The number of clusters, k, in which to split the dataset, is set by the user. Data were grouped using k-means methodology in the following way. First, randomly chosen k points from the dataset which is to be split into k groups, are defined as initial centroids. The remaining points of the dataset were then grouped with the centroid to which they are closest. Once the entire dataset has been assigned into groups, new centroids are calculated and grouping is performed again around the new centroids. This process continues iteratively until the centroids remain stable.

Here, the optimal number of clusters (k) for each season was determined using the Calinski–Harabasz index (Calinski & Harabasz, 1974) which compares within and between group variance (details in Appendix B). Briefly, Calinski–Harabasz method aims to minimise within group variance and maximise between group variance. For each season, clustering was performed separately for 2 to 15 clusters and the resulting Calinski–Harabasz index determined for each number of clustering. Where the Calinski–Harabasz index method was inconclusive, the optimal clustering number was chosen to correspond with groupings that produced a significant reduction to within group variance.

To complement cluster analysis, data from the Office of Environment and Heritage (OEH), Gipps St, Wollongong city station (Office of Environment and Heritage, 2013) was combined with the in situ FTIR record. Although the OEH data originates from a

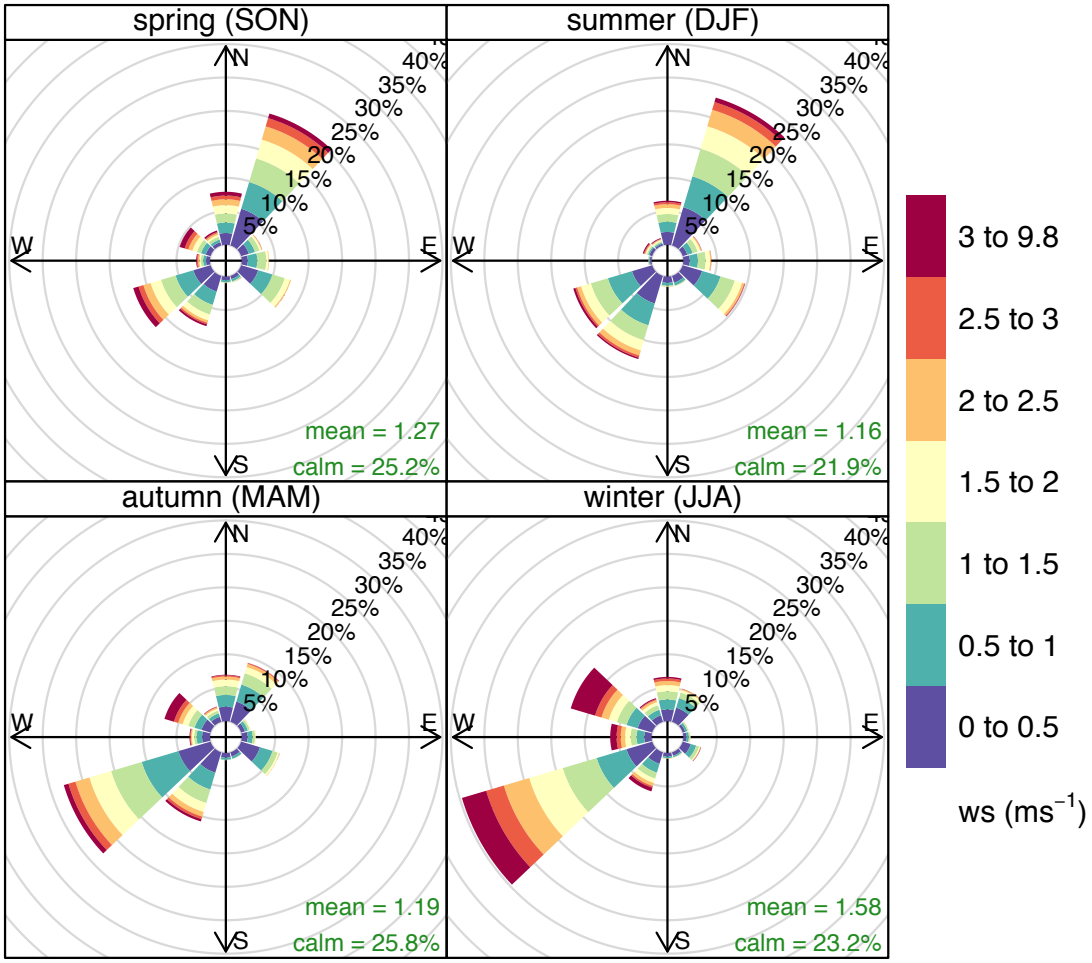

Figure 4.3.3: Seasonal wind direction and wind speed plots for UOW, 2011 to 2013. Compass directions equate to wind direction, wind wedges are coloured according to relative percent of wind speed.

site approximately 2 km southeast of UOW, they can be compared with UOW due to hourly time averaging of the datasets. Results from clustering are further averaged for the whole cluster, which produces results averaged over time periods of greater than a day. Time averaging minimises differences between sites in the region (case study in Appendix C). Two trace gases from the OEH record were of interest. NO_2, with a very short lifetime of 2 days gives insight into air influenced by local urban emissions; and O_3, used in enhancement ratio analysis with CO to give an indication of ozone production environment.

Clustering results

The seasonal bivariate polar plots of CO at UOW are shown in Figure 4.3.4 and indicate how CO measured at UOW varies with wind direction and wind speed. The characteristics of high CO contributions in these plots is different depending upon season. Spring and summer plots display two regions of high CO, from the northwest and south to southwest directions. Spring additionally has a contribution from low wind speeds from the northeast direction. In autumn, only the south to southwest region of high CO is prominent. Winter is characterised by two high CO regions, to the northeast and southwest.

To investigate the different features of the bivariate CO plots, the OpenAir clustering function "polarCluster" was applied in each season. Different optimal clustering was found depending upon season, and is displayed in Figure 4.3.5. Spring had the highest number of optimal clusters, with 6 clusters. Summer and autumn both had 5 optimal clusters, although they encompassed different spatial patterns, and winter had 2 optimal clusters.

Clusters were further analysed for atmospheric properties. Mean CO, mean NO_2, and enhancement ratios of $\Delta O_3/\Delta CO$ were determined for each cluster and are tabulated in Table 4.3.1. Enhancement ratios were calculated using reduced major axis (RMA) linear regression, which accounts for errors in both x and y variables. Enhancement ratios between O_3 and CO were only recorded where trace gases were deemed correlated. Quantitative analysis of O_3 production is more complicated due to differing background amounts, and not pursued here.

Enhancement ratios of O_3 relative to CO were used to gain insight into atmospheric oxidation environment characteristics. Enhancement ratio analysis with $\Delta O_3/\Delta CO$ is a valuable method for investigating photochemical characteristics of the troposphere and can indicate O_3 production (positive) or O_3 destruction and deposition (negative) (Fishman & Seiler, 1983). In autumn and winter, Wollongong atmosphere produces an ozone destruction environment, as indicated by negative $\Delta O_3/\Delta CO$ for all clusters where the correlation was valid and could be calculated (Table 4.3.1). In summer, the Wollongong atmosphere shows only ozone production, as indicated by positive $\Delta O_3/\Delta CO$. Ozone is produced in the troposphere photochemically from NO_X, therefore it is not surprising that ozone production would occur in summer, corresponding with maximum incoming solar radiation interacting with local and regional pollution, a large source of VOCs and NO_X.

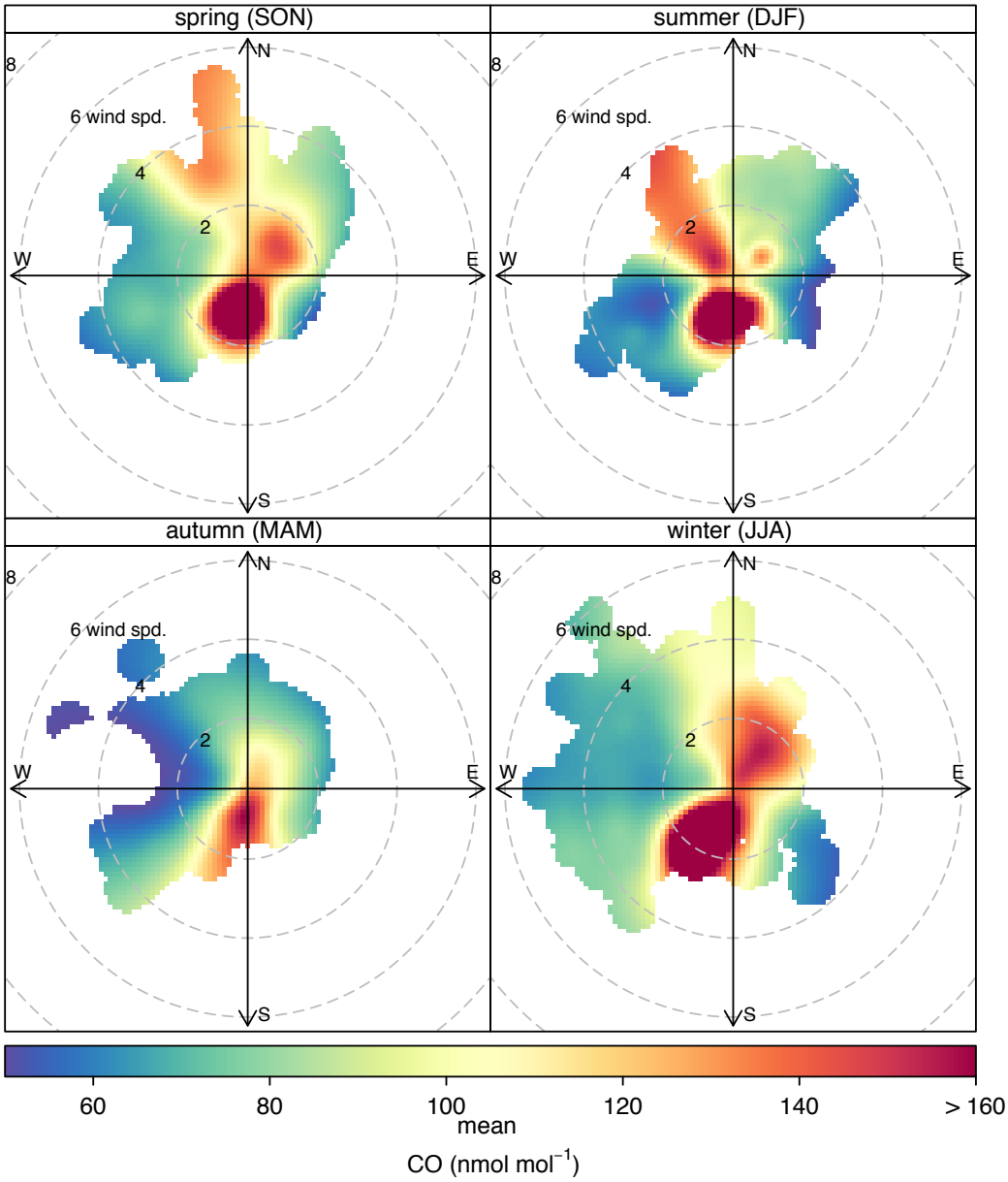

Figure 4.3.4: Seasonal bivariate polar pollution plots for CO at UOW, for the hour-averaged dataset 2011 to 2013. Plots show CO mole fraction as a function of wind direction and wind speed, relative to the centre which is positioned at UOW. Colours denote CO amount, concentric circles represent wind speed (in ms^{-1}), and compass directions equate to wind direction.

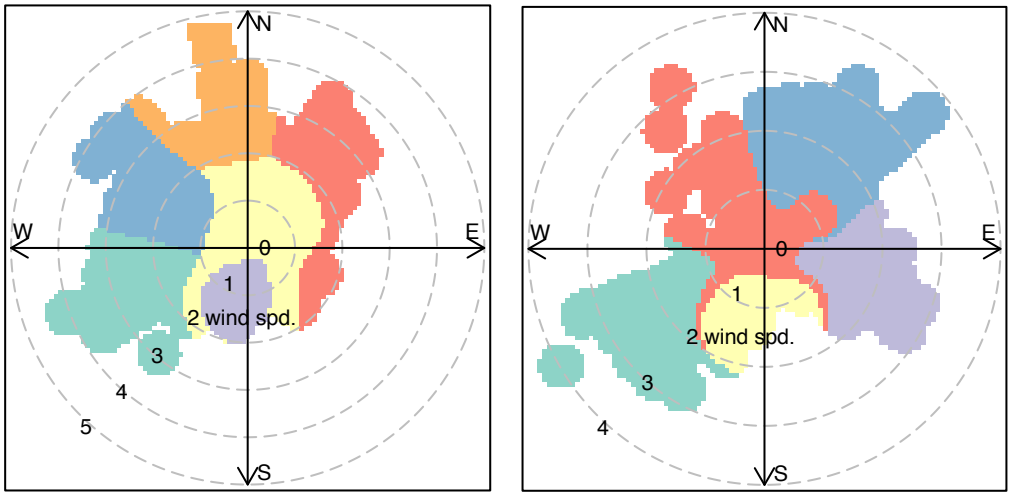

(a) Spring (SON)

(b) Summer (DJF)

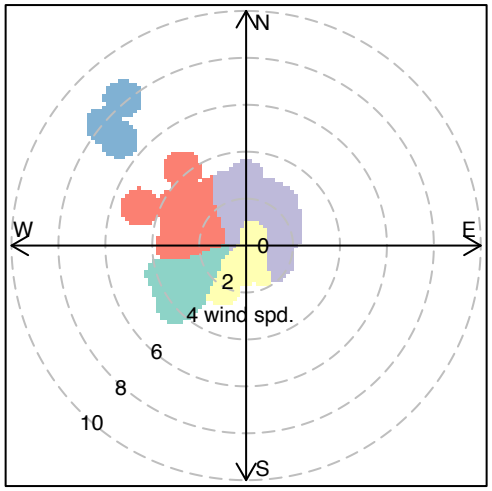

(c) Autumn (MAM)

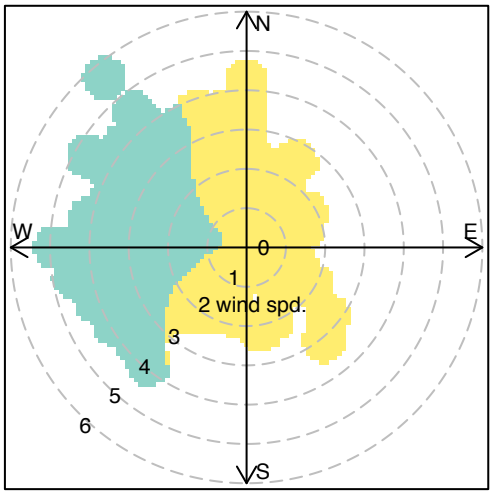

(d) Winter (JJA)

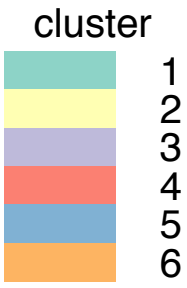

(e)

Figure 4.3.5: Optimum windspeed, wind direction and concentration k-means clustering results for seasonal subsets of the hour-averaged CO record at UOW, 2011 to 2012. Clustering was determined using the polarCluster function in OpenAir.

Table 4.3.1: Tabulated mean CO, enhancement ratios $\Delta O_3/\Delta CO$ and mean NO_2 for different air clusters arriving at University of Wollongong. Enhancement ratios are only displayed where correlations exist, with $\sim$ denoting uncorrelated results.

Season	**Cluster** (# values)	**mean CO** (σ) nmol mol^{-1}	**$\Delta O_3/\Delta CO$**	**mean NO_2** nmol mol^{-1}	**Mean wind direction and possible sources**
Spring	1 (91)	79 (23)	-0.321 (p:0.01, r:-0.3)	5.18	SW to W, escarpment/forest
(SON)	2 (483)	141 (77)	$\sim$	8.22	NW to NE, local urban & industry
	3 (77)	220 (168)	0.025 (p:0.03, r:0.2)	8.56	S, local urban & steelworks
	4 (82)	94 (23)	0.152 (p:0.01, r:0.4)	2.76	NE to E, ocean
	5 (42)	85 (28)	0.170 (p:0.03, r:0.3)	4.74	W to NW, escarpment/forest
	6 (85)	115 (25)	$\sim$	7.67	NW to N, local urban & Sydney outflow
Summer	1 (95)	71 (30)	$\sim$	5.22	SW, escarpment/forest
(DJF)	2 (88)	182 (141)	0.031 (p:0.01, r:0.3)	7.05	S, local urban & steelworks
	3 (112)	81 (60)	$\sim$	2.46	E to SE, ocean
	4 (302)	116 (103)	$\sim$	6.44	N to WNW, local urban & industry
	5 (191)	84 (22)	0.277 (p:0.03, r:0.2)	3.43	N to NE, ocean & Sydney outflow
Autumn	1 (519)	72 (30)	-0.593 (p:0.01, r:-0.2)	5.71	SW, escarpment/forest
(MAM)	2 (677)	131 (88)	$\sim$	8.66	S, local urban & industry
	3 (312)	105 (46)	-0.419 (p:0.01, r:-0.2)	8.01	NNW to E, local urban & industry
	4 (97)	58 (11)	-0.385 (p:0.02, r:-0.4)	4.44	W to NNW, escarpment/forest
	5 (2)	53 (0.30)	$\sim$	1.50	NW, escarpment/forest
Winter	1 (585)	78 (28)	-0.520 (p:0.01, r:-0.3)	4.62	NW to SW, escarpment/forest
(JJA)	2 (1139)	129 (79)	-0.510 (p:0.01, r:-0.2)	9.85	N & S, local urban & industry

Spring is a mixture of ozone production and destruction environments, depending upon air cluster. Spring clusters 3, 4 and 5 are ozone productive and cluster 1, ozone destructive (Table 4.3.1). Peak biomass burning season in the Southern Hemisphere occurs during Austral spring (Edwards et al., 2006b), and ozone is produced photochemically in the biomass burning plume. Peak biomass burning also occurs in spring over the northern tropical and savanna region of the Australian continent (Craig et al., 2002). Therefore, ozone production environments during Austral spring are likely a combination of transported smoke plumes and urban pollution sources.

Results found here are in agreement with a global study using the TES satellite instrument (Voulgarakis et al., 2011) which determined $\Delta O_3/\Delta CO$ enhancement ratios in two seasons. Voulgarakis et al., 2011 showed positive $\Delta O_3/\Delta CO$ around the east coast of Australia during Austral summer and negative correlations during Austral winter. Results here also agree with a study using OMI/AIRS satellite products in 2008 (Kim et al., 2013), which investigated seasonal $\Delta O_3/\Delta CO$ enhancement ratios in the free troposphere. Kim et al., 2013 also found summer (DJF) gave positive correlations localised around the east Australian coast, while autumn (MAM) gave negative correlations across the bottom half of Australia. The spring correlation map in Kim et al., 2013 showed a large latitudinal band of strong positive correlation over much of the Southern Hemisphere, between 0 and 40°S, a result of highly efficient ozone production in long-range biomass burning plumes. However, the region around eastern Australia, near Wollongong, was a mixture of positive and negative correlations in spring, which supports the variable correlation found in this study during spring (Table 4.3.1). Variable spring $\Delta O_3/\Delta CO$ indicates that air parcels would be influenced by different ozone production environments, depending upon which direction they originated. Winter did not provide sufficient satellite data below 30°S to give an estimate of $\Delta O_3/\Delta CO$ from Kim et al., 2013. The agreement of $\Delta O_3/\Delta CO$ signs between in situ and the spatially averaged satellite correlations suggests that Wollongong in situ results on average represent the ozone production environment of the free troposphere.

Back trajectory analysis was used to further understand atmospheric properties of different ozone production regimes. Pre-calculated back trajectories from UOW for 2011 and 2012 using the HYSPLIT model (Hybrid Single Particle Lagrangian Integrated Trajectory Model http://ready.arl.noaa.gov/HYSPLIT.php) were available for use with the OpenAir package. Trajectories were calculated backwards in 3 hour intervals for 96 hours, from a 10 metre surface level, using the Global NOAA-NCEP/NCAR reanalysis meteorological fields at 2.5° horizontal resolution. These back trajectories

were grouped with corresponding clusters and back trajectory frequency plots were determined, along with average back trajectory in each cluster.

It was found that positive $\Delta O_3/\Delta CO$ enhancement ratios at UOW were associated with slow moving trajectories possessing anticyclonic behaviour. Positive correlations indicate ozone production environments, therefore the trajectory analysis suggests the source of ozone production is from photochemical reactions of local and regional pollution, trapped and recirculated on the Australian east coast by slow-moving atmospheric dynamics. An example of this slow-moving, anticyclonic behaviour can be seen in trajectory frequency plot for the positively correlated summer cluster 5 (Figure 4.3.6). Back trajectories are gridded by frequency of direction of travel, for the whole of summer cluster 5.

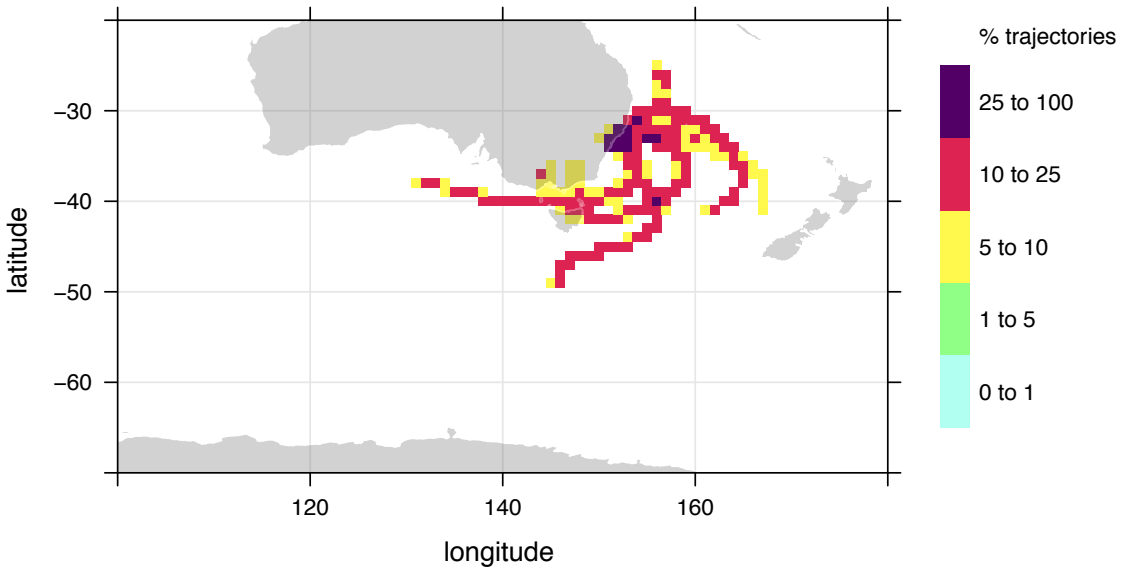

Figure 4.3.6: Gridded back trajectory frequencies for summer cluster 5. Surface is coloured by percentage of total trajectories which pass through each gridbox.

In contrast, negative $\Delta O_3/\Delta CO$ enhancement ratios were found to be associated with faster moving trajectories displaying less anticyclonic behaviour. For example, the trajectory frequency plot for the negatively correlated autumn cluster 1 (Figure 4.3.7) shows many fast moving trajectories, indicated by the greater distance covered in the 4-day back trajectory, compared with summer cluster 5. Some trajectories in autumn even originate from Antarctica, a source of air with low amounts of CO.

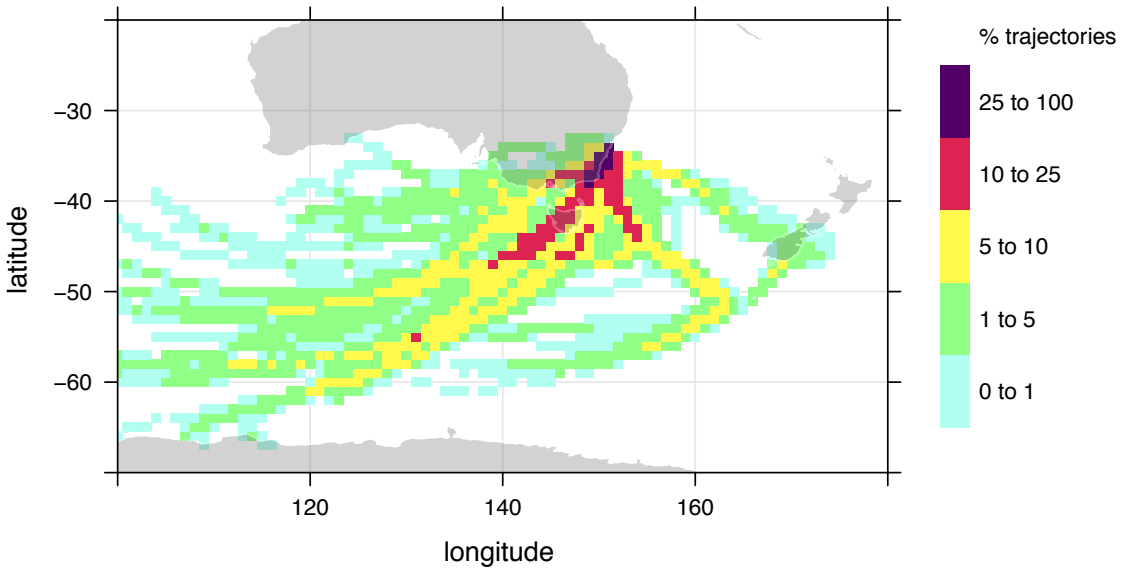

Figure 4.3.7: Gridded back trajectory frequencies for autumn cluster 1. Surface is coloured by percentage of total trajectories which pass through each grid-box.

A summary of the difference between these two trajectory types can be clearly seen in the plots of mean trajectories of each cluster, for the example between summer cluster 5 and autumn cluster 1, as shown in Figure 4.3.8.

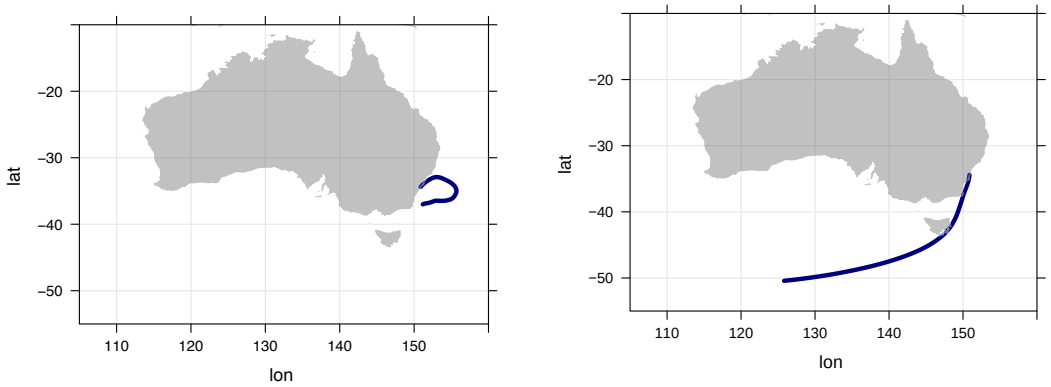

(a) Summer #5: slow, anticyclonic behaviour. (b) Autumn #1: fast moving

Figure 4.3.8: Mean back trajectory for (a) Summer cluster 5 and (b) Autumn cluster 1.

4.4 Discussion and Conclusion

The in situ FTIR dataset at Wollongong represents a site influenced by local urban and industrial pollution. Although strongly influenced by urban pollution, it was found that air having close to background composition arrived at Wollongong approximately 10% of the time, sampled when sourced from the directions 50° to 150°, and 245° to 300°, at wind speeds greater than 0.4 ms^{-1}. The annual mean of UOW Clean Air N_2O matched the annual mean at Cape Grim clean air baseline station. CO and CH_4 annual mean values were higher than Cape Grim, but were close to values expected when accounting for latitudinally induced concentration gradients.

Annual cycles from June 2012 through May 2013 were analysed for CO, CO_2 and CH_4. Spring-time peaks were evident for CO and CH_4, well-known to coincide with Southern Hemispheric peak biomass burning. Annual cycles for these two trace gases at UOW followed the same seasonality as Cape Grim. The CO_2 annual cycle at UOW was anti-phase to Cape Grim, reflecting influence from a combination of sources, possibly indicating contribution from transported Northern Hemisphere air. Further investigation using tagged tracer modelling would help assess contributions to the CO_2 seasonal cycle at UOW.

Preliminary trend analysis was completed for UOW Background and Clean Air datasets of CO, CO_2 and CH_4. A downward trend resulted for CO (Background: -3.79 ±3.4 nmol mol^{-1} per annum; Clean Air: -3.75 ±1.0 nmol mol^{-1} per annum), and upward trends were found for CO_2 (Background: 2.05 ±0.86 μmol mol^{-1} per annum; Clean Air: 1.45 ±0.89 μmol mol^{-1} per annum) and CH_4 (Background: 2.9 ±3.3 nmol mol^{-1} per annum; Clean Air: 3.5 ±3.3 nmol mol^{-1} per annum). The downward CO trend is substantially more negative than the clean-air station Cape Grim, which was attributed to the UOW site being closer to changing atmospheric sources of CO. UOW CO_2 and CH_4 trends were generally representative of global average trends. It is important to reiterate that results here must only be used as a preliminary guide of temporal trends in the Wollongong region. With extended measurements, robust trends in the background amounts of trace gases will be determined, adding to the global investigation of changing atmospheric composition. Therefore, the UOW ambient record that was begun during this PhD provides a valuable record for interpreting future atmospheric change.

Analysis of the non-background conditions for the in situ dataset included determining daily cycles in Wollongong. The results confirmed a strong local urban influence on the Wollongong atmosphere, with some possible influence from transported sources

of Sydney urban outflow. Atmospheric composition in the Wollongong region is also strongly influenced by boundary layer dynamics.

Seasonal bivariate polar plots were used to analyse the in situ FTIR timeseries of CO to determine directional influences on atmospheric composition. Strong sources from the southern direction are likely due to a combination of local urban and Port Kembla industrial pollution. High CO was also seen to be transported from the north/northwest in spring and summer, and from the northeast in winter, reflecting influences from local vehicular and Sydney urban outflow. Seasonal cluster analysis was subsequently performed, and $\Delta O_3/\Delta CO$ enhancement ratio analysis of clusters allowed determination of tropospheric ozone production environments around Wollongong. In autumn and winter the atmosphere in Wollongong supports ozone destruction (negative correlations), while spring and summer generally experience ozone production (indicated by positive correlations). Trajectory analysis helped determine that at UOW, ozone production environments are associated with slower moving, anticyclonic trajectories, while ozone destruction environments correspond with fast moving, direct trajectories.

UOW was found to be a useful site to study atmospheric composition for both background values and polluted atmospheric composition. Although there are complex influences at the UOW site, the dataset provides information to help understand the Australian atmosphere near a populous area, rather than the usually selected remote "clean air" sites. In addition to the analysis performed in this thesis, the in situ timeseries is envisaged to be a useful record for future research, particularly as the dataset grows.

Chapter 5

Wollongong total column CO, from ground–based and satellite remote sensing

5.1 Motivation for comparing ground–based and satellite column datasets

This chapter presents an analysis of atmospheric CO over Wollongong using ground– and satellite–based instruments. A detailed comparison between total column CO, measured by ground–based solar FTS and satellite-borne MOPITT (Measurements Of Pollution In The Troposphere) is made. Generally, total column values can be more sensitive to long-range transport of trace gases compared to surface measurements. Total column values capture information of the whole atmosphere above a particular location. Transported CO from long–range sources has a maximum above the surface level. Thus, total column CO measurements can indicate long–range transport to Wollongong, which often occurs from southern Africa or South American biomass burning sources (Edwards et al., 2006a,b). Ground–based total column measurements retain the added advantage of recording small-scale local urban pollution and local biomass burning sources of CO.

Importantly, there are sensitivity differences between ground–based and satellite instruments with respect to trace gas retrievals. There are four main reasons measurements may differ between the ground–based and satellite instruments, namely, vertical sensi-

tivity, sampling bias, non-coincidence of measurements or spatial dilution.

This study is not focused on validating the MOPITT product, as that has been achieved elsewhere (e.g. Deeter et al., 2010). Figure 5.1.1 shows the viewing geometries of ground–based and satellite instruments. Different viewing geometries leads to different vertical sensitivity. When using ground–based measurements to validate satellite retrievals, the instrument with greater vertical information (FTS) is degraded to the instrument with reduced information (MOPITT), using the averaging kernel from the lower-information instrument, following the method described in Rodgers & Connor, 2003 (a brief theory of averaging kernels was introduced in Chapter 2). In the study presented here, averaging kernels are not applied, allowing datasets to retain information unique to each instrument. Differences in vertical sensitivity between instruments are therefore used to an advantage to understand contributions to total column CO, over a 10 year timeseries.

MOPITT retrievals of CO in the thermal infrared are most sensitive to the lower free troposphere (approximately 700 hPa) (Edwards et al., 2006b), while the solar FTS retrievals have uniform sensitivity throughout the atmospheric column, including at ground level. This means solar FTS has the advantage of capturing local pollution, which has not yet entered into the free troposphere. In contrast, the MOPITT CO product may miss enhancements below 700 hPa, because at altitudes where sensitivity is reduced, measurements are weighted towards the a priori. An analysis of both records can consequently give insight into the relative impact of local and remote pollution sources to total column CO at Wollongong.

Measurement differences due to sampling bias, non-coincidence of measurements or spatial dilution are minimised for this study. Sampling biases are introduced due to limitations in the instrument retrieval processes. For example, satellite instruments may be biased by retrieval issues in a particular region, such as over highly reflective surfaces or due to persistent cloud cover. Measurements with both instruments are required to be under clear sky conditions, so the sampling bias due to clouds would be similar between instruments and are therefore not considered further. Also, Wollongong is not located near highly reflective surfaces such as desert or snow, thus this bias would be minimal in the MOPITT retrievals. A sampling bias for FTS is present due to limiting measurement of CO values during daylight hours. This has been accounted for by restricting MOPITT values to daytime retrievals. Overall, sampling bias is assumed to be minimal between instruments.

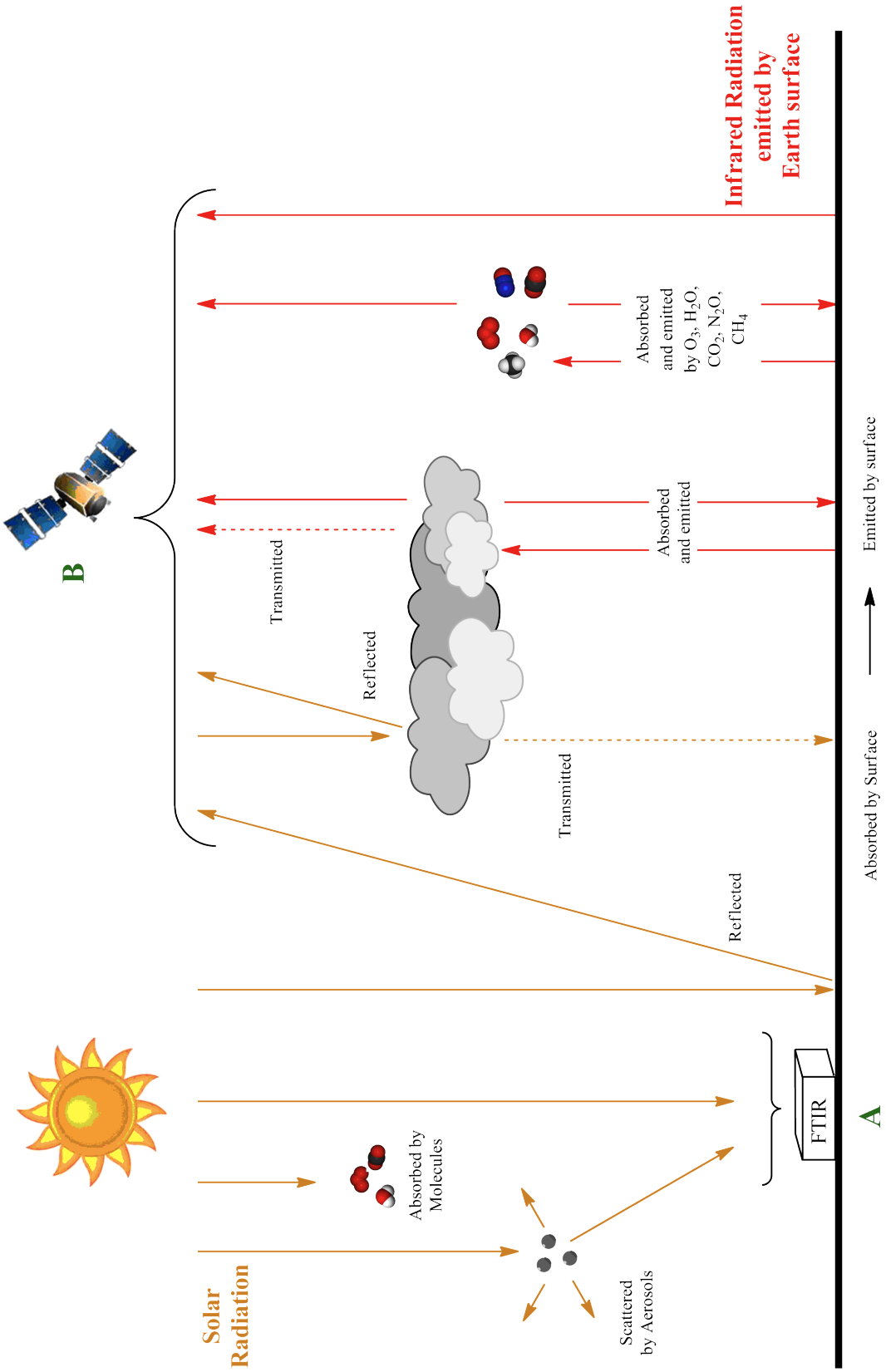

Figure 5.1.1: Viewing geometries of **A** ground– and **B** satellite–based instruments. Radiation is shown to be absorbed or scattered by atmospheric constituents (Houghton et al., 1984).

The 22 × 22 km horizontal resolution for the satellite records a diluted representation of any highly local surface sources, or indeed any plume narrower than 22 km. Additionally, in order to ensure sufficient data density, measurements from the satellite were averaged over a larger surface footprint of 300 km (within a 150 km radius of the Wollongong station), further diluting any local signals. The result is a spatially diluted representation of the atmosphere by the satellite data. Averaging satellite data within in a spatial "window" accounts for measurements being spatially non-coincident with the solar FTS. However, the spatial averaging exaggerates the spatial dilution bias and MOPITT values are therefore expected to be lower in magnitude than solar FTS, particularly for days that see influence from local sources.

Finally, due to satellite overpass times and solar FTS procedures, measurements may not be temporally coincident. Temporal averaging over a week is applied to smooth any time–related biases between instruments. Temporal averaging is expected to produce a similar result between instruments, leaving spatial dilution to have the most dramatic effect on MOPITT results, diluting signals that may be restricted to a local Wollongong area.

Wollongong (34.5 S, 150.9 E, 30 m altitude) has a complex combination of influences on the total column of CO. The solar FTS instrument site at the University of Wollongong (UOW) is close to local urban sources and is approximately 80 km south of Sydney, which had a population of over 4.3 million people in 2011 (Australian Bureau of Statistics, 2011). Significant local industry also affects the Wollongong atmosphere, with a steel-making industry to the south of the measurement site and coal-burning coke-ovens to the north (see Figure 4.0.1 in Chapter 4). Being located close to large forested areas such as the Royal National Park to the north and water-board catchment areas due west, local bushfires frequently impact the UOW site. An analysis of the two total column CO datasets help understand influences from these possible sources by comparing results between instruments.

In particular, an analysis of CO measured from the ground–based FTS and MOPITT led to identification of several CO enhancement events. Two major types of CO events were identified: I, enhancements in CO that are captured by both instruments and II, enhancements that are only captured by the solar FTS. In addition to enhanced CO values, there is an occurrence of unusually low CO, captured by both instruments. These event types are subsequently discussed with respect to atmospheric contribution.

5.2 Analysis methodology and identification of anomalous events in the CO record

Specifications and theoretical retrieval procedures have been discussed for both instruments in Chapter 2. Here, solar FTS measurements of CO retrieved using SFIT-2 were used in comparison with the MOPITT V4 record, covering the time period from 2000 to the end of 2009. Records from each instrument provided total column CO values at daily time resolution. Additionally, MOPITT data was considered within a 150 km radius of Wollongong, as a compromise between sufficient data density and dilution of signal due to spatial averaging. Land and ocean pixels were included in the Wollongong average region, as minimal bias was found between the different retrieval types. An example of the 300 km squared region around Wollongong is shown overlaid on MOPITT measurements for October 2008, in Figure 5.2.1. Spatial averaging results in a plume less than 300 km in extent being diluted in the MOPITT values.

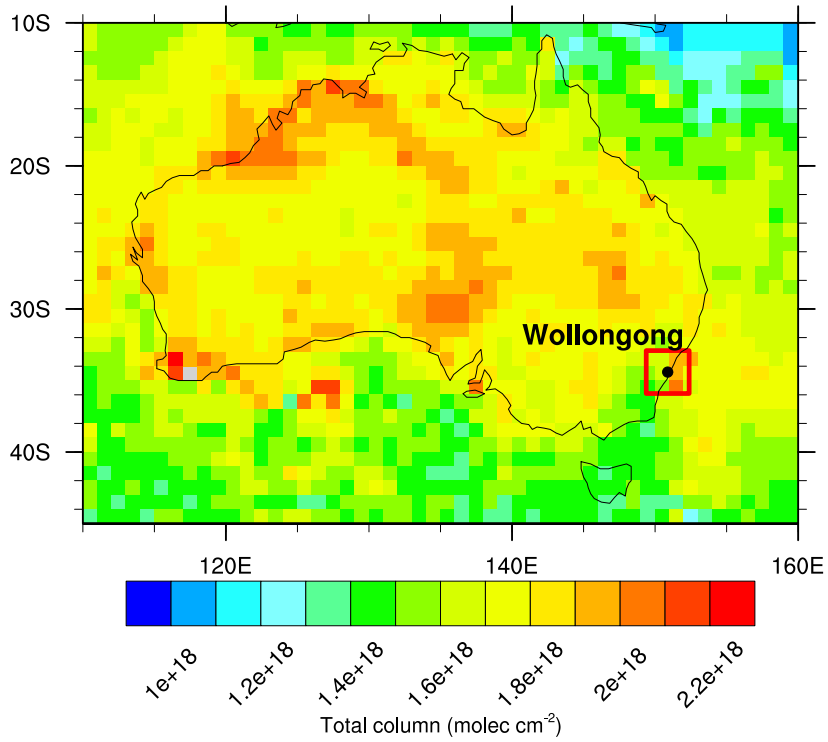

Figure 5.2.1: Example of MOPITT month averaged total column values plotted at 1° resolution for October, 2008. The region outlined in red indicates 150 km radius region around Wollongong, used here for spatial averaging.

Recently, a geolocation error has been identified in MOPITT retrievals (Deeter, 2012; Deeter et al., 2014). The error was determined to be most likely from a mis-alignment between the MOPITT instrument and the satellite platform Terra. Geolocation error would not have significantly affected results in this study, due to the spatial averaging of 150 km radius around Wollongong. The daytime longitude bias was determined to be approximately 30 km westward and up to 2 km southward, therefore the Wollongong location remains contained within the area of spatial average. It is recommended in future studies to use corrected MOPITT measurements.

The solar FTS instrument only measures during daylight hours, therefore MOPITT measurements were restricted to daytime as well. In general, daytime MOPITT V4 retrievals have higher information content than nighttime measurements (Deeter et al., 2010), therefore the exclusion of MOPITT nighttime retrievals does not severely degrade the instrument record.

Datasets were further averaged over 7-days before performing a comparison. Weekly averaged values ensured that multiple measurements were included for each of the FTS and satellite datasets, while keeping time resolution fine enough to resolve shorter timescale events. Background envelopes were developed for each instrument by calculating climatological monthly mean values, and combining with standard deviations. Standard deviations indicated expected ranges of CO within the bounds of interannual variability.

Anomalous events in weekly CO for each instrument were determined by comparing weekly values with the climatological envelope. Anomalous events were defined to be significant if outside the climatological background envelope for the corresponding month. Causes of these anomalous CO events were subsequently investigated using several methods.

The FTS dataset was mined for days that contributed the most to anomalous weekly values. Instrumental records included FTS operator comments about meteorologically interesting days, bushfire events, and instrumental details relevant for dataset interpretation. Wind data were obtained from the Australian Bureau of Meteorology (Australian Bureau of Meteorology, 2010) for sites at the University of Wollongong and the northern suburb of Bellambi. Influence from Port Kembla steelworks and industrial area was investigated by comparing wind data to a wedge of wind directions (150°-210°, Figure 5.2.2) designated likely to transport atmospheric pollution from Port Kembla to the FTS at UOW. Meteorology was also investigated for anomalous events using the British

Atmospheric Data Centre (BADC) web trajectory service (NCAS British Atmospheric Data Centre, 2010). Five day (or eight day) back trajectories were run from 18:00, with output frequencies of 1 hour and at starting altitude levels of 950, 750 and 450 hPa.

In order to locate fire events that may have influenced the measurement records, MODIS fire location and duration data were investigated using the FIRMS web fire mapper (Davies et al., 2009). Fire maps were acquired from Rapid Response for specific events. The use of FIRMS data and Rapid Response imagery is acknowledged from the Land Atmosphere Near-real time Capability for EOS (LANCE) system operated by the NASA/GSFC/Earth Science Data and Information System (ESDIS) with funding provided by NASA/HQ (http://rapidfire.sci.gsfc.nasa.gov/cgi-bin/imagery/firemaps.cgi).

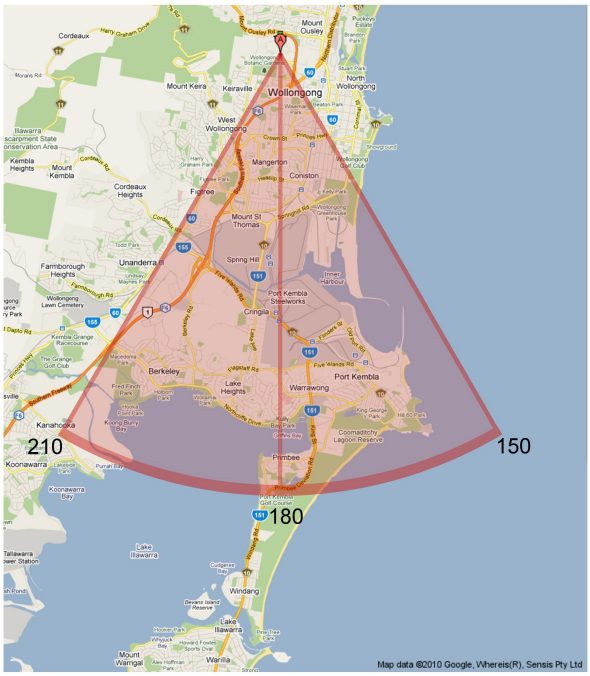

Figure 5.2.2: Wind wedge showing most likely wind directions at UOW (point A at the apex of the wedge) to include influence from the Port Kembla steelworks and industrial area. Map courtesy of Google Maps, 2010.

5.3 Results and discussion of anomalous CO events

A comparison between weekly averaged total column CO values from UOW ground–based solar FTS and the satellite instrument MOPITT is shown in the top panel of Figure 5.3.1. Anomaly plots for each instrument are in the lower two panels of Figure 5.3.1, which were used to identify total column CO values lying outside the climatological background envelopes. Weekly values outside the climatological envelope were identified for further investigation and are indicated by coloured vertical lines and defined as "events". Events were originally identified by the letters a to z when determined with a preliminary version of the FTS data. An updated FTS retrieval algorithm altered the significance of events previously determined, so that they were removed from further analysis and are no longer indicated in Figure 5.3.1. Specifically, **b**, **e**, **f**, **h**, **m**, **n**, **v** and **y** were deemed no longer significant anomalies.

General seasonal cycle

The average annual cycle of total column CO at Wollongong (Figure 5.3.1, smooth curves in top panel) is dominated by long–range transport of biomass burning plumes from southern Africa and South America. The October peak in column CO at Wollongong is induced by a spring peak in Southern Hemisphere biomass burning sources for the southern African and South American regions (Edwards et al., 2006a,b). Wollongong is also significantly impacted annually by northwestern Australian and Indonesian biomass burning, which peaks during Austral spring (Edwards et al., 2006a; Russell-Smith et al., 2007). In particular, interannual variability in the CO loading is influenced by northern Australian and Indonesian biomass burning, which in turn has been found to be influenced by the El Niño Southern Oscillation climate regime (Edwards et al., 2006b). Anomalies contributing outside the average annual cycle are of interest and are further investigated here.

Compared to the MOPITT data, the FTS data show approximately 50% greater spread in the standard deviation of the monthly mean background, indicating greater variability in the FTS dataset. Greater variability in the FTS record is a result of the vertical sensitivity of the FTS picking up plumes closer to the ground, combined with the dilution of some signals for MOPITT through spatial averaging. The FTS is therefore able to capture more variable fine–scale local pollution events within the urban air-shed, whereas the satellite data primarily observes regional scale events. Greater variability in the FTS record also results in a number of FTS-only observed anomalous events (aqua vertical lines in Figure 5.3.1).

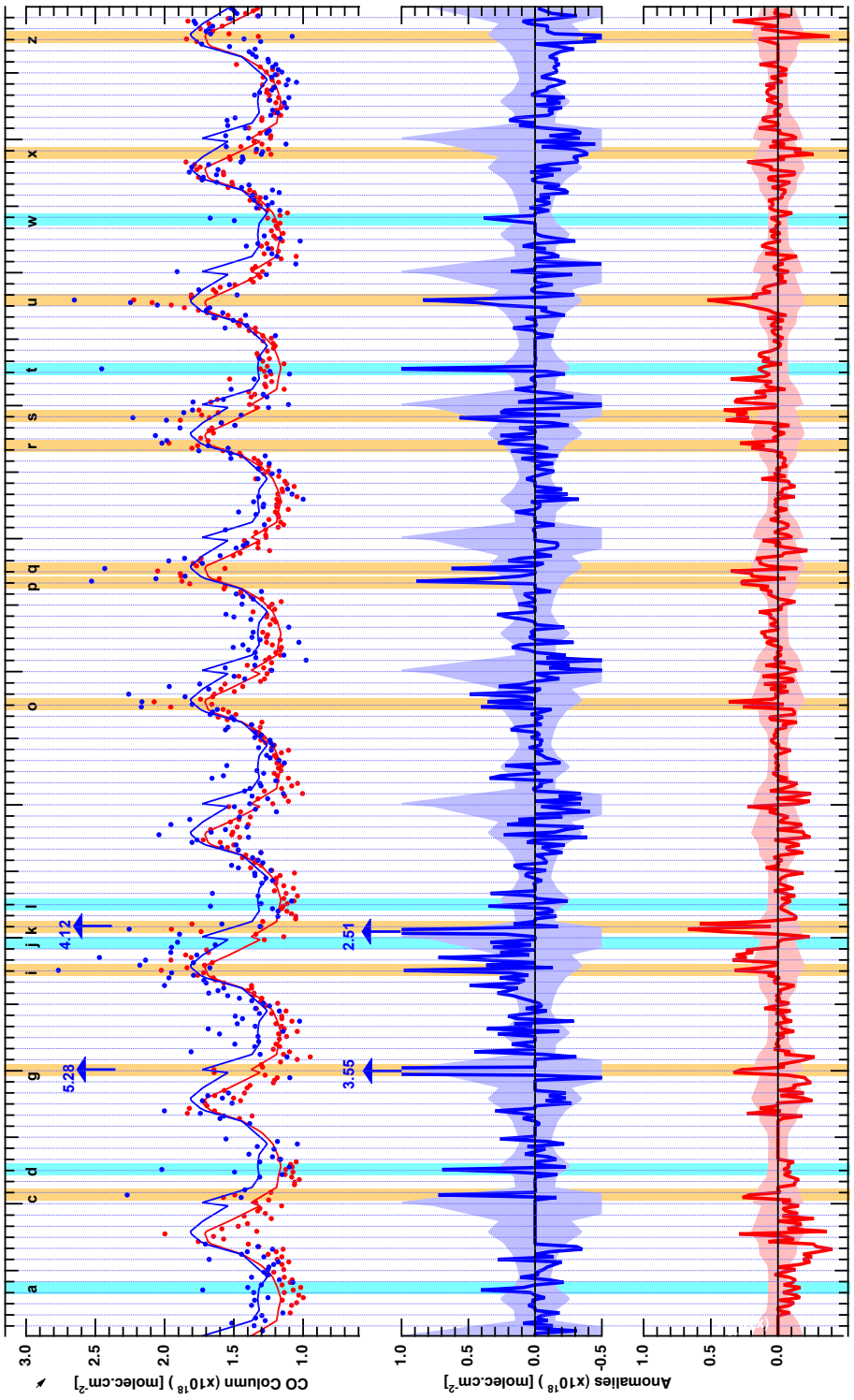

Figure 5.3.1: FTS (blue) and MOPITT (red) weekly averaged total column CO observations over Wollongong (upper panel) with mean annual cycles plotted as smooth curves. Lower panels show anomalies relative to a climatological background, with standard deviation shown as a shaded envelope. Events are denoted with letters and coloured vertical lines, defined as anomalies rising above the background envelope. Aqua blue vertical lines indicate FTS-only events, while orange vertical lines indicate events captured by both instruments. See Table 5.3.1 and main text for event analysis.

Overall, two main CO event type categories were determined: those that were observed by both instruments, denoted as event type I (**c**, **g**, **i**, **k**, **o**, **p**, **q**, **s**, **u**, **x**, **z**) and those that were only observed by the FTS, denoted as event type II (**a**, **d**, **j**, **l**, **t**, **w**).

Event type I: Large-scale events detected by FTS and MOPITT

The first event type, in which both MOPITT and FTS observed anomalies (indicated with orange bars in Figure 5.3.1), shows generally good agreement between the two instruments (events **c**, **g**, **i**, **k**, **o**, **p**, **q**, **s**, **u**, **x**, **z**). Measurement of CO enhancement by both instruments indicates that the total column CO anomaly is widespread, often as a result of being influenced by long and medium–range, high altitude transport of CO sources.

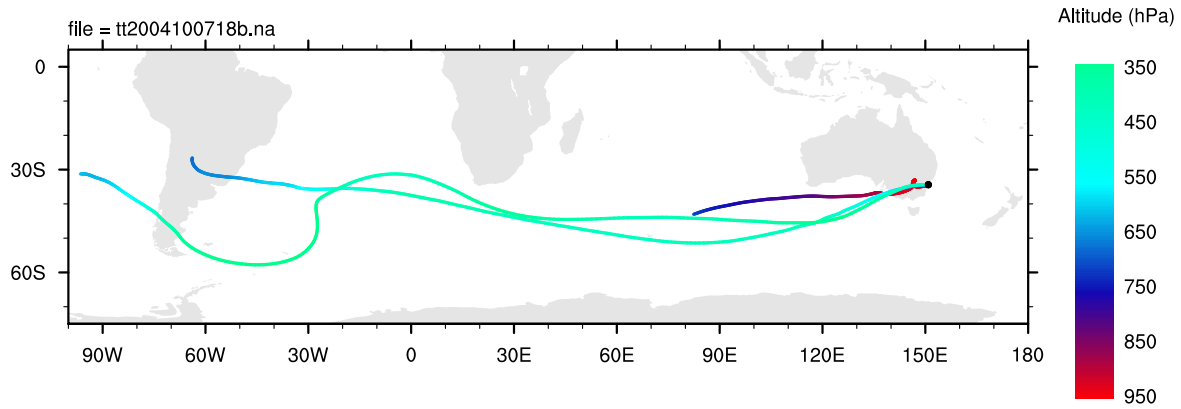

(a) Long–range transport from South America to Wollongong, 07 October, 2004 (8–day back trajectory)

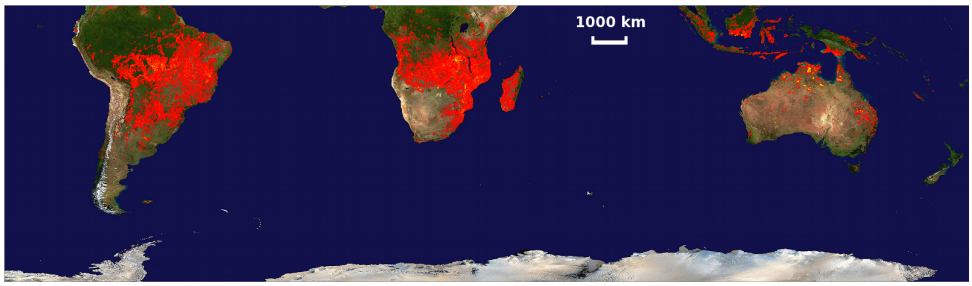

(b) MODIS fire count 27 September to 6 October, 2004 (Giglio et al., 2003; Davies et al., 2004)

Figure 5.3.2: Long–distance transport of CO sources from biomass burning in South America (event **o**).

Main sources of CO in these cases are dominated by seasonal biomass burning emissions and therefore occur during Southern Hemisphere biomass burning season from September to November. Examples of transport from South America and southern Africa can be seen in Figures 5.3.2 and 5.3.3, respectively. Three trajectories are indicated, beginning at altitudes of 950, 750 and 450, which were initiated at Wollongong. Fire maps are also shown to indicate that fires were present in the region of trajectory origin.

Fire maps show 10-day accumulated fires, detected by MODIS on board the Terra and Aqua satellites. Each red or yellow square pixel indicates a location where at least one fire was detected during the 10-day accumulation period. Red squares corresponds to low fire count while yellow squares indicate a large fire count.

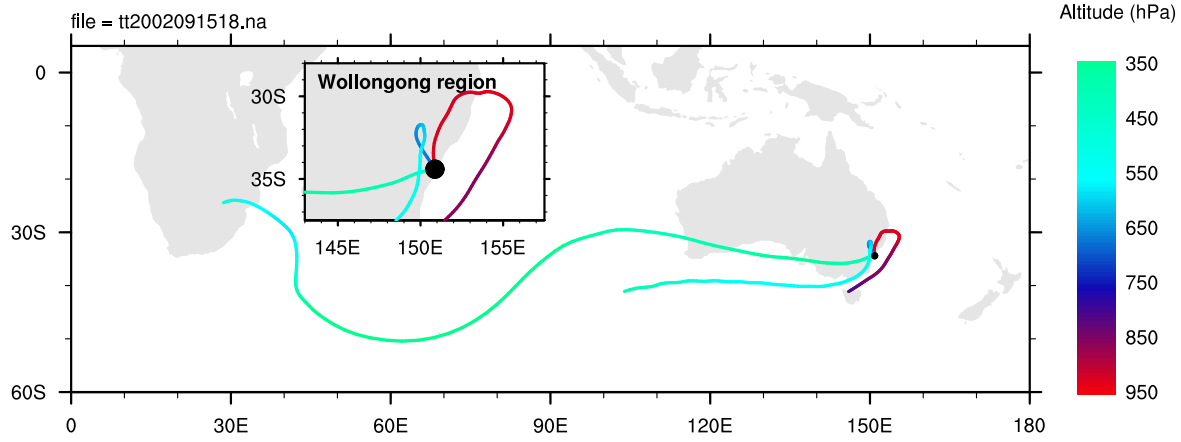

(a) Transported CO from African biomass burning air in the 450 hPa trajectory. Trajectory at 950 hPa transports air directly from local Wingecarribee county (north) during a bushfire day, 15 September, 2002.

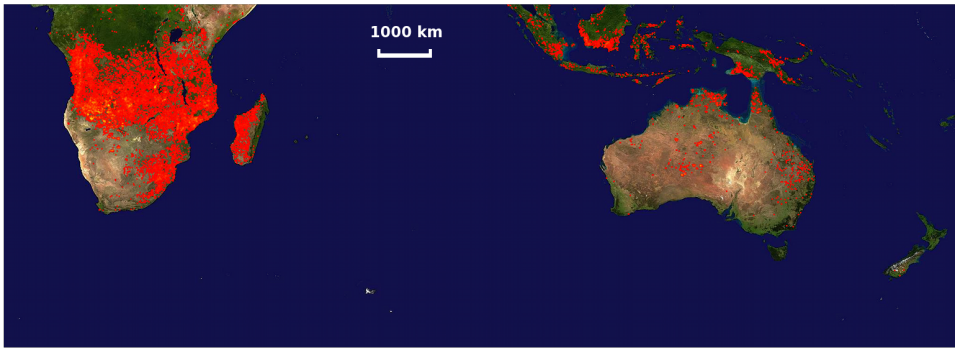

(b) MODIS fire count 8 to 17 September, 2002 (Giglio et al., 2003; Davies et al., 2004)

Figure 5.3.3: Long–distance transport of CO sources from biomass burning in southern Africa (event **i**).

Events for which both instrument records produce anomalies of approximately the same magnitude are **o**, **s** and **u**. For these events, the slightly lower response in the MOPITT CO may be explained by spatial and temporal dilution, as discussed in Section 5.1.

In some cases, FTS measurements are enhanced much more than the MOPITT retrievals, with FTS showing a substantially higher anomaly signal for the events **c**, **g**, **i**, **k**, **p**, and **q**. The higher CO value indicates influence on FTS measurements by local sources of CO. For example event **i** experiences additional influence from local biomass burning to the north of Wollongong (Figure 5.3.3a), which is reflected in a larger anomaly for the FTS dataset compared with the MOPITT dataset. The local biomass burning either remains below the free troposphere where MOPITT sensitivity is low, or is diluted over larger spatial scales before being measured by MOPITT.

Type I events may include medium–range transport of biomass burning CO from northern and western Australian for example as seen for event **c** (Figure 5.3.4) and event **o** (Appendix Figure E.0.5). An example of local urban pollution influencing only the FTS record is seen for event **c**, which experiences direct transport of pollution from Sydney in the 950 hPa trajectory (Figure 5.3.4).

Local enhancement in the FTS can be further influenced by significant impact from large local Australian fires. Fires on the eastern temperate coast of Australia tend to be most severe during Austral summer (Russell-Smith et al., 2007). Bushfires in Sydney during summer 2001-2002 (event **g**) and Canberra fires during summer 2003 (event **k**, Figure 5.3.5) were captured by both instrument datasets, but show off-scale values for the FTS instrument in Figure 5.3.1. Extremely large values in the FTS record reflects the close proximity of these biomass burning events to Wollongong.

Sydney bushfires in 2001–2002 were closer to UOW than Canberra fires in 2003, therefore produced a higher total column value in the FTS than seen for Canberra fires. The highest anomaly in the MOPITT record occurred for the Canberra mega-fire in 2003, which was due to the intensity of the fire creating pyro-cumulonimbus clouds (Fromm et al., 2006), injecting much of the biomass burning emissions into the upper troposphere and stratosphere, where MOPITT was more easily able to detect the plume. The FTS measurements during Canberra fires 2003 remained larger than MOPITT values, and was in part due to direct transport from Canberra to UOW in the 750 hPa trajectory (Figure 5.3.5). Additionally, the 450 and 950 hPa trajectories indicate that anticyclonic meteorological behaviour would have aided in trapping and recirculating the biomass burning plume over the eastern Australian coastal region.

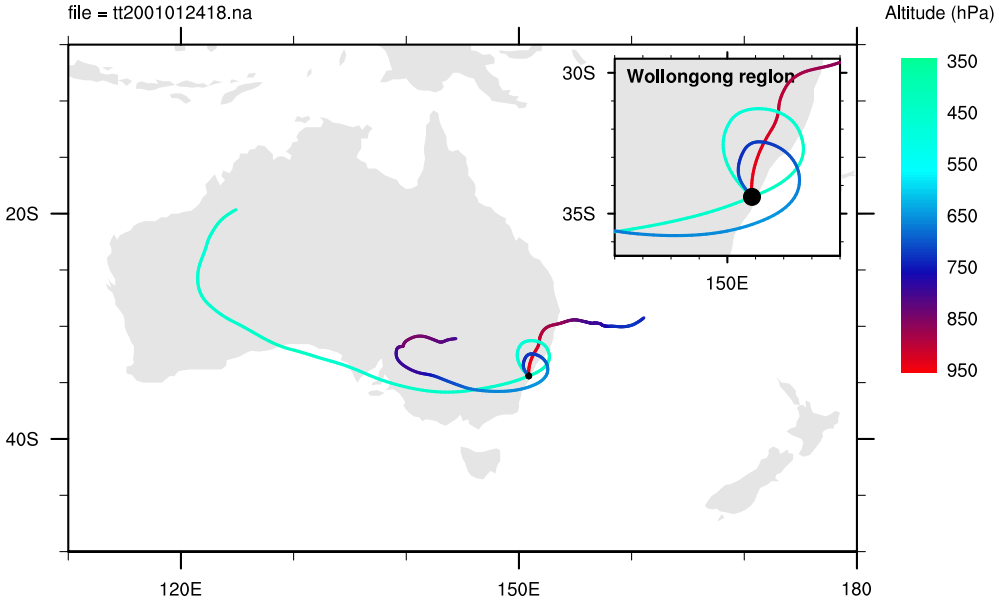

(a) Back trajectory plot (5-days), for 24 January, 2001. Trajectory at 950 hPa moves directly over Sydney (inset) transporting urban pollution.

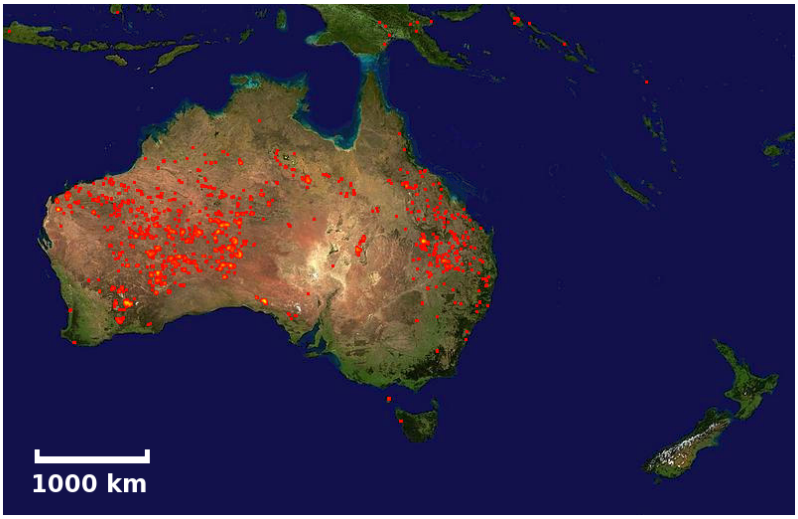

(b) MODIS fire count 11 to 20 January, 2001 (Giglio et al., 2003; Davies et al., 2004)

Figure 5.3.4: Medium-range transport from biomass burning sources in north-western Australia. Anticyclonic behaviour of 750 hPa and 450 hPa trajectories trap and recirculate both local and transported CO (event **c**).

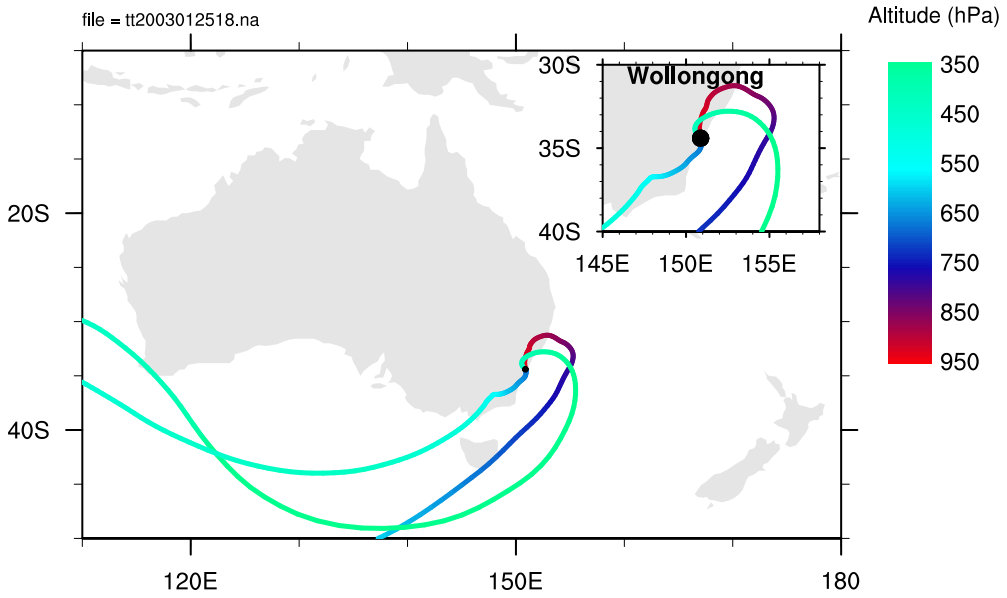

(a) The 750 hPa trajectory passes directly over Canberra during large-scale biomass burning.

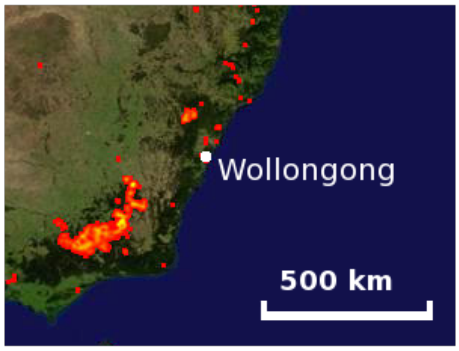

(b) MODIS fire count 21 to 30 January, 2003 (Giglio et al., 2003; Davies et al., 2004)

Figure 5.3.5: Direct transport of CO sources from large-scale Australian biomass burning (Canberra 2003, event **k**).

Finally, there are events of type I, which show anomalously low CO values (e.g. events **x** and **z**). Events with depleted total column CO are due to long–range transport of lower concentrations of CO, sourced from higher (more southern) latitudes. Southern latitudes have lower CO due to the latitudinal gradient of CO, induced by trace gas diffusion and transport, combined with the two month lifetime of CO (Novelli et al., 1998; Holloway et al., 2000; Yashiro et al., 2009). Back trajectory analysis of events **x** and **z** indicate air parcels at the three altitudes spend a substantial amount of time over the southern ocean, consequently lacking proximity to sources of CO. Additionally, some air

can be transported from Antarctica, as is the case for the 950 hPa trajectory of event **z** (Figure 5.3.6). This, combined with reduced long–range transport from South America and southern Africa during the Southern Hemisphere biomass burning season leads to lower CO over Wollongong and consequently anomalously low CO measurements by both instruments.

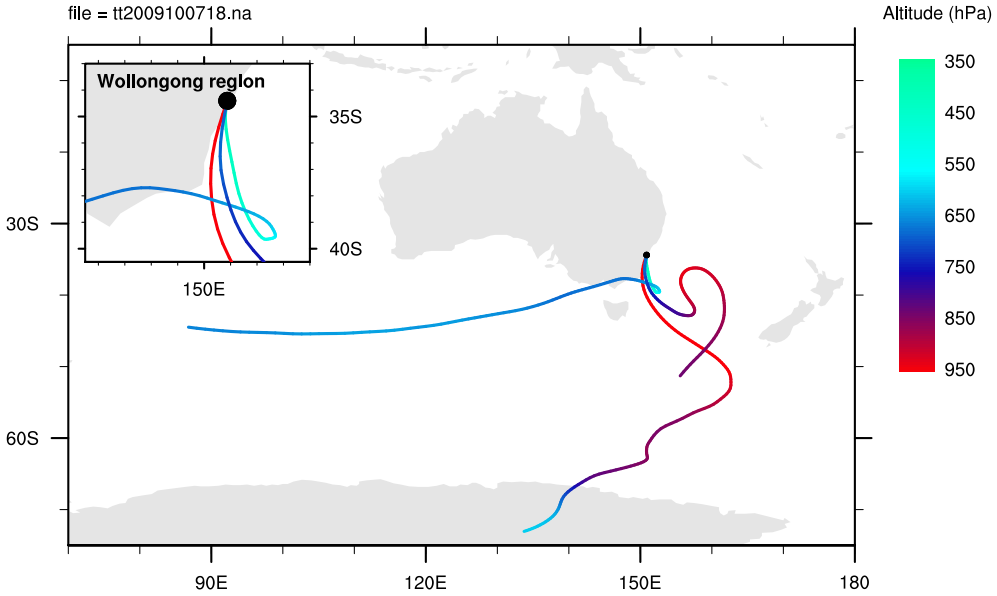

Figure 5.3.6: Trajectories at all altitudes spend much time over the southern ocean, which has low CO. The 950 hPa was influenced by the atmosphere over Antarctica (event **z**).

Event type II: Local-scale events detected by FTS only

The second event type is defined as an anomaly only present in the FTS record and not significant in the MOPITT record, indicated by an aqua vertical bar in Figure 5.3.1 (events **a**, **d**, **j**, **l**, **t** and **w**). Events that only occur in the FTS record are due to highly local CO sources, which have not yet entered the free troposphere, where MOPITT is more sensitive and would also capture information. Local meteorology often favours development of an inversion layer, which encourages pollution from local sources to remain at lower altitudes (Bryant, 1982). Alternatively, sources may be too small to be captured in the 150 km radius MOPITT weekly average value, and are therefore greatly diluted by spatial and temporal averaging.

Local CO sources may be from low altitude plumes of biomass burning or urban/industrial pollution. Locally enhanced CO air may arrive to influence the UOW FTS record in two ways: either being directly transported from the source to the UOW site; or transported back over the region after being transported away from the source. Direct transport of urban pollution was found to occur for events **j**, **l**, **t** and **w** with additional direct transport of local biomass burning for events **j** and **w**.

Indirect transport was seen to occur for event **d**, where Sydney urban outflow was re-circulated back over Wollongong, depicted in Figure 5.3.7. Outflow from Sydney was seen to travel over the ocean before heading to Wollongong. An outflow event may also occur with local pollution, as determined for event **a**, where pollution from the south, most likely from Port Kembla industrial park, is swept out over the ocean and circulated back over Wollongong (Appendix Figure E.0.4). Sydney pollution may also indirectly influence Wollongong in the opposite direction, by urban pollution building up northwest of Wollongong over the Blue Mountain, before being transported to Wollongong. Blue Mountains build up was also determined to contribute to the high FTS measurements for event **w**, in addition to direct transport mentioned earlier.

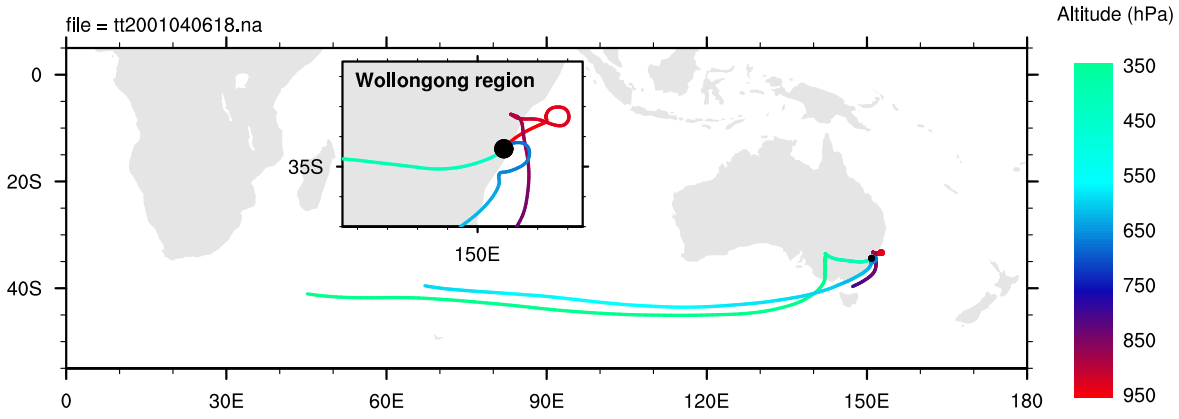

Figure 5.3.7: BADC Back trajectory examples for events of type II showing indirect transported pollution. Example of Sydney urban outflow event at 950 hPa (event d).

Several anomalous events have been discussed above. Contributions to all events was determined and results are summarised in Table 5.3.1, including comments on the most likely causes for CO enhancement (or depletion).

Table 5.3.1: Description of anomalous events determined at Wollongong and discussion of likely causes, (BB = Biomass burning, M = MOPITT).

Event	Date	FTS	M	Comments
a	May, 2000	y	−−	**Local pollution:** Slow moving trajectories and wind directions suggest sea breezes create an inversion layer, trapping local industrial and urban pollution (May 11).
c	Jan, 2001	y	y	**Medium–range BB transport and Sydney pollution:** Back trajectories suggest medium–range transport from Western Australian fires (MODIS) with local enhancement due to Sydney urban pollution.
d	Apr, 2001	y	−−	**Local and Sydney pollution:** FTS operator noted a milky horizon (Apr 5-6) indicative of photochemical smog; FTS collection times indicate measurements captured local morning urban pollution. Trajectories show outflow from Sydney over the ocean to Wollongong. Wind data indicate likely inversion layer assisted.
g	Dec, 2001 – Jan, 2002	y	y	**Large Australian BB, Sydney:** Regional plumes from extensive bushfires around Sydney (Dec 22, 2001–Jan 15, 2002; MODIS). FTS data is significantly enhanced due to proximity to BB (off scale in Figure 5.3.1). In particular, the hill directly behind UOW was ablaze Dec 25, 2001–Jan 14, 2002 (MODIS, FTS operator witnessed). Trajectories and wind directions indicate measured air travelled over fire regions and was assisted by Sydney outflow conditions.
i	Sep – Oct, 2002	y	y	**Long–range BB transport and local BB:** Trajectories indicate long-range transport of CO from fires in Southern Africa (Sep 15, MODIS). Enhancements due to local BB: (FTS operator and MODIS) in the Shoalhaven (S, Sep 14 & 15) and Wingecarribee (NW, Oct 02, 03 & 06) regions. Wind data supports transport of smoke from local BB. Local enhancements inversion meteorology assisted (FTS operator, Sep 10).
j	Dec, 2002	y	−−	**Local BB:** Smoke noted by FTS operator on all enhanced days, local BB in the Blue Mountains and Southern Highlands (NW and SW, MODIS), trajectories and wind data indicate transport. Slow, looping trajectories indicate air is remaining in the region and highly influenced by land.

Continued on next page –

– continued from previous page

Event	Date	FTS	M	Comments
k	Jan, 2003	y	y	**Large Australian BB, Canberra:** Transport of regional air from fires at Canberra (Jan 08–Feb 12; MODIS). The fire was so powerful it caused a stratospheric injection of smoke via pyro-cumulonimbus (Fromm et al., 2006). FTS is significantly enhanced (off scale in figure 5.3.1), due to the relative close proximity of Wollongong to Canberra (200 km). Additional Blue Mountains BB influence (Jan 25, MODIS and BOM wind data).
l	Mar, 2003	y	−−	**Local industrial and Sydney pollution:** Low altitude pollution identified by trajectories and wind data, originating from Sydney (Mar 28), local morning traffic and Port Kembla Steelworks pollution (Mar 30).
o	Sep – Oct, 2004	y	y	**Long and medium–range BB transport:** Trajectories indicate long–range transport from southern African and South American BB. Medium–range transport occurs from Western Australia and Northern Territory. Local contributions likely occur due to fires in the Sydney region (Oct 12&13, MODIS). Wind data supports air originating from this area.
p	Aug, 2005	y	y	**Long–range BB transport and local pollution:** Long–range transport from South America indicated in trajectories. Local enhancement in FTS (Aug 01) due to nightly build up of Sydney urban pollution over the Blue Mountains, followed by transport to Wollongong, supported by wind data.
q	Sep, 2005	y	y	**Long and medium–range BB transport and local pollution:** Trajectories indicate long–range transport from southern Africa and South America, increasing the CO background due to BB season. Medium–range transport is seen from Northern Territory BB region. Local enhancements in FTS are due to local Sydney urban pollution (Sep 07, 08 & 21)
s	Nov, 2006	y	y	**Medium–range transport:** The significantly enhanced day, December 1, was included in the last week average of November. Trajectories and wind data suggest this enhancement is due to medium–range transport from Victorian fires, overlaid on CO enhancement due to medium–range transport from Darwin BB.

Continued on next page –

– continued from previous page

Event	Date	FTS	M	Comments
t	Apr, 2007	y	−−	**Local pollution:** Wind data and trajectories indicate creation of an inversion layer, trapping local urban pollution, noted by FTS operator as white haze. Trajectories transport clean air originating from the south, and the time of year is outside BB season.
u	Oct, 2007	y	y	**Long–range transport:** Trajectories indicate long–range transport from Africa (Oct 14). Local enhancement due to fires in Sydney and Cooma (SW) regions (MODIS).
w	May, 2008	y	−−	**Local BB and Sydney pollution:** Local BB in Shoalhaven region (May 23; MODIS), wind data and trajectories support a low altitude plume from this direction. Enhancement from nightly build up of Sydney pollution over Blue Mountains followed by morning transport over Wollongong (May 27 & 29, wind data).
x	Nov–Dec, 2008	y	y	**Transport of low CO:** Trajectories (Nov 21) and wind data indicate transport of low CO air from the southern latitudes to Wollongong.
z	Oct, 2009	y	y	**Transport of low CO:** Five significantly low retrieval days are influenced by southern air. Trajectories spend a majority of time over the southern ocean, collecting air with low CO. A 950 hPa trajectory originates in Antarctica (Apr 06).

5.4 Conclusion

Wollongong is a site influenced by varied atmospheric sources of CO. This study used the different viewing geometries of ground–based and satellite borne instruments to help distinguish transported and local contributions to column CO at Wollongong. Sources of CO were linked to global and local scales through incorporating BADC back trajectory, meteorological, MODIS fire count data and observational analysis. Differing sensitivities between instruments aided in interpreting the 10 year total column CO timeseries with respect to anomalous events. Anomalous events were those defined to be outside the range of a climatological mean seasonal envelope. Using both instruments enabled distinction between contributions from multiple sources to column CO during selected events.

Long–range transport events of CO from southern Africa and South America were observed to directly influence the atmosphere at Wollongong on several occasions, particularly during the Southern Hemispheric biomass burning season. These long–range transport events of enhanced CO contributed to anomalies measured by both instruments. Long–range transport from Antarctica was also seen to influence anomalously low CO measurements for both instruments. Also, regional transport events were identified from northern and western Australian biomass burning.

The satellite instrument MOPITT was seen to generally capture large–scale anomalous atmospheric CO events. Direct and indirect transport of local pollution was seen to influence measurements in the FTS record. Local pollution influenced either only the FTS record of CO, or alternatively was measured by the FTS in addition to an anomalous regional signal. Regional signals were also picked up by the satellite, while local signals were not. Indirect transport was often accompanied by anticyclonic episodes, seen to cycle urban pollution outflow from Sydney and the local region back over Wollongong to produce very high CO atmospheric conditions.

In addition to understanding sources of atmospheric CO at Wollongong, this research has highlighted a set of events that are useful for future research. For example, several events of transported air from the biomass burning region in northern Australia were identified. Tagged tracer modelling could quantify the contribution of CO from northern Australia to the Wollongong atmosphere for these events. Additionally, a comparison of solar FTS measurements between Darwin and Wollongong would be a valuable study, including other trace gas species, in order to follow the chemical evolution of the northwestern Australian biomass burning plume.

Part III

Modelling

Chapter 6

Global Models

6.1 Modelling Atmospheric Composition

Atmospheric models are extensively used in atmospheric research, and are key in linking observations with theoretical knowledge. Models take our best current understanding of processes and simplify them into a workable tools. Due to assumptions and simplifications, model output must be verified and uncertainties quantified, before simulations can be used confidently to probe atmospheric properties (Seinfeld & Pandis, 2006b; Dameris & Jöckel, 2013).

The coarse resolution of model grid-boxes often means more than one source-type is present within a single grid-box. Importantly, a combination of source signatures means a trace gas can often be diluted due to spatial averaging within the grid-box. Model results are therefore not always expected to be identical to measurements, especially when measurements are taken close to sources of trace gases, such as within an urban environment. For example, measurements taken near a road would include vehicular sources and record high concentrations, while in comparison a model grid-box at the same location may not deliver the same magnitude as measurements, due to spatial dilution. However, as long as the spatial dilution effect and combination of sources is kept in mind, model output may be compared with measurements to interpret atmospheric composition. Often, spatial or time averaging of measurements helps minimise differences due to model spatial effects.

For this PhD, two global 3D Eulerian models were used, the Chemical Transport Model, GEOS-Chem and the Earth System Model, ACCESS. This chapter introduces running

parameters of each model and summarises main differences. Two case studies are included, one of chemistry choice and another of resolution differences and the effect each has on atmospheric composition is described. Quantifying the effects on atmospheric composition due to different run parameters is important in order to determine any likely model biases before comparison of model output with measurements. Here, major drivers of atmospheric composition bias are being sought. The case study of resolution effects on trace gases is completed in section 6.6. Comparison with measurements is subsequently completed in Chapters 7 and 8.

6.2 Global Chemical Transport Models

Global Chemical Transport Models (CTMs) are used extensively to study atmospheric composition. They combine real-world data into a model-system to predict and interpolate atmospheric composition in space and time. Global CTMs enable investigation of large-scale atmospheric processes and the effect they have on atmospheric composition. In some models, implementation of nested higher resolution grids over smaller areas allows for higher resolution analysis of regional-scale processes.

Global CTMs are usually used to simulate changes in atmospheric composition and chemistry over time, often in order to help interpret observations. Application of CTMs in atmospheric composition studies are varied and include chemical forecasting, assisting satellite atmospheric data retrievals, investigating chemical interactions and locating sources and sinks of trace gases. CTMs may focus on one part of the atmosphere, such as troposphere– or stratosphere–only, or aim to model and integrate both stratospheric and tropospheric chemistry. A drawback of CTMs is that they lack feedback of composition into the dynamical system, which means they can be limited to one-way studies with respect to climate change (Dameris & Jöckel, 2013).

There are three major components of a CTM, namely meteorology, chemistry and emissions, which are shown in figure 6.2.1. Deposition is another important modelled process which is split between the chemistry and meteorology components in Figure 6.2.1 (Seinfeld & Pandis, 2006b). The dynamical system in a CTM is know as non-interactive. Prescribed meteorological fields are used to drive a CTM and may be either reanalysis products or saved meteorological output from a Global Circulation Model (GCM). Reanalysis products result from assimilating measured meteorological data into Numerical Weather Prediction Models to provide gridded meteorological fields, such as

those produced by NASA Goddard Earth Observing System Model, version 5 (GEOS-5, Rienecker et al., 2008). Alternatively, GCMs simulate climate dynamics of the Earth System, by solving atmospheric conservation equations, and often include some driving force such as measured sea surface temperatures, or alternatively a dynamical coupled ocean model. GCM output is often used to drive CTMs in past or future climate studies (Dameris & Jöckel, 2013).

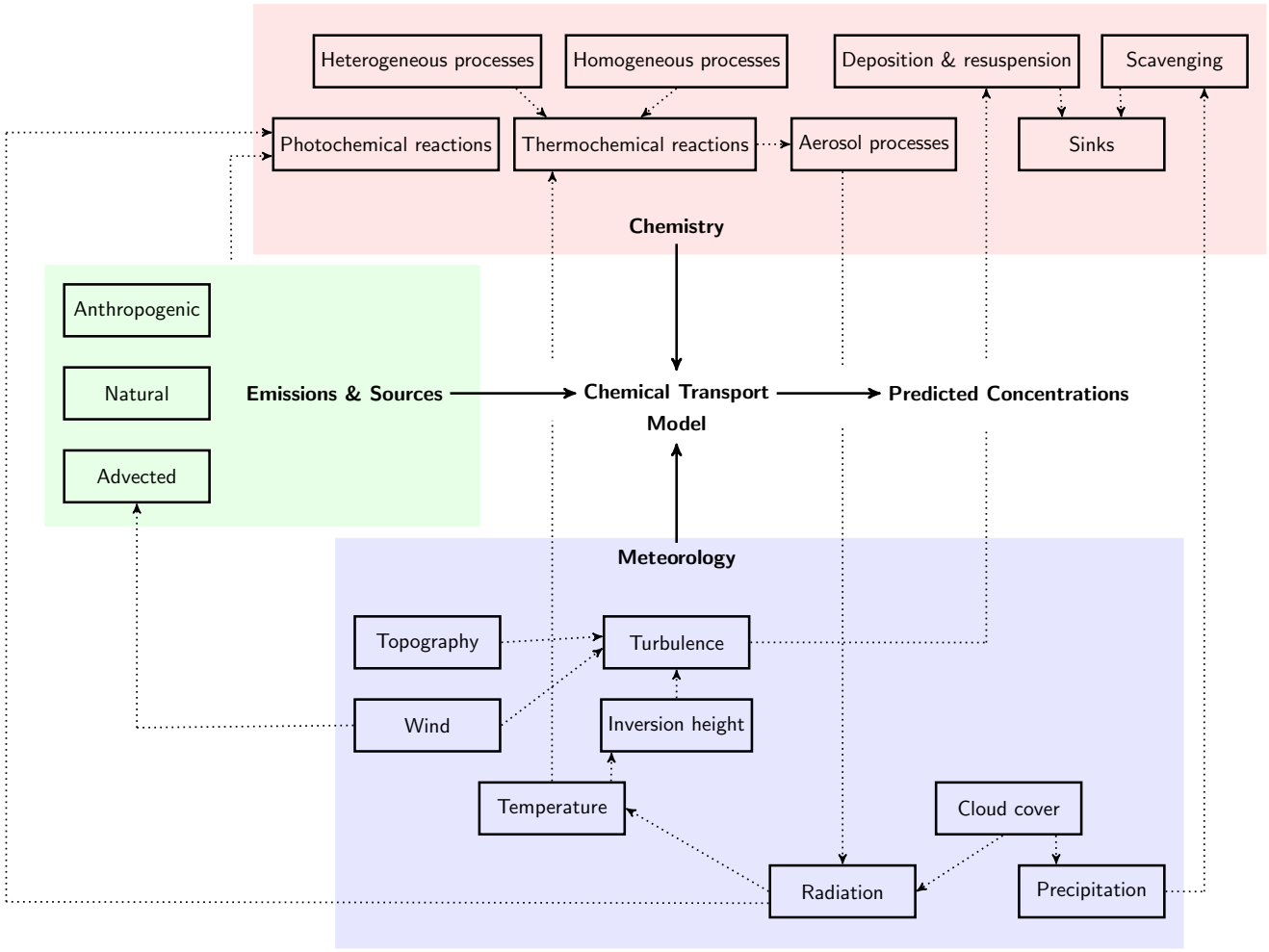

Figure 6.2.1: The three main components of a Chemical Transport Model: chemistry, emissions and meteorology. Dotted lined indicate links between subcomponents (displayed in outlined boxes). Diagram is adapted from (Seinfeld & Pandis, 2006b).

In addition to dynamics, CTMs incorporate the processes of chemical reactions and species emission and loss. CTMs contain condensed chemical schemes which are de-

rived from more complete mechanisms, such as those used in the box model Master Chemical Mechanism (MCM). In the MCM, chemical reactions rates are determined from numerous reported laboratory studies, and are updated regularly. CTMs often lump similar reactions together for computational expediency, and depending upon the application purpose.

The chemistry scheme may model one part of the atmosphere, such as the troposphere (as in GEOS-Chem) or the stratosphere (for example SLIMCAT), or the whole atmosphere (WACCM). As our knowledge of the chemical reactions taking place in the atmosphere grows, so do the chemical schemes of CTMs, and consequently the computational effort required. The main demand on computational resources is for solving the chemical reactions, therefore lumping of certain chemically related species is essential for completing simulations within an acceptable timeframe.

Emission data originates from inventories which are often compiled using "bottom up methods" of measuring emissions over smaller regions and scaling to the globe. In some cases, emissions are sub-modules which are coupled to physical parameters of the model such as temperature. Compiling emission inventories requires great effort, therefore inventories often corresponds to a base set of years, with scaling parameters used for years outside those covered by the inventory. Loss of a chemical species may be either chemical or physical deposition, the latter of which is a combination of chemistry and dynamics.

6.3 GEOS-Chem

GEOS-Chem (http://geos-chem.org/, originally described in Bey et al., 2001) is a 3D global CTM developed at Harvard University, USA. Several model configurations exist, and are used for different atmospheric applications. GEOS-Chem simulates tropospheric chemistry and may be run in tagged-tracer modes or as full-chemistry. Tagged-tracer modes allow faster computational times by focusing on a small group of trace gases. Tagged tracer runs are valuable for investigating transport and source apportionment of a particular species or family of trace gases, of which the chemistry is easily parametrisable. Main chemical fields such as the hydroxyl radical are read in from archived full-chemistry output. Tagged versions exist for CO_2, CH_4, CO, O_X, HCN, mercury and aerosols. Adjoint model configurations also exist for tagged modes, and may be used to constrain surface fluxes. Full chemistry includes extensive ozone-HO_X-

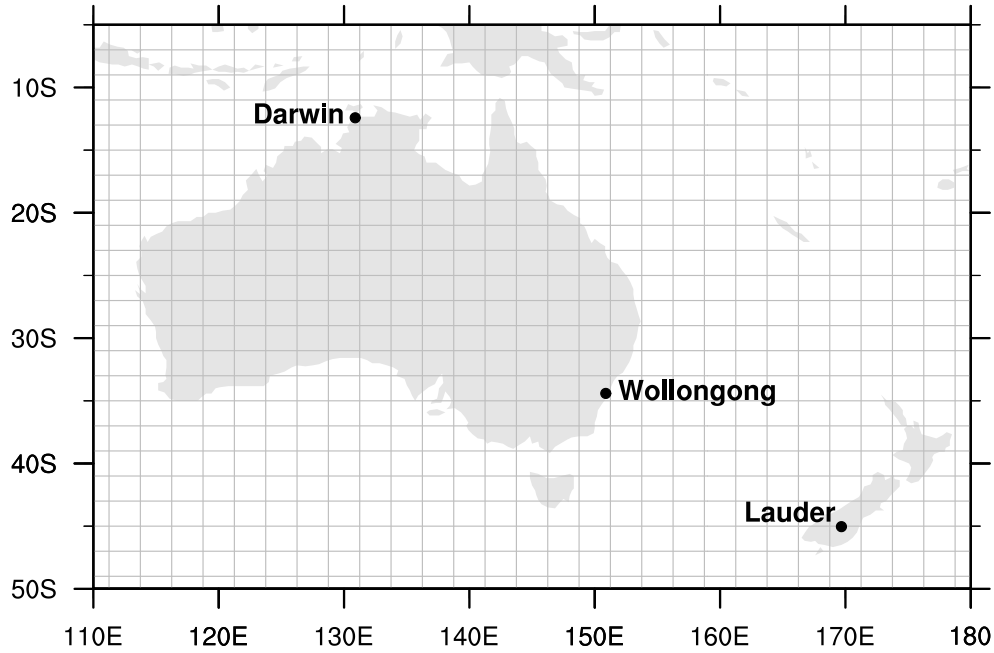

(a) Horizontal resolution over Australasia for 2°× 2.5° GEOS-Chem simulation.

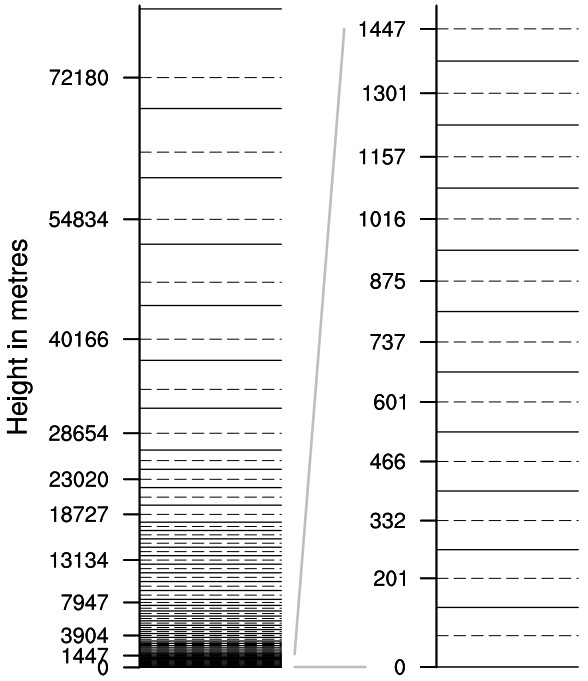

(b) Example vertical resolution over Wollongong for the 47 level reduced vertical layer GEOS-Chem set-up, level centres are indicated. Left shows all 47 levels to 80 km and right indicates levels within the planetary boundary layer.

Figure 6.3.1: GEOS-Chem resolution.

NO_X-hydrocarbon chemical reactions and exists as a standard version or with extensions to isoprene chemistry, dicarbonyl compounds, or secondary organic aerosols. The more comprehensive chemistry requires increased computational power. Full chemistry mode is useful for interpreting measurements and understanding the complex interactions of atmospheric reactive gases.

This study used GEOS-Chem v8-03-01 in full-chemistry configuration. The reduced 47 hybrid eta vertical level grid was used (up to approx. 80 km), which simplified the native GEOS-5 vertical resolution of 72 levels by merging stratospheric levels above ∼17 km, in order to increase computational efficiency. Horizontal resolution was 2°× 2.5° globally. Examples of these gridspaces are shown in Figure 6.3.1. A lower resolution of 4°× 5° was used for some preliminary studies to determine optimum model parameter set-up, of which the chemistry settings are further discussed in this Chapter (Section 6.3.4). Higher resolution nested grids exist only for China, North America and Europe, therefore were not used here.

6.3.1 Dynamics

The model used assimilated meteorological fields provided by the Goddard Earth Observing System (GEOS) within the NASA Global Modeling and Assimilation Office (GMAO, http://gmao.gsfc.nasa.gov/). Specifically, GEOS-5 meteorological fields were used, which were produced using the GEOS Data Assimilation System (GEOS-DAS), with GEOS5-GCM version 5.2.0 (Rienecker et al., 2008). Native resolution of GEOS-5 fields is 0.5°× 0.67° horizontal with 72 vertical hybrid levels. These were reduced to 2°× 2.5° horizontal with 47 levels for use in GEOS-Chem. Time resolution of GEOS-5 dynamic fields is generally 6 hours with 3 hours for surface fields and mixing depths.

Advection in GEOS-Chem is named TPCORE and follows the semi-Lagrangian algorithm developed in Lin & Rood, 1996, in line with that used in the GEOS5-GCM. Convective transport in GEOS-Chem was supplied by the meteorological archive, and convective mass flux was computed according to Wu et al., 2007. A non-local planetary boundary layer mixing scheme was used, based on the scheme in Holtslag & Boville, 1993, and implemented in GEOS-Chem by Lin & McElroy, 2010.

6.3.2 Emissions

GEOS-Chem includes a comprehensive set of the latest emission inventories for different sectors. Emission inventories cover four major areas: anthropogenic, biofuel, biomass burning, and biogenic; with smaller contributions from aircraft, shipping, lightning, ocean and volcanic sectors. The range of total global average emissions over 2004-2009 from GEOS-Chem in this study are shown for the trace gases of interest in Table 6.3.1. A summary of emission inventories used in this work follows.

Table 6.3.1: Range of total global annual emissions for species of interest in GEOS-Chem v8-03-01 for years 2004-2009.

	Trace Gas Emissions (Tg (species) a^{-1})				
	CO	**HCHO**	**C_2H_6**	**isoprene**	**NO_X**
Total	943–1139	4.1–5.7	17–20	443–506	46–47 (Tg N)

Anthropogenic: Anthropogenic emissions include sources from both fossil fuel and biofuel use. Default anthropogenic emissions were defined by global inventories. In particular the EDGAR 3.2-FT2000 inventory (Emissions Database for Global Atmospheric Research, (Olivier et al., 2005)) defined default CO, $NO_X$and, SO_2 for the year 2000 and the GEIA inventory (Global Emissions InitiAtive, (Wang et al., 1998; Bouwman et al., 1997)) defined NMVOC and ammonia emissions. Default global biofuel emissions were from Yevich & Logan, 2003. Default anthropogenic inventories were scaled for subsequent years based on the method in van Donkelaar et al., 2008, which makes use of government statistical and economic data. Additionally, default inventories were overwritten where improved and more recent inventories were available. Specifically, updated emission inventories were used for the US (EPA/NEI2005) that was regridded from the $0.04° \times 0.04°$ product available at `ftp://aftp.fsl.noaa.gov/divisions/taq/emissions_data_2005`, Canada (The Criteria Air Contaminants, CAC, `http://www.ec.gc.ca/inrp-npri/`), Mexico (Big Bend Regional Aerosol and Visibility Observational study, BRAVO, (Kuhns et al., 2003)), Europe 1990 - 2005 (European Monitoring and Evaluation Programme, EMEP, (Vestreng et al., 2007)), and China and Southeast Asia (Streets2000: (Streets et al., 2003, 2006) Streets2006, a.k.a. INTEX-B: (Zhang et al., 2009)). Anthropogenic carbon-based aerosols (BC/OC) were also emitted in GEOS-Chem (Bond, 2007).

Biomass burning: Emissions due to biomass burning sources are included for 15 tracers: the reactive gases NO_X, CO, acetone, butanone, acetaldehyde, C_3H_8, HCHO, C_2H_6, lumped $\geq$C4 alkanes and lumped $\geq$C3 alkenes; the aerosol species SO_2, NH_3, BC and OC; and non-reactive CO_2. Biomass burning species are incorporated into GEOS-Chem for specific years using the Global Fire Emissions Database version 2 (GFED2) inventory in monthly resolution (van der Werf et al., 2009). Month resolution was chosen for consistency as it was available over the entire simulation time-period 2004-2009. GFED2 determines biomass burning emissions by incorporating satellite information of vegetation and fire activity, which is used to produce fuel load and burnt area. These results are then coupled with emissions factors for specific trace gases to produce gridded emissions data.

Biogenic: Biogenic VOC emissions for isoprene, monoterpenes, methyl butenol, acetone, and alkenes in GEOS-Chem were by default from the GEIA inventory. Some biogenic species were overwritten by results from the Model of Emissions of Gases and Aerosols from Nature (MEGAN v2.1, (Guenther et al., 1995, 2006; Sakulyanontvittaya et al., 2008), `http://bai.acd.ucar.edu/Megan/index.shtml`). In MEGAN, isoprene, monoterpenes, and methyl butenol emissions are computed using a combination of vegetation factors multiplied by a base emission rate (Equation 6.3.1).

$$E_{species} = E_0 \times \gamma_{CE} \times \gamma_{Age} \tag{6.3.1}$$

where E_0 = Base species emission rate, γ_{CE} = canopy environment factor and γ_{Age} = leaf age factor. The canopy environment factor was determined from temperature, light and leaf area, while the leaf age factor was a function of leaf area and temperature. Total emissions were consequently a function of temperature, solar radiation, leaf area index (LAI). MEGAN used surface air temperature and radiation for photosynthesis from the GEOS-5 meteorological fields and a MODIS-derived leaf area index product (Myneni et al., 2002, 2007). MEGAN was implemented into GEOS-Chem by Palmer et al., 2006 and Millet et al., 2008.

Others: Several additional contributions to NO_X emissions were accounted for, namely from aircraft (Wang et al., 1998); soil (Yienger & Levy, 1995; Wang et al., 1998) and lightning (Sauvage et al., 2007).

Global shipping emissions are by default from EDGAR, overwritten by EMEP. Ship emitted SO_2 was overwritten by ARCTAS (based on (Eyring et al., 2005)). Emissions of SO_2 due to eruptive and non-eruptive volcanic activity are from the AEROCOM data base (http://www-lscedods.cea.fr/aerocom/AEROCOM_HC/) that was implemented into GEOS-Chem by Fisher et al., 2011.

6.3.3 Deposition

Physical loss of species follows several deposition algorithms to cover both dry and wet regimes. Dry deposition is calculated using meteorological fields of momentum, heat flux, temperature and solar radiation. The algorithm is based on the scheme presented by Wesely, 1989 and implemented in GEOS-Chem by Wang et al., 1998. Deposition velocity ($v_{d,i}$) for a species i follows the equation:

$$v_{d,i} = \frac{1}{R_a + R_{b,i} + R_{c,i}} \tag{6.3.2}$$

where total resistance is a sum of three sequential resistances, namely R_a - a surface resistance due to aerodynamic properties, $R_{b,i}$ - a quasi-laminar boundary resistance that depends on species atmospheric diffusivity and molecular properties, and $R_{c,i}$ - a resistance of species dependent interactions with the vegetation canopy. The dry deposition equation is analogous to electrical resistance, where instead of current the deposition velocity is inversely proportional to the resistance to deposition. That is, high resistance will give low deposition velocities, and low resistance will have high deposition rates.

Wet deposition in GEOS-Chem uses the meteorological fields for wet convection and precipitation to calculate trace gas and aerosol losses, described in depth in Liu et al., 2001, and Mari et al., 2000. Briefly, tracers may be scavenged either during deep convective episodes or during stratiform precipitation events, and the treatment of each is slightly different. As air is lifted in convective updrafts, a fraction of tracer ($f_{c,i}$) with in a grid box is lost according to the equation:

$$f_{c,i} = 1 - \exp\left[-k_i \frac{\Delta z}{\omega}\right] \tag{6.3.3}$$

where k_i is tracer specific loss rate, Δz is vertical distance travelled and ω accounts for vertical velocity. Tracer specific loss rates (k_i) are calculated as a fraction of the rate

of cloud to precipitation conversion, and depend on phase partitioning of the tracer, which is determined using Henry's Law.

Comparatively, stratiform precipitation events incur a first-order scavenging of tracers, and depend upon precipitation rates, following equation 6.3.4.

$$f_{p,i} = f(1 - \exp[-k_i \Delta t]) \tag{6.3.4}$$

Where $f_{p,i}$ is the fraction of trace gas scavenged, f is horizontal fraction of a grid box undergoing precipitation determined at the top of a grid-box, k_i is the tracer specific loss rate, as defined for Equation 6.3.3, and Δt represents the model time step. This method also accounts for release of tracer due to evaporation.

6.3.4 Chemistry

The full-chemistry version of GEOS-Chem includes comprehensive tropospheric ozone-HO_X-NO_X-hydrocarbon chemistry. The standard configuration simulates chemistry for 102 species with 43 of these advected (see Table 6.3.2). Modelled chemical mechanisms were originally described in Bey et al. 2001.

GEOS-Chem v8-03-01 standard full-chemistry included 230 gas phase and 48 photolysis reactions. Interaction between trace gases and aerosols is accounted for in terms of the effect on photolysis rates (Martin et al., 2003), heterogeneous chemistry (Jacob, 2000), and gas-aerosol partitioning (reversible: (Liao et al., 2007; Henze & Seinfeld, 2006; Henze, 2008), irreversible: (Fu et al., 2008; Evans & J., 2005)). Sea-salt and dust aerosols were both modelled online (Alexander et al., 2005; Fairlie et al., 2007).

Chemical mechanisms were updated to the most recent JPL/IUPAC reaction rates. Numerical integration was performed over a 30 minute time-step using the KPP solver with Rosenbrock method (Damian et al., 2002), implemented into GEOS-Chem by Eller et al., 2009. Rates of photolysis were calculated using Fast-J code (Wild et al., 2000), implemented into GEOS-Chem by Mao et al., 2010.

GEOS-Chem is mainly used to simulate tropospheric chemistry. However, stratospheric chemistry and atmospheric processes were parameterised in order to account for stratosphere-troposphere exchange and consequently those trace gases that have sources or losses in the stratosphere. Simplified stratospheric chemistry incorporated parameterised loss of tropospheric tracers and included a tropospheric NO_Y source.

Simulation of stratospheric ozone follows the linearized ozone (or Linoz) algorithm of McLinden et al., 2000.

Table 6.3.2: Advected tracers in GEOS-Chem standard and isoprene mechanisms. Tracers of interest in this thesis are highlighted in red. Emitted traces are indicated with a Y.

Standard Mechanism Advected Tracers							
	Tracer	**Formula /Definition**			**Tracer**	**Formula /Definition**	
1	NOx	NO_2, NO, NO_3, HNO_2	Y	23	HNO4	HNO_4	
2	Ox	$O_3, NO_2, 2NO_3$	Y	24	MP	CH_3OOH	
3	PAN	$CH_3C(O)OONO2$		25	DMS	$(CH_3)_2S$	
4	CO	CO	Y	26	SO2	SO_2	Y
5	ALK4	$\geq C_4$ Alkanes	Y	27	SO4	SO_4	Y
6	ISOP	C_5H_8	Y	28	SO4s	SO_4 on sea-salt aerosol	
7	HNO3	HNO_3	Y	29	MSA	CH_3SO_3H	
8	H2O2	H_2O_2		30	NH3	NH_3	Y
9	ACET	$(CH_3)_2CO$	Y	31	NH4	NH_4	
10	MEK	$CH_3C(O)CH_2CH_3$	Y	32	NIT	Inorganic nitrates	
11	ALD2	CH_3CHO	Y	33	NITs	NIT on sea-salt aerosol	
12	RCHO	$\geq C_3$ Aldehyde		34	BCPI		
13	MVK	$CH_3C(O)CHCH_2$		35	OCPI	Carbon aerosol	Y
14	MACR	$CHOC(CH_2)CH_3$		36	BCPO		
15	PMN	$CH_2C(CH_3)C(O)OONO_2$		37	OCPO		
16	PPN	$CH_3CH_2C(O)OONO_2$		38	DST1		
17	R4N2	Alkyl Nitrate		39	DST2	Dust aerosol	
18	PRPE	$\geq C_3$ Alkenes	Y	40	DST3		
19	C3H8	C_3H_8	Y	41	DST4		
20	CH2O	CH_2O	Y	42	SALA	Sea salt aerosol	
21	C2H6	C_2H_6	Y	43	SALC		
22	N2O5	N_2O_5					

Isoprene Mechanism Additional Advected Tracers		
	Tracer	**Formula /Definition**
44	HCOOH	HCOOH
45	ACTA	CH_3COOH
46	ISOPN	$CH_2C(CH_3)CH(ONO_2)CH_2OH$
47	MOBA	5C acid from isoprene
48	PROPNN	$CH_3C(O)CH_2ONO_2$
49	HAC	$CH_3C(O)CH_2OH$
50	GLYC	$CHOCH_2OH$
51	MMN	Nitrate from MACR + MVK
52	RIP	PeroxidefromRIO2
53	IEPOX	C_5H_8O Isoprene epoxide
54	PYPAN	Pyruvic acid PAN
55	MAP	$CH_3C(O)OOH$
56	AP	Grouped peroxides

Optimum chemistry scheme for isoprene

The original standard chemical scheme is described in Bey et al., 2001 with the isoprene oxidation scheme described by Horowitz et al., 1998. Recently, advances in knowledge about the photo-oxidation of isoprene (Paulot et al., 2009) were used to update the isoprene scheme in GEOS-Chem as a beta option for v8-03-01. Inclusion of the Paulot et al., 2009 Caltech isoprene oxidation mechanism introduced 36 new chemical species to GEOS-Chem, with 13 of these advected (listed in Table 6.3.2). Additionally, 114 new chemical and photochemical reactions were implemented.

Briefly, daytime oxidation of isoprene begins with addition of the OH radical at the 1 or 4 position (Equations 6.3.5 and 6.3.6 respectively). Resulting β or δ-hydroxyl peroxy radicals are converted under high NO_Xconditions to formaldehyde, methylvinylketone (MVK) and methacrolein (MACR) for the β case and δ-hydroxyl isoprene nitrates in the δ case. Under low NO_Xconditions, isoprene peroxy radicals can either react with HO_2 to form isoprene hydroxyperoxides, or proceed via an isomerisation to hydroperoxyaldehydes and consequently be 100% photolysed yielding among other products, HCHO (Mao et al., 2013). Oxidation products undergo further oxidation. Full details of the new isoprene chemical scheme, as used in this study, can be found at `http://wiki.seas.harvard.edu/geos-chem/index.php/New_isoprene_scheme_prelim`.

First step in the Caltech Isoprene Oxidation Scheme

$$C_5H_8 + OH + O_2 \longrightarrow CH_2CHC(CH_3)(OO^-)CH_2OH \qquad 71\% \qquad (6.3.5)$$

$$C_5H_8 + OH + O_2 \longrightarrow CH_2(OH)CHC(CH_3)CH_2OO^- \qquad 29\% \qquad (6.3.6)$$

Isoprene was not a directly targeted trace gas for this study of the Australasian troposphere. Atmospheric isoprene degrades rapidly, having a lifetime of 2 to 5 hours (Warneck & Williams, 2012). Oxidation of isoprene affects atmospheric OH levels and is a major source of HCHO. Isoprene oxidation additionally produces CO (Wayne, 2000). Therefore, a change in isoprene chemistry may affect trace gases targeted in this thesis, either directly through changes in source amounts, or indirectly through affecting atmospheric oxidation potential. Hence, amounts of trace gases of interest in this study, namely CO, HCHO and C_2H_6 may be altered by using different isoprene chemical schemes in GEOS-Chem. In order to quantify the effect of isoprene chemistry on other trace gases, a comparison between two model runs was performed.

GEOS-Chem was run over 2004 to 2009, implementing the standard chemical mecha-

nism. A separate run was performed using the Caltech isoprene chemistry. Run parameters between GEOS-Chem simulations were identical apart from isoprene oxidation chemical scheme. In particular, isoprene emissions were identical between runs, therefore any difference between isoprene composition results was solely due to differences in the chemical scheme. Simulations were performed on 4×5° resolution on reduced 47 vertical layers, chosen for computational expediency. Meteorology followed GEOS-5 reanalysis fields and emissions were taken from inventories as previously described 6.3.2. Monthly averaged total column values were compared between simulations, for isoprene and the trace gases CO, HCHO and C_2H_6, at three Australasian sites Wollongong, Darwin and Lauder. Modelled results were saved as 24-hour average mole fraction vertical profiles, on 47 level vertical resolution. Modelled profiles were converted into total column values by pressure weighted integration, using programs developed in Perl and NCL, and as described in Appendix D. Subsequently, modelled daily total column values were averaged over each month. Surface values were also investigated for isoprene.

Isoprene emissions in GEOS-Chem originate only from biogenic sources. Yearly global isoprene emissions in GEOS-Chem vary between: 426 TgC (484 Tg isoprene) to 486 TgC (552 Tg isoprene). Figure 6.3.2 indicates the yearly and seasonal variation in month averaged isoprene emissions. Isoprene emissions are plotted both globally and in the Australasian region over 2004 to 2009. Biogenic isoprene emissions are proportional to light and heat, therefore Australasian emissions peak in Austral summer. In contrast, global emissions are dominated by the influence from Northern Hemisphere summer. Photochemical reaction rates also scale with light intensity, and were therefore expected to have major contributions to isoprene chemistry at Australasian sites during Austral summer.

Results of monthly averaged isoprene total column values are plotted in Figure 6.3.3 for Wollongong. Total column values from the simulation that included the Caltech isoprene mechanism are lower than the standard simulation, indicating that more isoprene has reacted via oxidation in the new simulation. Greatest difference between runs occurs during Austral summer, as expected, due to the maximum influence of a combination of isoprene emissions and photochemical oxidation. Seasonality is unchanged between runs, reflected by a correlation coefficient of 0.997.

An alternate method of viewing the total column values between simulations is to calculate a difference between month average values. Differences were calculated by subtracting the result from Caltech simulation from the standard simulation. Difference

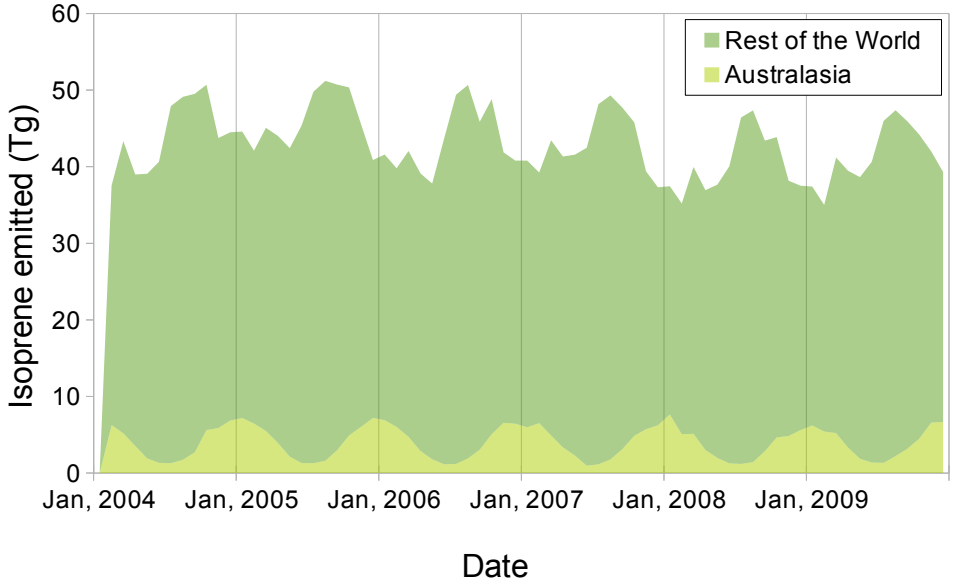

Figure 6.3.2: Global and Australasian monthly isoprene emissions in GEOS-Chem. Curve area is cumulative.

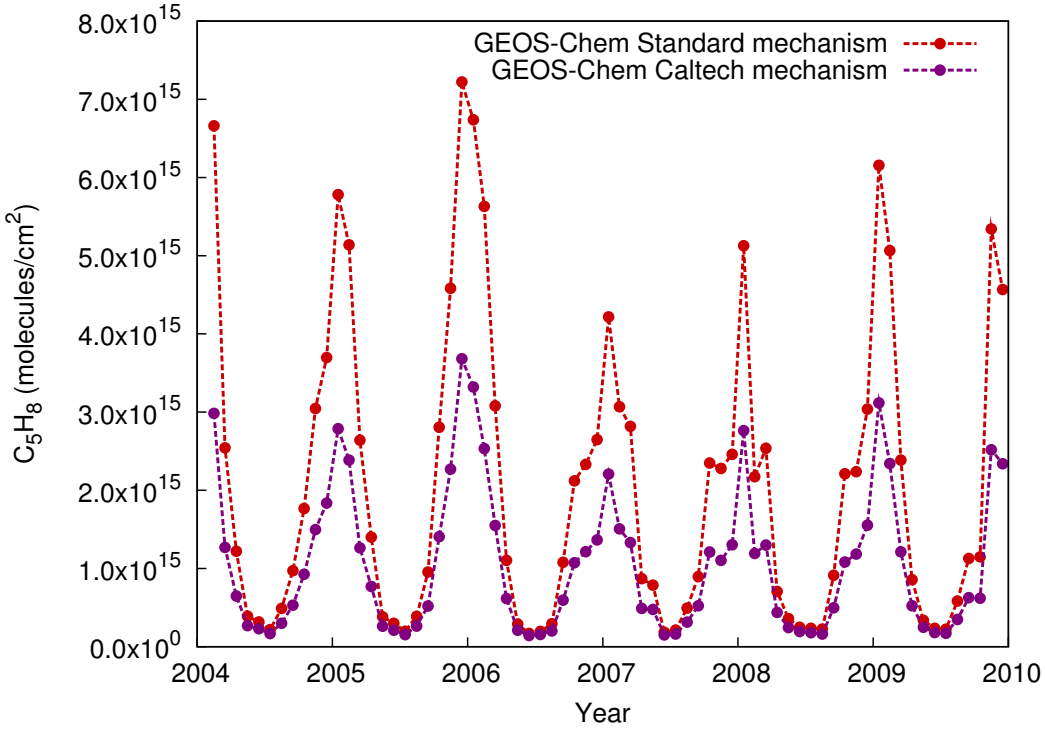

Figure 6.3.3: Isoprene monthly total column values for both model runs at Wollongong.

between total column values for isoprene at each location are shown in Figure 6.3.4. The top panel in Figure 6.3.4 re-iterates that maximum difference at Wollongong is seen between runs during Austral summer, with an average difference of 50%. Darwin in the middle panel also indicates higher isoprene column in the standard simulation with a 50% difference between runs. However, there is no clear seasonality. Little seasonality in the difference at Darwin is a reflection of the site being close to the equator and therefore receiving smaller variations in incoming solar radiation. Reduced variation in solar radiation feeds into reduced variation in light and heat, drivers of the isoprene seasonal cycle. Difference in isoprene total column values at Lauder (lower panel, Figure 6.3.4) follows a similar pattern to Wollongong, but to a much smaller magnitude, with only 30% difference between runs. Reduced difference at Lauder is a reflection of the lower influence of isoprene at a more remote site. Similar differences for isoprene surface values were seen (Figure in Appendix, E.0.6), with greater average differences of 60% at Wollongong and Darwin and 40% at Lauder.

Atmospheric measurements of isoprene are limited, particularly in the Southern Hemisphere. However, in order to ascertain the version of GEOS-Chem chemistry that produces more accurate results, new measurements from a SIFT-Mass Spectrometer were used. Surface measurements of isoprene were obtained at Wollongong, from March 23 to March 25, 2012 (private communication, Elise-Andreé Guerette). GEOS-Chem average seasonal cycle of surface level mole fraction over 2004 to 2009 was determined for each run and plotted against SIFT measurements (Figure 6.3.5). This preliminary comparison indicated improved comparison between model and measurements for the Caltech isoprene scheme with respect to surface values at Wollongong in March. However, more measurements both at Wollongong and other sites are certainly required to confirm the improved accuracy in isoprene results moving from standard to Caltech isoprene schemes.

In addition to changes in isoprene, the response in other trace gases to a change in isoprene chemistry was determined. Differences for CO total column were determined at the three sites (Figure 6.3.6). All locations show on average approximately 4% reduction in total column CO, moving to the Caltech scheme. Seasonality of total column values between runs does not change, indicated by correlation values 0.994–0.998. Seasonality in the difference is again most prominent at Wollongong and Lauder. Maximal difference in CO occurs before the maximum difference in isoprene, suggesting a more complex relationship linking these trace gases. That is, influence over CO is not exclusively related to a reduction in CO source from a reduction in isoprene. Influences

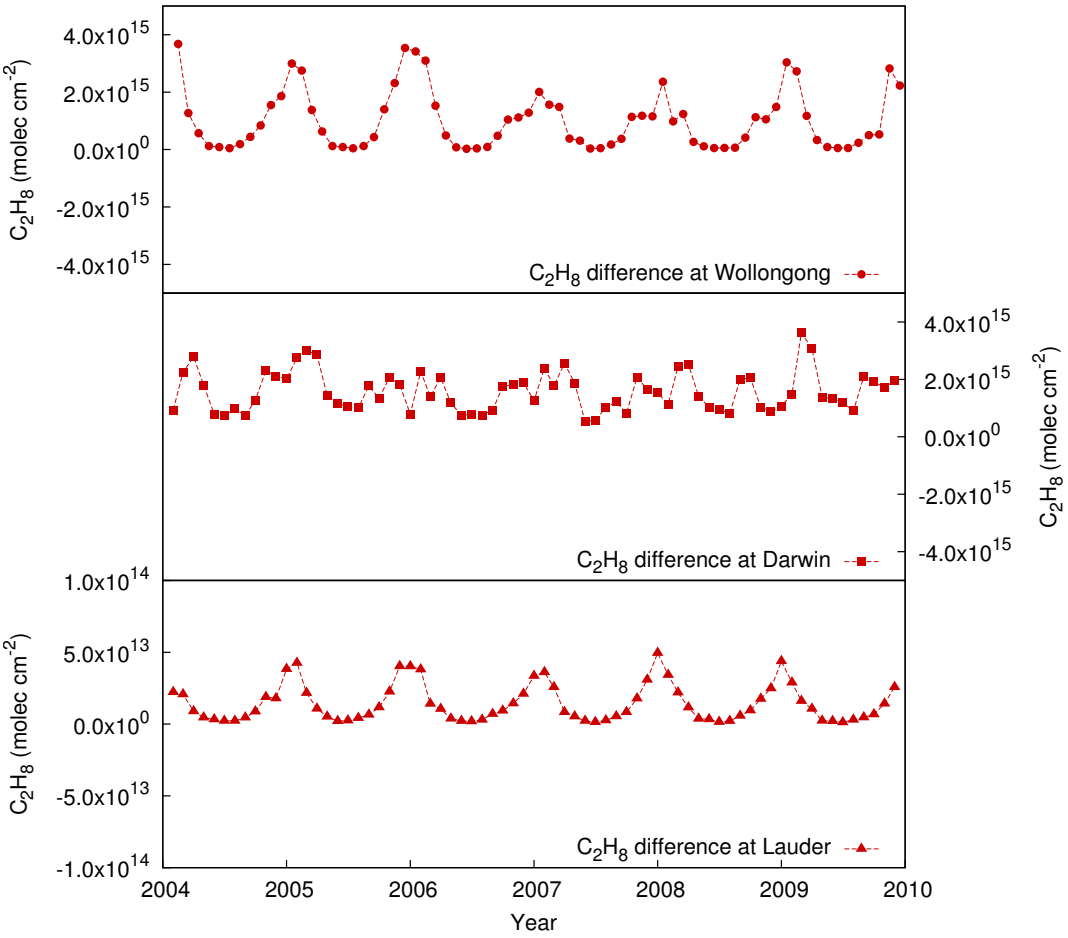

Figure 6.3.4: Differences between isoprene monthly total column values for standard and Caltech isoprene oxidation schemes.

are likely from other indirect links such as through the hydroxyl radical.

Differences were also determined for HCHO (Appendix, Figure E.0.7) and C_2H_6 (Appendix, Figure E.0.8). Differences in HCHO between model runs at Wollongong and Darwin follows a similar seasonal pattern to isoprene differences at these sites, indicating differences in the isoprene oxidation scheme is a major source for HCHO differences. Interestingly, while HCHO decreases (∼5%) at Wollongong and Darwin for the Caltech scheme, an increase is seen at Lauder (∼11%). Also, the seasonality of HCHO differences at Lauder is the inverse of isoprene. Increase for Lauder HCHO reflects the remote nature of the site and the tendency to follow low NO_Xchemistry, rather than high NO_Xas in Wollongong and Darwin. C_2H_6 shows limited seasonality in differences and an average 10% reduction in total column moving to the Caltech scheme.

Average monthly standard deviations were used to evaluate the significance of differ-

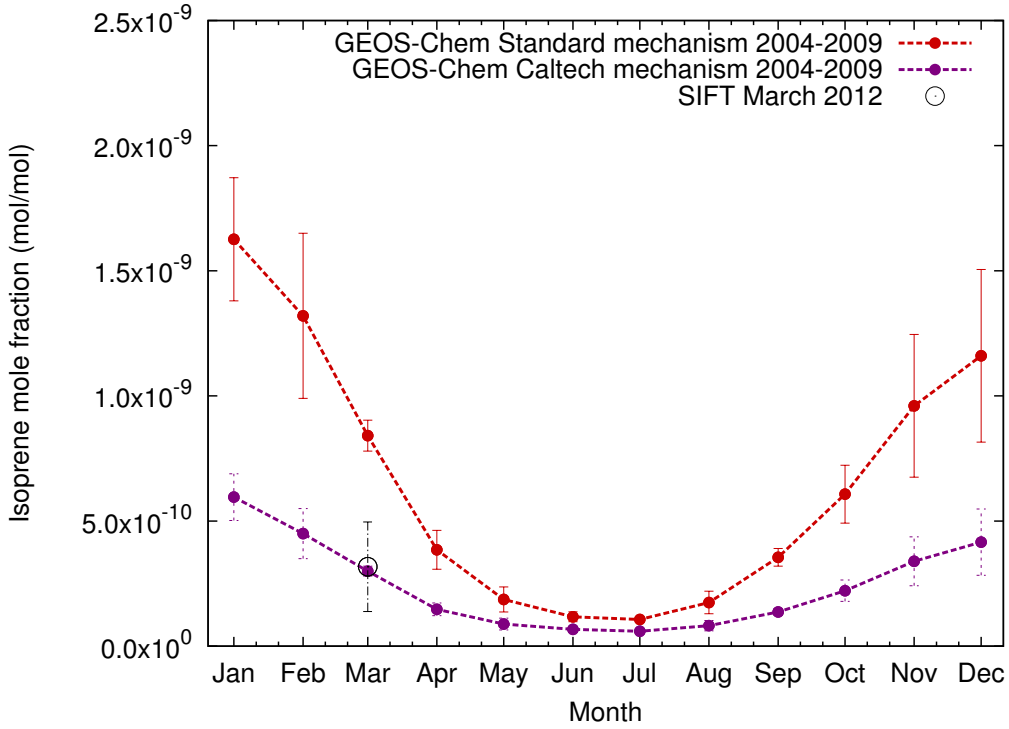

Figure 6.3.5: Isoprene, seasonal surface mole fraction.

ences induced in trace gases by a change in isoprene chemistry. Those values lying outside one standard deviation were defined to be significant changes. While not a rigorous statistical test, this method gives an idea of whether the isoprene chemistry mechanism has a major influence on the other trace gases. A summary of average differences, both absolute values and percentages of the mean total column or surface value are collated in Table 6.3.3. Also collated in Table 6.3.3 are average monthly standard deviations relating to total column values (and surface values for isoprene) for comparison. Finally, in Table 6.3.3, correlation coefficients are recorded. High correlations indicated no change in seasonality was observed between runs for any trace gas studied here.

Isoprene total column and surface differences, are approximately two to three times the 1σ, meaning changes in isoprene are highly significant. CO total column mean differences (4.8×10^{16} to 6.7×10^{16}) are approximately an order of magnitude lower than 1σ (1.3×10^{17} to 2.0×10^{17}), therefore changes were determined not highly significant. At Wollongong and Darwin, HCHO differences are also an order of magnitude below 1σ, and are insignificant. At Lauder, the increase in HCHO column for the Caltech scheme lies just outside 1σ. This indicates changes in modelled HCHO in the Caltech

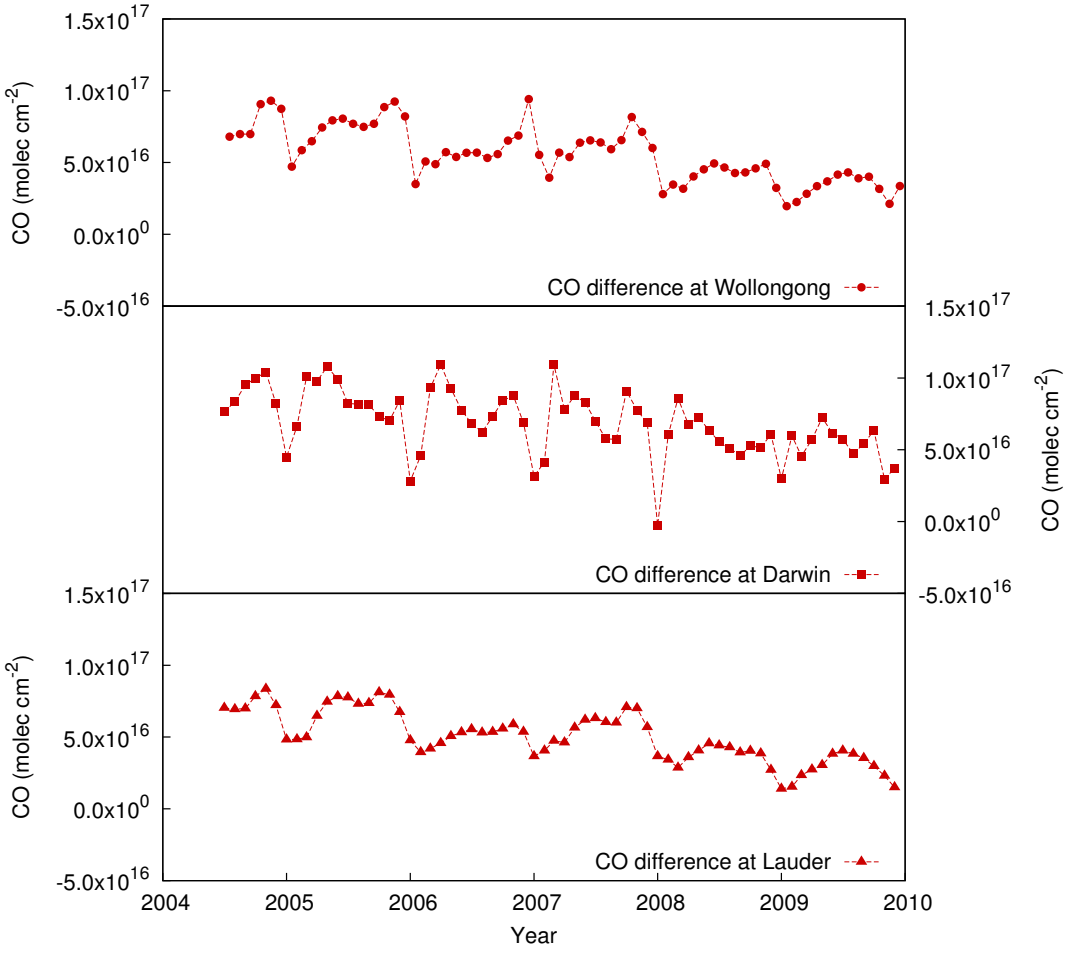

Figure 6.3.6: Carbon monoxide monthly total column differences between chemical schemes.

simulation scheme could be significant for Lauder and other remote areas. Care must be taken when analysing this HCHO with respect to measurements in remote regions. C_2H_6 differences at all sites are of the same magnitude as, but below, 1σ, therefore deemed insignificant.

Overall, a significant change in total column and surface isoprene was seen after including the new Caltech isoprene oxidation chemical scheme into GEOS-Chem. The new scheme is likely to have improved isoprene results, as suggested by preliminary comparison with measurements at Wollongong. However, the implied improvements in model representation of isoprene need to be confirmed by study with more measurements over longer time periods and over greater spatial extent in the Australasian region.

Generally, no large influence was observed for total column values of other trace gases

Table 6.3.3: Mean differences (absolute value and percentage) between standard and Caltech isoprene scheme GEOS-Chem simulations for total column values and isoprene surface values. Correlation coefficients between simulations indicate no change in seasonality. Differences outside an average total column month one σ are indicated in red.

	Trace Gas				
	CO	HCHO	C_2H_6	C_5H_8	C_5H_8 surface
Wollongong					
Mean difference	5.6×10^{16}	4.7×10^{14}	2.2×10^{15}	1.0×10^{15}	4.10×10^{-10}
Percent of average value	4.1%	5.2%	11%	49%	63%
Mean average month 1σ	2.0×10^{17}	3.1×10^{15}	6.1×10^{15}	5.6×10^{14}	1.4×10^{-10}
Correlation Coefficient	0.997	0.999	0.993	0.997	0.997
Darwin					
Mean difference	$6.7\times10^{16\dagger}$	5.5×10^{14}	$1.8\times10^{15\dagger}$	1.6×10^{15}	8.07×10^{-10}
Percent of average value	4.2%	4.6%	14%	47%	58%
Mean average month 1σ	1.5×10^{17}	1.9×10^{15}	2.1×10^{15}	7.1×10^{14}	2.7×10^{-10}
Correlation Coefficient	0.994	0.982	0.991*	0.976	0.977
Lauder					
Mean difference	$4.8\times10^{16\dagger}$	2.3×10^{14}	$2.0\times10^{15\dagger}$	1.4×10^{13}	2.11×10^{-11}
Percent of average value	3.9%	11%	10%	22%	41%
Mean average month 1σ	1.3×10^{17}	1.8×10^{14}	3.9×10^{15}	9.7×10^{12}	9.9×10^{-12}
Correlation Coefficient	0.998	0.995	0.996 *	0.999	0.997

† Mean difference taken from 2005 to 2009 to avoid spin-up influences.
* Correlation taken from July 2004 to 2009 to avoid spin-up influences.

CO, HCHO and C_2H_6, with the exception of HCHO at Lauder and possibly other remote sites. Therefore, either version of the model may be chosen to be used for further study of total column of these trace gases. The standard mechanism was chosen for computational expediency and due to previous validation of v8-03-01 by the GEOS-Chem community. However, it is recommended to move to the Caltech scheme when implementing a newer version of the model at Wollongong. The Caltech scheme is now standard in current versions of GEOS-Chem. According to this comparison, CO, HCHO and C_2H_6 should remain minimally affected by the isoprene mechanism in an updated GEOS-Chem version.

6.4 Earth System Models

Earth System Models (ESMs) aim to consider multiple feedback processes between bio-geochemical and physical processes of earth. The general atmospheric processes dynamics, emissions, losses and chemistry are modelled in an ESM, including links between other components. For example, changes in atmospheric composition due to chemistry are fed back into the radiative transfer module to affect atmospheric heating and consequently dynamics. In addition to the general components, processes such as land-surface exchange, ocean bio-geochemistry, sea ice and radiative transfer are explicitly modelled and included using coupling methodology (Dameris & Jöckel, 2013).

Modelling interconnections and feedbacks between components is a more accurate representation of atmospheric processes, and has the potential to be a powerful tool for understanding drivers of atmospheric composition. However, the increasing complexity in ESMs means that model output is increasingly difficult to understand. Attributing causes of determined outcomes can become a difficult task. Therefore, consideration needs to be made whether using a fully-coupled ESM will answer a particular hypothesis. In fact, a single component of an ESM may be sufficient for testing a hypothesis, thereby reducing both computation time and complexity of output (Dameris & Jöckel, 2013).

6.5 ACCESS

One such Earth System model being developed is the Australian Community Climate Earth System Simulator, or ACCESS. Development is a joint project between the Australian Bureau of Meteorology and the Commonwealth Scientific and Industrial Research Organisation (CSIRO) [http://www.accessimulator.org.au/]. The project aims to develop a fully coupled ACCESS model within an Australian context, that is capable of both numerical weather prediction and climate modelling.

During this study, ACCESS was in an early development stage, and was consequently run in atmosphere-only mode. Components in ACCESS were based on established models, and were further developed by Australian researchers. A diagram indicating all planned modules of ACCESS is presented in Figure 6.5.1. A full description of the basis models for ACCESS dynamics and chemistry modules can be found in O'Connor et al., 2013. Here, a brief summary is given of configuration of ACCESS modules

relevant for this study, specifically the UKCA atmospheric chemistry module coupled with MetUM 7.3 atmospheric dynamics.

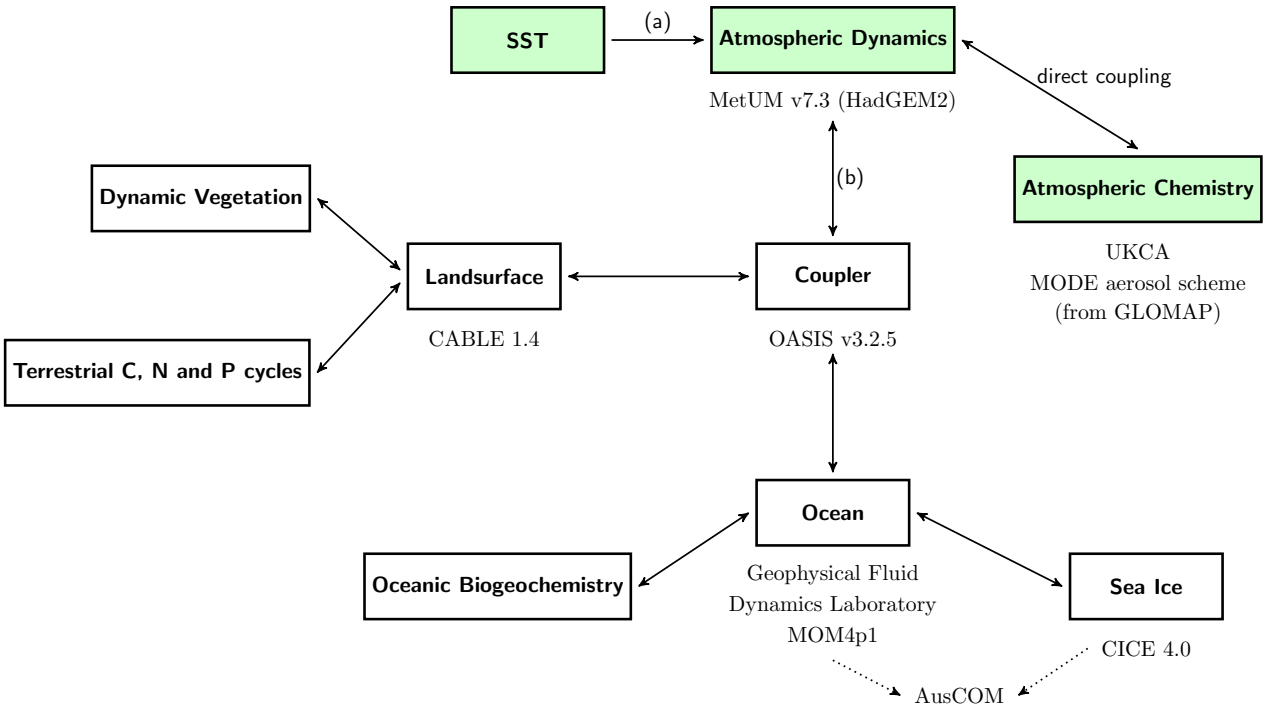

Figure 6.5.1: Earth system components to be included as explicit modules in ACCESS. Figure is adapted from Puri, K., 2005. MetUM may be driven by (a) sea surface temperature measurements (SST) or (b) fully coupling with an ocean model. Green shading indicates components of ACCESS used in this study.

ACCESS is a global 3D model with horizontal resolution 1.875°x 1.25° and 38 vertical levels (up to approx. 40 km). Examples of these gridspaces are shown in Figure 6.5.2.

6.5.1 Dynamics

ACCESS transport was driven by the Global Circulation Model (GCM) component that was based on the United Kingdom Meteorological Office Unified Model [MetUM version 7.3, (Johns, 1997)] and used in HadGEM2 configuration (Martin et al., 2010). The GCM component may be driven by sea surface temperature measurements, or by fully coupling with an ocean model. Here, prescribed sea surface temperatures were used to drive the ACCESS GCM. ACCESS GCM and chemistry were run interactively, where MetUM simulations were coupled with UKCA such that dynamics directly fed into the

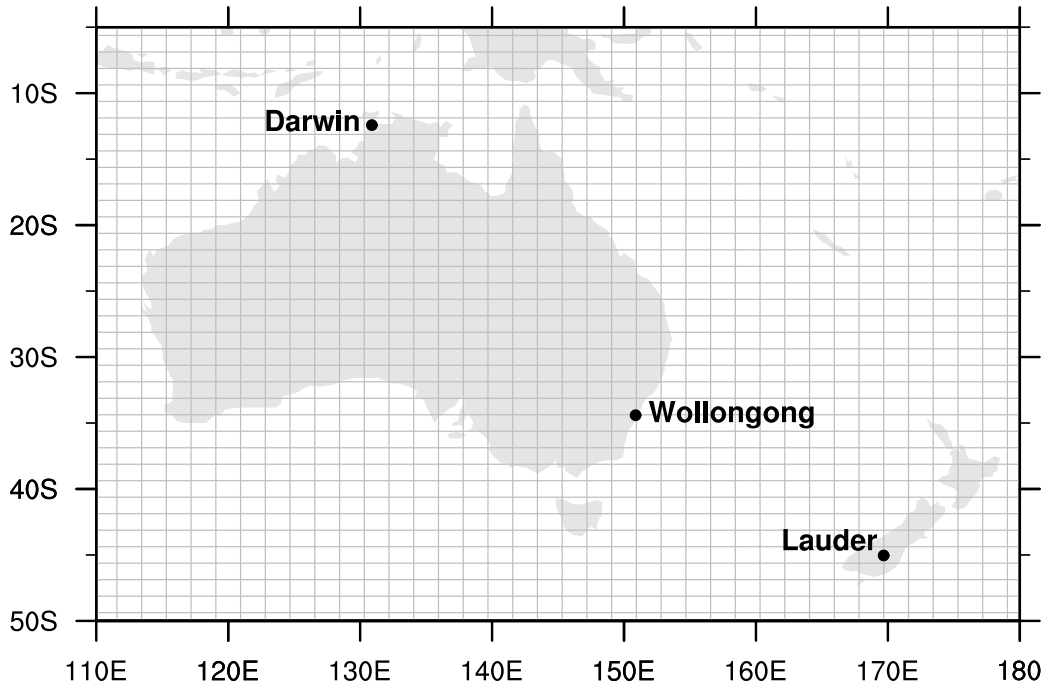

(a) Horizontal resolution over Australasia for 1.25°× 1.875° ACCESS simulation.

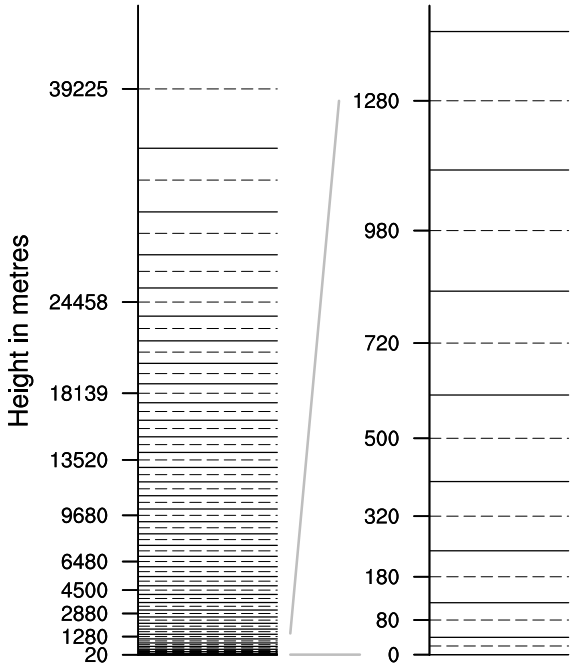

(b) Example vertical resolution over Wollongong for the 38 vertical layer ACCESS set-up. Left shows all 38 levels to 45 km and right indicates levels within the planetary boundary layer.

Figure 6.5.2: ACCESS resolution.

chemistry module. Although coupling was activated, not all feedback mechanisms were turned on during this preliminary phase.

Within the chemistry module, large-scale advection, convection, and boundary layer mixing is supplied by the GCM. Specifically, tracer advection follows semi-Lagrangian treatment as in Davies et al., 2005 and is conservative, monotonic and accurate, based on the scheme in Leonard et al., 1995. Moist and dry convection follows the mass flux scheme in Gregory & Rowntree, 1990. Boundary layer mixing follows the turbulent mixing scheme of Lock et al., 2000.

6.5.2 Emissions

The standard tropospheric scheme included eight emitted species, generally as monthly mean emissions in kg (species) m^{-2} s^{-1}. Global annual emissions for ACCESS in 2000 are tabulated in Table 6.5.1. Emissions were based off the UKCA dataset and are similar to those used in Zeng & Pyle, 2003, which were interpolated to a higher model grid-resolution. Seasonally varying emissions were held constant at year 2000 values and were based on IPCC Special Report on Emissions Scenarios (SRES) A2 emission scenario for year 2000 (Nakićenović et al., 2000). Constant year emissions, while unable to model inter-annual source variability, allows the modelling of a climatological background, which is influenced by climate-driven changes in dynamics.

Table 6.5.1: Global total annual emissions in ACCESS for year 2000.

	Trace Gas Emissions (Tg (species) a^{-1})							
	CO	**HCHO**	**C_2H_6**	**C_3H_8**	**Acetone**	**CH_3CHO**	**NO_X**	**CH_4**
Total	1800	14.2	16.3	16.3	49.2	0.31	45.0(Tg N)	511

Scenarios combine biomass burning with anthropogenic emissions as annual values. Therefore, biomass burning emissions required extraction and imparted seasonality. Seasonal partitioning factors for biomass burning were from Hao & Liu, 1994.

Emissions not defined or included by the SRES inventory were additionally incorporated. CO from isoprene oxidation was parameterised based off the global source of isoprene 503 Tg C a^{-1} (Guenther et al., 1995) and a global average 30% oxidation to CO (Pfister et al., 2008). Therefore, a total of 354 Tg CO a^{-1} was included from isoprene oxidation. Natural emissions of CH_4, such as from termites and water-soaked land-surfaces (e.g. wetlands) were taken from Fung et al., 1991. Emissions of HCHO,

C_2H_6 and C_3H_8 were defined from Piccot et al., 1992.

Three-dimensional NO_Xemissions were also included. Parameterisation of $NO_X$from lightning used GCM convection fields to calculate lightning NO_Xonline, implementing the same methodology as Price & Rind, 1994. Lightning NO_Xemission rates were scaled to give a final global annual total of 4 Tg (N) a^{-1}. Aircraft emissions were added, as a total of 0.7 Tg (N) a^{-1} (Zeng & Pyle, 2003).

6.5.3 Deposition

The chemical scheme covers loss of tracers via chemical processes. However physical loss is also possible in the atmosphere and is included in the model using deposition schemes for dry and wet regimes. ACCESS used the UKCA default dry deposition scheme, which is non-interactive and converts dry deposition velocities to rates via the equation:

$$\tau_d = v_d/h \tag{6.5.1}$$

where τ_d is dry deposition rate, v_d dry deposition velocity, and h is the lowest model level height. Dry deposition velocities (v_d) were previously determined and tabulated for use in the model. Velocities vary depending upon season, time of day and surface land-type. (Ganzeveld & Lelieveld, 1995; Sander & Crutzen, 1996). Using this method, dry deposition is only applied in the lowest model level.

ACCESS wet deposition was based on the scheme implemented in the TOMCAT CTM. Precipitation and convection fields from MetUM were used to calculate first-order loss rates in wet deposition (Giannakopoulos et al., 1999). The scavenging rate τ_w is described by:

$$\tau_w = S_j \times p_j(l) \tag{6.5.2}$$

where S_j is the scavenging coefficient for precipitation type j (convective or large-scale), and $p_j(l)$ is precipitation rate at level l, for precipitation j. Scavenging coefficients were scaled for each species by the fraction of species in the aqueous phase. Henry's Law was used to determine the fraction of a species in the aqueous phase. Specific parameters for wet scavenging calculations are given in O'Connor et al., 2013.

6.5.4 Chemistry

The ACCESS chemistry module was developed from the chemical transport model UKCA (United Kingdom Chemistry and Aerosols) [http://www.ukca.ac.uk]. Chemistry was run in standard tropospheric configuration (StdTrop), which was designed to include the major atmospheric chemical reactions. The reduced chemical scheme of StdTrop optimises computational requirements, allowing model runs over longer timescales. The scheme included 46 chemical species with 26 of these being advected (see Table 6.5.2). Species with constant atmospheric amounts are H_2, O_2, CO_2 and N_2. Water vapour was taken from MetUM at each timestep.

The chemistry scheme was developed based on the model TOMCAT (Law & Pyle, 1993) and includes major inorganic atmospheric chemistry together with methane, ethane and propane chemistry, overall in 129 reactions including 102 gas-phase and 27 photolysis reactions. Reaction rates are taken from the Master Chemical Mechanism (MCM). The chemical solver is explicit backward-Euler with a 5-minute chemical integration timestep, based on (Hertel et al., 1993). The Fast-J photolysis algorithm was used to update photolysis rates hourly, which have been calculated based on cloud and aerosol layer properties (Wild et al., 2000).

While whole-atmosphere chemistry is the ultimate aim in ACCESS, a stratospheric chemistry scheme was not implemented in the model at this stage, therefore production and loss of stratospheric ozone and halogen chemistry was not modelled. Although stratospheric chemical mechanisms were not explicitly modelled, upper-atmospheric conditions of key trace gases were defined to ensure contribution from stratospheric sources were captured and in particular, stratosphere-troposphere exchange could be modelled. Several options were available for defining top boundary conditions of the reactive species O_3, CH_4 and NO_Y. Top boundary conditions of O_3 are and CH_4 were chosen to as their default definitions. Default for O_3 was to overwrite certain levels of the model stratosphere with O_3 used to drive the MetUM radiation scheme (Edwards & Slingo, 1996). Stratospheric removal of CH_4 was given a specified loss rate in the three top model levels (2.0×10^{-7} gives CH_4 loss in line with Prather et al., 2001). The advantage of both these default options is that stratospheric composition values may vary over simulation years.

The default choice for defining NO_Y was to use a fixed O_3:HNO_3 ratio defined by (Murphy & Fahey, 1994) to overwrite HNO_3 in selected stratospheric levels. Alternatively, NO_Y may be defined at pressures below 70 hPa using output from the Cambridge 2D

Table 6.5.2: Advected tracers in ACCESS. Tracers of interest are highlighted in red.

	Advected Tracers		
	Tracer name	Formula	Emitted
1	O3	O_3	
2	NO	NO	as NO_2
3	NO3	NO_3	
4	NO2	NO_2	as NO_2
5	N2O52	N_2O_5	
6	HO2NO2	HO_2NO_2	
7	HONO2	$HONO_2$	
8	H2O2	H_2O_2	
9	CH4	CH_4	Y
10	CO	CO	Y
11	HCHO	HCHO	Y
12	MeOOH	CH_3OOH	
13	HONO	HONO	
14	C2H6	C_2H_6	Y
15	EtOOH	C_2H_5OOH	
16	MeCHO	CH_3CHO	Y
17	PAN	$CH_3O_3NO_2$	
18	C3H8	C_3H_8	Y
19	n-PrOOH	$n - C_2H_7OOH$	
20	i-PrOOH	$i - C_2H_7OOH$	
21	EtCHO	C_2H_5CHO	
22	Me2CO	CH_3COCH_3	Y
23	MeCOCH2OOH	CH_COCH_2OOH	
24	PPAN	$C_2H_5CO_3NO_2$	
25	MeONO2	CH_3ONO_2	
26	O3S	O_3 (Stratospheric)	

model (Law & Pyle, 1993). It was found that model results were sensitive to NO_Y boundary condition choice. Briefly, NO_Y becomes important when combining in an ESM due to eventual coupling between earth system components that requires certain boundary values to move between modules. Comparisons and results of the two NO_Y boundary conditions are further discussed in depth in Section 8.5.

6.6 Effect of model horizontal resolution

6.6.1 Model resolution affects atmospheric composition

As previously introduced, the coarse horizontal resolution in models can introduce spatial dilution effects into modelled results. Additionally, it is important to select a model grid-box which best represents a measurement site. Model grid-box edges are often arbitrarily created, and are not optimised for every measurement station. Consequently an adjacent grid-box to the one containing the station may more appropriately reproduce measured air composition. For example, a station such as Wollongong, which lies on the east coast of Australia, may be located just inside the corner of an ocean spanning grid-box. However, measurements at Wollongong would be expected to have an atmospheric signature more akin to a land grid-box. Therefore it is always important to understand placement of the measurement station within the model grid space. Understanding station placement will help interpret model results and make appropriate comparisons.

Hypotheses about atmospheric signatures within different grid-boxes can be made by employing land-use types. Land-use types are determined from satellite measurements and are qualitatively indicative of different emission patterns. For example, urban environments correspond with elevated levels of CO, while oceans have comparatively low levels of CO. Atmospheric composition within a model grid-box is a combination of signatures from several surface environments, which is further complicated by transport. While model output describes these complex contributions quantitatively, expected differences between grid-boxes can be inferred by investigating land-types.

This section assesses how robust a chosen ACCESS pixel represents an observed location by comparing several adjacent grid-boxes within the location region. Horizontal resolution in ACCESS is $1.25° \times 1.875°$ (Figure 6.5.2a), corresponding on average to 125 by 187.5 km. Therefore, a large number of different and varying land-types and consequently trace gas contributions may be present within one ACCESS grid-box. Here, ACCESS results are assessed for the variability introduced by different grid-box choice.

When comparing two models that have different horizontal resolution, differences may be introduced due to higher spatial dilutions in the model with larger grid-boxes. Therefore, in order to compare the fundamental model processes, spatial dilution needs to

be accounted for. Here, the contribution of dilution to model differences is assessed between GEOS-Chem and ACCESS horizontal resolutions. GEOS-Chem horizontal resolution is $2^\circ \times 2.5^\circ$ (Figure 6.3.1a), a larger area than ACCESS. GEOS-Chem grid is also offset to ACCESS. Therefore, in preparation for comparison between models, an assessment is made on the validity of comparing the ACCESS representative grid-box with the corresponding GEOS-Chem grid-box.

6.6.2 Resolution analysis methodology

ACCESS simulation results were used to quantify the effect of grid-box choice on atmospheric composition around a measurement location. Trace gases, CO, HCHO, C_2H_6, NO_2, and O_3, were sampled from the model at several distinct grid-boxes around a central grid-box, chosen to be representative of the measurement location. Central and surrounding ACCESS grid-boxes at Wollongong, Darwin and Lauder are shown in Figures 6.6.1a, 6.6.2a and 6.6.2c respectively. Numbering and colours of surrounding grid-boxes correspond with numbers and colours used in subsequent analysis.

Figures 6.6.1b, 6.6.2b and 6.6.2d present land-types around each measurement station, overlayed with the ACCESS grid. Land-type plots were produced from MODIS 0.05° resolution yearly product for 2001 (MCD12C1 downloaded from the United States Geological Survey (USGS) data pool, 2014) and were separated into land cover types following International Geosphere-Biosphere Programme (IGBP) classifications. Land types, and therefore atmospheric sources, differ depending upon grid-box. For example the central grid-box for Wollongong sees contribution from forest, cropland and urban environments. In comparison, the grid-box directly east (4) includes a majority of ocean, while directly west (8) includes a majority of cropland, which would all be expected to have distinctly different emission and chemistry. Major land-types for each grid-box at each site are listed in Table 6.6.1.

Quantitative assessment of the effect of different environments within grid-boxes was undertaken. Average annual cycles of month-averaged values were calculated for the central grid-box and eight adjacent grid-boxes (shown later). Absolute percentage difference relative to the central grid-box was calculated for each surrounding grid-box. The range of percentage differences gave an indication of trace gas variability between grid-boxes. Total column values were investigated for all trace gases.

In addition to determining atmospheric variability in surrounding grid-boxes, the con-

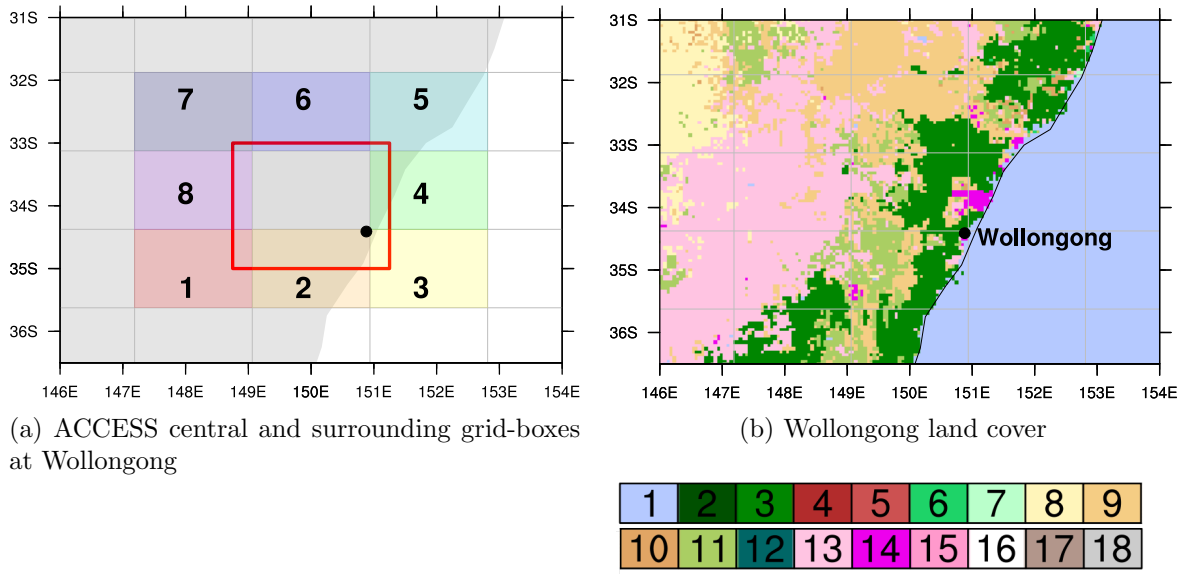

(a) ACCESS central and surrounding grid-boxes at Wollongong

(b) Wollongong land cover

Figure 6.6.1: ACCESS grid with GEOS-Chem pixel comparison (left, (a)) and land cover plots (right, (b)) at Wollongong. ACCESS horizontal resolution is displayed as grey gridbox. Station location is displayed as a filled black circle. (a) Central ACCESS pixel is used as the main representative of the measurement site. Numbers and colours of surrounding pixels are used in further analysis of pixel influence. Red outline indicates the equivalent GEOS-Chem gridbox used to represent Wollongong; (b) Uses International Geosphere-Biosphere Programme (IGBP) classifications of land cover: **1**-water bodies, **2**-evergreen needleleaf, **3**-evergreen broadleaf , **4**-deciduous needleleaf, **5**-deciduous broadleaf, **6**-mixed forests, **7**-closed shrubland , **8**-open shrublands, **9**-woody savannas, **10**-savannas, **11**-grasslands, **12**-permanent wetlands, **13**-croplands, **14**-urban and built-up, **15**-cropland/natural mosaic, **16**-snow and ice, **17**-barren/sparsely vegetated, **18**-unclassified & fill values.

tribution of larger horizontal resolution to atmospheric composition was assessed. ACCESS grid-space was degraded to the larger resolution of GEOS-Chem in order to gain insight into whether chosen model resolution could significantly contribute to simulated atmospheric composition. This analysis was completed in order to quantify the magnitude of atmospheric composition differences between ACCESS and GEOS-Chem due to resolution difference, in preparation for comparison between models in Chapter 8.

GEOS-Chem grid-boxes for each station are overlaid on the ACCESS grid in Figures 6.6.1a, 6.6.2a and 6.6.2c. At each station, a weighted combination of atmospheric composition resulting from ACCESS grid-boxes was produced. The combined product was weighted based on area-overlap with the corresponding GEOS-Chem grid box at each

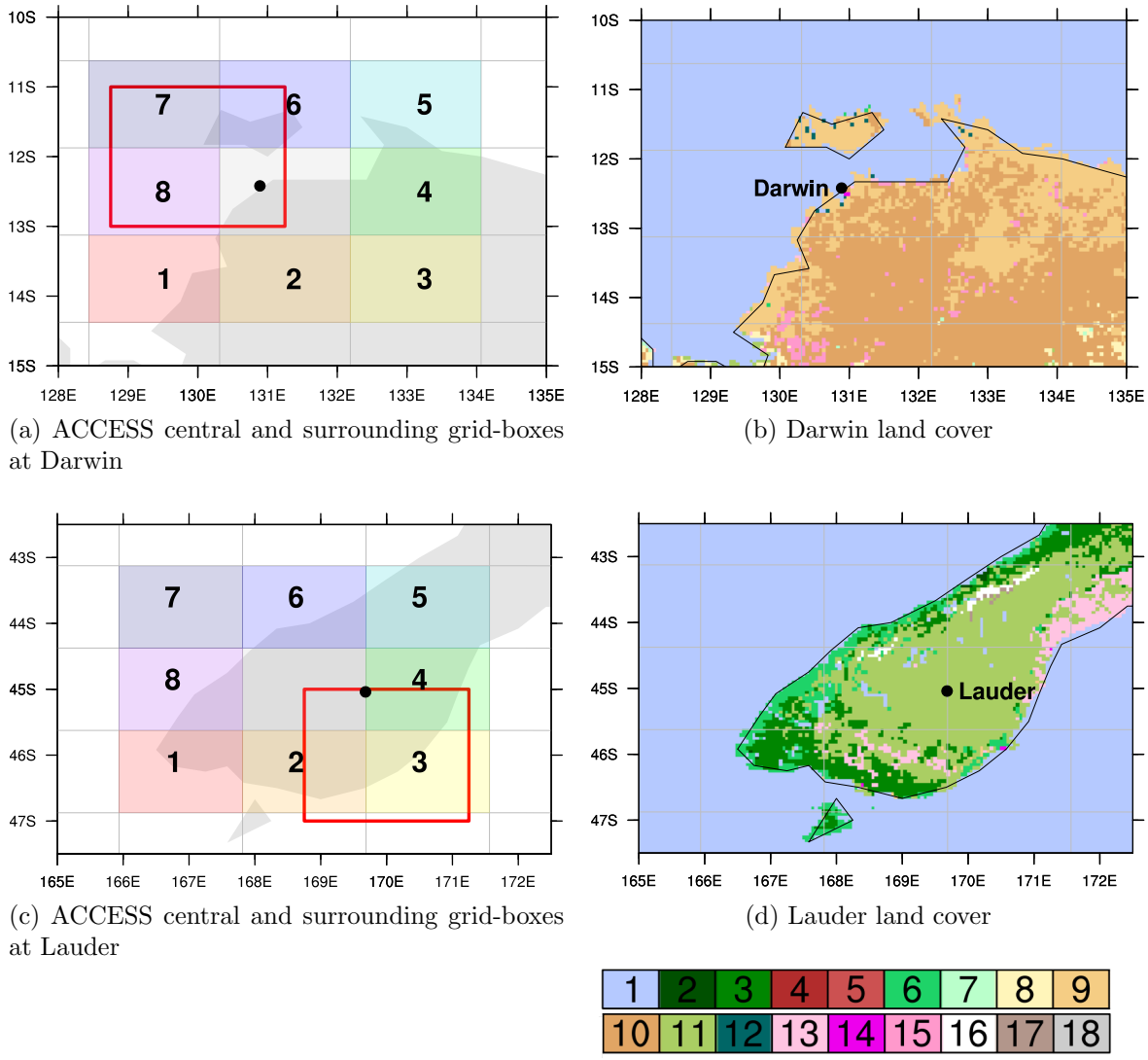

(a) ACCESS central and surrounding grid-boxes at Darwin

(b) Darwin land cover

(c) ACCESS central and surrounding grid-boxes at Lauder

(d) Lauder land cover

Figure 6.6.2: The same as for figure 6.6.1a but for Darwin (a) and Lauder (c). Land cover plots for Darwin (d) and Lauder (f). IGBP land cover classification: **1**-water bodies, **2**-evergreen needleleaf, **3**-evergreen broadleaf , **4**-deciduous needle-leaf, **5**-deciduous broadleaf, **6**-mixed forests, **7**-closed shrubland , **8**-open shrub-lands, **9**-woody savannas, **10**-savannas, **11**-grasslands, **12**-permanent wetlands, **13**-croplands, **14**-urban and built-up, **15**-cropland/natural mosaic, **16**-snow and ice, **17**-barren/sparsely vegetated, **18**-unclassified & fill values

Table 6.6.1: Major IGBP land surface type contributions within each ACCESS pixel. ACCESS pixels that also overlap with the GEOS-Chem box over the station are shown in red.

	Description of major land type		
Pixel	Wollongong	Darwin	Lauder
1	cropland/forest	ocean/savanna	ocean/forest
2	grassland/forest	savanna	forest/grassland
3	ocean	savanna	ocean/grassland
4	ocean/forest/urban	savanna	grassland
5	forest/ocean/urban	ocean/savanna	grassland/cropland/forest
6	savanna/forest	ocean/savanna	ocean/forest
7	cropland	ocean	ocean
8	cropland	ocean	ocean/forest
center	forest/cropland/urban	savanna/ocean	grassland

station. Specifically, the proportion contribution of each ACCESS grid-box residing within the GEOS-Chem 2° × 2.5° grid-box was computed at each location, relative to the GEOS-Chem grid-box size.

Fractional contributions of ACCESS pixels to a combined product were calculated based on the area overlapping with the GEOS-Chem grid-box. For example at Wollongong, the central ACCESS grid-box lies entirely within the GEOS-Chem grid-box and therefore contributes 47% fraction to the combined ACCESS product. Comparatively, at Darwin only about half of the central ACCESS box lies within the GEOS-Chem grid-box, therefore only contributes 21% to the combined product. Fractional contributions at each location are collected in Table 6.6.2. There is a small contribution at Lauder from ACCESS pixels below numbers 2 and 3. However, output from these grid-boxes was not provided, therefore in this case are taken to have the same atmospheric composition as pixels 2 and 3.

Fractional contribution was applied to the corresponding average annual cycles of each trace gas in each grid-box, before being combined. The combined annual cycle product was compared with the central box annual cycle and differences determined as absolute percentages.

Table 6.6.2: Calculated contribution of ACCESS pixels to GEOS-Chem pixel over each location Wollongong, Darwin and Lauder.

	Fraction of equivalent GEOS-Chem gridbox		
	Wollongong	Darwin	Lauder
1	0.0078125	0	0
2	0.234375	0	0.2578125
3	0.0078125	0	0.4296875
4	0.078125	0	0.1953125
5	0.0390625	0	0
6	0.046875	0.1640625	0
7	0.0390625	0.2734375	0
8	0.078125	0.3515625	0
center	0.46875	0.2109375	0.1171875

6.6.3 Quantification of resolution effect on variability

Variation exists between trace gas total column values of central and surrounding ACCESS grid-boxes for each of the three sites Wollongong, Darwin and Lauder. Greater deviation from the central box resulted in those grid-boxes with markedly different majority land-type contributions. For example, grid-boxes with major ocean contribution generally show lower trace gas amounts compared with grid-boxes that have minimal ocean influence.

Dependence of total column CO upon grid-box was observed at all three locations (Figure 6.6.3). Similar variation in atmospheric composition between grid-boxes was seen for other trace gases: HCHO (Figure in Appendix E.0.9), C_2H_6 (Figure in Appendix E.0.10), NO_2 and O_3 (not shown).

At Wollongong, ocean grid-boxes (numbers 3 and 4, Figure 6.6.1a) show lower total column values for all trace gases except O_3. Lower atmospheric amounts are due to trace gas sources being mainly land-based. Differences between ocean and land-majority pixels are most prominent for trace gases with tropospheric majority. The O_3 column is greatly influenced by stratospheric O_3, which depends upon latitute. Specifically, latitudes closer to the poles show increased stratospheric O_3 and hence column O_3. The latitude effect on column O_3 is seen at all three sites.

Greatest variation was seen at Darwin for CO, HCHO and C_2H_6, which was likely due to the large differences in sources between ocean and land grid-boxes. Large local

biogenic and biomass burning sources originate over land in this region with biomass burning sources being highly variable. Grid-box differences at Darwin are particularly pronounced during biomass burning season July-October.

Lauder, being the most remote and clean site studied here, showed the lowest variability between grid-boxes. Total column HCHO combined product values show small variance, with greater variance between pixels in the beginning of the year (Jan – Mar). This is similar for the surface values in the beginnning of the year, suggesting different seasonality between pixels for this time of year. Pixels showing lower values in this part of the year include a substantial portion of ocean (pixels 3, 4 and 5). Since a main source of HCHO is biogenic, and that the trace gas is short-lived, pixels 3, 4 and 5 including the ocean fail to capture the summer biogenic signal as prominently as the remaining pixels over land.

In order to determine the significance of grid-box variations, the absolute difference between central and surrounding grid-box annual cycles was calculated at each station for each trace gas. Comparison of maximum differences with the corresponding average monthly standard deviation of the central grid-box led to a quantification of significance. Ranges of absolute difference are summarised in the top panel of Table 6.6.3 and average monthly standard deviations are listed in the bottom panel.

For CO total column, Wollongong differences due to grid-box choice range from well below standard deviation of monthly averaged values (1σ) to just below 2σ. Darwin has the largest range of below 1σ to just below 4σ. Maximum difference at Lauder remains below 1σ. This indicates that grid-box choice is less important for total column CO at clean and remote sites such as Lauder. However, careful consideration of the grid-box representability of measurement site should be undertaken for locations closer to sources, like Wollongong and Darwin.

Total column C_2H_6 shows similar differences as CO, being of similar lifetime and sources. Darwin C_2H_6 range of difference is below 3σ, better than for CO. HCHO has a shorter atmospheric lifetime, therefore is more sensitive to variation in local sources, and consequently shows a larger range in grid-box differences. Wollongong HCHO maximum difference is outside 2σ, Darwin outside 4σ and Lauder outside 1σ.

Trace gases with maximum contributions to the column in the stratosphere show lower ranges in differences between grid-boxes, with all differences under 4 % for NO_2 and O_3. Stratospheric sources for these trace gases are driven by large-scale processes, therefore total column for these trace gases change minimally between pixels. However, monthly

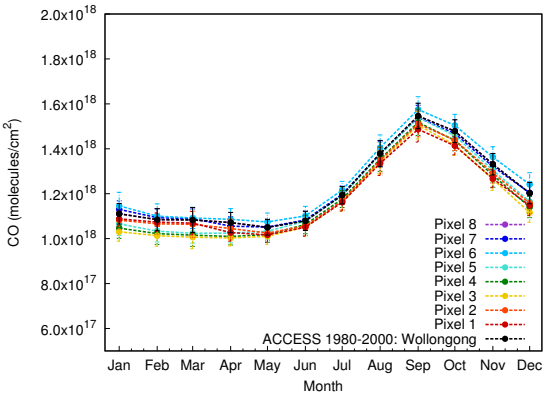

(a) Wollongong total column CO by grid-box

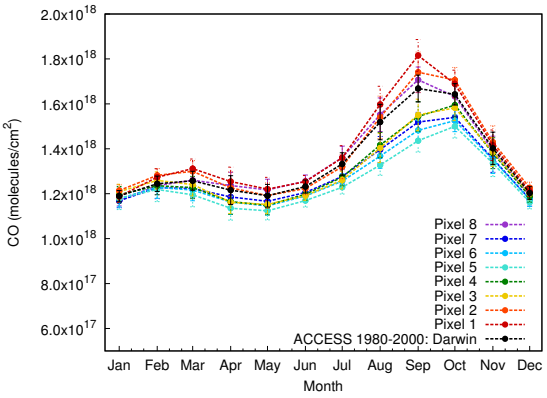

(b) Darwin total column CO by grid-box

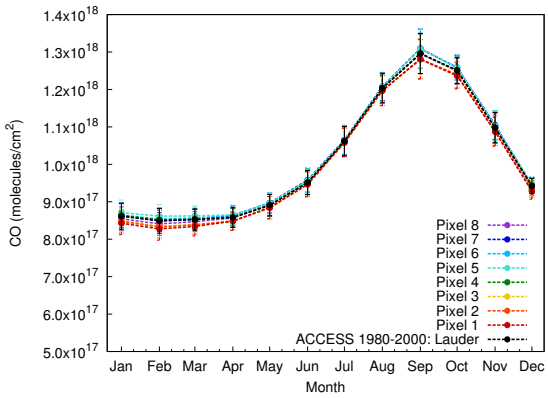

(c) Lauder total column CO by grid-box

Figure 6.6.3: Total column CO average annual cycles for central and surrounding ACCESS grid-boxes at (a) Wollongong, (b) Darwin and (c) Lauder. Colours correspond to pixel colouration in Figure 6.6.1a, 6.6.2a and 6.6.2c respectively. Monthly 1σ are shown for each grid-box.

standard deviation in these trace gas columns are also lower, meaning significant differences are still possible. Wollongong and Darwin NO_2 are below 2σ and Lauder within 1σ. Wollongong O_3 column maximum difference is just below 3σ and Darwin and Lauder are within 1 and 2σ respectively.

ACCESS results were degraded to a lower resolution product, in order to match the spatial resolution of GEOS-Chem. The lower resolution ACCESS product was subsequently compared with the higher resolution ACCESS results to assess resolution effects on atmospheric composition. The comparison of the higher resolution central pixel with the lower resolution result for total column CO is seen in Figure 6.6.4a, 6.6.4b and 6.6.4c.

Table 6.6.3: Top panel indicates range of absolute percent differences in total column atmospheric composition between eight ACCESS grid-boxes relative to a centre grid-box at each station: Wollongong (WOL), Darwin (DAR) and Lauder (LAU). Middle panel collates differences between centre grid-box and a lower resolution composite product (see text for details). Average monthly standard is shown for comparison in the lkower panel.

	Range of absolute difference (in percentage)				
	CO	HCHO	C_2H_6	NO_2	O_3
WOL	0.01 – 7.2	0.01 – 16	0.01 – 11	0.01 – 3.6	0.01 – 1.4
DAR	0.04 – 14	0.02 – 29	0.01 – 14	0.01 – 3.4	0.02 – 0.8
LAU	0.1 – 2.5	0.2 – 16	0.01 – 3.2	0.01 – 2.2	0.01 – 0.7
	Composite product versus centre pixel difference (absolute percentage)				
WOL	0.6 – 1.3	1.6 – 2.6	1.1 – 2.3	0.3 – 0.8	0.04 – 0.2
DAR	0.4 – 3.5	0.3 – 15	0.3 – 3.7	0.3 – 1.9	0.06 – 0.2
LAU	0.3 – 1.2	0.5 – 5.9	0.5 – 1.8	0.01 – 1.3	0.01 – 0.4
	Average monthly standard deviation (percentage)				
WOL	4.0	7.6	5.5	2.5	0.5
DAR	3.6	5.5	6.2	1.7	0.8
LAU	3.4	13	4.8	2.5	0.5

From Figure 6.6.4, total column CO annual cycle resulting from the combined product is slightly lower, but almost unchanged compared with the central grid-box. This is confirmed by maximum differences (middle panel, Table 6.6.3) remaining below 1σ, meaning moving to a lower resolution did not significantly alter model output of total column CO at each of the stations.

Combined ACCESS products of lower resolution were calculated for HCHO (Appendix, Figure E.0.11) C_2H_6 (Appendix, Figure E.0.12), NO_2 and O_3 (not shown). Range of differences between the combined product and central grid-box were also determined for each trace gas.

Similar to CO, C_2H_6 showed non-significant reductions in the lower resolution total column product, with differences well within 1σ. HCHO and NO_2 also produced lower total column values in the lower resolution ACCESS product. At Wollongong and Lauder, these reductions were deemed to be non-significant, indicated by differences

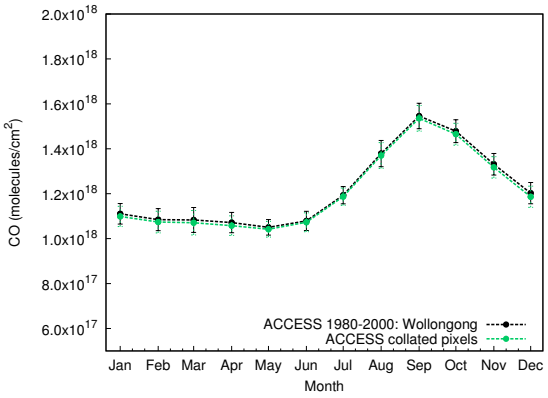

(a) Resolution effect on Wollongong total column CO

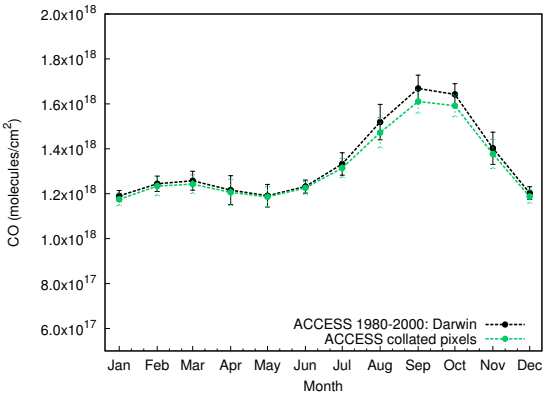

(b) Resolution effect on Darwin total column CO

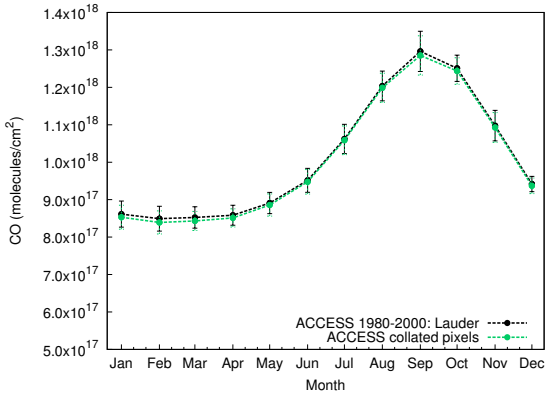

(c) Resolution effect on Lauder total column CO

Figure 6.6.4: Plots show ACCESS total column CO annual cycle for the central grid-box against the combined lower resolution ACCESS product at each location (a) Wollongong, (b) Darwin and (c) Lauder.

within 1σ. However, at Darwin, HCHO and NO_2 were outside 1σ. For HCHO especially, maximum difference was just below 3σ, meaning for some months the change in total column HCHO at Darwin due to lower resolution was significant.

Ozone is the only trace gas that shows a consistent increase upon inclusion of surrounding pixels. This is linked to the reduction seen in NO_2 in a larger grid-box. Lower NO_2, means less O_3 has been removed in reaction with O_3.

6.6.4 Implications for trace gas analysis

In general, atmospheric composition dependence upon grid-box was observed at all three locations, Wollongong, Darwin and Lauder. Therefore, careful analysis of grid-box representativeness was required. Wollongong station lies just south of the southeast corner of the central grid-box, in grid-box 2. However, grid box 2 is within monthly standard deviation of the central grid box. Also, the central grid box is positioned to more appropriately capture influence from Sydney urban pollution, a major contributor to Wollongong atmospheric composition. Other grid boxes that show major differences to the central grid-box have different land-type contributions than is seen around Wollongong, in particular majorities either from the ocean or cropland. Therefore, the most appropriate representation of the Wollongong station was determined to be by the central grid box.

The major differences between Darwin grid-boxes originated from grid-boxes including majority ocean influence, whereas Darwin atmosphere would be expected to be highly influenced by land sources. Therefore the central grid-box at Darwin was also deemed an appropriate representation.

Lauder difference values were generally within one average monthly standard deviation of the central grid box for CO, C_2H_6 and O_3, meaning the central grid box is appropriate to use in representing the Lauder measurement site. The trace gases HCHO and NO_2 showed maximum difference outside 1σ for grid-boxes that included additional land-use types compared with the Lauder measurement station. Specifically, grid-box 1 included majority ocean influence and grid-box 5 included influence from croplands. Therefore, for these two trace gases the central grid box at Lauder was also deemed an appropriate choice for comparison.

In comparison with GEOS-Chem, only CO, HCHO and C_2H_6 were required to be considered due to GEOS-Chem predominantly modelling tropospheric chemistry. NO_2 and O_3 columns are significantly influenced by stratospheric amounts, which are not modelled in GEOS-Chem. The lower resolution combined ACCESS product was analysed to determine if any systematic biases could occur from comparing the higher resolution central grid-box with GEOS-Chem results. Inclusion of surrounding pixels reduced the total column amount in all cases, reflecting the property of increased spatial dilution in a larger horizontal resolution grid. However, generally, this reduction in total column was not significant and was within the monthly standard deviation of the central pixel. Therefore, it is acceptable to compare the higher resolution central ACCESS grid-box

with the GEOS-Chem results, without biasing the comparison.

The one exception is for Darwin HCHO, in which conversion to lower resolution reduced the total column in some months to below 3σ of the central ACCESS box. However, as we will see in Chapter 8, the comparison with GEOS-Chem would become more disparate by accounting for resolution differences, as ACCESS results of the central box were already low compared with GEOS-Chem. Therefore, for this study it is also valid to use the higher resolution central grid box in comparison with GEOS-Chem. In future, when model differences are within 5% the combined lower resolution HCHO product would be more appropriate for use at Darwin.

It should be noted that variability of surface model values would be greater as they are closer to sources and would show more sensitivity to changes in land type than column values. Column measurements somewhat dilute the surface signal by vertical integration, especially in the case of short-lived trace gases.

6.7 Summary of differences between GEOS-Chem and ACCESS

Detailed information about dynamics, emissions and chemistry for GEOS-Chem and ACCESS has been discussed throughout this Chapter. Here, a summary of comparisons is performed between GEOS-Chem and ACCESS and is presented in Table 6.7.1, which lists major components of each model.

Simulation results are further compared between models in Chapter 8 with the aim of quantifying ACCESS accuracy. The GEOS-Chem chemical scheme is more complex in comparison with ACCESS, including over double the number of species and reactions. GEOS-Chem, being a model devoted to chemistry and highly validated, is expected to out perform ACCESS with a reduced chemical scheme. While the reduced scheme in ACCESS is necessary to optimise computational efficiency in coupling, ACCESS chemistry is nonetheless required to model the major atmospheric components it includes correctly. Assumptions and simplifications need to be validated in order to have confidence in results of simulations of future atmospheric conditions.

Table 6.7.1: Summarised major components for ACCESS and GEOS–Chem.

	ACCESS	**GEOS-Chem**
Meteorology	Inline MetUM-UKCA MetUM driven by SSTs	GEOS-5 reanalysis meteorological fields
Chemistry	46 species 26 advected tracers 129 reactions ***photolysis***: FAST-J ***chemistry***: Backward Euler	102 species 43 advected tracers 278 reactions ***photolysis***: FAST-J ***chemistry***: KPP
Emissions	Constant at year 2000 values based on IPCC SRES emission scenario	***Anthropogenic:*** Fossil Fuel: EDGAR and Biofuel: Yevich & Logan, 2003 overwritten regionally: Europe (EMEP), Mexico/USA (BRAVO), China/SE Asia (Streets), Canada (CAC), North America (NEI2005, EPA/NEI99) ***Biogenic***: MEGAN 2.1 with PCEEA ***Biomass Burning***: GFED2–monthly ***Other NO_X***: aircraft Wang et al., lightning (Sauvage et al., 2007), soil (based on the work of Yienger & Levy, 1995 and Wang et al., 1998)
Deposition	***wet***: based on TOMCAT and includes Henry's Law ***dry***: previously calculated, lowest level only	***wet***: convection and stratiform precipitation spearated - both include Henry's Law ***dry***: resistance model
Years Run	1980 – 2000	2004 – 2009
Resolution	***horizontal***: 1.875°× 1.25° ***vertical***: 38 levels (to approx. 35 km) ***surface layer***: approx. 40 m	***horizontal***: 2.0°× 2.5° ***vertical***: 47 levels (to approx. 80 km) ***surface layer***: approx. 130 m

Resolution differences were determined to be unlikely to contribute in a major way to model differences, as indicated by lower resolution minimally affecting trace gas columns in ACCESS. Therefore, differences found in modelled atmospheric composition may be due to any of the three components introduced in this Chapter: Emissions, Dynamics and Chemistry/Deposition. Emission inventories are the most likely area models may be different, and is a difference that can be relatively easily remedied. That is, a large difference in emissions would lead to a large difference in modelled composition, however could be improved by scaling or replacing inventory files. Emissions are further discussed in Chapter 8.

Dynamics in ACCESS are simulated, where as GEOS-Chem uses reanalysis fields, which means comparisons of specific years is not possible. However, as this research is only concerned with major differences, a valuable comparison can be made using average annual cycles for each dataset. Chemical reactions are sourced from the same database therefore specific reactions are not likely to cause differences between models. However, the lack of some reactive chemistry, in particular isoprene chemistry would be expected to affect atmospheric composition such as for short lived gases like HCHO.

Chapter 7

Evaluation of GEOS-Chem simulations, using total column measurements

Chemical Transport Models (CTMs) are dedicated to providing accurate representations of atmospheric photochemical reactions and composition. Over time, as knowledge of natural and anthropogenic sources improve, and as more trace gas species and reaction pathways have been included in these models, their ability to predict atmospheric composition has improved. Global CTMs are used to simulate changes in atmospheric composition and chemistry over time, often in order to help interpret observations. GEOS-Chem is a global CTM that uses our best current knowledge of complex real-world processes to provide a simulation of atmospheric composition. CTMs are helpful in a range of atmospheric research, often used for areas where measurements are sparse, difficult to obtain, or are simply unavailable. GEOS-Chem is used by more than 70 groups worldwide to study a range of atmospheric research including constraining emission sources, investigating chemistry-climate feedbacks, interpreting multi-platform observational data, and testing new theories of atmospheric processes.

Compromises are made in constructing GEOS-Chem, with processes often being parameterised to account for sub-grid scale processes and to allow for efficient computing times. Biases may therefore be introduced through these assumptions, combined with gaps in current understanding of atmospheric processes, therefore it is important to gain estimates on model output uncertainty through evaluation studies. Evaluation is particularly necessary to determine if a model can be used for intended research.

GEOS-Chem is developed by researchers in the Northern Hemisphere, and atmospheric simulations have primarily aimed to answer questions relating to Northern Hemispheric regions. Although limited comparisons have been made for the Southern Hemisphere, the region is an ideal location to assess models, as urban locations are often distinctly separated. This leads to sources being less convoluted than seen in the Northern Hemisphere, and interpreting source characteristics can consequently be less complex. Additionally, studies in the Southern Hemisphere help us understand the background state of the atmosphere, as a majority of the Southern Hemisphere is considered "clean" in comparison with the Northern Hemisphere.

Many studies have evaluated GEOS-Chem modelled carbon monoxide for the Northern Hemisphere (e.g. Griffin et al., 2013; Kumar et al., 2013; Heald et al., 2003). Use of GEOS-Chem for Southern Hemispheric CO has generally occurred during global studies (e.g. Duncan et al., 2007; Bey et al., 2001), and mainly for inverse studies (Arellano et al., 2006; Jones et al., 2009a; Kopacz et al., 2010; Jiang et al., 2011) which aim to provide updated global estimates of emission budgets. Global studies are concerned with improving annual or global model-measurement comparisons, and some regional mis-representation may remain in the model.

In addition, Southern Hemisphere comparisons of CO have so far tended to be with surface in situ measurements. Comparison with in situ measurements can be misleading, as the large spatial regions represented by a GEOS-Chem grid-box ($4°\times5°$ or $2°\times2.5°$) dilute sub-grid-scale sources. Reduction of a spatial dilution bias has been addressed to some extent by studies generally limiting comparisons to remote stations, such as Cape Grim or Antarctica (e.g. in Duncan et al., 2007). In remote regions, the atmosphere is likely to be well mixed with few local sources, and a surface measurement is more likely to be representative of an entire GEOS-Chem grid box and therefore appropriate to compare.

Comparison with total column values somewhat alleviate the issue of dilution of local sources. Column values represent the total atmospheric column above a location, and the viewing geometry of the ground–based instrument means the values represent a wider region than a point source. Total column values also compare to a better degree with models because they are less dependent on errors in vertical mixing, which are a problem in many global CTMs, including GEOS-Chem (Liu et al., 2013). There has been limited use of Southern Hemispheric profile and total column data in GEOS-Chem comparisons, often restricted to short time periods. Lauder column CO from 1994 to 2000 was compared in Duncan et al., 2007. A comparison of GEOS-Chem

profile CO has been made for tropical Indonesian fires in 2006, studied using satellite instrument Microwave Limb Sounder (MLS) (Zhang et al., 2011) and column average mole fraction CO with Tropospheric Emission Spectrometer (TES) (Worden et al., 2013b). These satellite comparisons were performed for an atypically high biomass burning year. Comparisons of MLS and TES were also performed for South America and southern African region during 2005 and 2006, in Liu et al., 2010. Recently, a ship borne study using FTS total column values was completed in the Western Pacific, however this was also limited in time to two months, October–November, 2009 (Ridder et al., 2012).

Studies of atmospheric formaldehyde using GEOS-Chem have mainly focused on global or regional inversion studies using satellite measurement. Inversion studies use satellite measurements of HCHO to constrain isoprene emissions, as HCHO is an intermediate in the isoprene oxidation pathway (Barkley et al., 2013, 2008; Fu et al., 2007; Marais et al., 2012; Millet et al., 2008; Palmer et al., 2003; Shim et al., 2005; Stavrakou et al., 2009). A couple of comparison studies have been made, one with satellite and in situ measurements over the Amazon (Barkley et al., 2011), and another investigating global seasonal cycles in the upper-troposphere (Dufour et al., 2009). Ground based total column measurements have been unused thus far with respect to HCHO.

The use of GEOS-Chem for studying atmospheric ethane has been mainly limited to regions in the Northern Hemisphere: USA (Liang et al., 2007), Canada (Griffin et al., 2013) and Germany (Salau et al., 2009). Ethane has been used in correlation study with propane for northern middle and high latitudes, and over the tropical Pacific (Wang & Zeng, 2004). A satellite study showed mean absolute bias of less than 40% between modelled and satellite measured upper tropospheric C_2H_6 in the Southern Hemisphere (Abad et al., 2011). Additionally, one study has assessed the global emission inventory of C_2H_6 using a tagged tracer run (Xiao et al., 2008), which found the C_2H_6 modelled seasonal cycle compared well with the average seasonal cycle between 1997-2003 from the Southern Hemisphere total column site, Lauder.

Here, the aim is to broaden the validity of using GEOS-Chem to study atmospheric composition, to include the Southern Hemispheric region of Australasia (10°S to 60°S, 110°E to 180°E). Evaluation of GEOS-Chem for Southern Hemisphere atmospheric composition was investigated with respect to total column values of CO, HCHO and C_2H_6. Model evaluation was completed by comparison of output with ground-based and satellite total column measurements. Total column amount from ground-based FTS measurements for the target trace gases are compared with output from GEOS-Chem

at several sites, spanning latitudes in the Australasian region, namely Darwin (12.4° S, 130.9° E), Wollongong (34.4° S, 150.9° E), and Lauder (45.0° S, 169.7° E). These sites include remote and non-remote locations. Comparisons with satellite total column CO values are also performed, in order to include a spatial analysis of the GEOS-Chem model results. Quantification of model skill is achieved using correlation analysis.

7.1 Comparison methodology

In this study, GEOS-Chem (v8-03-01, http://geos-chem.org/) was used to simulate global atmospheric composition between 2004 and 2009 in standard full-chemistry mode, which included extensive O_X-NO_X-VOC chemistry. GEOS-Chem is a 3-D Eulerian global chemical transport model (Bey et al., 2001) which was introduced in detail in Chapter 6, Section 6.3. Briefly, the model incorporated over 100 chemical species in over 250 reactions. Meteorology was driven by the NASA GEOS-5 reanalysis product. Simulation was performed using 2°× 2.5° horizontal resolution and 47 vertical layers, up to 80 km. Biomass burning emissions are from the GFED2–monthly gridded inventory, biogenic emissions from MEGAN 2.1, and a range of various inventories describe anthropogenic and other emissions of trace gases, outlined in Chapter 6, Section 6.3.2. Model output was saved as hourly averaged profiles. In order to compare with total column measurements, GEOS-Chem results were averaged over a 24 hour period. An algorithm to compare model and measurements was developed using the programming language NCAR command Language (NCL, http://www.ncl.ucar.edu/, UCAR, 2013).

Model results were first compared with total column measurements from ground-based solar Fourier Transform Infrared Spectrophotometers (FTS). Solar total column FTS instruments use the sun as an infrared source and work from the principle that molecules absorb in the infrared. FTS record solar spectra over 2–5 minutes, after which, inverse methods are used to retrieve total column values. A full description of the FTS instruments, including retrieval procedure can be found in Chapter 2, Section 2.4.

Three well-established FTS sites exist in the Australasian region with which to compare model results, namely Wollongong, Darwin and Lauder. These stations span latitudes in the region, 12° S to 45° S and are listed in table 7.1.1 with a short description of local environments. Station location is also represented in a map of the Australasian region in figure 7.1.1. Due to the range of latitudes and local influences, FTS stations were expected to capture a range of atmospheric compositional environments. Wollongong

FTS was commissioned in 1996, Darwin in 2005, and Lauder in 1994. Wollongong CO, HCHO and C_2H_6 FTS measurements have been thoroughly described in Chapter 2, Section 2.4. Darwin CO, HCHO and C_2H_6 timeseries have been taken from Paton-Walsh et al., 2010a. The Lauder timeseries of CO and C_2H_6 was previously described by Zeng et al., 2012, and Lauder HCHO has only been retrieved to 2005 and is described in Jones et al., 2009b.

Table 7.1.1: Locations descriptions of the three FTS total column measurement sites used in this study.

Location	Latitude	Longitude	Site Description
Darwin	12.425° S	130.891° E	Tropical, monsoonal
Wollongong	34.406° S	150.874° E	Urban, temperate coastal
Lauder	45.038° S	169.684° E	Rural, temperate grassland

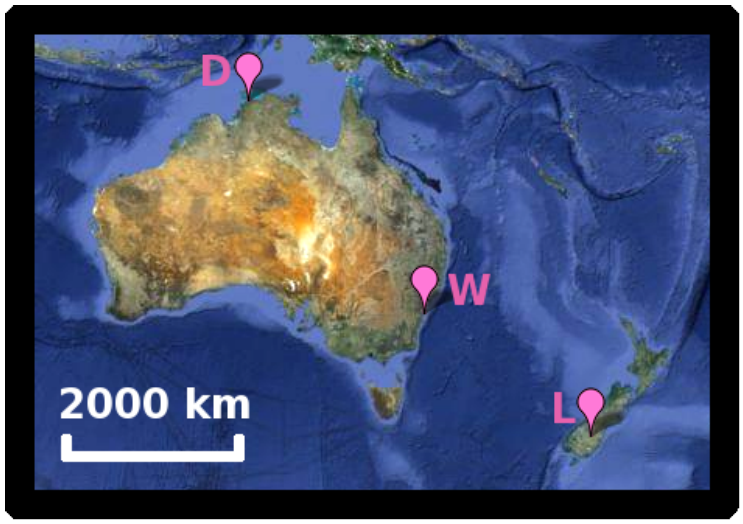

Figure 7.1.1: Relative locations of the three FTS total column measurement sites in Australasia. W = Wollongong; D = Darwin, L = Lauder. Map image was adapted from Google satellite images.

CO in the Australasian region was compared for 2008 with column retrievals from the Measurements Of Pollution in the Troposphere (MOPITT) satellite-based instrument (Drummond & Mand, 1996). MOPITT uses both the sun (reflected) and earth (thermal) as infrared sources for the on-board correlation radiometer. Detailed information about the MOPITT instrument has been provided in Chapter 2, Section 5.1. The MOPITT level 3, month averaged product was used, in which column CO was calculated from retrievals of combined near and thermal infrared radiances, and was gridded at

1°×1° resolution (MOPITT Science Team, 2013).[1] Recent incorporation of reflected solar retrievals has enhanced information of surface concentrations. However, enhanced retrievals are only available during the day (Deeter et al., 2010). For this reason, only day-time retrievals were considered in this analysis.

An algorithm for model-satellite comparison was also developed during this PhD using the NCL programming language. Month averaged 3-D gridded GEOS-Chem CO values over Australasia were converted to the 1°×1° horizontal and 10-level vertical resolution of MOPITT, prior to being convolved with MOPITT averaging kernels. Modelled CO was subsequently integrated to column values and GEOS-Chem–MOPITT differences were then determined. Differences were converted back to GEOS-Chem horizontal resolution of 2°×2.5° before plotting. Correlation analysis has been used to quantify the comparison between model and measurements.

7.1.1 Accounting for instrument sensitivity

Instrumental sensitivity to altitude for remotely-sensed measurements is described by averaging kernels (AK), as discussed in Section 2.6. When comparing model results with measurements from remotely sensed instruments, it is necessary to combine the raw model output with the instrument averaging kernel. Smoothing model results with instrument averaging kernels is standard practice to ensure accurate comparison of model output with instrument measurements.

Both FTS and MOPITT instruments have trace gas specific averaging kernels. Combining model output with averaging kernels produces a smoothed model product, which is theoretically what the instrument would have retrieved, had the true atmosphere been described exactly by the model. In this way, instrument sensitivity may then be discounted from influencing model-measurement differences. Smoothing of model output has been completed using the method described in Rodgers & Connor, 2003.

The profile scaling algorithm of GFIT was used to calculate the averaging kernels for Darwin CO, as well as HCHO and C_2H_6 at both Wollongong and Darwin. These averaging kernels therefore tend to be influenced by the shape of the a priori. Wollongong CO and Lauder CO and C_2H_6 were retrieved using the SFIT2 program, which used optimal estimation techniques. These retrievals therefore produce averaging kernels less dependent on the a priori, reflected in a different shape to those retrieved by GFIT.

[1]Data were obtained from the NASA Langley Research Center Atmospheric Science Data Center.

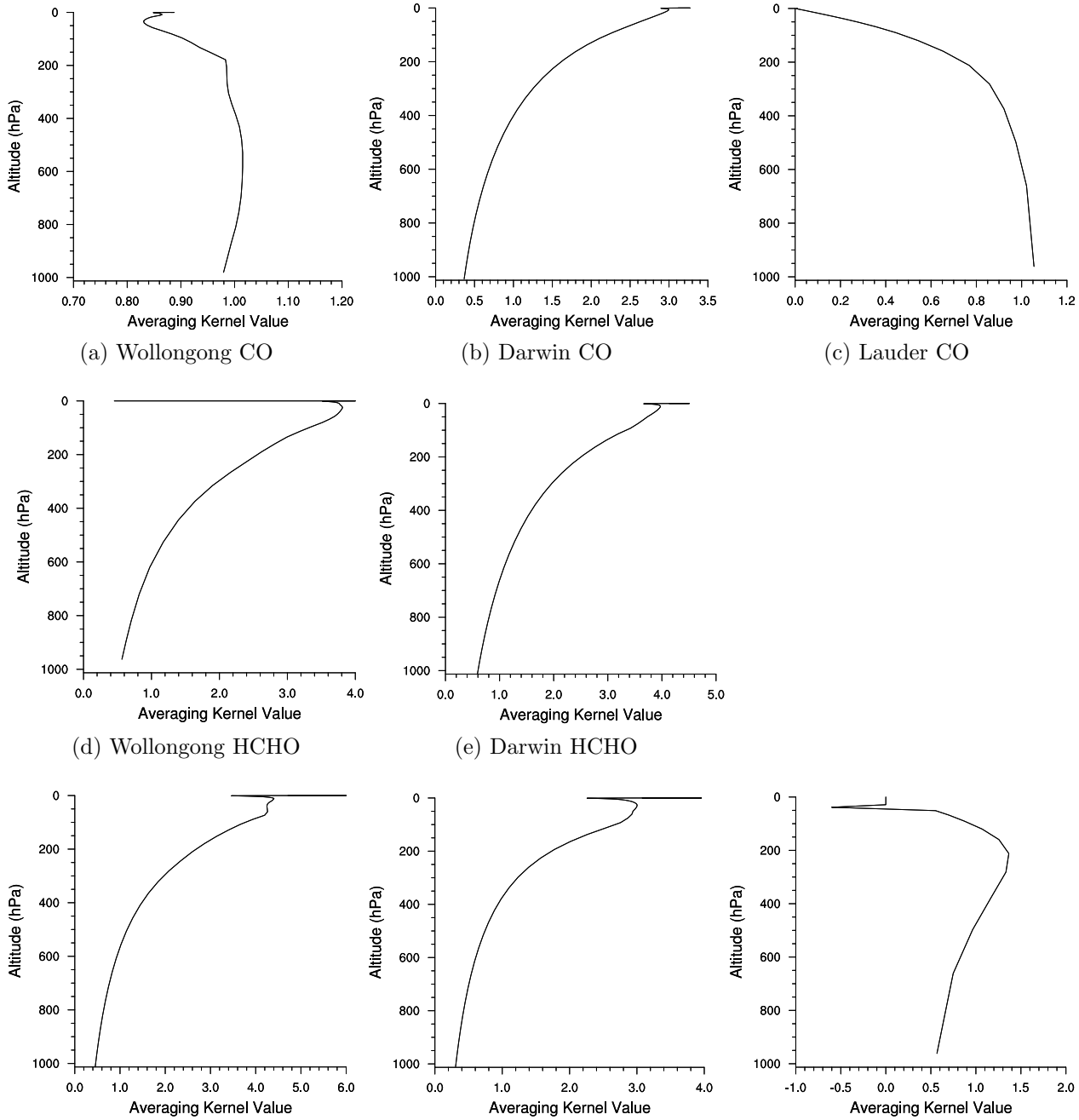

(a) Wollongong CO (b) Darwin CO (c) Lauder CO

(d) Wollongong HCHO (e) Darwin HCHO

(f) Wollongong C_2H_6 (g) Darwin C_2H_6 (h) Lauder C_2H_6

Figure 7.1.2: FTS total column mean averaging kernels (molec cm^{-2}/molec cm^{-2}) for each trace gas at each station. Averaging kernels are in vector form. Note at Lauder averaging kernels were not available for HCHO, therefore Wollongong mean HCHO averaging kernel was used.

All trace gases studied here are predominantly tropospheric, therefore averaging kernel values below 100 hPa contribute the most. Over-counting represented in the GFIT averaging kernels above 100 hPa do not contribute significantly to the column values.

When comparing model output for CO, HCHO and C_2H_6 with their respective measurements from solar FTS, the vector form of the averaging kernel was applied to modelled partial column profiles. Averaging kernel matrices can be simplified to vector form due to profile scaling in the retrievals, as described in (Washenfelder et al., 2006). A smoothed model total column value (c_{smooth}) is determined by implementing Equation 7.1.1.

$$c_{smooth} = c_a + \mathbf{a}(\mathbf{pc}_{GEOS-Chem} - \mathbf{pc}_a) \tag{7.1.1}$$

where: c_a is the FTS a priori total column, $\mathbf{a}$ is the instrument total column averaging kernel, $\mathbf{pc}_{GEOS-Chem}$ is modelled GEOS-Chem partial column profile and $\mathbf{pc}_a$ is the instrument a priori partial column profile.

For model comparison with daily averaged FTS measurements, mean representatives of instrument averaging kernels and a priori profiles were used at each measurement site for each trace gas species. Mean FTS averaging kernels are plotted in Figure 7.1.2.[2]

Modelled CO has also been compared with MOPITT satellite based measurements. In this instance, the averaging kernel matrix is applied to modelled mole fraction profiles. Averaging kernel convolution produced a smoothed model mole fraction profile, which was then pressure-weight integrated to produce a smoothed total column value. The smoothed vmr profile ($\mathbf{vmr}_{smooth}$) was calculated by:

$$\mathbf{vmr}_{smooth} = \mathbf{vmr}_a + \mathbf{A}(\mathbf{vmr}_{GEOS-Chem} - \mathbf{vmr}_a) \tag{7.1.2}$$

where: $\mathbf{A}$ is the MOPITT averaging kernel matrix, $\mathbf{vmr}_{GEOS-Chem}$ is the GEOS-Chem mole fraction profile, and $\mathbf{vmr}_a$ is the MOPITT mole fraction a priori profile.

[2]As HCHO averaging kernels and a priori profiles were not available for Lauder, those from Wollongong were used. Wollongong is closer in latitude to Lauder than Darwin, and had more retrievals than Darwin, therefore was deemed to produce a mean averaging kernel adequate to apply at Lauder. It is envisaged with updated HCHO retrievals at Lauder past 2005, averaging kernels will become available.

Averaging kernel matrices and a priori profiles are provided for each MOPITT pixel in the publicly available product. The MOPITT averaging kernel matrix is a 10×10 array, describing instrument sensitivity for each of the 10 vertical layers of retrieval. As the month average MOPITT product was used here, month averaged a priori profiles and averaging kernels from MOPITT retrieval files were convolved with month averaged GEOS-Chem output. Figure 7.1.3 provides an example of the MOPITT averaging kernel matrix at Wollongong for January 2008.

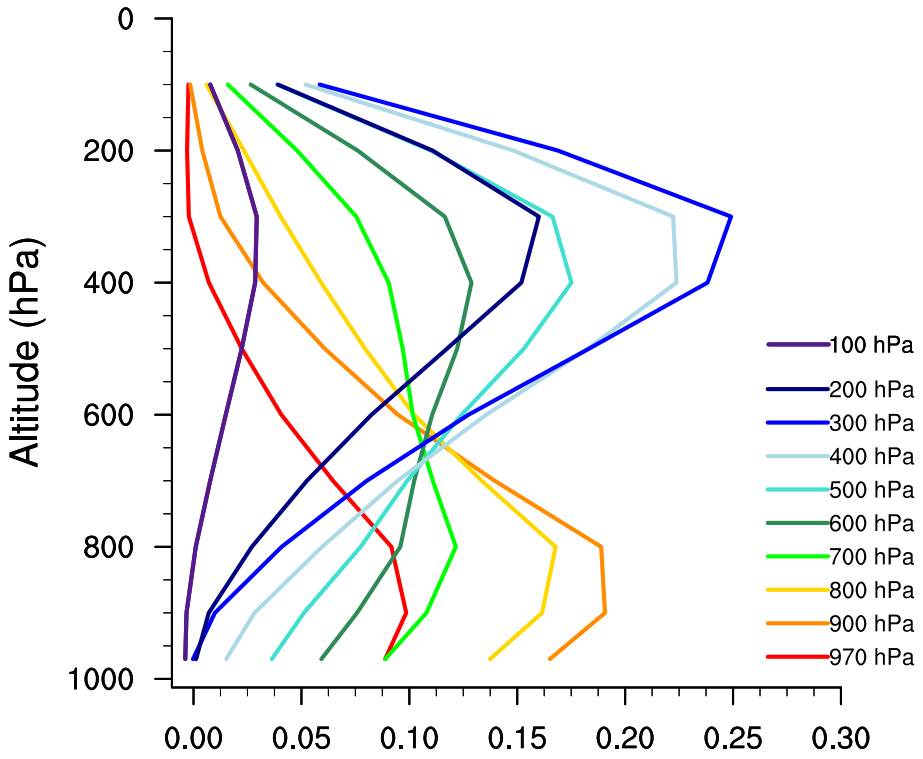

Figure 7.1.3: Example MOPITT CO mole fraction averaging kernels (mol mol^{-1}/mol mol^{-1}), at Wollongong for January, 2008. Each line corresponds to the averaging kernel centred at the specified altitude in a 10-layer grid: a floating surface altitude (970 hPa in this example) plus nine equally spaced levels from 900 to 100 hPa.

7.2 Comparing GEOS-Chem output with FTS measurements

Application of averaging kernels generally improves model-measurement comparisons. For example, correlation analysis was performed between GEOS-Chem and ground based FTS for pre- and post- averaging kernel application. Correlation values remained consistent and significant following convolution with averaging kernels however model-measurement correspondence was better (see Table 7.2.1).

Table 7.2.1: Tabulated correlation values (Pearson's r) for CO between FTS measurement timeseries and GEOS-Chem results with and without averaging kernel (A_K) application. All correlations are significant ($p<0.01$) and are recorded for Wollongong (WOL) Darwin (DAR) and Lauder (LAU). Slope and intercept (int) values are from standard linear regression.

Location	**Without A_K**			**With A_K**		
	r	slope $\frac{(\text{molec cm}^{-2})}{(\text{molec cm}^{-2})}$	intercept molec cm^{-2}	r	slope $\frac{(\text{molec cm}^{-2})}{(\text{molec cm}^{-2})}$	intercept molec cm^{-2}
DAR	0.787	0.895	1.79×10^{17}	0.739	1.07	3.61×10^{16}
WOL	0.685	0.862	2.33×10^{17}	0.685	0.871	2.33×10^{17}
LAU	0.837	0.801	9.48×10^{16}	0.838	0.869	6.10×10^{16}

In Figure 7.2.1 the daily averaged total column CO from GEOS-Chem (with AK application) and FTS measurements at Wollongong, Darwin and Lauder, are presented along with corresponding correlation information. Generally, GEOS-Chem represents atmospheric CO column well at each station, corresponding well with measurements. Seasonality of both model and measurement timeseries at all stations indicates a maximum in October, well known to coincide with maximum biomass burning source in the Southern Hemisphere. Darwin is more sensitive to local biomass burning, as displayed by greater interannual variability in the October peak. Biomass burning in the region around Darwin is influenced by climate conditions, such as those related to El Niño Southern Oscillation (ENSO).

Further analysis between model and measurements identified model biases. The Wollongong CO column peak in October is often underestimated by GEOS-Chem, as in 2005, 2007 and 2008. This may be due to dilution effects of local biomass burning. Underestimation is more likely due to biases in distant sources due to a peak in transported biomass burning emissions to Wollongong for October. Plume dilution from

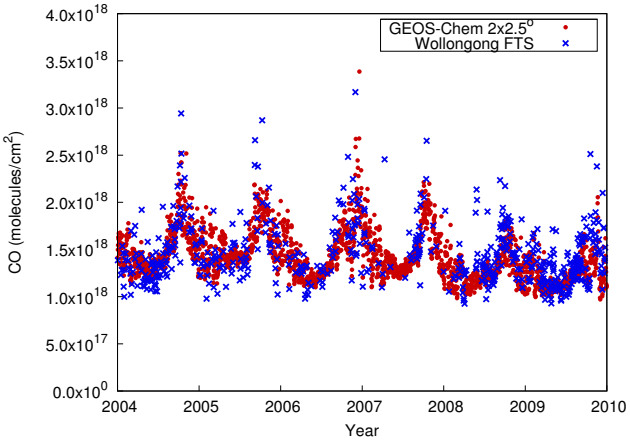

(a) Wollongong CO timeseries

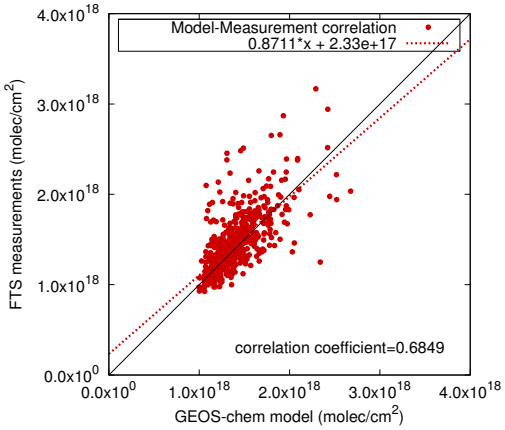

(b) Wollongong CO correlation

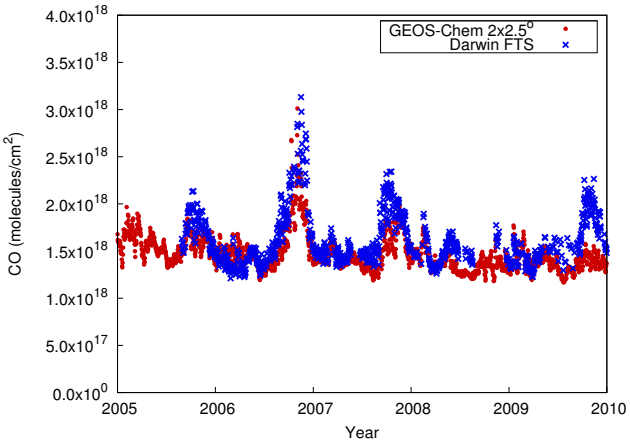

(c) Darwin CO timeseries

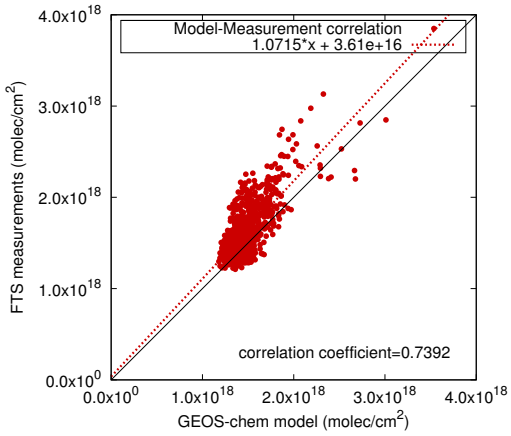

(d) Darwin CO correlation

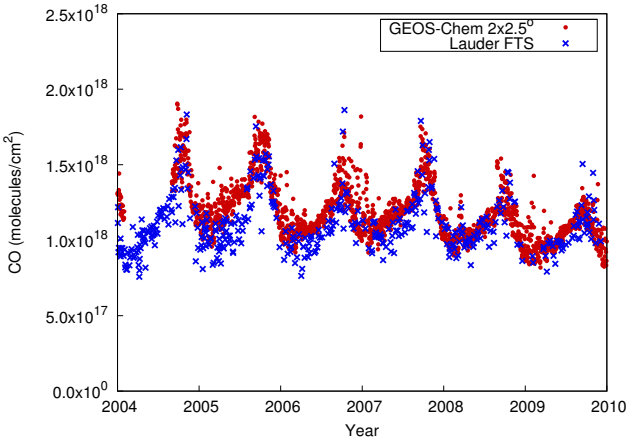

(e) Lauder CO timeseries

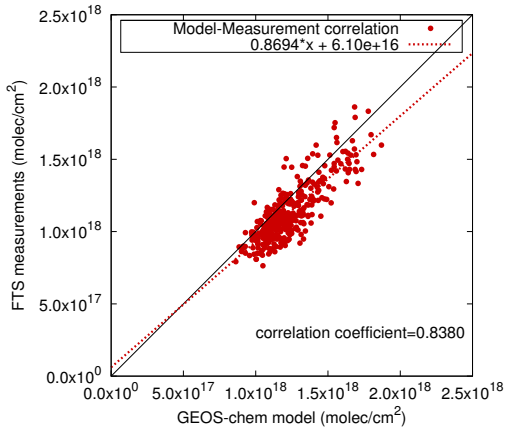

(f) Lauder CO correlation

Figure 7.2.1: Timeseries and model-measurement correlation of total column CO. Model data has been convolved with instrument averaging kernels.

distant sources is a known source of error in CTMs due to numerical diffusion effects (Rastigejev et al., 2010). The next section (7.3), compares model with satellite data and shows this underestimation in October is widespread, supporting a bias in transported CO. Darwin CO is consistently underestimated by GEOS-Chem, particularly during the October maximum, indicating underestimation in biomass burning from local and/or transported sources. In comparison, GEOS-Chem overestimates Lauder column CO, with a higher bias in the earlier years 2004-2006, than in the later 2007-2009 years.

The CO timeseries plots in Figure 7.2.1 show a good level of agreement in correlation analysis. Correlation analysis reflects how well the model seasonal cycle matches the measurements. Moderate correlation is seen at Wollongong (Pearson's r = 0.685, $p<0.01$) with Darwin showing good correlation (r = 0.739, $p<0.01$), and correlation is best at Lauder (r = 0.838, $p<0.01$). The correlation at Lauder is an improvement on the previously determined 0.65 using tagged tracer run of GEOS-Chem in Duncan et al., 2007. Lower correlation occurring at Wollongong is likely due to this site being influenced by many local sources and losses, as compared with the other sites. For example, land types surrounding the FTS sites were presented in Chapter 6, Section 6.6, which showed Wollongong to have a more variable surrounding land use than the other two stations. These variable local influences at Wollongong may be difficult to represent with GEOS-Chem due to spatial dilution.

Model-measurement comparison for HCHO at Wollongong, Darwin and Lauder is presented in Figure 7.2.2. GEOS-Chem predicts the magnitude of Australasian HCHO quite well, being generally within the correct magnitude at all stations. As HCHO is a shorter-lived trace gas, it is influenced by local sources. A major source of HCHO in the Australasian region is from the oxidation of biogenic isoprene (Pfister et al., 2008), emissions of which are dependent upon light and heat (Guenther et al., 2006). Wollongong has the greatest annual variability in temperature among the three stations, and also has the greatest variability in HCHO column due to corresponding variability in the isoprene emissions. Additionally, Wollongong is located near forested regions, while the other two stations are located near extensive grasslands, which would also affect the extent of local isoprene emissions.

The HCHO total columns, for both model and measurements, peak in summer months at Wollongong, coinciding with the increase in temperature. Except for 2009, GEOS-Chem overestimates the summer HCHO peak, suggesting perhaps inconsistencies in the MEGAN biogenic emission sub-module of GEOS-Chem. (Results of an isoprene sensitivity study reported in Chapter 8.) Model-measurement correlation at Wollongong is

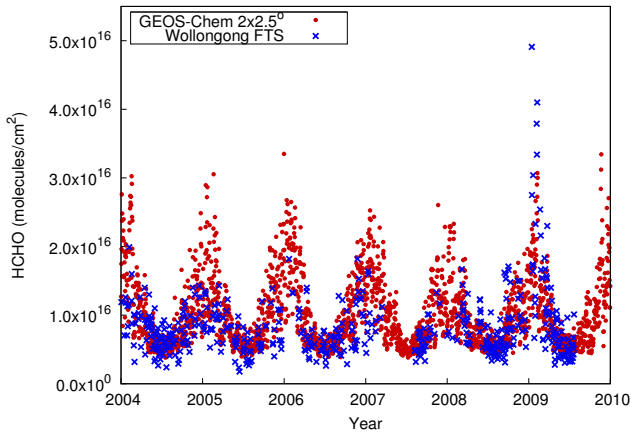

(a) Wollongong HCHO timeseries

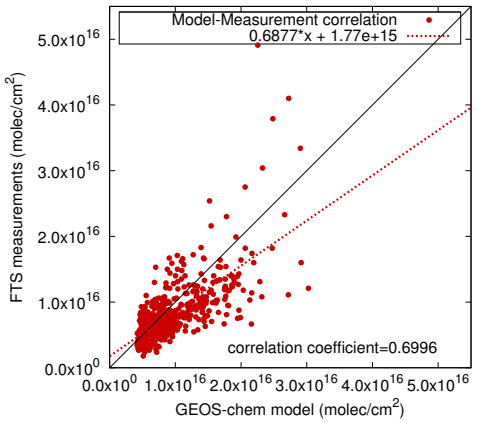

(b) Wollongong HCHO correlation

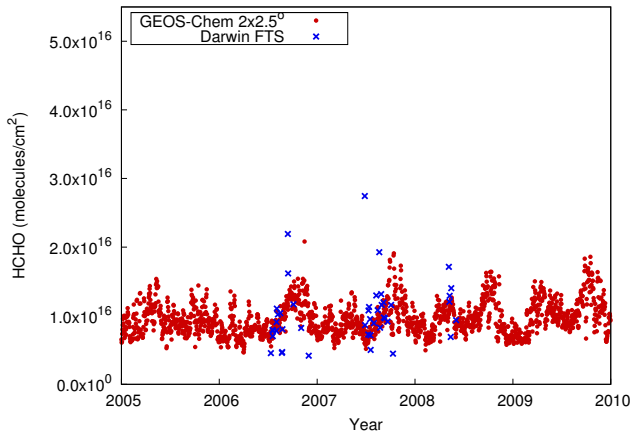

(c) Darwin HCHO timeseries

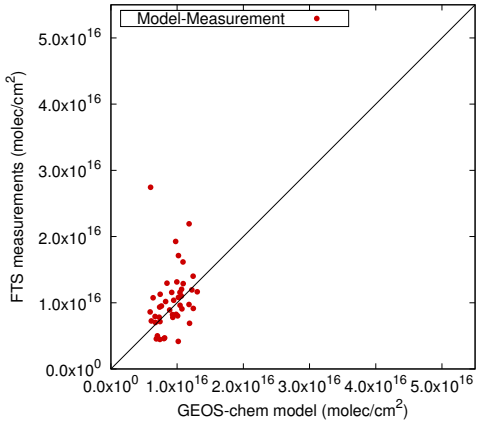

(d) Darwin HCHO correlation

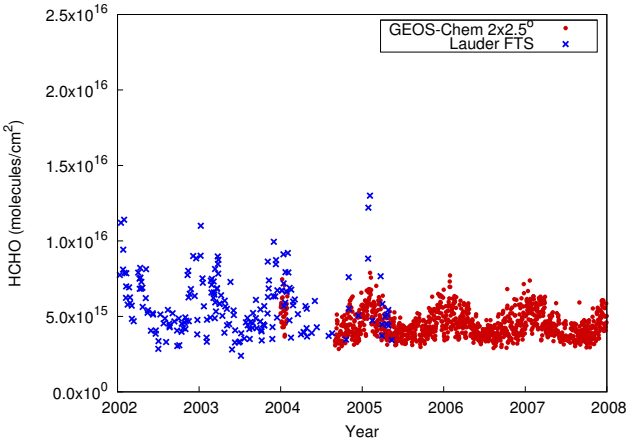

(e) Lauder HCHO timeseries

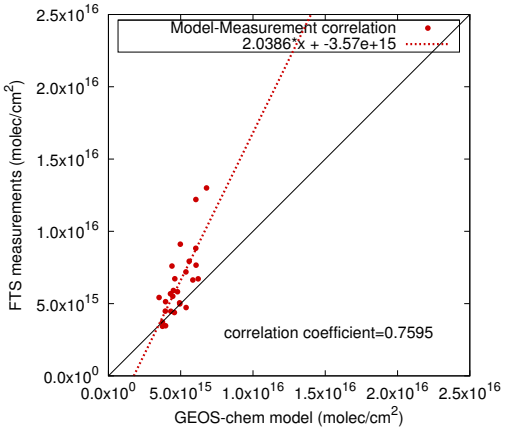

(f) Lauder HCHO correlation

Figure 7.2.2: Timeseries and model-measurement correlation of total column HCHO. Model data has been convolved with instrument averaging kernels. Darwin correlation was not significant at the 0.01 level, and therefore is not plotted.

good (r = 0.700, p<0.01), with the slope of the regression line reflecting modelled high bias in summer.

Model-measurement HCHO comparison at Darwin suggest correct magnitude, but does not provide conclusions about seasonality. Model results suggest Darwin sees the most inter-annually varying HCHO annual cycle, which is likely to also be related to ENSO climate phases through affecting the strength of local biomass burning and drought conditions. The Darwin correlation was not significant (p=0.07), and therefore more measurements are required before rigorous statistical comparisons can be made.

The HCHO column at Lauder also peaks in summer, although to a lesser extent than Wollongong. Timeseries have been plotted in Figure 7.2.2e from 2002 to 2008 to show multiple years of the measurement record. Due to measurements only being retrieved up to 2005, there is little overlap between model and measurements. From the overlap that is observed, and if retrievals after 2005 are similar to those prior to 2005, GEOS-Chem underestimates summertime HCHO. A study of isoprene sensitivity (full details in Chapter 8) shows this bias in HCHO cannot be overcome by increasing the source strengths for isoprene emissions already present in GEOS-Chem, therefore implying a missing source of HCHO. One possibility for a missing source of HCHO is a missing source of isoprene from marine origins (Shaw et al., 2010), as the model does not include ocean isoprene sources. New Zealand is a well-known area of ocean upwelling (Comiso et al., 1993), promoting a large population of marine organisms, and therefore likely to produce high isoprene emissions. Future experimental research is required in this area to address this hypothesis.

The model measurement comparison for C_2H_6 is presented in Figure 7.2.3. It is immediately apparent that GEOS-Chem vastly overestimates C_2H_6 column values at all three sites. GEOS-Chem C_2H_6 results are approximately five-times larger than FTS measurements at Wollongong and Lauder. The mis-match in C_2H_6 was unexpected, as a previous comparison with a GEOS-Chem tagged tracer run showed good agreement for Wollongong (Paton-Walsh et al., 2010b). Comparison at Darwin is difficult due to minimal measurements and which do not provide enough C_2H_6 data to make a valid comparison (p=0.3). However, initial comparisons suggest GEOS-Chem also overestimates Darwin by a factor of two to three.

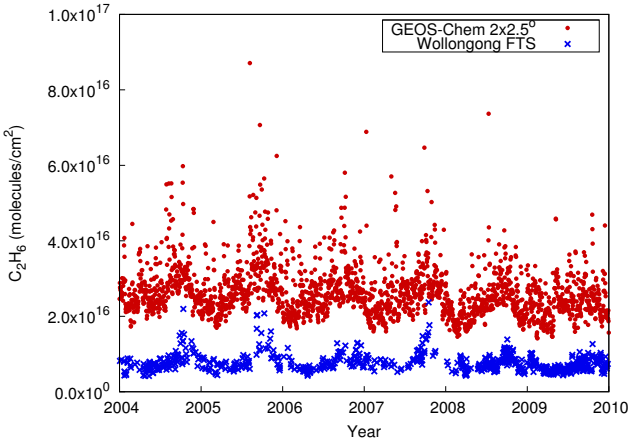

(a) Wollongong C_2H_6 timeseries

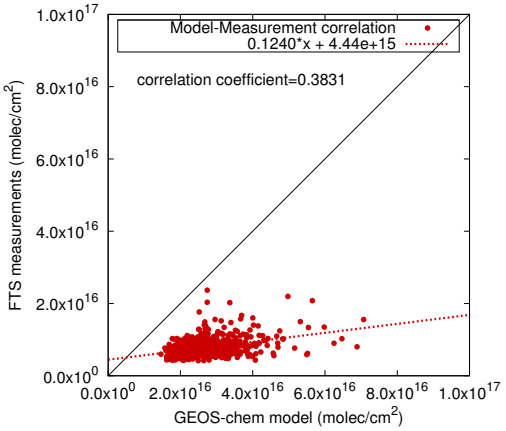

(b) Wollongong C_2H_6 correlation

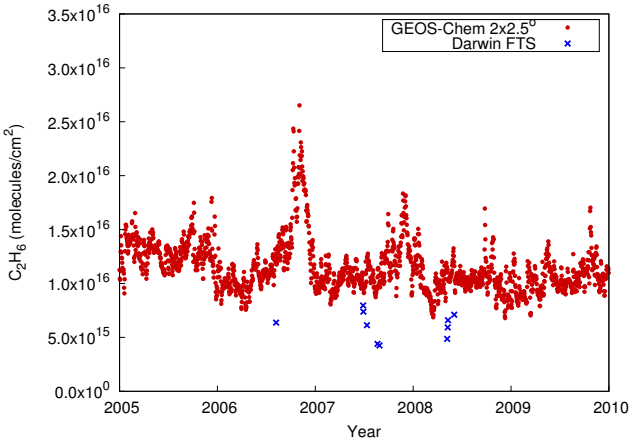

(c) Darwin C_2H_6 timeseries

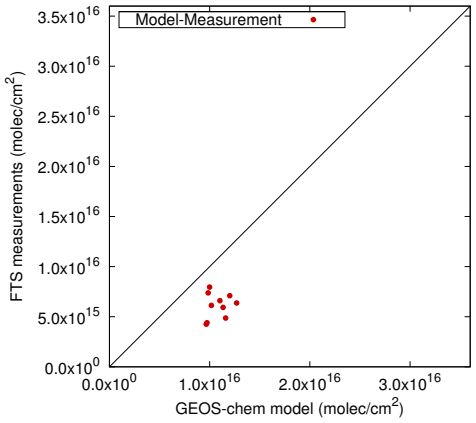

(d) Darwin C_2H_6 correlation

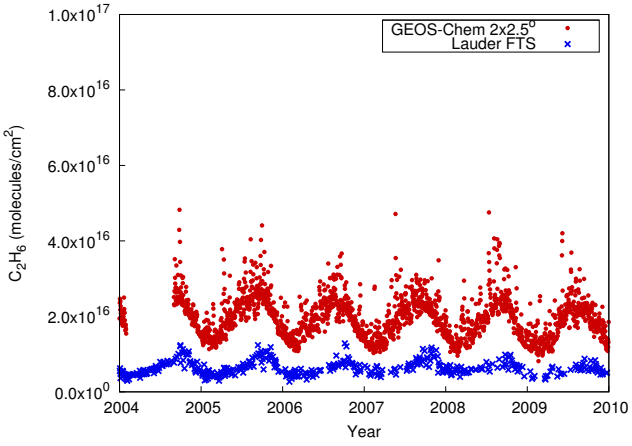

(e) Lauder C_2H_6 timeseries

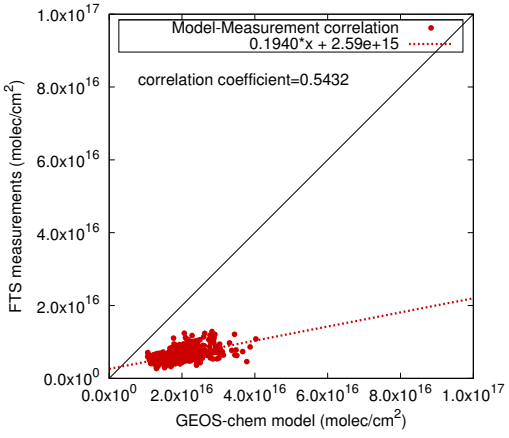

(f) Lauder C_2H_6 correlation

Figure 7.2.3: Timeseries and model-measurement correlation of total column C_2H_6). Model data has been convolved with FTS averaging kernels. Darwin correlation was not significant to the 0.01 level, and therefore is not plotted.

Correlation values between model and measurements at Wollongong (r=0.383, p=0.01) and Lauder (r=0.543, p=0.01) indicate seasonality of C_2H_6 is not well represented by GEOS-Chem. The annual cycle of the measurement timeseries at Wollongong and Lauder produces a maximum in October. Ethane is mainly sourced from biomass burning in the Southern Hemisphere, and therefore like CO, the maximum C_2H_6 in October coincides with maximum biomass burning. Modelled C_2H_6 column at Wollongong rises sharply in August, while measurements rise in September. At Lauder, the peak in model C_2H_6 occurs in September, a month earlier than measurements. Additionally, at both Wollongong and Lauder, modelled seasonal variability is much greater than measurements indicate.

Overestimation of C_2H_6 by GEOS-Chem is most likely due to biases in model emission inventories. In the Southern Hemisphere, C_2H_6 is emitted mainly from biomass burning, with some contribution from anthropogenic sources, therefore biases could exist in either inventory. Additional comparison and analysis of ethane is completed in Chapter 8, where seasonal cycles are further investigated and the source of ethane overestimation is identified to be from the anthropogenic inventory.

7.3 Comparing GEOS-Chem and MOPITT CO

Model-measurement comparisons were studied for CO over the entire Australasian region, plus a portion of Indonesia using MOPITT satellite-based measurements from 2008. Differences between month averaged values are displayed in Figures 7.3.1 and 7.3.2, which were calculated by subtracting measured values from corresponding model values (with AK applied). Red areas in the figures indicates model high bias and blue indicates model low bias.

A consistent high bias in GEOS-Chem is apparent in the tropical region 10° N to 15° S. During February and December much of the tropical region is obscured by clouds (grey pixels), however, data from surrounding areas suggest the region is overestimated by GEOS-Chem. In January, overestimation extends to the Australian continent. May through August, there is a high bias over Java centred about 0°, 100°E. The small spatial extent of this high bias, suggest the model overestimation is likely due to biases in tropical region emissions rather than transported biases. These are probably due to biases in GFED2, which uses satellite data of fire activity, burnt area and vegetation productivity to estimate fire emissions. It is likely these products are affected by visibility during cloudy events, frequent in the tropics. GFED2 may therefore miss biomass burning events, requiring estimation of biomass burning for cloudy scenes, which the results here suggest may be too high.

A low bias in GEOS-Chem transported CO is apparent in the comparisons from April to December, extending from approximately 20° S to 60° S. The consistent spatial extent of this low bias is indicative of a general underestimation in modelled background CO over Australasia. Maximum underestimation occurs in October, coinciding with Southern Hemisphere biomass burning peak, which suggests the model bias is due to biomass burning sources.

Underestimation of CO in this latitudinal band by GEOS-Chem may be due to biases in model transport or emissions from distant sources. Emissions of CO from biomass burning in South America and southern Africa occur during April to December (Edwards et al., 2006a,b). GFED2 has been found to include forest fire sources from South America, with inadequately small tropical forest source of CO from southern Africa and Madagascar (Vigouroux et al., 2012). Therefore, it is likely the low model bias found here is due to low fire emissions in southern Africa. The new GFED3 inventory includes updated emissions for southern African forest fires, and it would be valuable for future work to determine if this updated inventory improves model results.

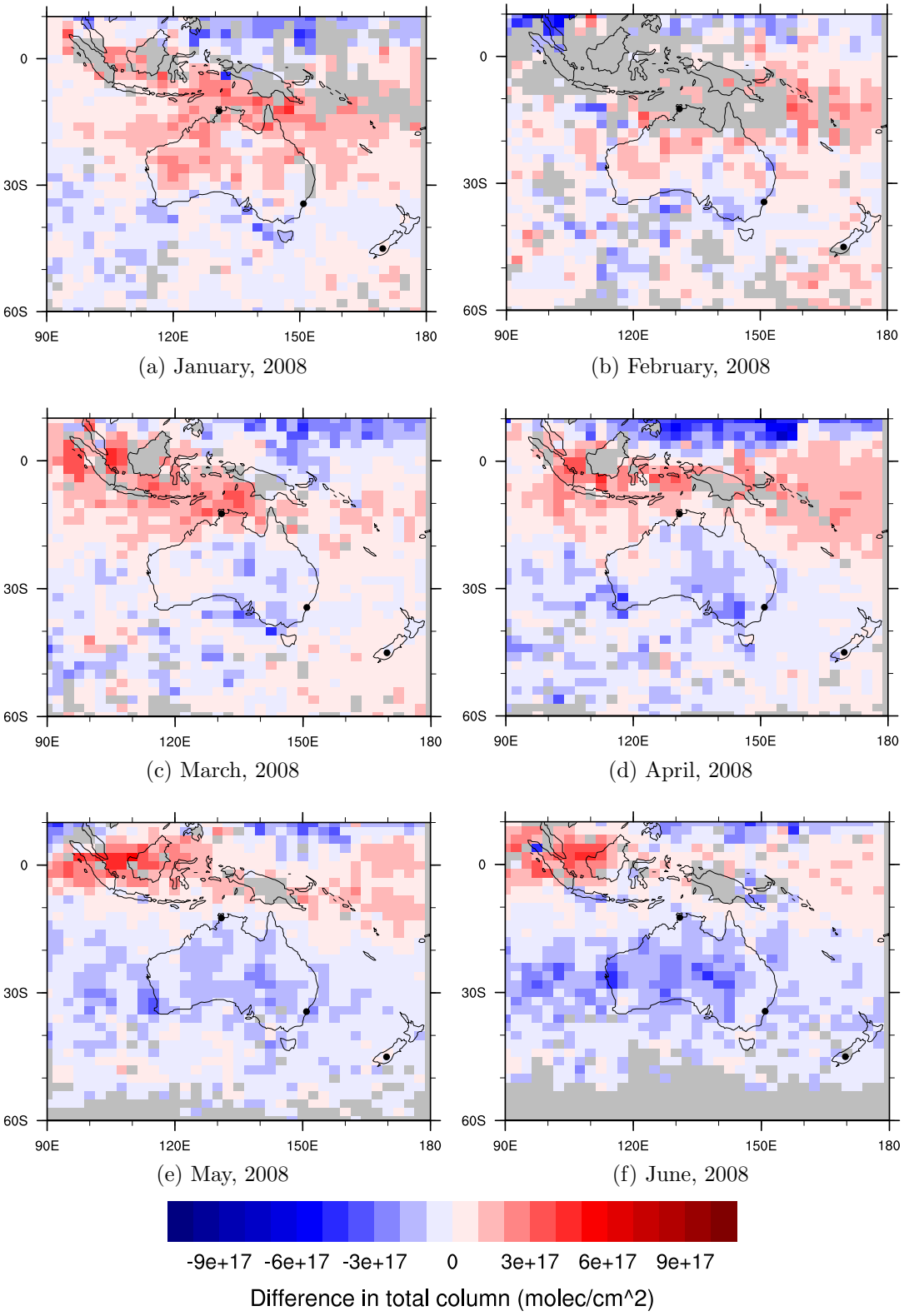

(a) January, 2008 (b) February, 2008

(c) March, 2008 (d) April, 2008

(e) May, 2008 (f) June, 2008

Figure 7.3.1: GEOS-Chem – MOPITT for month average total column CO over the Australasian and Indonesian region, January to June, 2008, plotted at 2°×2.5° resolution. Red shading indicates high- and blue shading indicates low- model bias. Grey pixels represent missing/cloudy values for MOPITT. Black circles = FTS stations.

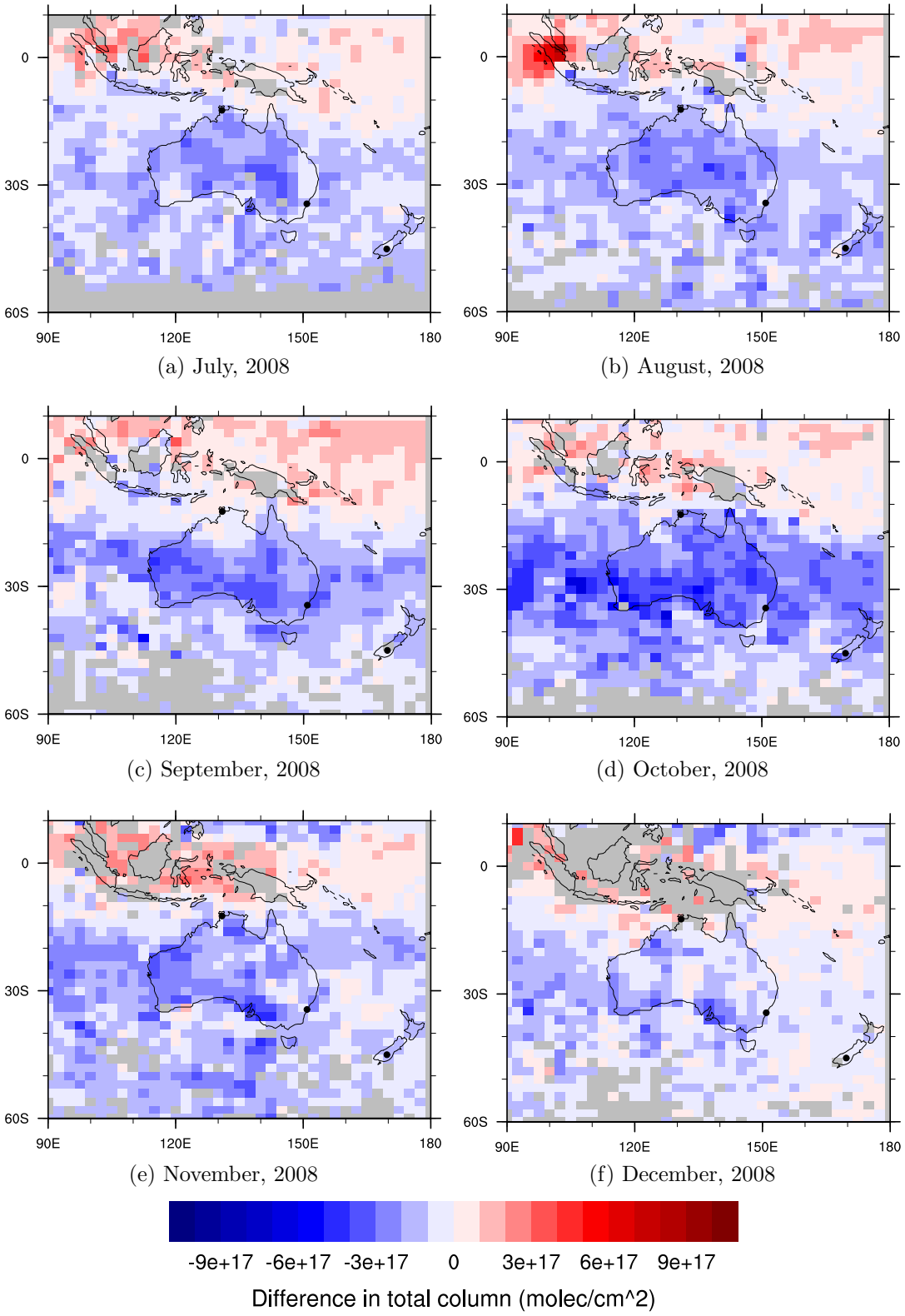

(a) July, 2008 (b) August, 2008

(c) September, 2008 (d) October, 2008

(e) November, 2008 (f) December, 2008

Figure 7.3.2: GEOS-Chem – MOPITT for month average total column CO over the Australasian and Indonesian region, July to December, 2008, plotted at 2°×2.5°resolution. Red shading indicates high- and blue shading indicates low- model bias. Grey pixels represent missing/cloudy values for MOPITT. Black circles = FTS stations.

A correlation analysis between GEOS-Chem and MOPITT total column CO measurements over the Australasian region for each month of 2008 is presented in Table 7.3.1. Correlation plots are shown for March and September in Figure 7.3.3.

Table 7.3.1: Tabulated correlation values (Pearson's r) between GEOS-Chem and MOPITT measurement timeseries in the region 10° S to 60° S, 110° E to 180° E. All correlations are significant (p<0.001). Correlations >0.70 are coloured blue.

Month	**MOPITT–GEOS-Chem correlation values**		
	r	slope $\frac{(\text{molec cm}^{-2})}{(\text{molec cm}^{-2})}$	intercept molec cm^{-2}
January	0.90	0.767	2.38×10^{17}
February	0.86	0.865	1.25×10^{17}
March	0.85	0.790	2.22×10^{17}
April	0.75	0.644	4.08×10^{17}
May	0.83	0.770	3.04×10^{17}
June	0.65	0.829	2.74×10^{17}
July	0.58	1.019	7.43×10^{16}
August	0.66	1.243	-1.93×10^{17}
September	0.82	1.474	-5.30×10^{17}
October	0.82	1.409	-3.87×10^{17}
November	0.74	0.868	2.71×10^{17}
December	0.84	0.851	2.13×10^{17}

Comparisons are consistent with the annual global correlation values (r = 0.81) between MOPITT and GEOS-Chem determined for 1 May 2004 to 30 April 2005 (Kopacz et al., 2010). From January–May and September–December correlations are very good (r >0.7), indicating that although biases exist which affect the magnitude of modelled column, GEOS-Chem never the less reproduces spatial distribution of column CO in the region. Lower correlations exist for June to August (r <0.7), suggesting GEOS-Chem is less able to represent the column CO spatial pattern in these months. It is of note that these months include the high bias seen over Java. The reduced correlation in June to August may therefore be due to biases in the emission inventory over Indonesia.

In addition to correlation values, regression slopes and intercepts were determined using standard linear regression (Table 7.3.1). These values indicate the Australasian region is dominated by high bias November through January (slopes <1), with major error due to Indonesian overestimation. A low bias dominates the region August to October (slopes > 1), with the major source of model error due to transported CO. For July, the

relationship between model and measurement is at its best for the region, with close to 1:1 comparison and small intercept.

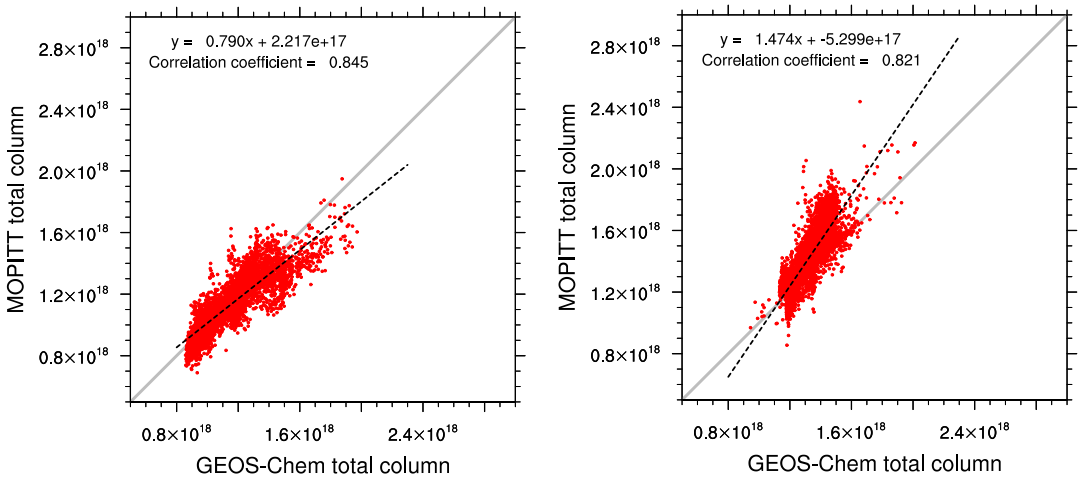

(a) March, 2008 (b) September, 2008

Figure 7.3.3: Example correlations between GEOS-Chem and MOPITT total column CO values for (a) March and (b) September. Dotted line indicates regressed line of best fit. Grey line indicates 1:1 for comparison. Correlations are significant ($p<0.001$).

7.3.1 Linking satellite and ground station comparisons

Spatial analysis comparing FTS station total column CO with the model lends insight into the MOPITT comparison results and can help interpret atmospheric composition over a wider area. Figure 7.3.4 presents the difference between GEOS-Chem and ground-based FTS measurements at each station for 2008. The differences between model and FTS at all stations are in the range of difference found for model-MOPITT comparisons, generally within $\pm 5 \times 10^{17}$ molec cm^{-2}. Some biases of larger magnitude exist on particular days at Wollongong (approx. -1×10^{18} molec cm^{-2}), likely due to the greater influence of local sources contributing to the FTS column. These local sources would not be expected in either GEOS-Chem or MOPITT due to spatial dilution.

Wollongong FTS CO (top panel of Figure 7.3.4) is shown to be generally underestimated by GEOS-Chem throughout 2008. This is consistent with model-MOPITT comparisons (Figures 7.3.1 and 7.3.2). The model-MOPITT plots show the low bias at Wollongong

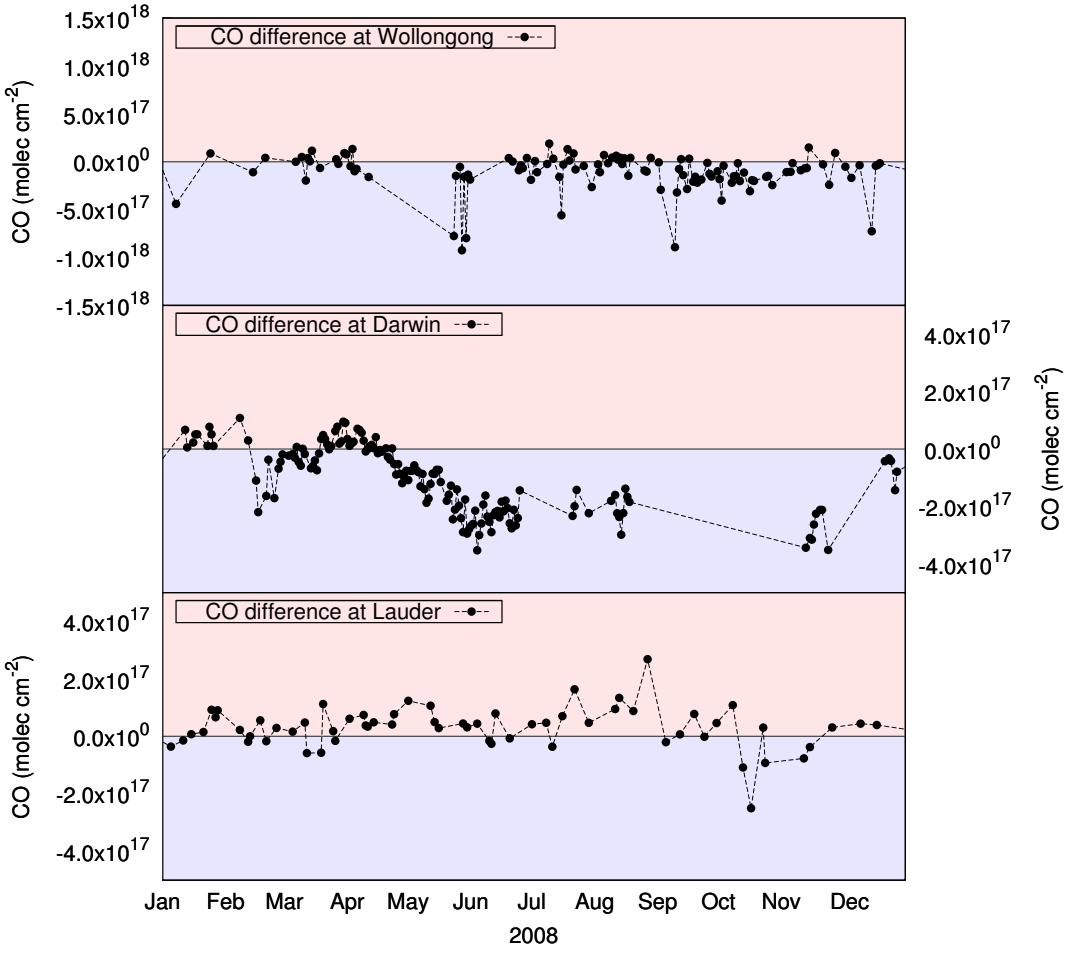

Figure 7.3.4: Difference between GEOS-Chem CO and FTS measurements in 2008. Red shading indicates model is biased high, and blue shading indicates low bias.

extends over the east coast of Australia. Because the same bias exists for Wollongong FTS as for MOPITT, this suggests the cause of the bias at the Wollongong station is affecting a wider east coast region. From April to the end of the year this low bias at Wollongong is representative of the bias for the Australian continent. Additionally from August to November, Wollongong bias is similar to the band stretching from 15° S to 45° S.

Darwin CO is also underestimated by GEOS-Chem, from May to December. Although measurement data is missing in September and October, other years have shown low bias in modelled values for these months. In the beginning of the year (January-April) there is an overestimation of Darwin CO by GEOS-Chem. This high/low bias is also consistent with the region around Darwin in model-MOPITT comparisons (Figures

7.3.1 and 7.3.2). Examining the low bias of Darwin in the latter half of the year shows it is consistent with the general underestimation of background CO. Therefore, low bias is mostly affected by error in transported sources, rather than error in local and Indonesian regional sources.

Comparisons of GEOS-Chem with ground-based measurements, for both Wollongong and Darwin, produce differences in the same direction as those determined in the comparison with MOPITT. Lauder model comparisons in 2008 show insignificant differences (Figure 7.3.4). Satellite comparison at Lauder also experiences very low bias in GEOS-Chem throughout 2008. Also, Lauder CO was found to have high correlation between GEOS-Chem and FTS measurements (r = 0.84). Therefore, this study concludes GEOS-Chem represents Lauder column CO robustly. This is not unexpected as Lauder is the most remote of the three stations and most likely to have well mixed background air, with minimal local sources, which is more easily reproduced by the model.

7.4 Conclusions

This research was the first to compare GEOS-Chem full chemistry simulation results with long-term timeseries of Australasian total column values of CO. Additionally, it is the first time total column amounts of HCHO and C_2H_6 have been compared with GEOS-Chem full-chemistry runs in Australasia.

Generally, GEOS-Chem represented CO well at all sites with minimal differences, suggesting the processes for this trace gas are well understood. The low bias in modelled October CO peak at Wollongong and Darwin was most likely due to underestimated southern African forest biomass burning in GFED2. A model comparison with GFED3 inventory would help support this conclusion.

Australasian model-measurement mismatch was further studied for CO using MOPITT satellite-based measurements from 2008. This showed that biases at Wollongong and Darwin FTS sites generally represented biases for wider local regions. Wollongong was well represented by modelled CO for most of the year, apart from September and October when transported CO was low. The bias at Wollongong was found to be representative of a larger stretch of the east coast. The model tended to overestimate tropical CO north of Darwin during the beginning of the year, supported by FTS mis-match in summer. Importantly, the satellite comparison indicated the October

low bias at Darwin was due to a low transported source, rather than underestimating local/Indonesian biomass burning. Lauder comparison showed insignificant bias.

Modelled HCHO summer maximum was biased high at Wollongong and biased low at Lauder. These results suggest an overestimation of summertime maximum biogenic sources at Wollongong and a missing summertime source at Lauder. Further measurements at Lauder and Darwin are required to build a more complete picture of HCHO at these stations. HCHO analysis would also benefit from a comparison with satellite measurements, such as HCHO from the Ozone Monitoring Instrument (OMI), with specific focus on the Australasian region.

Modelled C_2H_6 was biased high at all stations and uncorrelated seasonally. The cause of this was found to be an emission inventory bias (discussed in detail in the next Chapter, 8). The inventory bias was determined without time to perform an additional corrected simulation, which is left for future research.

Overall, this study concludes that GEOS-Chem is a valid tool for studying Australasian atmospheric CO and HCHO, while additional model evaluation of C_2H_6 with corrected emission inventories is required.

Chapter 8

Evaluation of the Earth-System Model, ACCESS

8.1 Introduction

Recent advances in computational performance have allowed development of Earth System Models, which aim to couple simulations of many components involved in Earth's biogeochemical cycles. Here, a new Earth System Model, the Australian Community Climate and Earth-System Simulator (ACCESS) is evaluated for skill in representing atmospheric composition. ACCESS is developed by Australian researchers at CSIRO and the Bureau of Meteorology.

ACCESS was in its infancy throughout the duration of this PhD, therefore the comparison performed here was a first-look at output from the ACCESS chemistry module, with respect to evaluating the representation of atmospheric composition for trace gases CO, HCHO and C_2H_6. Preliminary evaluation had been performed at CSIRO with AGAGE surface measurements of CH_4 and O_3, however, no total column comparisons had been completed. As no such comparison had yet been performed with ACCESS, the aim of evaluation was to determine whether general magnitude and patterns of atmospheric composition were realistic over Australasia.

Evaluation was performed for the trace gases CO, HCHO and C_2H_6 by comparing with measurements and the chemical transport model (CTM), GEOS-Chem. The objective of ACCESS is to provide simulations for climate studies, and as a first-run used fixed emissions at year 2000 values. Therefore, the interest was not in comparing specific

detailed atmospheric events. Instead, a general understanding of the skill of ACCESS was investigated by using mean annual cycles over a climatological period. The skill of ACCESS to reproduce mean seasonal variability would lend confidence to its chemical mechanism.

Comparison with measurements evaluated the absolute accuracy of each model. There are a number of potential causes for model-measurement mis-match, namely biases in the modelled emissions, chemistry or dynamic processes. The ACCESS chemistry module included a basic chemical scheme, in order to optimise computational time during module coupling. It was therefore useful to compare with a well-established CTM such as GEOS-Chem that included a more extensive representation of chemistry, and which is devoted to reproducing chemical composition in all environments. Where GEOS-Chem out-performed ACCESS, an analysis of differences between models was then used to indicate relatively simple improvements to the ACCESS emission inventories and chemistry scheme, ultimately aiming to improve ACCESS atmospheric representation.

ACCESS emission inventories for CO and C_2H_6 were found to require updating, for magnitude and seasonal cycle mis-representation. Isoprene and related chemistry was found to be poorly parameterised in ACCESS and it was therefore recommended to include explicit representation in future simulations. Dynamics contributed a minimal role in changing atmospheric composition at the magnitude of ACCESS underestimation. However, the varying meteorology of the El Niño-Southern Oscillation climate regime explained some interannual variability of measurements. Additionally during the comparison, the stratospheric boundary condition of NO_2 was corrected. Overall, this evaluation of ACCESS has led to several recommendations for model improvements and suggestions for further model study.

8.2 Comparison Procedure

Although ACCESS aims to simulate interconnected aspects of the earth system, including atmospheric composition and chemistry, the model was run in an atmosphere-only coupled mode, to streamline development on specific ACCESS modules. Here, analysis was performed on the chemistry module of ACCESS, which is based on UK model UKCA. Simulation was performed over the climatological period 1980 to 2000 and was carried out at the CSIRO Marine and Atmospheric Research division, using the Aus-

tralian National Computing Infrastructure (http://nci.org.au/). Specific ACCESS running parameters were detailed in Chapter 6, Section 6.5. Briefly, model dynamics was driven by simulated meteorology and uses constant emissions based on year 2000 emissions from IPCC AR4. As the purpose of this study was to determine skill in representing general patterns in atmospheric composition, output was provided as monthly averaged mole fraction profiles, at each of the selected stations.

ACCESS monthly averaged profiles were converted into total column values by integrating the pressure weighted product, using programs developed in Perl and NCL, and as described in Appendix D. Averaging kernels from ground based solar Fourier Transform Infrared Spectrophotometer (FTS) measurements were convolved with model profiles where appropriate, prior to calculating total columns. Target trace gases were CO, HCHO and C_2H_6. Trace gases NO_2 and O_3 were also used in the study of stratospheric NO_2 model conditions.

Measurements from ground based solar Fourier Transform Infrared Spectrophotometers (FTS) were used to compare total column values. FTS are located at the University of Wollongong (-34.406, 150.879), Darwin (-12.425, 130.892) and Lauder (-45.038, 169.684). Solar FTS measurements have been previously explained in Chapter 2, Section 2.4. Briefly, Solar FTS uses the infrared absorption of direct sunlight by molecules in the atmosphere to determine a total column amount of trace gas. Total column values were retrieved from infrared spectra via the programs GFIT (Washenfelder et al., 2006) and SFIT-2 (Pougatchev et al., 1995). Retrievals were combined into daily averages, followed by monthly averages.

ACCESS total column values were also compared with output from the chemical transport model GEOS-Chem. GEOS-Chem v8-03-01 full–chemistry Ox-NOx-VOC simulation was performed using $2^\circ \times 2.5^\circ$ horizontal and 47 level vertical resolution from 2004 to 2009, using the GEOS5 reanalysis meteorological product to drive dynamics, and various emission inventories. Details of GEOS-Chem run parameters and emission inventories were discussed in Chapter 6, Section 6.3. GEOS-Chem output was in daily averaged profiles, which were convolved with instrument averaging kernels and converted into total column values in the same manner as for ACCESS. Daily values were then averaged to yield mean monthly values.

As the interest was determining the general skill of ACCESS simulations, algorithms were developed using Perl and NCL to compare and plot mean annual cycles of monthly total column values. Mean annual cycles were calculated for each of the multi-year

month-averaged timeseries from ACCESS, FTS measurements and GEOS-Chem.

Due to the nature of the ACCESS evaluation being a first-look, comparison algorithms were required to overcome some challenges. Specifically, there was no complete temporal overlap between the three datasets for the entire time period 1980 to 2009. ACCESS simulations ran 1980 to 2000, while GEOS-Chem simulations ran from 2004 to 2009, according to meteorological file availability. Additionally, measurement stations were commissioned at various dates: Wollongong in 1996, Darwin in 2005 and Lauder in 1994. Therefore, mean annual cycles were calculated for the periods of overlap between datasets. This resulted in two averaging periods for the FTS measurement timeseries, one overlapping with ACCESS and the other with GEOS-Chem.

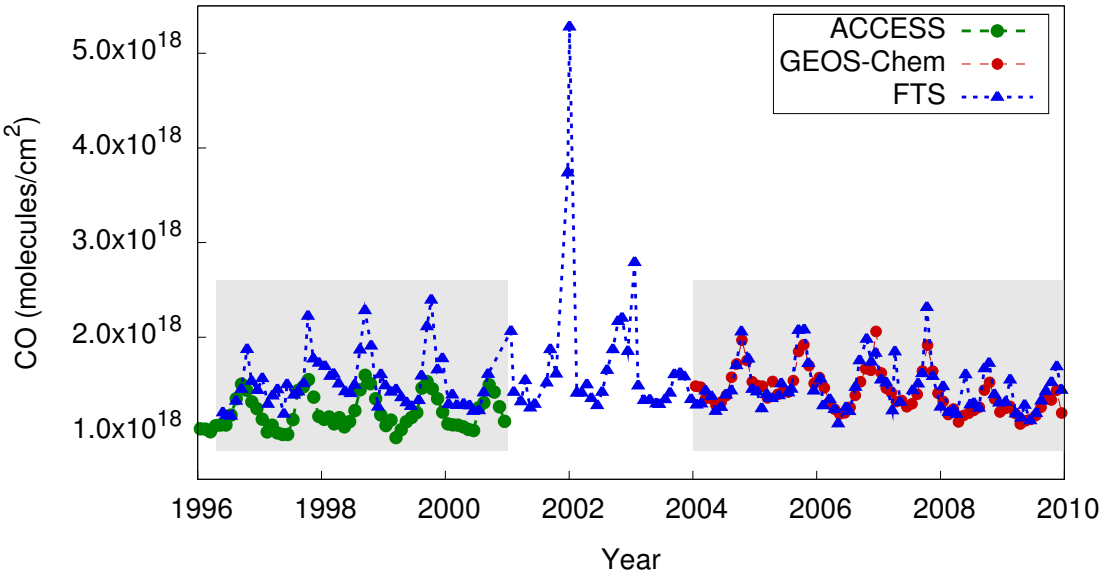

Figure 8.2.1: Timeseries of monthly averaged total column CO at Wollongong. ACCESS is shown in green circles, GEOS-Chem in red circles and ground–based FTS measurements in blue triangles. Shaded areas indicate regions of overlap. Error bars are omitted for clarity.

For example, timeseries of the three datasets for monthly total column CO is displayed for Wollongong in Figure 8.2.1. At Wollongong, overlaps occur between the ACCESS and FTS datasets from 1996 to 2000, and between the GEOS-Chem and FTS datasets from 2004 to 2009. These overlap dates specify the two averaging periods at Wollongong. As a result, ACCESS is compared with a different mean measurement annual cycle than GEOS-Chem. ACCESS results were then indirectly compared with GEOS-Chem output, by comparing the average annual cycles of measurements from the two

time periods. Whilst this is not the most stringent of tests, it nevertheless was capable of identifying major deficiencies in the early development of the ACCESS chemistry module.

Overlap methodology was also applied to Darwin and Lauder. At Lauder, the two time periods of overlap were 1994 to 2000 and 2004 to 2009. At the time of writing, Lauder HCHO was only retrieved up to 2005, so a measurement mean cycle from 2003 to 2005 was used overlap with GEOS-Chem mean cycle 2004 to 2007. Darwin FTS was commissioned in 2005, therefore only the GEOS-Chem results overlapped with measurements at this location. Additionally, Darwin predominantly measures near infrared spectra, therefore records of mid-infrared species HCHO and C_2H_6 are sparse. All these complicating factors were taken into account when analysing mean annual cycles.

8.3 Analysis of mean annual cycles of total column values

Generally, ACCESS was found to be biased low for CO, HCHO and C_2H_6 column values at Wollongong, Darwin and Lauder. For CO and C_2H_6 columns, both magnitude and seasonal cycle were mis-represented by ACCESS. In contrast, GEOS-Chem gave a closer match of CO and HCHO to measurements than ACCESS, but overestimated the C_2H_6 column at all three sites. Detailed comparison for each trace gas follows.

8.3.1 Comparison for carbon monoxide

Mean annual cycles of total column CO for ACCESS, GEOS-Chem and FTS are presented for Wollongong, Darwin and Lauder in Figure 8.3.1. Annual cycles are displayed by mean monthly values averaged over the overlap periods previously described (Section 8.2) and are plotted with respective standard deviations. Smaller monthly standard deviation values in ACCESS indicate interannual variability is lower than for measurements or GEOS-Chem results, a reflection of non-varying emissions.

ACCESS CO results are significantly lower than measurements at Wollongong and Lauder and generally lie outside one standard deviation of the measurements, apart from the month of August. Specifically, ACCESS CO is biased low by $\sim$0.3–0.5$\times10^{18}$

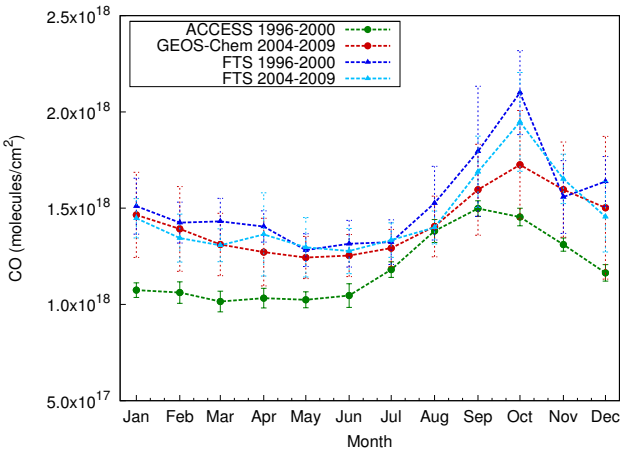

(a) Wollongong CO column annual cycle

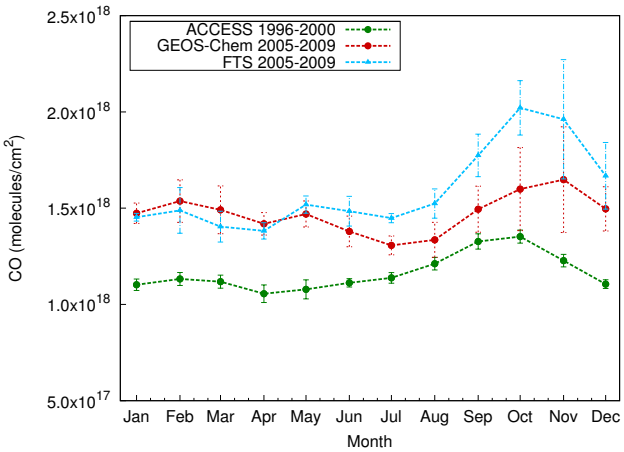

(b) Darwin CO column annual cycle

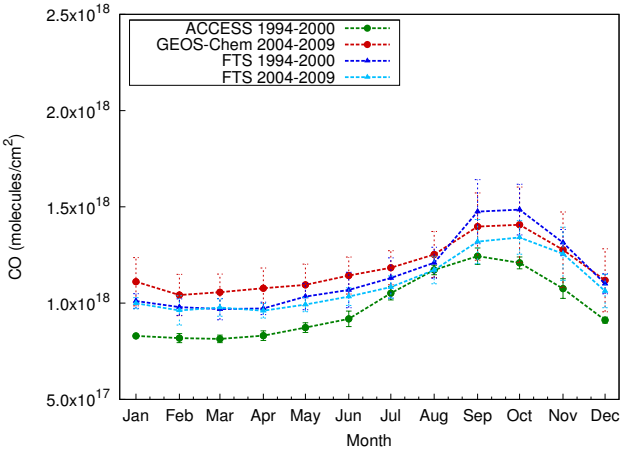

(c) Lauder CO column annual cycle

Figure 8.3.1: Annual cycles of average monthly total column CO at (a) Wollongong, (b) Darwin and (c) Lauder. Average annual cycles are shown for ACCESS (green circles), GEOS-Chem (red circles) and FTS (light blue and blue triangles). FTS results are split into time periods that overlap with ACCESS (blue) and time periods that overlap with GEOS-Chem (light blue). One standard deviation is shown about each month value.

molecules/cm^2 at Wollongong and Lauder. FTS timeseries does not overlap with ACCESS output at Darwin, therefore direct comparison can not be made. Trend analysis of CO from satellites shows column CO has decreased in the last decade (–0.88±0.52 % a^{-1} S.H., Worden et al., 2013a). Therefore, the Darwin annual cycle from 1996 to 2000 would have greater magnitude than the 2004-2009 annual cycle, similar to what is seen for the Wollongong and Lauder FTS records. Using this reasoning, Darwin ACCESS CO was indirectly determined to be biased low to the FTS measurements by $\sim 0.5 \times 10^{18}$ molecules/cm^2.

Additionally, ACCESS CO annual cycle peaks early by one month at all stations. ACCESS CO peaks at Wollongong and Lauder in September whereas the measurement annual cycle peaks in October. This suggests an underestimation or early timing of the Southern Hemisphere biomass burning CO source.

In contrast, GEOS-Chem column CO compares well with FTS measurements for mean monthly values, generally lying within one standard deviation of the measurements. Exceptions are for Darwin July to October, where GEOS-Chem is biased low to measurements outside of one measurement standard deviation. Also, for Lauder from January to July, GEOS-Chem results are biased high to measurements, over measurement standard deviations. The shape of the annual cycle generally matches the measurements, although the November peak at Darwin is a month later than measurements.

Annual cycles from FTS measurements between the two average time periods (1996-2000 and 2004-2009 at Wollongong or 1994-2000 and 2004-2009 at Lauder) are within one standard deviation of each other, indicating small change in measurements over the entire time period 1996 to 2009. Since ACCESS and GEOS-Chem are supposed to represent these respective time-periods, it would be expected that output from each model would lie within model standard deviation of each other. However, they do not, and GEOS-Chem is closer to measurement results. This allows ACCESS to be indirectly compared with GEOS-Chem, arriving at the conclusion that GEOS-Chem more accurately represents total column CO compared to ACCESS. Limitations of ACCESS which may be contributing to modelled underestimation are further discussed in Section 8.4.

8.3.2 Comparison for formaldehyde

ACCESS HCHO results are biased low to the measurements at all three sites and underestimate the column by ~ 0.5–1.0×10^{16} molecules/cm^2 (Figure 8.3.2). Underestimation is greatest at Wollongong and Lauder during Austral summer and minimal underestimation occurs during Austral winter. Darwin HCHO measurements only overlap with GEOS-Chem time period, therefore ACCESS results were compared with measurements indirectly. GEOS-Chem and ACCESS HCHO results were expected to be within the standard deviation of each other due to the measurement mean annual cycles from both overlap periods being within standard deviation of each other at Wollongong and Lauder. Using this reasoning, the low bias of ACCESS is most pronounced at Darwin. Lack of interannually varying emissions in ACCESS led to smaller annual variability in total column values, which is represented by smaller monthly standard deviations compared with measurements.

In comparison, GEOS-Chem HCHO total column annual cycle compares well with corresponding measurements, reproducing the overall measurement magnitude well. Exceptions exist, specifically where GEOS-Chem overestimates summer column HCHO in Wollongong, from November to February (Figure 8.3.2a). Also, GEOS-Chem summer HCHO column at Lauder is underestimated. These summer mis-matches suggest a bias in HCHO sources or losses within GEOS-Chem.

Both ACCESS and GEOS-Chem reproduce the correct annual cycle at Wollongong and Lauder, with a winter minimum and summer maximum. Minimal measurements at Darwin limit the analysis of the seasonal cycle. GEOS-Chem and ACCESS both simulate a double-peak in column HCHO at Darwin, which is confirmed by measurements. However, offsets in the timing of the peaks is present in both models. More data is required from Darwin to confirm these comparisons.

A major deficiency in the version of ACCESS used for this study, was the lack of emitted isoprene and related chemistry. While CO was parameterised for isoprene oxidation, no such parametrisation existed for HCHO. This is of concern as HCHO is a major intermediate in the oxidation pathway of isoprene and is therefore highly influenced by isoprene emissions. Consistent underestimation of HCHO column by ACCESS was therefore likely to be due to lack of isoprene in the model system. Influence of isoprene emissions on the HCHO column was investigated with a sensitivity study using GEOS-Chem, and is discussed further in Section 8.4.2.

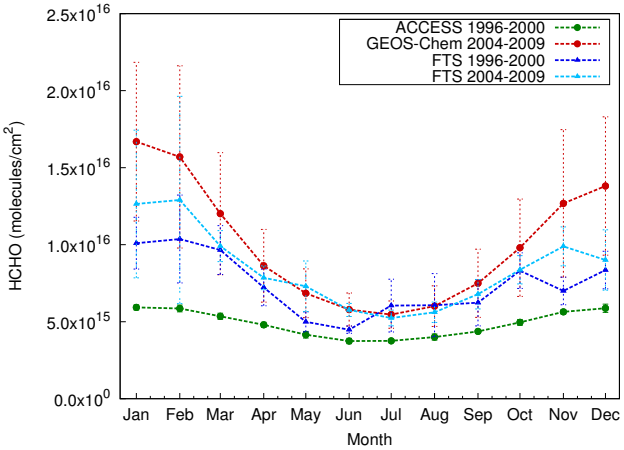

(a) Wollongong HCHO column

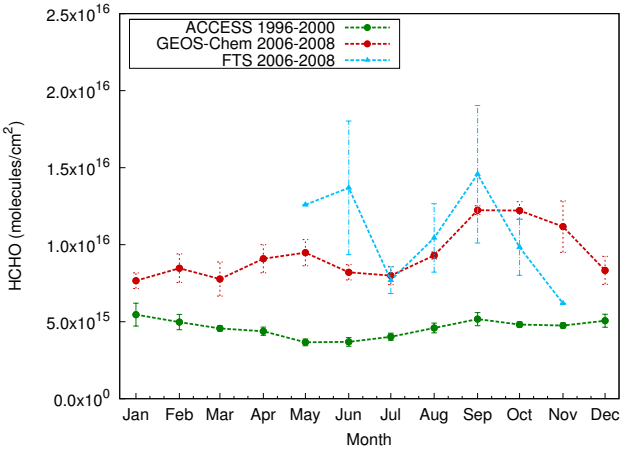

(b) Darwin HCHO column

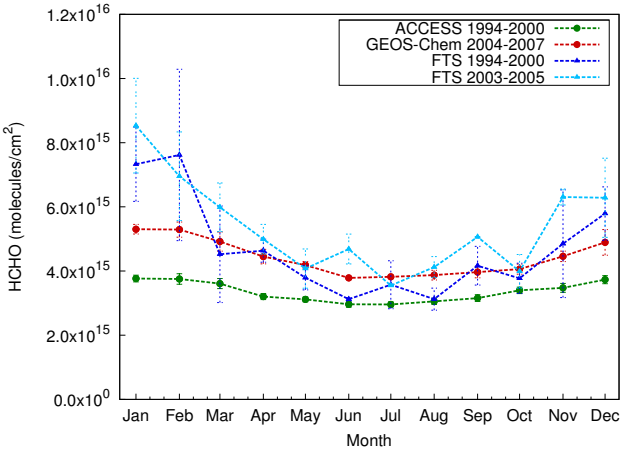

(c) Lauder HCHO column

Figure 8.3.2: Annual cycles of average monthly total column HCHO at (a) Wollongong, (b) Darwin and (c) Lauder. Average annual cycles are shown for ACCESS (green circles), GEOS-Chem (red circles) and FTS (light blue and blue triangles). FTS results are split into time periods that overlap with ACCESS (blue) and time periods that overlap with GEOS-Chem (light blue). One standard deviation is shown about each month value.

8.3.3 Comparison for ethane

Both models show difficulty representing ethane total column average annual cycle. ACCESS C_2H_6 generally underestimates the measurements at Wollongong and Lauder, outside the standard deviation of the measurements. Limited measurements at Darwin preclude conclusions, but ACCESS results fall within the magnitude of available Darwin measurements. At Wollongong and Lauder, ACCESS C_2H_6 peaks one month early in September, where as measurements peak in October, associated with peak in biomass burning. This timing bias for ACCESS C_2H_6 is similar to the annual cycle mis-match for total column CO, which suggests a common source mis-representation, most likely biomass burning.

In contrast, GEOS-Chem C_2H_6 column is biased high at all three sites, suggesting major source over-estimations. The high bias in GEOS-Chem C_2H_6 was surprising, as the model did a good job of representing CO and HCHO. Ethane has a strong biomass burning source, and due to GEOS-Chem CO comparing well with measurements, the magnitude of model biomass burning is predicted to be correct. Biases may therefore exist in other emissions inventories such as anthropogenic sources. Alternatively, loss mechanisms may be underestimated in the model. Further investigation into this mis-match is completed in Section 8.4.

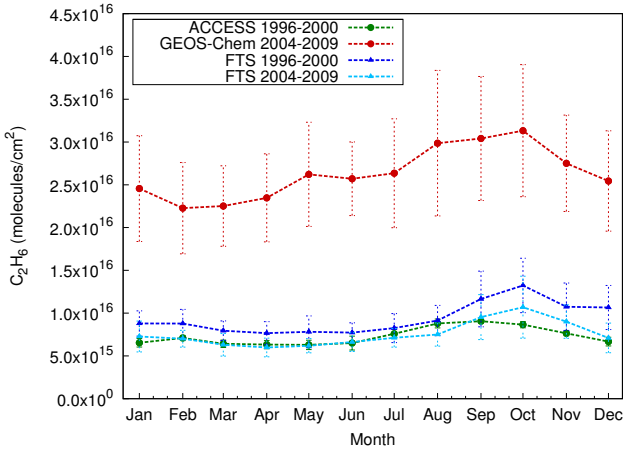

(a) Wollongong C_2H_6 column

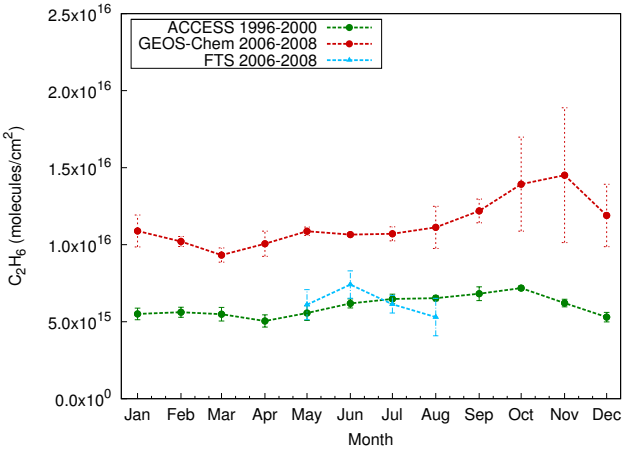

(b) Darwin C_2H_6 column

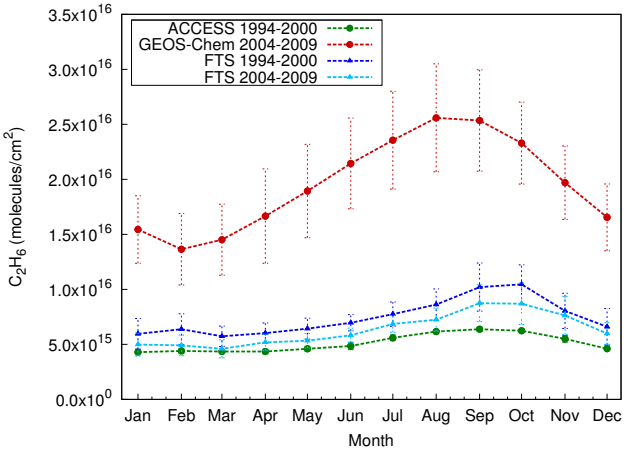

(c) Lauder C_2H_6 column

Figure 8.3.3: Annual cycles of average monthly total column C_2H_6 at (a) Wollongong, (b) Darwin and (c) Lauder. Average annual cycles are shown for ACCESS (green circles), GEOS-Chem (red circles) and FTS (light blue and blue triangles). FTS results are split into time periods that overlap with ACCESS (blue) and time periods that overlap with GEOS-Chem (light blue). Standard deviations are shown for each month value.

8.4 Discussion of ACCESS limitations

Evaluation of ACCESS showed that the model generally underestimated trace gases CO, HCHO and C_2H_6 at Wollongong, Lauder and Darwin, when compared with measurements. Additionally, CO and C_2H_6 annual cycle peaks are mis-timed. The chemical transport model GEOS-Chem performed better in comparison with CO and HCHO measurements, and was therefore used to investigate the cause of ACCESS limitations. Some model-measurement mis-match also occurred for GEOS-Chem, specifically for summer HCHO at Wollongong and Lauder as well as a general high bias of C_2H_6 at all stations.

Here, most likely causes for model biases and recommendations for ACCESS model improvement are discussed. Three main model components may be the cause of model bias: emissions, chemistry and dynamics. Each of these possibilities is investigated in the following sections, beginning with model emissions.

8.4.1 Emissions: ACCESS and GEOS-Chem differences

Emissions differences between models is an obvious cause of atmospheric composition differences between models. ACCESS and GEOS-Chem emissions were quantitatively investigated as a cause of different model responses. Annually averaged emissions for global and Australasian ($-10°$ to $-60°$, $110°$ to $179°$) regions were determined for each model and are recorded in Table 8.4.1.

Annual global and Australasian emissions for CO and HCHO are greater in ACCESS than in GEOS-Chem. Previously, it was shown that column results for these two trace gases are higher in GEOS-Chem than ACCESS. Total column differences imply GEOS-Chem includes additional secondary sources of CO and HCHO from chemistry, which are missing in ACCESS. Therefore, direct emissions in ACCESS are not the cause of column values to be biased low, which are instead due to a missing chemical source.

The most likely missing chemical source of CO and HCHO is from oxidation of isoprene. ACCESS does not include isoprene emissions, while GEOS-Chem does. In Australasia, isoprene oxidation is a very important source of CO and HCHO. In GEOS-Chem, oxidation of isoprene emissions annually contributed 24% over direct CO emissions on the global scale (Table 8.4.1). Comparatively in Australasia, isoprene oxidation annually contributed 57% over direct CO emissions. This is supported by Pfister et al., 2008,

who determined all photochemical sources of CO were of the same order as direct emissions. Isoprene oxidation over Australasia accounted for 50-80% of the photochemical CO sources, while over other continents contribution varied from 15-60%. Additionally, Pfister et al., 2008, determined 50-80% of annual column HCHO originated from isoprene over Australasia, while elsewhere the contribution was 10-60%. Thus, isoprene oxidation is highly relevant to Australasian atmospheric composition and is important to accurately include in atmospheric models. While ACCESS parameterises CO from isoprene oxidation, biases may exist in its magnitude and spatial representation. Additionally, no parametrisation was implemented for HCHO from isoprene oxidation.

Table 8.4.1: Global averaged emission comparison between ACCESS and GEOS-Chem. ACCESS emissions were kept constant at year 2000. GEOS-Chem emissions were averaged between 2004 and 2009.

	Trace Gas Emissions (Tg a^{-1})		
	CO	HCHO	C_2H_6
ACCESS			
Global	1800[a]	14.2	16.3
Australasia	64.1	0.526	0.291
GEOS-Chem			
Global	1040, *331*[b]	5.88	18.5[c]
Australasia	23.8, *31.0*	0.197	0.413
Literature			
Global[d]	1048–1640 *354–800*	9.7	13

[a] ACCESS CO emissions included an isoprene oxidation source, globally of 354 Tg CO a^{-1} (O'Connor et al., 2013).
[b] GEOS-Chem CO sources are the sum of direct emissions. Italics show indirect sources of CO calculated from oxidation of isoprene emissions, following a global average 30% oxidation to CO as determined in (Pfister et al., 2008).
[c] C_2H_6 emissions in GEOS-Chem were converted from TgC to TgC_2H_6
[d] Literature values are from (Warneck & Williams, 2012). CO values are sums of direct emissions. Italics for CO emissions describe oxidation of natural hydrocarbons, which include isoprene.

Ethane emissions in ACCESS (16.3 Tg) are of a similar magnitude to literature values (13 Tg), but simulated total column values were lower than measurements. This may indicate C_2H_6 direct emissions are underestimated or a chemical source is missing in ACCESS. Due to emissions already being greater than literature values, a missing chemical source is more likely.

The significant high bias of GEOS-Chem C_2H_6 columns to measurements and ACCESS may be explained by ethane emissions being much greater in GEOS-Chem than in ACCESS. This was further investigated by determining annual emissions at each of

the studied stations (Table 8.4.2). The relative difference of GEOS-Chem to ACCESS emissions was determined at each station and compared with the relative difference in total column values. For example, GEOS-Chem ethane emissions at Wollongong are 3 times the respective ACCESS emissions and approximately the same relative difference was determined for total column differences. As is evident in Table 8.4.2, Wollongong and Darwin total column differences between models are matched almost exactly with emissions differences. The large difference between ACCESS and GEOS-Chem C_2H_6 emissions at Lauder may be tempered by dynamic dilution effects. Atmospheric mixing of emissions is expected and combination with clean air from the ocean regions surrounding Lauder would give the lower difference in total column values. Also, since ACCESS total column values are closer to measurements, it can be concluded that the high C_2H_6 column simulated by GEOS-Chem are likely the result of a biased emissions inventory.

Table 8.4.2: Annual C_2H_6 emission comparison between ACCESS and GEOS-Chem at Wollongong, Darwin and Lauder. GEOS-Chem emissions were averaged between 2004 and 2009. Factor difference is defined as the number of multiples of ACCESS required to give GEOS-Chem values.

	Trace Gas Emissions (Tg a^{-1})			
	ACCESS	GEOS-Chem[a]	Factor difference	Column factor difference (σ)
Wollongong	3.61×10^{-3}	1.07×10^{-2}	3.0	3.6 ($\pm$0.3)
Darwin[b]	1.50×10^{-3}	2.59×10^{-3}	1.7	1.9 ($\pm$0.2)
Lauder	2.65×10^{-4}	1.93×10^{-3}	7.3	3.8 ($\pm$0.4)

[a] C_2H_6 emissions in GEOS-Chem were converted from TgC to Tg C_2H_6
[b] Due to grid-box alignment, GEOS-Chem at Darwin emissions are from the adjacent grid-box over land in order to accurately compare with ACCESS emissions over land.

Emission seasonality was determined for CO and C_2H_6 in each model to investigate ACCESS mis-timed total column peaks. Monthly global and Australasian emissions were calculated for each model, with GEOS-Chem emissions averaged between 2004 and 2009, and ACCESS emissions for the year 2000. Figure 8.4.1 displays the annual cycle of global and Australasian CO emissions. Differences exist between models globally and in the Australasian region. Globally, ACCESS CO emissions peak in September, while GEOS-Chem peak from August to September. For Australasia, ACCESS emissions peak in September while GEOS-Chem peaks in October. This indicates ACCESS total column CO values peak one month early in Australasian sites due to a timing bias in the emission inventory.

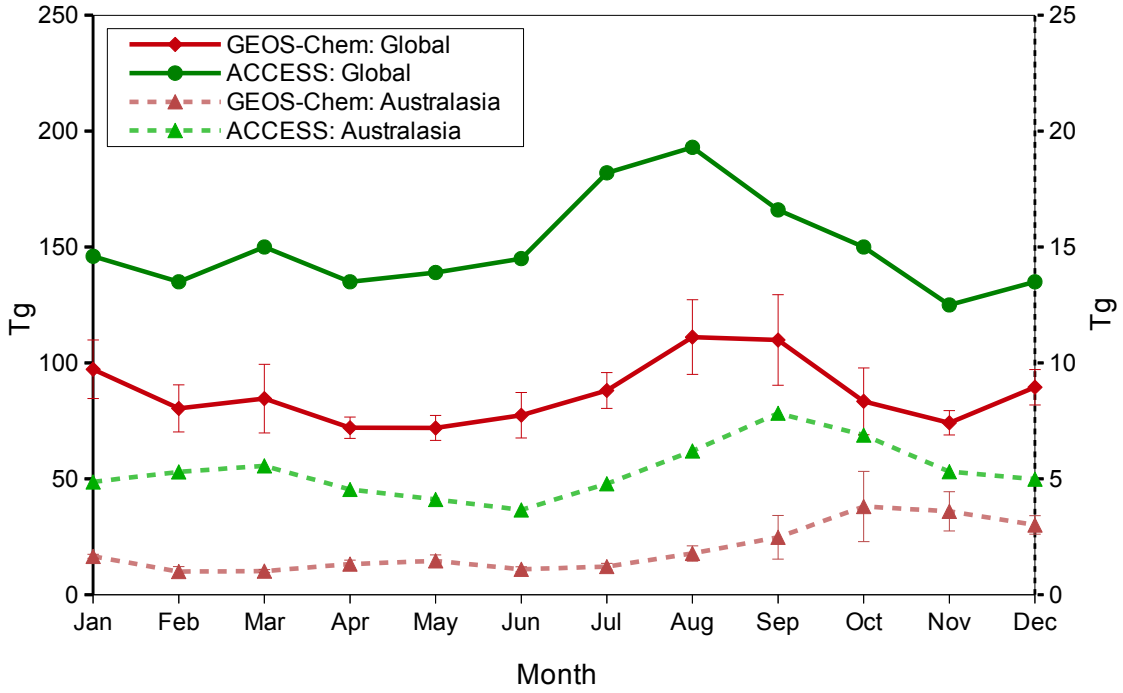

Figure 8.4.1: Annual cycle of ACCESS and GEOS-Chem emissions. (a) CO monthly emissions in ACCESS for 2000 (green) and GEOS-Chem for 2004-2009 (red). Left axis corresponds to global emissions (solid plot) and right axis corresponds with Australasian emissions (dashed plot).

It is important to note that the timing bias may be accurate for the year 2000, for example due to the effect of atypical biomass burning. The year 2000 was in the middle of the only continuous 3-year La Niña pattern between 1980 and 2009, which may be expected to have different emission patterns to previous and subsequent years. Although the timing of emissions may be correct for 2000, the results from this comparison show that on average over a longer time-period, emissions for Australasia are required to peak in October. Therefore, an emission inventory more representative of the mean emissions over 20 years is required, perhaps taken from a year other than 2000, if planning to run ACCESS with non-varying emissions.

Source contributions to CO emissions in Australasia are presented for GEOS-Chem in 2008 (Figure 8.4.2). The source of CO with highest variability is biomass burning, which drives variability in total emissions. The Australasian annual peak of CO emissions in October is driven by the peak in biomass burning contribution. Therefore, although ACCESS emissions are not able to be split into components, analysis of GEOS-Chem emissions indicate the cause of ACCESS CO emission timing bias is most likely due to a timing bias in biomass burning.

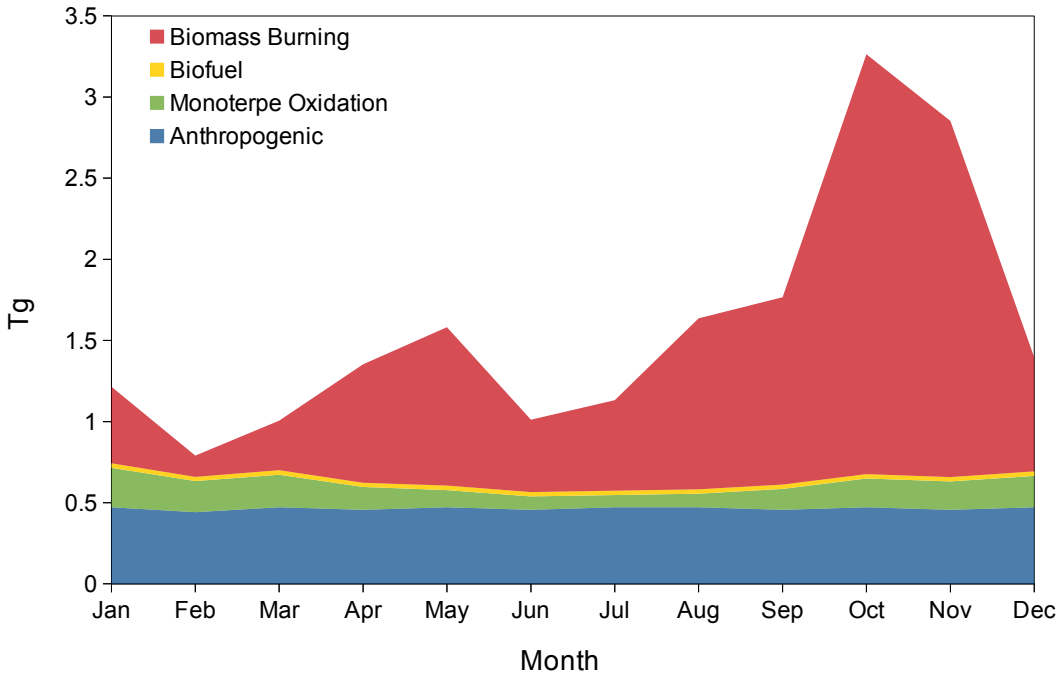

Figure 8.4.2: Annual cycle of GEOS-Chem emissions by source-type in 2008. Contribution to CO emissions are shown from biomass burning (red), biofuel (yellow), anthropogenic (blue) and monoterpene oxidation sources (green) to total emissions. Curve area is cumulative.

Figure 8.4.3 displays the annual cycle of global and Australasian C_2H_6 monthly emissions in ACCESS and GEOS-Chem. Globally, the annual cycle between the two models generally agrees. However, differences are seen between peak model emissions in the Australasian region. ACCESS C_2H_6 Australasian emissions peak in September, while GEOS-Chem peak in October. Source allocation of Australasian GEOS-Chem emissions in Figure 8.4.4 indicates that biomass burning emissions drive this annual peak. Therefore, similar to CO, the early timing of the C_2H_6 total column values in ACCESS is likely due to emission timing biases, particularly in the biomass burning inventory.

Additionally, Figure 8.4.4 indicates the cause of high bias in GEOS-Chem C_2H_6 column values for the Australasian sites. Globally, most of the annual 13 Tg a^{-1} of ethane emissions is produced in the Northern Hemisphere from anthropogenic and biomass burning sources, with only approximately 1 Tg a^{-1} attributed to the Southern Hemisphere and predominantly due to biomass burning (Rudolph, 1995; Xiao et al., 2008). However, as displayed in Figure 8.4.4, anthropogenic sources over Australasia in GEOS-Chem are over double that of biomass burning, which is not in line with a majority source from biomass burning. Investigating further, annual anthropogenic ethane emissions in

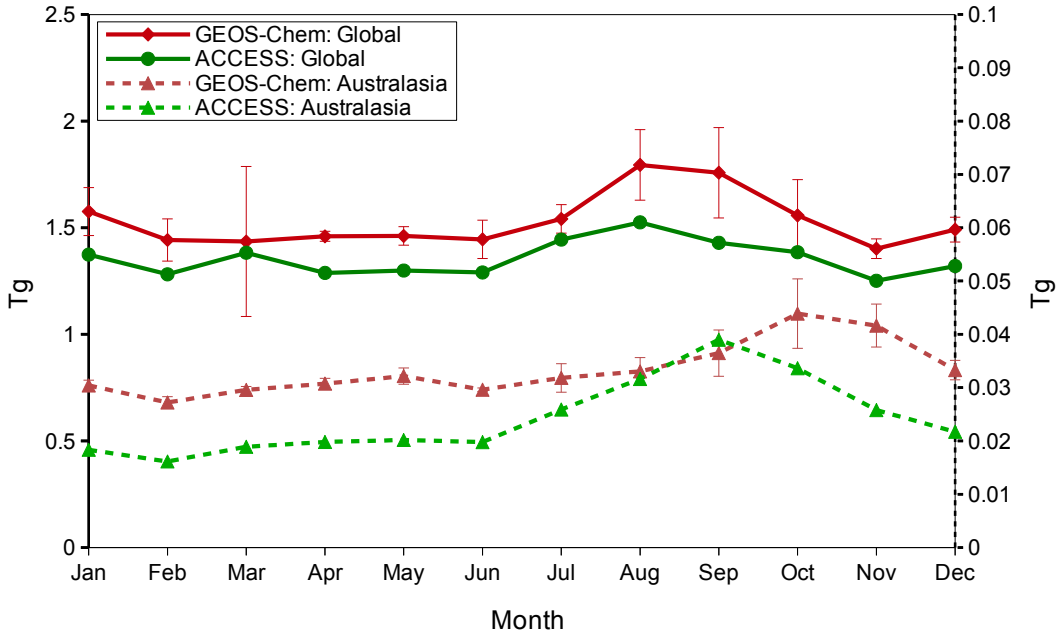

Figure 8.4.3: Global and Australasian monthly C_2H_6 emissions for ACCESS 2000 and GEOS-Chem 2004-2009. Left axis corresponds to global emissions (solid lines) and right axis with Australasian emissions (dashed lines).

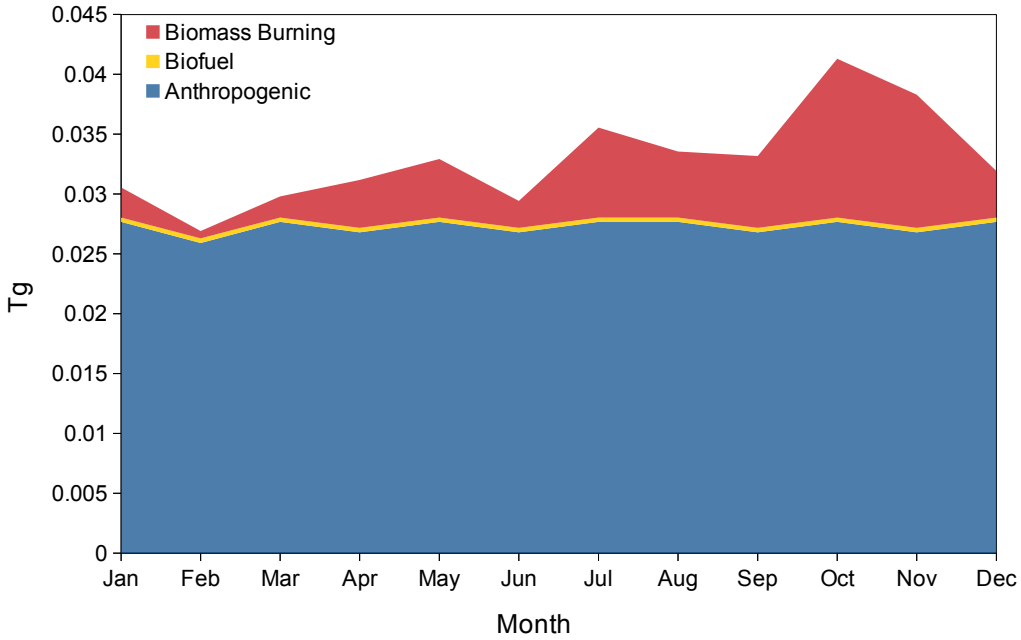

Figure 8.4.4: Contribution to monthly Australasian C_2H_6 emissions from biomass burning, biofuel, and anthropogenic sources for GEOS-Chem in 2008. Curve area is cumulative.

GEOS-Chem for the Southern Hemisphere in 2008 was 8.7 Tg, which was attributed to incorrect emissions over Southern Africa. This error has been fixed in the most recent version of GEOS-Chem v9-01-03, but was not changed in time for this study. Therefore, the high bias seen here in GEOS-Chem column C_2H_6 at Australasian sites is due to inaccurately high Southern Hemisphere background C_2H_6 from anthropogenic sources in Southern Africa.

While emission differences between models explain some major mis-matches, some discrepancies remain. Specifically, the mis-timed annual peak for CO and C_2H_6 can be explained by time biases in ACCESS biomass burning emissions inventories. The anthropogenic C_2H_6 emission inventory in GEOS-Chem is responsible for consistent overestimation of C_2H_6 column. However, the underrepresentation of CO, HCHO and C_2H_6 total column by ACCESS is due to missing chemical sources, which are further investigated in the next section.

8.4.2 Chemistry: isoprene sensitivity study

As determined in the previous section, a key deficiency of the ACCESS chemistry module employed here is the lack of isoprene and associated chemistry. CO parametrisation from isoprene oxidation was performed in ACCESS based off the global source of isoprene 503 TgC a^{-1} (Guenther et al., 1995), and was distributed spatially and temporally according to the same publication. Parametrisation and distribution based on values from 1995 values may not be accurate for other years, especially in locations where isoprene oxidation is a major contributor to the total column of CO, such as Australasia. In particular, (Guenther et al., 2006) have recently revised isoprene emissions to 440–660 TgC a^{-1}. Also, while a CO source in ACCESS is parameterised from isoprene oxidation, no such parametrisation was performed for HCHO or C_2H_6. This is particularly concerning for HCHO, which is a major intermediate in the oxidation pathway of isoprene. In order to investigate the contribution from isoprene oxidation to total columns of CO and other trace gases, a sensitivity study to isoprene emission amount was performed using GEOS-Chem.

GEOS-Chem v8-03-01 full-chemistry was run in identical conditions as previously described (Section 6.3) with the addition of an isoprene emissions scaling factor. Scaling factors were applied at 1.5, 0.5 and 0.1 of the standard run. Zero emissions were not implemented to avoid possible numerical errors. The year 2008 was chosen as a compromise between optimal data density in measurements and model representability. Specifically, model emissions from the GFED database were scaled after 2008, meaning 2008 is more consistent with reality. Also, FTS data density increased dramatically after mid-2007, following instrument automation. Total column annual cycles for CO, HCHO and C_2H_6 were compared for scaled and non-scaled GEOS-Chem simulation, the ACCESS simulation and FTS. Average annual cycles from FTS measurements were determined over 2008 to 2009.

It was determined that the low bias in ACCESS CO total column values could be accounted for by lack of isoprene oxidation sources (Figure 8.4.5). As isoprene emission amount was altered in GEOS-Chem, the magnitude of resulting CO total column changed in the same direction, however the annual cycle pattern remained consistent. A 50% reduction in isoprene emissions was found to reduce the GEOS-Chem CO total column within range of the ACCESS results for January to June at all three stations (Figure 8.4.5). At 10% of standard emissions, GEOS-Chem CO column magnitude reduced further (25–30% compared with standard simulation) and resulted in an improved match to ACCESS results at Lauder and Darwin for earlier months January to March. An improved match upon reduction of isoprene emissions suggests that isoprene oxidation parametrisation within ACCESS is too low for Australasia in the first half of the year. Alternatively, there may be a missing chemical source of CO that is equivalent to isoprene oxidation, possibly due to the lack of higher order VOCs and corresponding oxidation.

ACCESS CO was within the range of standard GEOS-Chem simulation results from July to December, which at Wollongong and Lauder are also within range of the FTS measurements. This indicated ACCESS CO parametrisation from isoprene oxidation is likely correct at these stations for the second half of the year. In contrast, at Darwin both models are biased low to the measurements in the latter half of the year. An improved match was seen between GEOS-Chem simulation with 150% standard emissions and Darwin FTS results from June to September suggest inadequately low isoprene emissions may be responsible for the mis-match in the middle of the year. However, remaining mis-match between this higher isoprene GEOS-Chem simulation and FTS in October and November, indicates a missing CO source not explained by

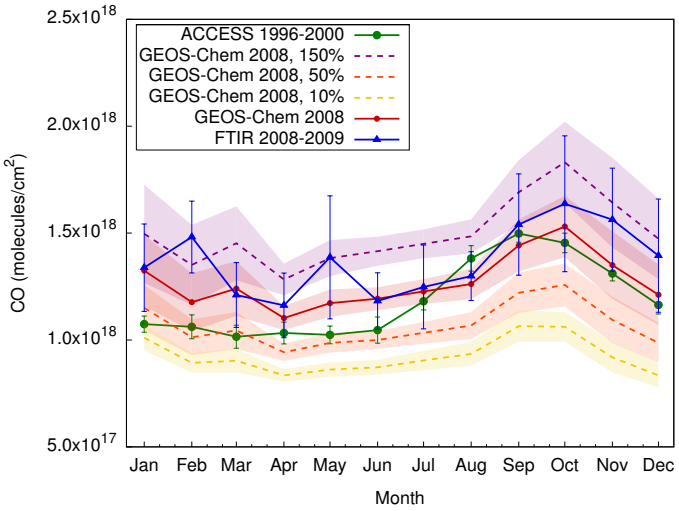

(a) Wollongong CO column annual cycles.

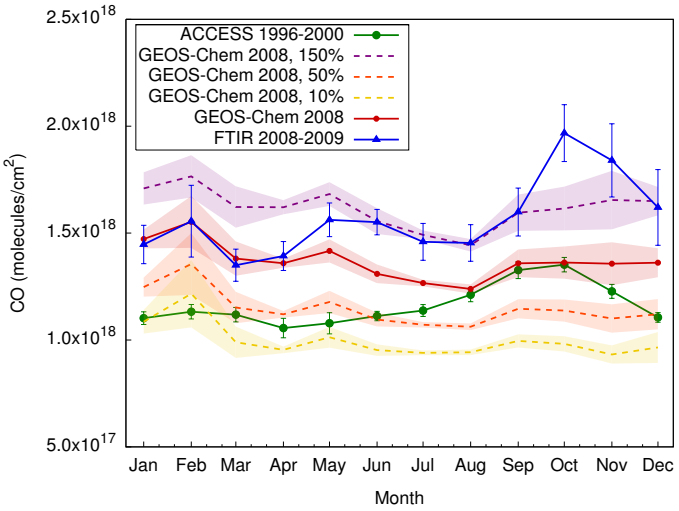

(b) Darwin CO column annual cycles.

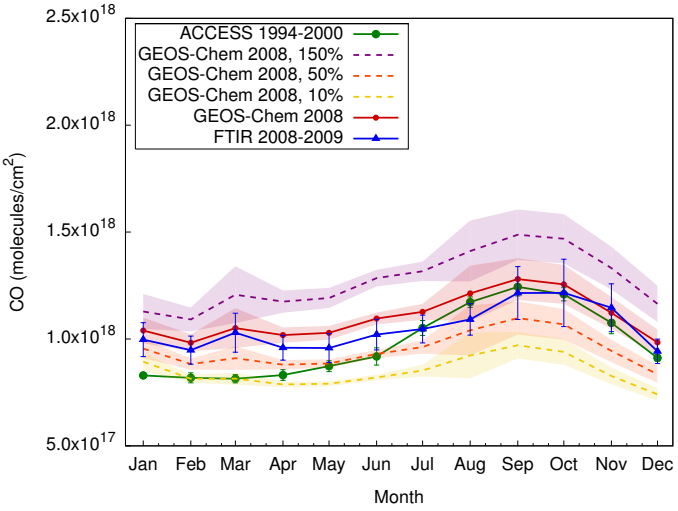

(c) Lauder CO column annual cycles.

Figure 8.4.5: Results for total column annual cycles of CO from the isoprene sensitivity study, for each station (a) Wollongong, (b) Darwin and (c) Lauder. GEOS-Chem results from isoprene sensitivity runs are plotted with shaded standard deviation, specifically, 10% of standard emissions in yellow, 50% in orange, standard emission run in red and 150% in maroon. ACCESS annual cycles (green) and FTS annual cycles from 2008-2009 (blue) are shown for comparison.

isoprene. This remaining mis-match coincides with a peak in Southern Hemispheric biomass burning suggesting biomass burning emissions are not properly replicated in the model at Darwin. Model-measurement mis-match is therefore most likely due to the high uncertainty in tropical biomass burning estimates due to limited measurements in the region. Overall for CO, the GEOS-Chem isoprene sensitivity study has highlighted deficiencies in the ACCESS CO parameterisation from isoprene oxidation.

It was also apparent that lack of isoprene oxidation was likely the main reason ACCESS under-represented HCHO columns at Wollongong and Darwin, with Lauder results inconclusive (Figure 8.4.6). A reduction in isoprene emissions resulted in a reduction in GEOS-Chem HCHO column amounts at all three sites, which brought values closer to ACCESS results. This indicated lack of isoprene oxidation in ACCESS as a source of HCHO was concluded to be likely the major reason for vastly underestimated column HCHO.

In addition to altering column HCHO magnitude, the isoprene oxidation source was found to be responsible for variability in column HCHO annual cycle. At Wollongong, the influence of isoprene on HCHO is greatest in Austral spring-summer, from October to March. During these months, a 90% reduction in isoprene emissions reduces HCHO column by 30–45%, while in the middle of the year, it only reduces HCHO column by 10–20%. Similarly for Darwin, the dual peaks of March to June and September to October are enhanced by increasing amounts of isoprene emissions, indicating these seasonal features are driven by processes involving isoprene, namely biogenic processes. Reduced seasonal variability is seen in ACCESS HCHO results, which further supports a missing isoprene oxidation source. Influence on seasonality is a reflection of isoprene being the main contributor to column HCHO in this region, as introduced by (Pfister et al., 2008).

Limited changes in HCHO column at Lauder are seen in GEOS-Chem after changes to isoprene emission amount. This is a reflection of isoprene emissions at Lauder initially being much lower than at the other two stations, hence a 90% reduction in isoprene at Lauder is not as significant. A low bias for HCHO at Lauder in GEOS-Chem occurs from November to March and indicates isoprene emissions may need to be increased in these months. A missing summer source of isoprene at Lauder could originate from the ocean, which is currently not accounted for in GEOS-Chem simulations. Marine isoprene sources have the potential to be significant, particularly around coastal areas (Shaw et al., 2010). Given the geography, it is likely that all areas of New Zealand may be influenced by coastal air-masses, therefore Lauder has the possibility of being affected

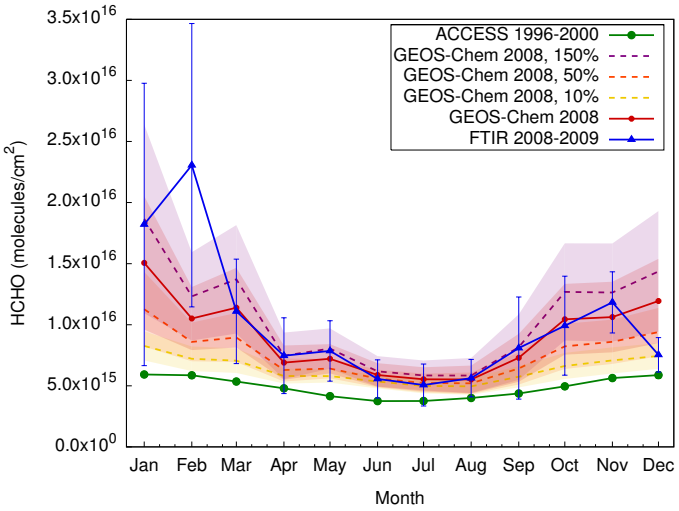

(a) Wollongong HCHO column annual cycles.

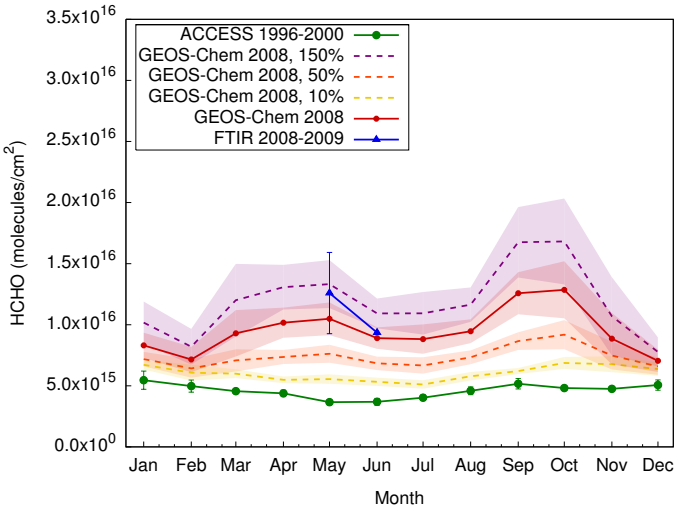

(b) Darwin HCHO column annual cycles.

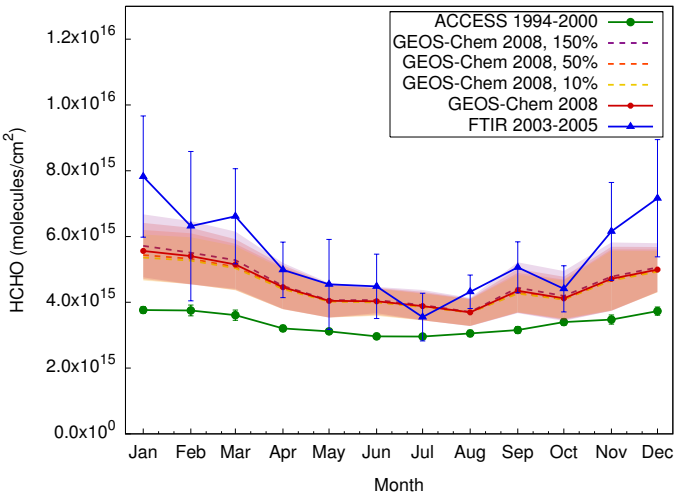

(c) Lauder HCHO column annual cycles.

Figure 8.4.6: Results for total column annual cycles of HCHO from the isoprene sensitivity study, for each station (a) Wollongong, (b) Darwin and (c) Lauder. GEOS-Chem results from isoprene sensitivity runs are plotted with shaded standard deviation, specifically, 10% of standard emissions in yellow, 50% in orange, standard emission run in red and 150% in maroon. ACCESS annual cycles (green) and FTS annual cycles from 2008-2009 (blue) are shown for comparison.

by significant marine isoprene emissions. Future study on HCHO column values at Lauder would benefit from measurements of isoprene in the oceanic atmosphere around New Zealand.

Altering isoprene emissions did not affect GEOS-Chem column C_2H_6 at a great enough magnitude to account for overestimation by the CTM (Figure 8.4.7). However, the contribution of isoprene oxidation to C_2H_6 column was of the correct magnitude to account for ACCESS model underestimation. For example at Wollongong, the 90% reduction in isoprene emissions produced a 14% reduction in GEOS-Chem C_2H_6 column. ACCESS, which does not account for C_2H_6 from isoprene oxidation, was on average 20% below FTS measurements. Additionally, altering isoprene emissions was seen to affect C_2H_6 column magnitude in GEOS-Chem but had no effect on annual cycle variability, indicating C_2H_6 variability remains driven by biomass burning as previously discussed (Section 8.4).

Overall, isoprene is an important trace gas for atmospheric composition modelling, especially over Australasia and for the trace gases studied here: CO, HCHO and C_2H_6. This sensitivity study has shown that a lack of isoprene emissions and related chemistry in ACCESS is of concern due to the inability to represent targeted trace gases accurately. As such, it is recommended to include isoprene and related chemistry in future simulations.

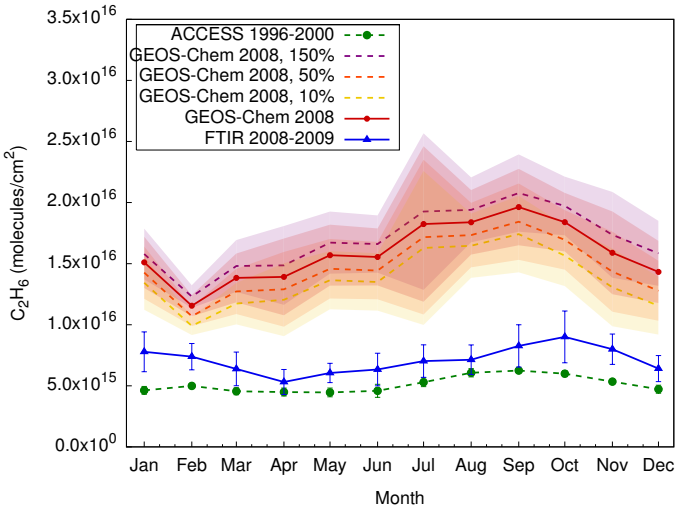

(a) Wollongong C_2H_6 column annual cycles.

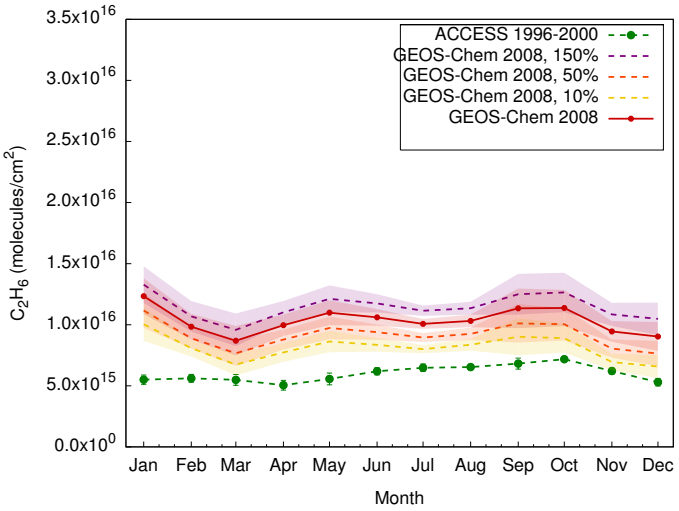

(b) Darwin C_2H_6 column annual cycles.

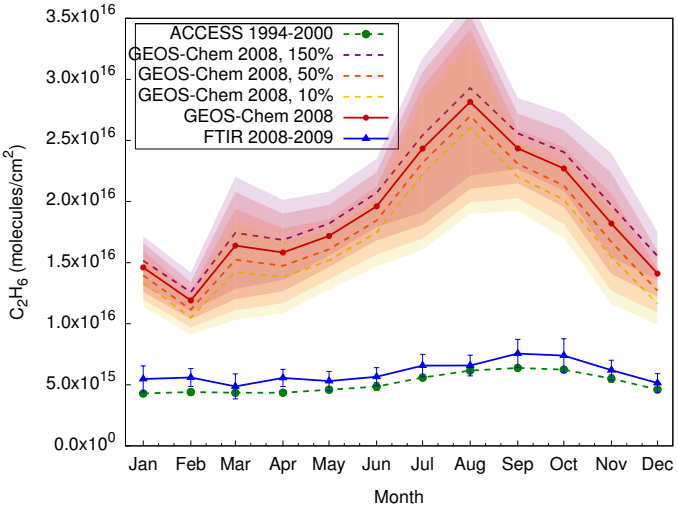

(c) Lauder C_2H_6 column annual cycles.

Figure 8.4.7: Results for total column annual cycles of C_2H_6 from the isoprene sensitivity study, for each station (a) Wollongong, (b) Darwin and (c) Lauder. GEOS-Chem results from isoprene sensitivity runs are plotted with shaded standard deviation, specifically, 10% of standard emissions in yellow, 50% in orange, standard emission run in red and 150% in maroon. ACCESS annual cycles (green) and FTS annual cycles from 2008-2009 (blue) are shown for comparison.

8.4.3 Dynamics: El Niño and La Niña climate regimes

ACCESS is driven by meteorology simulated using a Global Circulation Model (GCM), which is based off the U.K. met Office Unified Model (UM, version 7.3). The GCM is driven by prescribed sea-surface temperatures (SSTs), which in this study have been taken from measurements. Due to emissions being held constant at year 2000, interannual variability of atmospheric composition is dominated by the influence of varying dynamics in ACCESS. The magnitude of interannual variability imparted by dynamics to composition in ACCESS is much smaller in magnitude than differences between model and measurements. Therefore, it is concluded that ACCESS meteorology is not the driving cause of model-measurement mis-match.

The constant year-2000 emission scheme in ACCESS provided an opportunity to assess the influence of large scale dynamics upon atmospheric composition. By using constant emissions, only the effect of interannually varying dynamics, will affect model atmospheric composition variability. In particular, variability was assessed with respect to climate regimes of El Niño-Southern Oscillation (ENSO). ACCESS was expected to follow El Niño and La Niña phases, due to ACCESS incorporating prescribed SST measurements to drive meteorology and ENSO indices being determined from SSTs. Therefore, differences in atmospheric composition between El Niño and La Niña regimes was determined for ACCESS. ENSO dynamics was expected to contribute to variability due to difference in transport between climate regimes.

The Oceanic Niño Index (ONI) was used to calculate phases of ENSO. ONI are defined by the National Oceanic and Atmospheric Administration (NOAA) as 3-month running means of SST (ERSST.v3b) anomalies in the Niño 3.4 region (5°N-5°S, 120°-170°W), calculated relative to a 30-year base period mean, which is updated every five years. ONI values were obtained from the Climate Prediction Center (www.cpc.ncep.noaa.gov/products/analysis_monitoring/ensostuff/ensoyears.shtml). El Niño (La Niña) phases were determined according to NOAA definitions that ONI be greater than or equal to +0.5°C (less than or equal to −0.5°C) over five or more consecutive, overlapping three-month seasons. Neutral phase was defined where these criteria were not met. Neutral phase comprise approximately one third of data and is not considered for further analysis. A summary of years split into ENSO phases are listed in Table 8.4.3.

The ACCESS record 1980 to 2000 was split at each station according to ENSO phases defined by ONI values. Mean annual cycles of monthly values were then calculated for each phase, with associated standard deviation. FTS total column datasets were

Table 8.4.3: Summary of years between 1980 and 2011 belonging to climate regimes El Niño, La Niña and Neutral phases. Regime is defined by year in which climate phase begins.

El Niño	La Niña	Neutral
1982, 1986, 1987, 1991, 1994, 1997, 2002, 2004, 2006, 2009	1983, 1984, 1988, 1995, 1998, 1999, 2000, 2005, 2007, 2008, 2010, 2011	1980, 1981, 1985, 1989, 1990, 1992, 1993, 1996, 2001, 2003

analysed for comparison and were split over the entire available datasets at each station in order to maximise data available for each ENSO phase. Specifically Wollongong data covered 1996 to 2011, Lauder 1994 to 2011 (2005 for HCHO) and Darwin 2005 to 2011. At Darwin, only CO had sufficient data for ENSO analysis, and due to the short time period 2005 to 2011, not all months experienced El Niño or La Niña conditions, therefore gaps are seen in the FTS annual cycles (Figure 8.4.8d).

For CO, differences between climate phases for modelled data is not as extreme as differences in measurements (Figure 8.4.8). However, climate phase affects modelled total column CO generally in the same direction as measurements. At Wollongong and Lauder, measurements El Niño years show a reduced maximum in October, compared with La Niña. Model CO from El Niño phase are also lower at Wollongong and Lauder at the September peak, although the effect is much smaller. Interestingly, El Niño phase has an alternate effect on CO at Darwin. In both model and measurements, El Niño phase CO column throughout the year is higher than La Niña. FTS measurements reflect the strong local source of increased burning in Indonesia during El Niño. However, similar response in ACCESS with constant emissions indicates some of the higher CO in El Niño phase is due to dynamics. Darwin is influenced by the Australian summer monsoon, and a strong summer monsoon is associated with La Niña phase (Kajikawa et al., 2010). Stronger monsoon would be associated with increased atmospheric turbulence in the region, which would in turn increase transport of CO from Darwin and surrounds and subsequently produce lower CO values during La Niña. Therefore, during El Niño, decreased transport of CO from Darwin relative to La Niña is experienced, and higher CO values are produced.

Differences in FTS measurements being much greater than model between ENSO phases, which shows varying emissions is the main driver of CO variability during

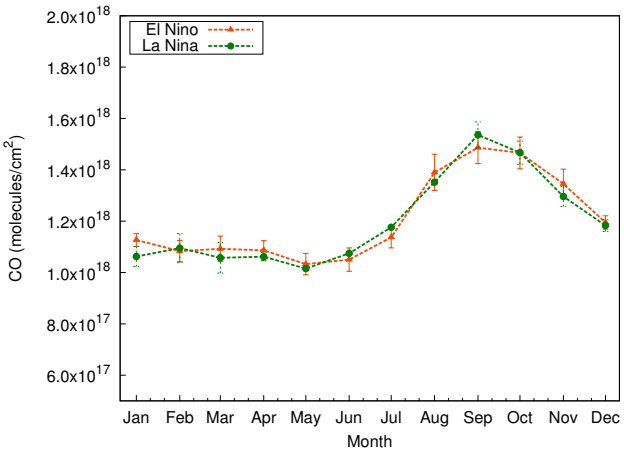

(a) ACCESS Wollongong CO column annual cycle.

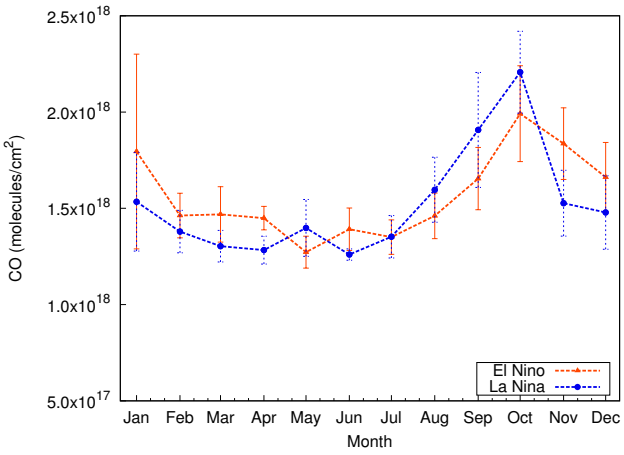

(b) FTS Wollongong CO column annual cycle.

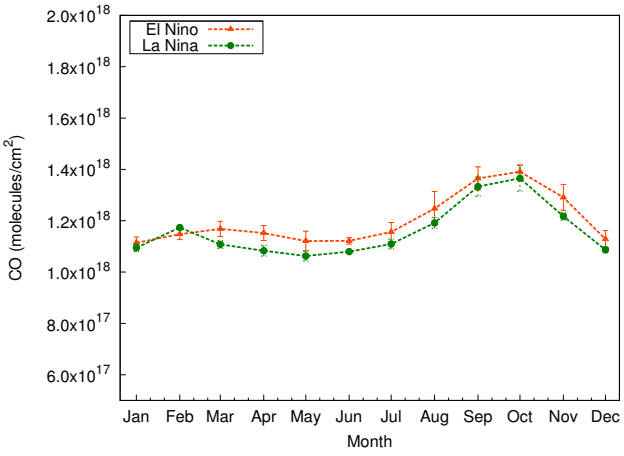

(c) ACCESS Darwin CO column annual cycle.

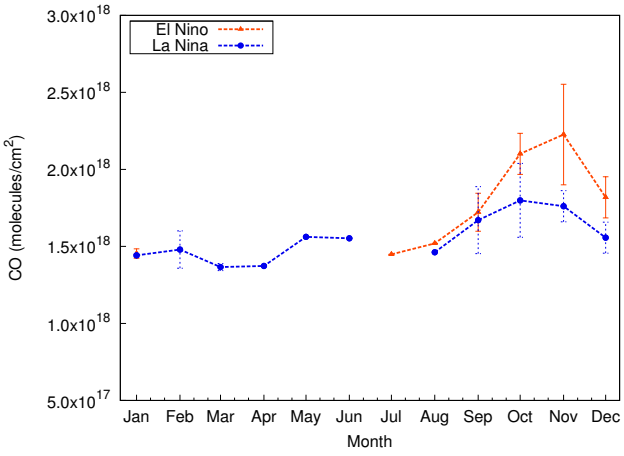

(d) FTS Darwin CO column annual cycle.

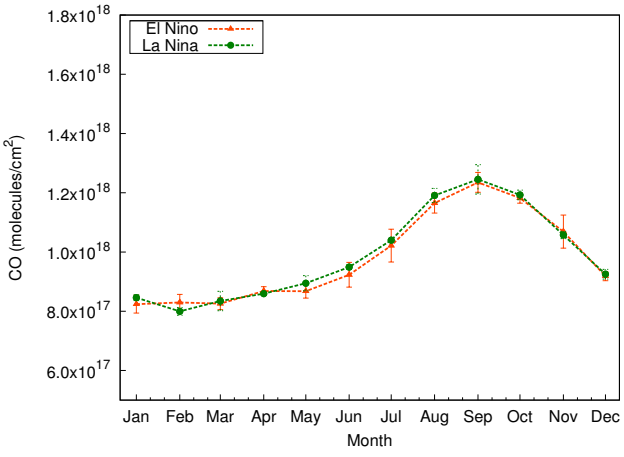

(e) ACCESS Lauder CO column annual cycle.

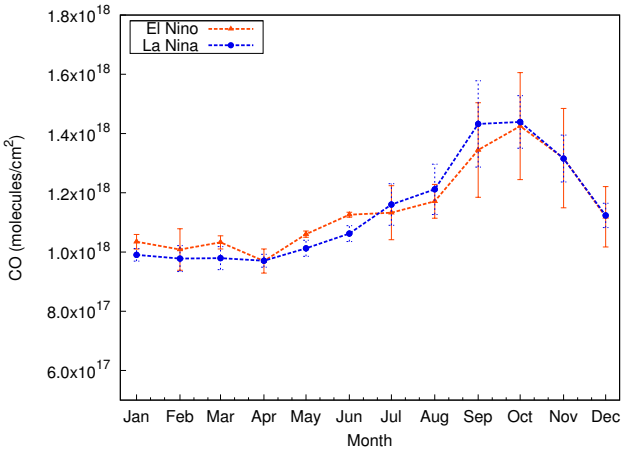

(f) FTS Lauder CO column annual cycle.

Figure 8.4.8: Average annual cycles of CO column values in El Niño (orange triangles) and La Niña (green for ACCESS or blue for measurements) phases. ACCESS (left column) and FTS measurements (right column) are plotted at each site Wollongong (a, b) Darwin (c, d) and Lauder (e, f).

ENSO phases. For example, a reduced precipitation in Australia during an El Niño cycle (Bhaskaran & Mulan, 2003) alters the extent of vegetation and therefore impacts biogenic emissions, as compared with a wetter La Niña climate. This is particularly apparent for Darwin, where a large difference is seen between phases for CO Figure 8.4.8d. El Niño years increase the drought conditions in Indonesia, increasing the likelihood of burning in the tropical environment and hence increasing amount of emitted CO from biomass burning. However, as previously discussed, measurements at Darwin have only been occurring from 2005, which means not enough data has been acquired to robustly confirm these observations.

Model HCHO at Wollongong and Lauder show little influence from ENSO phases (see Figure 8.4.9). Measurements at Wollongong and Lauder also show minimal difference for HCHO from May to December. However, from January to April, large difference are seen in HCHO measured column between phases, with El Niño phase generally lower than La Niña. As discussed in Section 8.4.2, the major contributor to HCHO column in the region is oxidation of isoprene emissions. Biogenic isoprene emissions would be greatly affected by climate phases. Specifically, El Niño phase produces a hotter, dryer climate (Bhaskaran & Mulan, 2003; Vicente-Serrano et al., 2011). Although plants have been found to increase isoprene emissions under water stress (Sharkey & F., 1993), in Australia, increased isoprene emissions were seen to correspond with the wet season (Ayers & Gillett, 1988). Therefore under dry conditions of El Niño phase, plants in Australia would produce less isoprene, whether by decreased plant cover or plant response mechanisms, and therefore supply less HCHO via isoprene oxidation. Lack of influence from climate regimes on modelled HCHO indicates this trace gas is mostly influenced by emissions, which are most likely local due to the short lifetime of HCHO.

Darwin HCHO model results indicate possible effect of dynamics on HCHO column, with El Niño phase generally lower than La Niña. This is different to the effect of climate phases on CO, indicating HCHO originates from a different source to CO. It is unclear what may be driving the ENSO phase differences in ACCESS HCHO. Higher HCHO in La Niña may be due to increased transport of HCHO and precursor emissions from the local region to Darwin, due to increased atmospheric turbulence during the stronger La Niña monsoon. Alternatively, HCHO differences may be seen due to differences in losses to HCHO. HCHO may be lost via direct photolytic processes, which would be reduced due to increased cloud cover during intense monsoon seasons of La Niña. Unfortunately, insight into HCHO differences cannot be gained from FTS

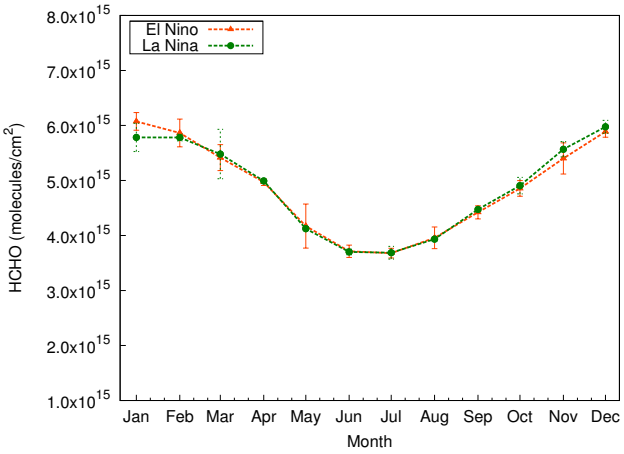

(a) ACCESS Wollongong HCHO column annual cycle.

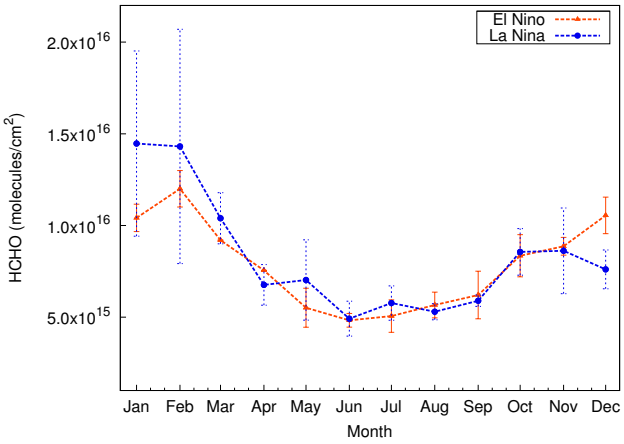

(b) FTS Wollongong HCHO column annual cycle.

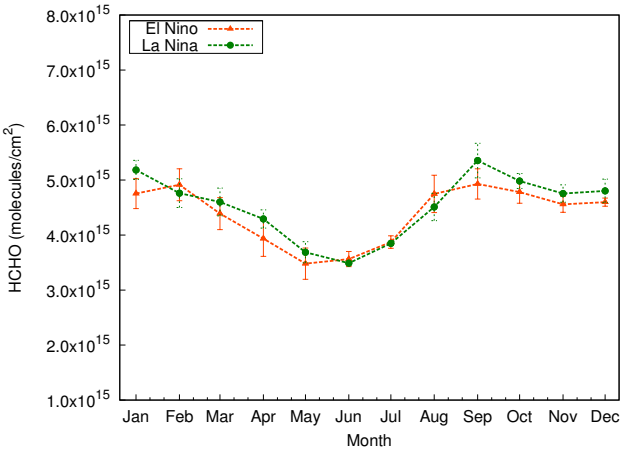

(c) ACCESS Darwin HCHO column annual cycle.

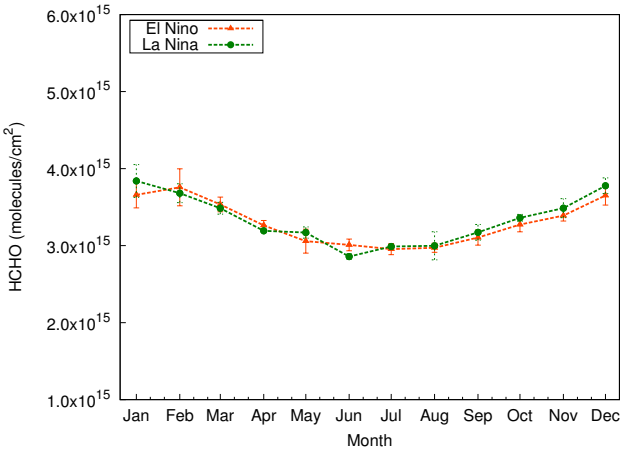

(d) ACCESS Lauder HCHO column annual cycle.

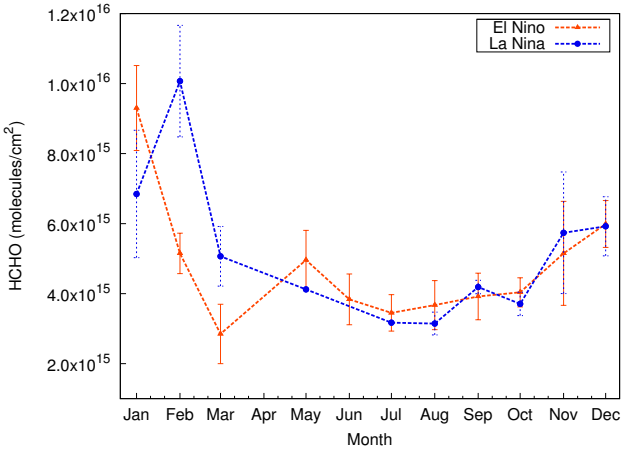

(e) FTS Lauder HCHO column annual cycle.

Figure 8.4.9: Same as Figure 8.4.8 but for HCHO.

HCHO measurements at Darwin as the timeseries was not yet long enough to perform ENSO analysis.

C_2H_6 results are similar to those found for CO. Wollongong and Lauder model results show a reduction in the annual cycle peak around October for El Niño years, which is in the same direction as measurements. Differences between ENSO phases for measurements is more intense than for the model, indicating emissions differences are driving atmospheric composition differences. Additionally, measurements in the first half of the year show an increased C_2H_6 column for El Niño years, reflecting transport from increased biomass burning in Africa and South America. The January-June increase is not captured by constant emissions in ACCESS. Most variability between modelled C_2H_6 in El Niño and La Niña is seen at Darwin. Greater C_2H_6 column from the model in El Niño years indicates decreased transport of locally emitted C_2H_6 and CO away from Darwin during El Niño phase. FTS C_2H_6 measurement timeseries at Darwin was not yet long enough to perform ENSO analysis.

Valuable future research would involve performing a 1980–2010 GEOS-Chem run using newly available meteorological fields and emission files. Output from a climatological run of GEOS-Chem simulation would be useful to further determine sources of atmospheric trace gases during the ENSO climate regimes and de-convolve differences due to emissions, as well as dynamics. Additionally, an ACCESS simulation using nudged meteorology, where dynamics is nudged towards the true state of the atmosphere, would strengthen the result for different climate phases of ENSO found here. A nudged simulation would also assess how accurate the dynamic contribution to atmospheric composition is in prediction mode.

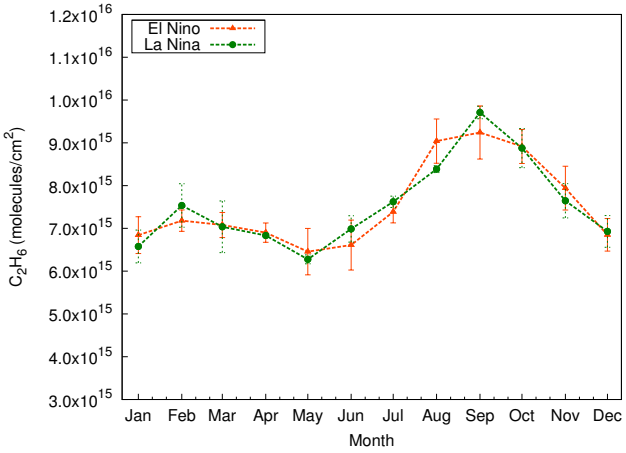

(a) ACCESS Wollongong C_2H_6 column annual cycle.

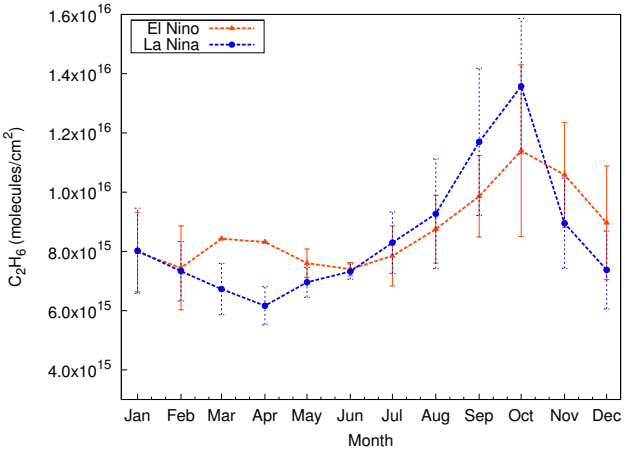

(b) FTS Wollongong C_2H_6 column annual cycle.

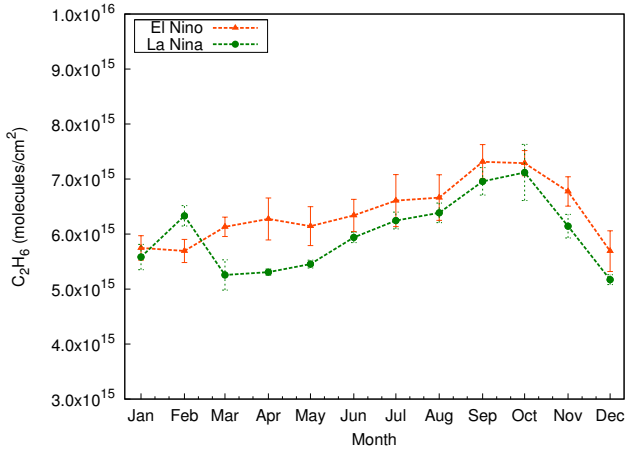

(c) ACCESS Darwin C_2H_6 column annual cycle.

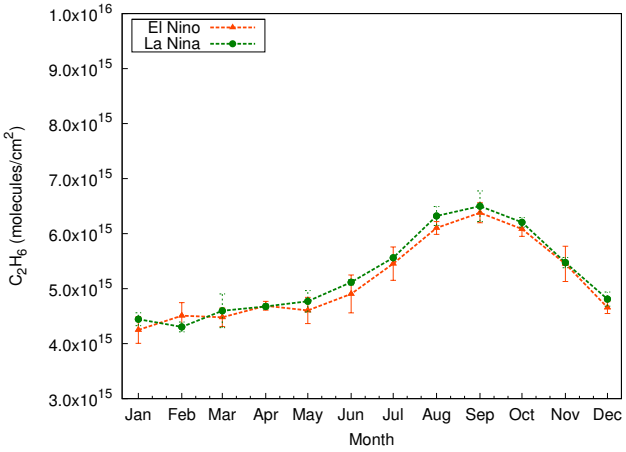

(d) ACCESS Lauder C_2H_6 column annual cycle.

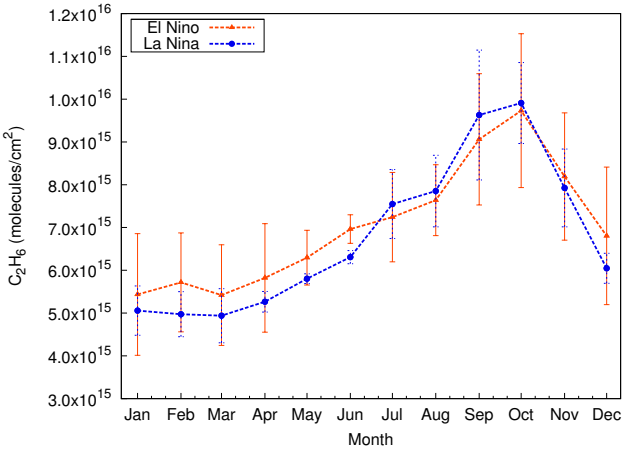

(e) FTS Lauder C_2H_6 column annual cycle.

Figure 8.4.10: Same as Figure 8.4.8 but for C_2H_6.

ENSO climate phases were found to play a small role in altering atmospheric composition through dynamic processes, for the trace gases CO, HCHO and C_2H_6. At Wollongong and Lauder, modelled variability in atmospheric composition between El Niño and La Niña phases is minimal, with model values changing in the same direction as measurement results, but to a much smaller degree. Darwin showed the most difference in atmospheric composition between phases due to dynamics, which is a reflection of significantly altered dynamic processes in the tropical region. A stronger monsoon during La Niña phase at Darwin increased atmospheric mixing in the region, producing a dilution effect by transporting trace gases CO and C_2H_6 from Darwin. This had an alternative effect on short-lived trace gas HCHO, which indicates contributions from different processes than CO and C_2H_6. Larger differences in FTS measurements compared to ACCESS indicated atmospheric composition is mainly driven by emission differences between El Niño or La Niña regimes.

8.5 Correcting the stratospheric NO_2 condition

ACCESS simulations also produced NO_2 profiles, and although not the main focus of this research, total column NO_2 is also measured at Wollongong by ground–based solar Fourier Transform Infrared Spectrophotometer (FTS). Therefore, an analysis of ACCESS NO_2 was included as a side project. Immense differences were found between model and measurements of NO_2 total columns (Figure 8.5.1). ACCESS total column NO_2 was approximately an order of magnitude greater than FTS measurements.

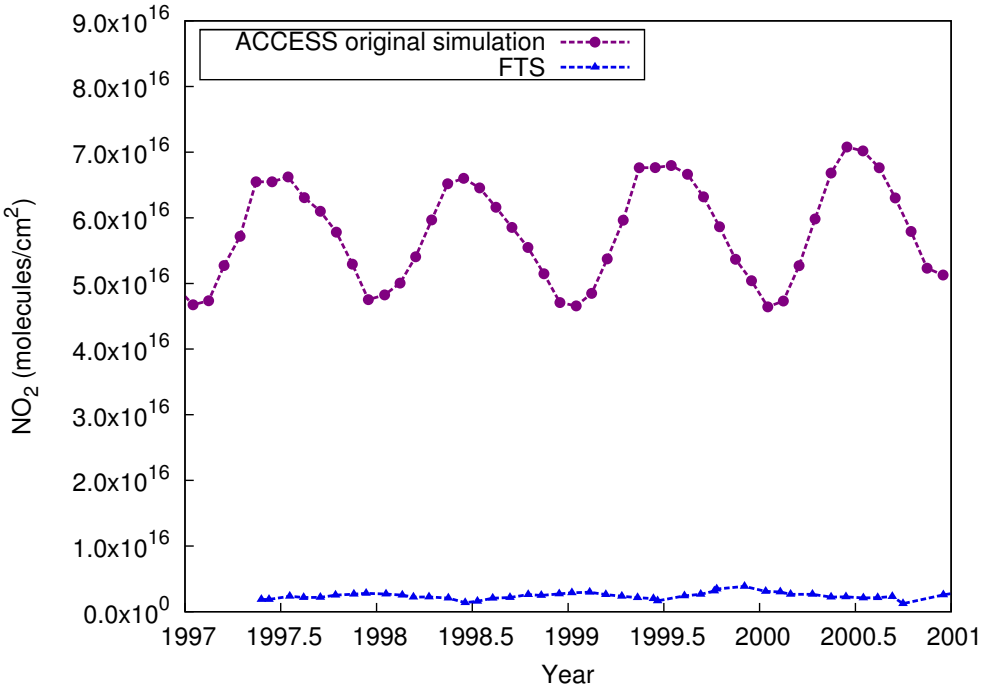

Figure 8.5.1: Monthly averaged total column values of NO_2 at Wollongong in ACCESS (purple) and FTS measurements (blue). The overlapping period of the two timeseries is shown, 1997 to 2001.

Investigation into the cause of inaccurately high NO_2 column in ACCESS revealed the issue was due to the definition of NO_2 at the top of the model stratosphere. Although stratospheric chemistry was not explicitly modelled in ACCESS, upper-atmospheric conditions of key trace gases were parameterised, as described previously in Section 6.5.4. Stratospheric NO_2 was originally defined relative to the amount of stratospheric O_3. However, in order to effectively couple the chemistry module with the radiative forcing module of ACCESS, O_3 above the top of the model atmosphere was compressed into the top model layer. The increased model stratospheric boundary of O_3 was small

relative to the total O_3 column, but produced a large effect in the NO_2 amounts. The result of the incorrectly defined stratospheric NO_2 is particularly clear when comparing the FTS a priori monthly vertical profiles and the ACCESS monthly averaged profiles as displayed in Figure 8.5.2. Stratospheric NO_2 in the ACCESS vertical profiles greatly exceeds the variability described by the a priori.

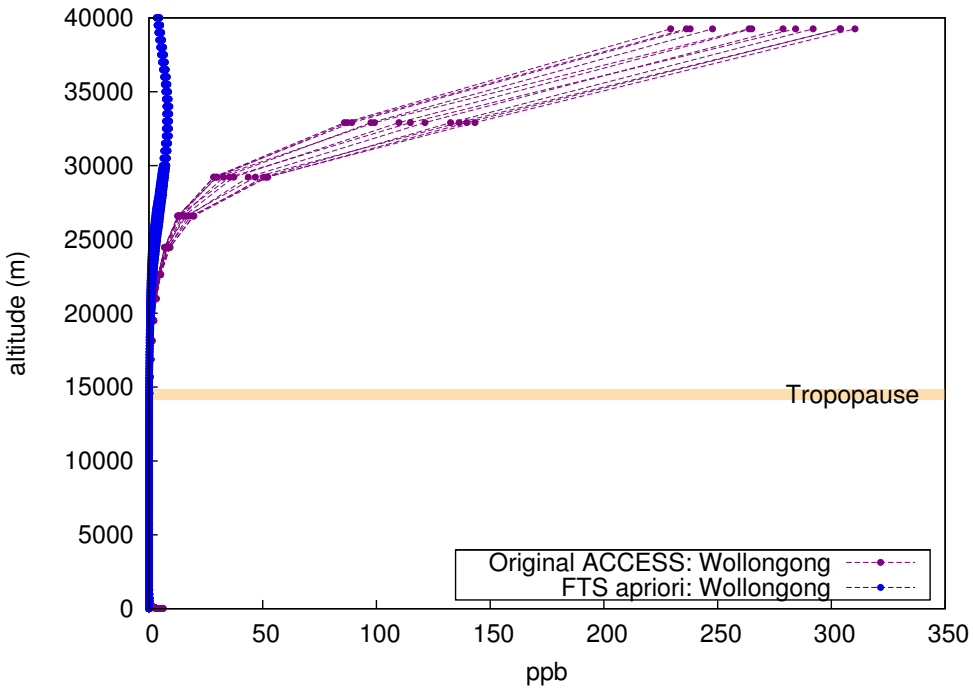

Figure 8.5.2: Vertical profiles of NO_2 mole fraction for FTS a priori (blue) and Original ACCESS (purple) at Wollongong. Average monthly profiles are shown for each dataset, giving an indication of monthly variability in the profiles.

As a result of this comparison, an updated ACCESS simulation was performed with stratospheric NO_2 conditions defined by output from the Cambridge 2D model (Law & Pyle, 1993). Output from the updated run was analysed relative to the initial run and is discussed in the following sections. Comparisons are made for NO_2 as well as determining effects for other trace gases.

8.5.1 Analysis procedure

Trace gas analysis was performed for three sites: Wollongong (-34.406, 150.879), Darwin (-12.425, 130.892) and Lauder (-45.038, 169.684). An updated ACCESS simulation was performed ensuring all variables were identical to the original simulation, with the

exception of corrected stratospheric boundary condition of NO_2, now defined by the Cambridge 2D model (Law & Pyle, 1993). The ACCESS simulation with updated NO_2 is herein referred to as "Updated ACCESS" and the original simulation is referred to as "Original ACCESS". Output from the two simulations were analysed using methods described below.

Month averaged vertical profiles of NO_2 from the updated ACCESS simulation were compared with FTS a priori profiles to assess improvements. FTS monthly a priori were used in GFIT analysis, and were produced by combining satellite data between 16,552 - 48,359 metres with lower levels from the HALOE transect at 34.5S ref. ACCESS monthly vertical profiles were averaged over the entire dataset in each simulation. In addition to profile investigation, differences between ACCESS simulations for NO_2 total column and surface timeseries were determined. Total column values were calculated from model output by integrating pressure weighted profiles. Model data was compared with NO_2 total column annual cycles from FTS measurements at Wollongong and surface NO_2 annual cycles from data obtained from the Office of Environment and Health (Office of Environment and Heritage, 2011). Annual cycles were averaged over all 20 years of each simulation.

The influence of stratospheric NO_2 conditions on other trace gases was also investigated. Timeseries comparison between model runs was performed for total column values of O_3, CO, HCHO and C_2H_6. Surface values were also compared for O_3. Mean differences between datasets and average monthly standard deviation were calculated for each trace gas. Significant differences between original and updated datasets were defined as mean differences outside one average monthly standard deviation. Correlation coefficients were also determined for each comparison.[1]

8.5.2 Response to boundary condition correction

Nitrogen Dioxide

Monthly vertical mole fraction profiles of NO_2 from the updated ACCESS simulation were greatly reduced compared with the original simulation and closer to the magnitude

[1] A single outlier existed for C_2H_6 in September 1998 at each of the stations and was only present in the original ACCESS datasets. This outlier was removed at each station prior to correlation and standard deviation analysis in order to prevent an inaccurate contribution. This C_2H_6 anomaly was classified as model error. Unusually low C_2H_6 values were not present in the updated ACCESS simulation.

of the FTS a priori profiles at Wollongong, shown in Figure 8.5.3. Updated ACCESS stratospheric NO_2 displays a maximum of approximately 12 ppb, compared to 10 ppb for the a priori. Although stratospheric NO_2 has moved in the correct direction, it may remain too high in the model. Similar reductions in NO_2 profiles are seen at Darwin and Lauder, plots in Appendix E (Darwin: Figure E.0.13a vs Figure E.0.13b and Lauder: Figure E.0.13c vs Figure E.0.13d).

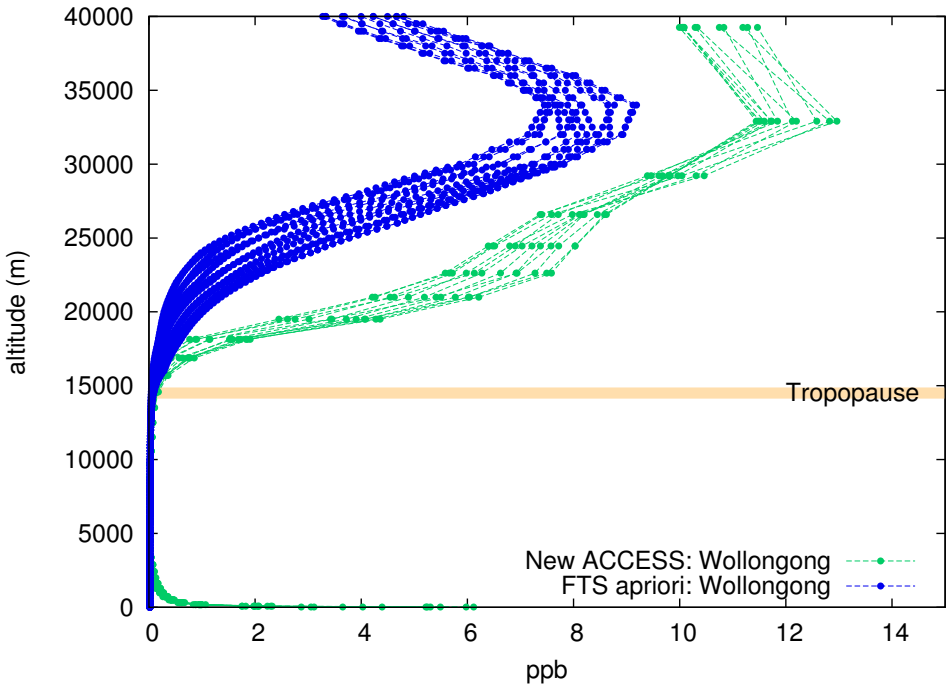

Figure 8.5.3: Vertical profiles of NO_2 mole fraction for FTS a priori (blue) and Updated ACCESS (green) at Wollongong. Average monthly profiles are shown for each dataset to indicate the annual range of variance. The global mean tropopause height is also indicated.

An obvious result of reducing stratospheric NO_2 is a reduction in total column NO_2. Substantial differences between original and updated total column timeseries were found at each of the three locations Wollongong (Figure 8.5.4), Darwin and Lauder (in Appendix E, Darwin: Figure E.0.14 and Lauder: Figure E.0.15). At all three locations, total column values were reduced by approximately 80%. Additionally, seasonal cycle structure was observed in the total column difference between simulations, indicating a reduction in the magnitude of seasonal variability for the updated ACCESS conditions.

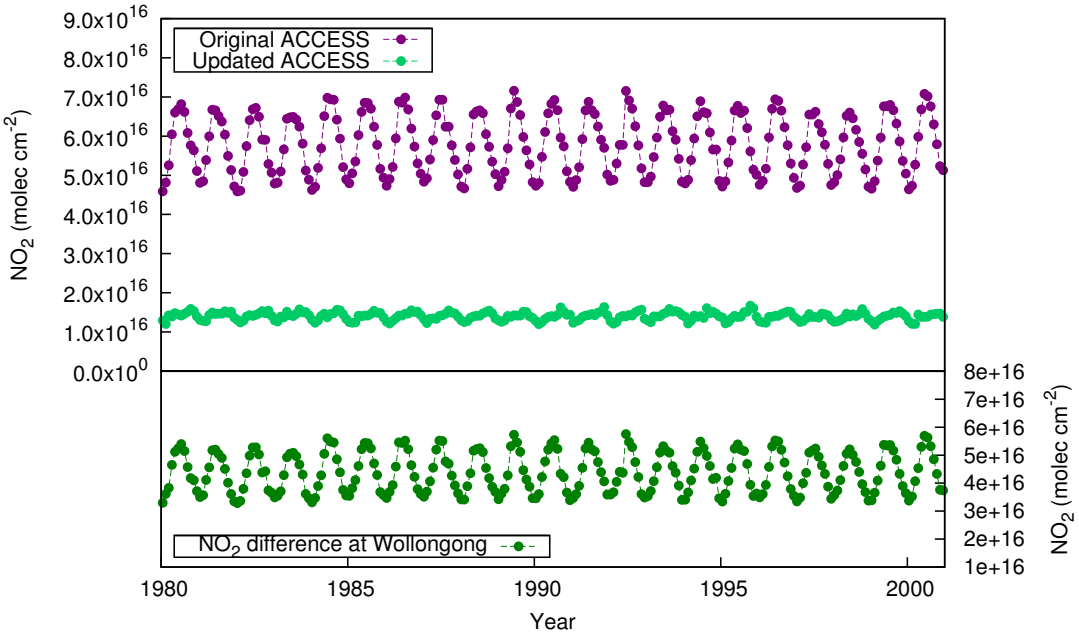

Figure 8.5.4: ACCESS NO_2 original (purple) and updated (light green) simulations at Wollongong. Lower panel plots the difference between original and updated NO_2.

In contrast to total column values, surface NO_2 values showed minimal difference between simulations at all three sites (Figure 8.5.5). The insignificant change in surface ACCESS results between simulations indicates that in the ACCESS model, boundary layer NO_2 is mainly influenced by surface emissions, and minimally by vertical transport of stratospheric NO_2

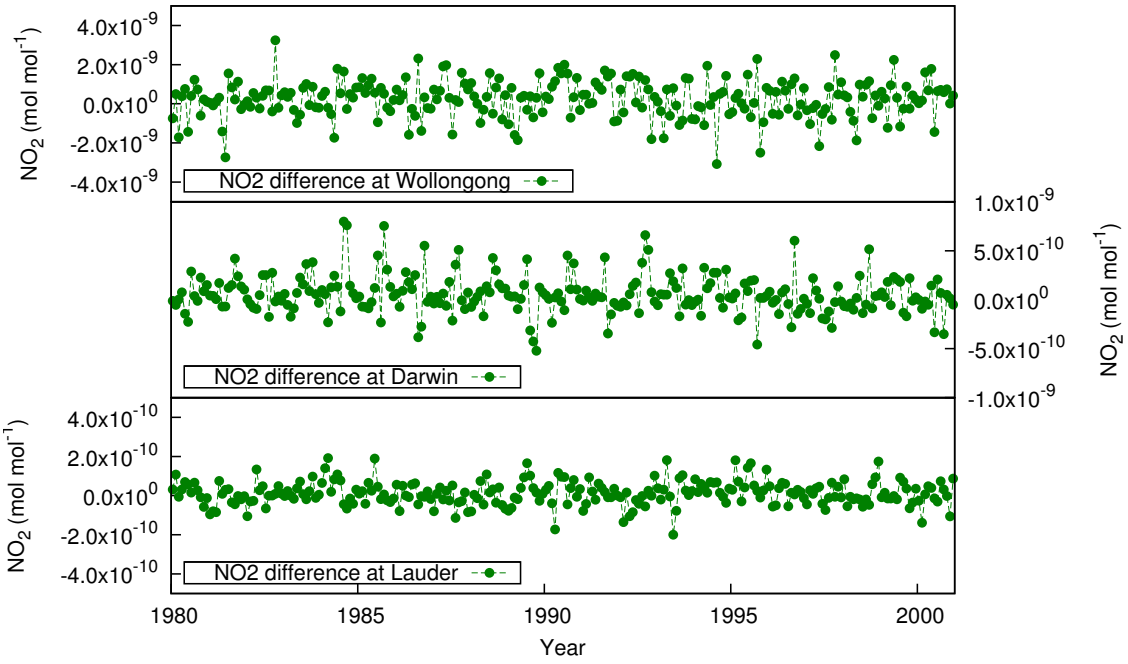

Figure 8.5.5: Timeseries of monthly surface NO_2 mole fraction differences between original and updated ACCESS simulations at Wollongong (top panel), Darwin (middle panel) and Lauder (bottom panel).

Seasonality was investigated through average annual cycles of NO_2 at Wollongong. Total column average annual cycles for overlapping datasets of the two ACCESS simulations and FTS measurements are presented in Figure 8.5.6. Annual cycles required plotting in separate panels due to magnitude differences, with the old ACCESS simulation approximately 20 times greater than measurements and new ACCESS simulation approximately 5 times greater than measurements.

The measured annual cycle of total column NO_2 peaks at Wollongong in Austral Spring/Summer from October to March, (lower panel of Figure 8.5.6). Both ACCESS simulations display a different annual cycle to the FTS measurements. The original simulation shows a seasonal cycle anti-phase to the FTS (upper panel of Figure 8.5.6). Updated ACCESS NO_2 maximum is arguably closer to the measurement cycle, although remains mis-aligned (middle panel of Figure 8.5.6). Updated ACCESS NO_2 peaks two months earlier than measurements in October. Also, the updated ACCESS minimum is 4 months earlier in February instead of June. Annual cycle changes between ACCESS simulations were also evident at both the other sites, Darwin and Lauder (Appendix B, Figure E.0.18a-E.0.18d).

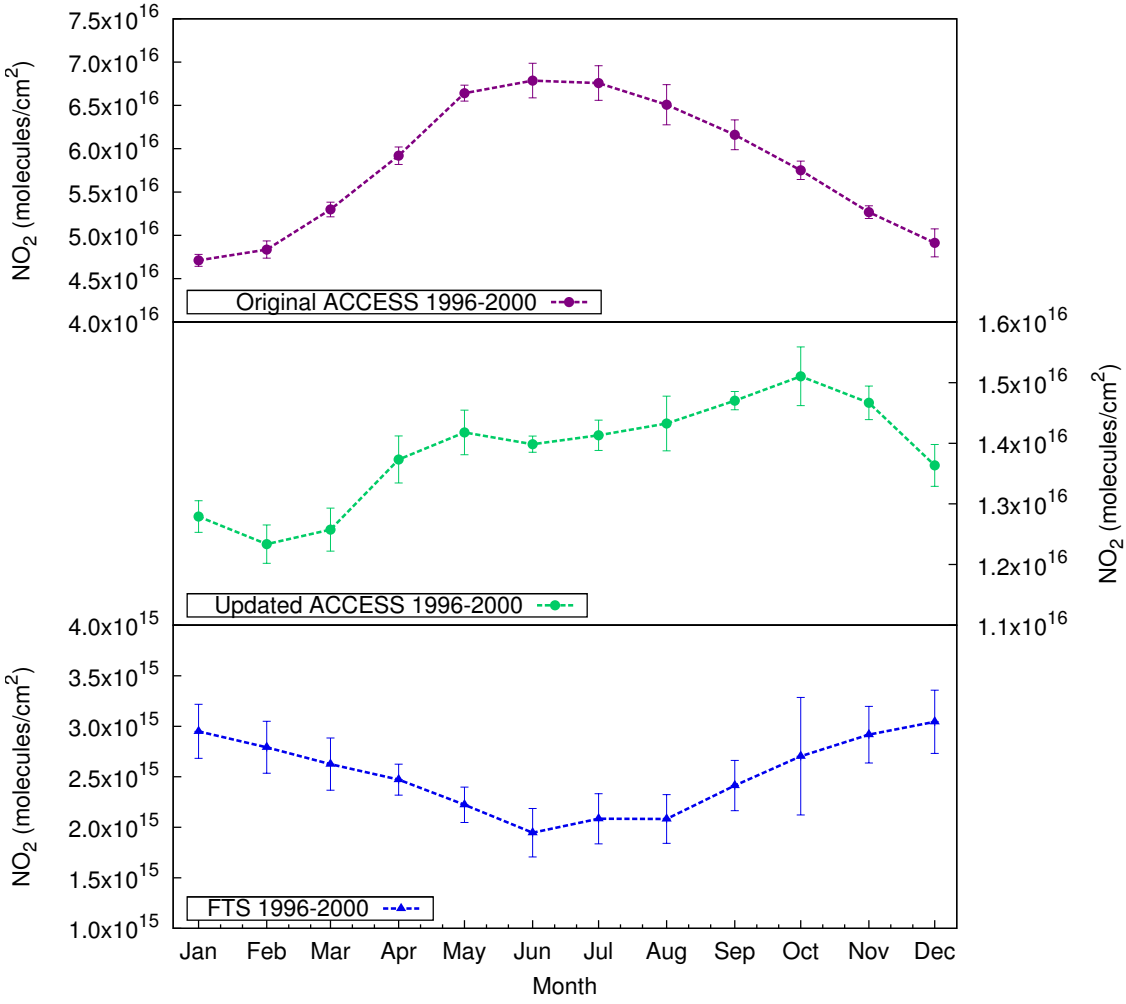

Figure 8.5.6: Average annual cycles of monthly total column values at Wollongong. Original ACCESS is shown in the top panel, Updated ACCESS in the middle, and FTS measurements in the lower panel.

NO_2 total column annual cycle is a combination of stratospheric and tropospheric annual cycles, which have different seasonalities. Specifically, the main source of stratospheric NO_2 is from the photolysis of N_2O (Equations 8.5.1 to 8.5.6), which has been transported from the surface, mainly originating from biogenic activity of denitrification by microorganisms (Seinfeld & Pandis, 2006a). Increased light intensity in Southern Hemisphere summer increases photolysis of N_2O, and is responsible for the summer stratospheric maximum of NO_2.

In comparison, tropospheric NO_2 sources are mainly due to direct emissions from biomass burning, lighting, microorganisms and anthropogenic sources (Seinfeld & Pandis, 2006a). Tropospheric annual cycle in urban regions is driven by urban emissions,

which exhibit a maximum May to August. Stratospheric NO_2 dominates the annual cycle for total column NO_2 at Wollongong as it displays a Austral Spring/Summer maximum from from October to March, consistent with the stratospheric annual cycle (lower panel of Figure 8.5.6). Both ACCESS simulations fail to reproduce this annual cycle.

$$N_2O + h\nu \longrightarrow N_2 + O(^1D) \tag{8.5.1}$$

a $$N_2O + O(^1D) \longrightarrow N_2 + O_2 \quad \textbf{42 \%} \tag{8.5.2}$$

b $$N_2O + O(^1D) \longrightarrow NO + NO \quad \textbf{58 \%} \tag{8.5.3}$$

$$2NO + 2O_3 \longrightarrow 2NO_2 + 2O_2 \tag{8.5.4}$$

---

net a $$2N_2O + h\nu \longrightarrow 2N_2 + O_2 \tag{8.5.5}$$

net b $$2N_2O + h\nu + 2O_3 \longrightarrow N_2 + 2NO_2 + 2O_2 \tag{8.5.6}$$

In contrast to total column annual cycle, surface ACCESS NO_2 annual cycles are generally consistent with OEH mole fraction measurements (Figure 8.5.7). Minimal change in surface annual cycle is observed between ACCESS simulations. Measurements exhibit a maximum May to August, reflecting influence from urban sources. The extent of winter maximum depends upon the extent of local urbanisation. For example, a more pronounced winter maximum is seen in the more populated area of Wollongong compared with a flatter curve for the less populated area of Albion Park.

The magnitude of model surface values lie between the cleaner Wollongong site (Albion Park) and the site highly influenced by urban pollution (Gipps St, Wollongong City). A value in between the two DECCW sites is expected from model results due to a coarse spatial resolution in the global model, which results in averaging clean and polluted sites.

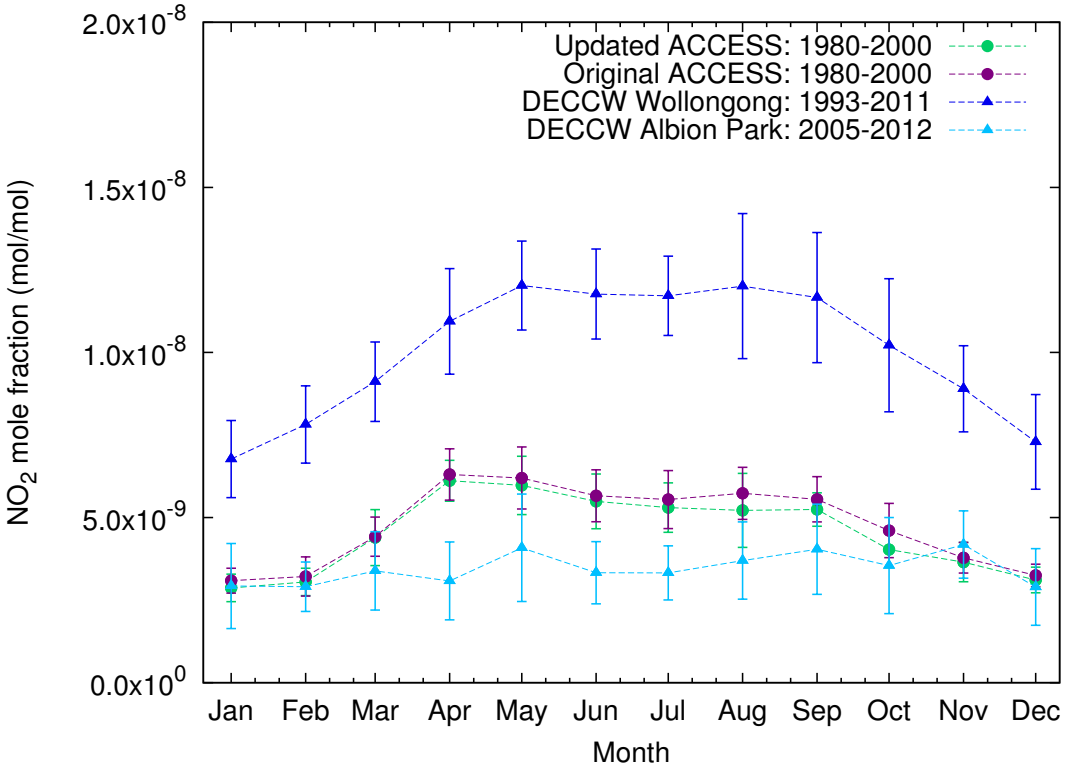

Figure 8.5.7: Average annual cycles of monthly surface layer NO_2 mole fraction values at Wollongong. Vertical bars indicate one standard deviation. Original ACCESS is shown in maroon circles, updated ACCESS in green circles, and surface measurements in blue and light blue triangles.

Although updated ACCESS NO_2 total column values are lower than the original simulation, model values remain biased high to FTS measurements, as previously indicated in the annual cycle comparison (Figure 8.5.7). This remaining overestimation of column NO_2 in updated ACCESS may be of either tropospheric or stratospheric origin. However, due to the consistent representation of Wollongong surface NO_2 measurements by ACCESS, errors are unlikely to originate from the model troposphere. Instead, stratospheric NO_2 is likely to remain overestimated in ACCESS, which may be a result of using archived stratospheric NO_2 model values calculated from an earlier version a 2D model, and which had been validated only for the Northern Hemisphere. Due to continued total column NO_2 magnitude overestimation with inaccurate annual cycle, it is recommended that stratospheric NO_2 in ACCESS receives additional updating.

Ozone

NO_2 and O_3 are linked in the atmosphere by photochemistry. It was therefore expected that a large change in model NO_2 would affect model O_3. Generally, total column and surface results for O_3 are higher in the updated ACCESS simulation, determined from differences between original and updated simulations being less than zero (Figures 8.5.8 & E.0.16). The large decrease in model stratospheric NO_2 in the updated simulation has resulted in an overall increase in both total column and surface O_3. Mechanisms of the NO_2-O_3 relationship contributing to this result are discussed below.

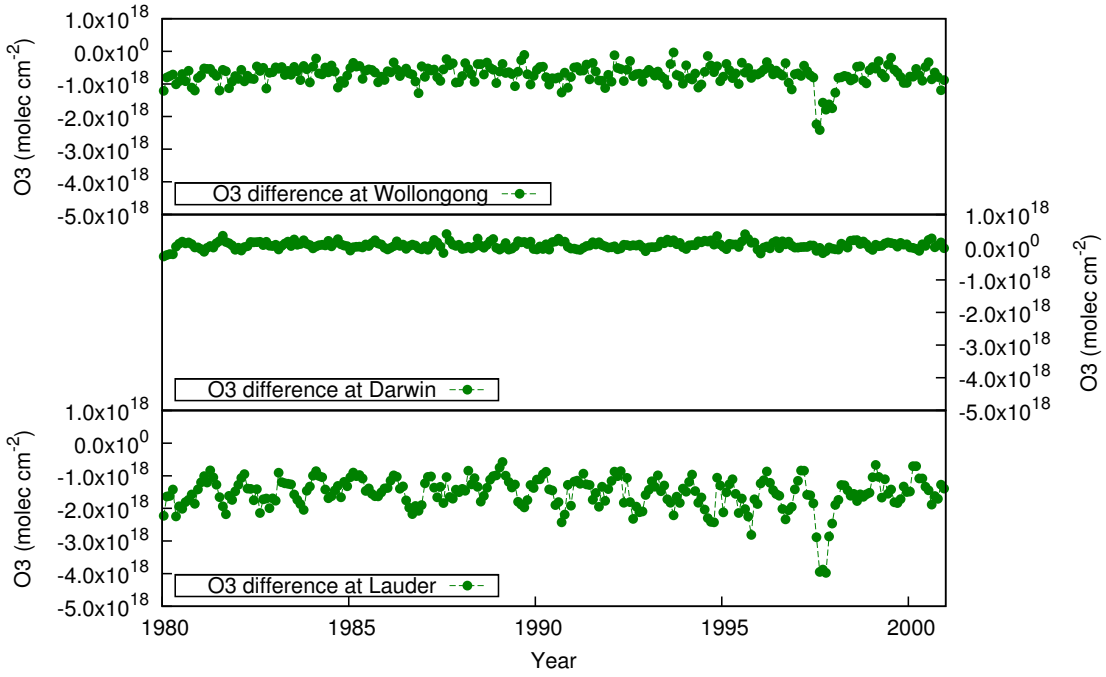

Figure 8.5.8: Timeseries of monthly total column O_3 differences between original and updated ACCESS simulations. Differences are plotted for Wollongong (top panel), Darwin (middle panel) and Lauder (bottom panel).

Nitrogen dioxide in a clean environment free of volatile organic compounds, such as the environment found in the stratosphere, catalytically titrates ozone via the following reactions (Equations 8.5.7 to 8.5.13, (Seinfeld & Pandis, 2006a)).

Lower Stratosphere

$$NO_2 + O_3 \longrightarrow NO_3 + O_2 \tag{8.5.7}$$

$$NO_3 + h\nu \longrightarrow NO + O_2 \tag{8.5.8}$$

$$NO + O_3 \longrightarrow NO_2 + O_2 \tag{8.5.9}$$

$$\textbf{net} \qquad 2O_3 \longrightarrow 3O_2 \tag{8.5.10}$$

Upper Stratosphere

$$NO_2 + O \longrightarrow NO + O_2 \tag{8.5.11}$$

$$NO + O_3 \longrightarrow NO_2 + O_2 \tag{8.5.12}$$

$$\textbf{net} \qquad O_3 + O \longrightarrow 2O_2 \tag{8.5.13}$$

A reduction in stratospheric NO_2 corresponds with reduced titration of O_3, and consequently increased stratospheric O_3. Increased stratospheric O_3 propagates throughout the column and into the surface layer via stratospheric intrusion and vertical transport. At some locations in the Southern Hemisphere, approximately 45% of surface O_3 may originate from transported stratospheric air (Wayne, 2000). Therefore, increased stratospheric O_3 results in both increased total column and surface amounts, as seen in the updated ACCESS simulation (Figures 8.5.8 & E.0.16).

The altered magnitude of updated ACCESS O_3 column values resulted in a high bias compared with measurements at Wollongong (Figure 8.5.9). In contrast, the original simulation reproduced Wollongong column O_3 well. This suggests a need for future investigation into ACCESS O_3 sources. While the magnitude was altered, column O_3 annual cycle remained consistent with FTS measurements at Wollongong.

Increasing atmospheric O_3 was expected to have an effect on the oxidising capacity of the troposphere, as O_3 is the major source of tropospheric hydroxyl radical. Altered atmospheric oxidising capacity has implications for tropospheric trace gases that are depleted via loss mechanisms with OH oxidation, such as CO, HCHO and C_2H_6. Thus, changing ACCESS NO_2 may indirectly affect other trace gases through affecting O_3.

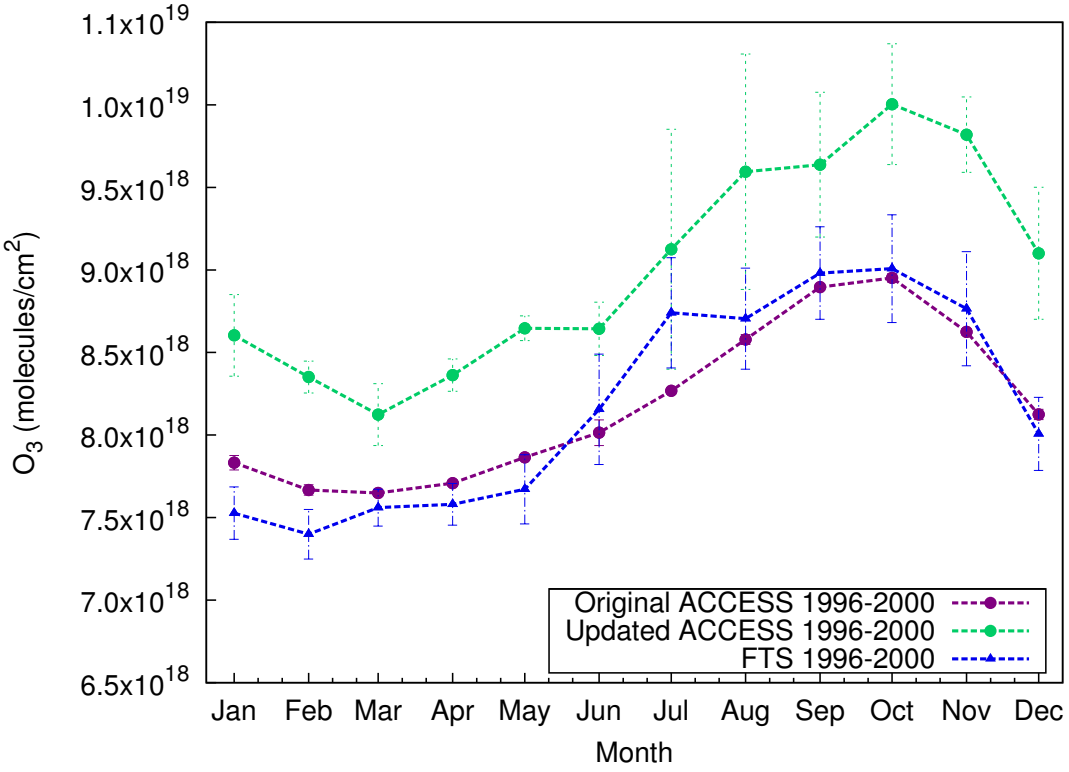

Figure 8.5.9: Average annual cycles of monthly total column O_3 at Wollongong. Measurements are shown in blue triangles, original ACCESS simulation in maroon circles and updated ACCESS simulation in green circles. Model results were convolved with averaging kernels prior to total column calculation.

Carbon monoxide, formaldehyde and ethane

Total column values for all three trace gases CO, HCHO and C_2H_6 at all three sites were not significantly altered between the simulations. CO is shown here (Figure 8.5.10) and HCHO and C_2H_6 are shown in Appendix E (Figures E.0.17a and E.0.17b respectively). Surface values for these three trace gases are also unchanged at all three sites (not shown). This indicates, that while changing the stratospheric NO_2 did significantly alter atmospheric O_3, the resulting change in oxidising capacity was not great enough to alter the atmospheric composition with respect to organic compounds.

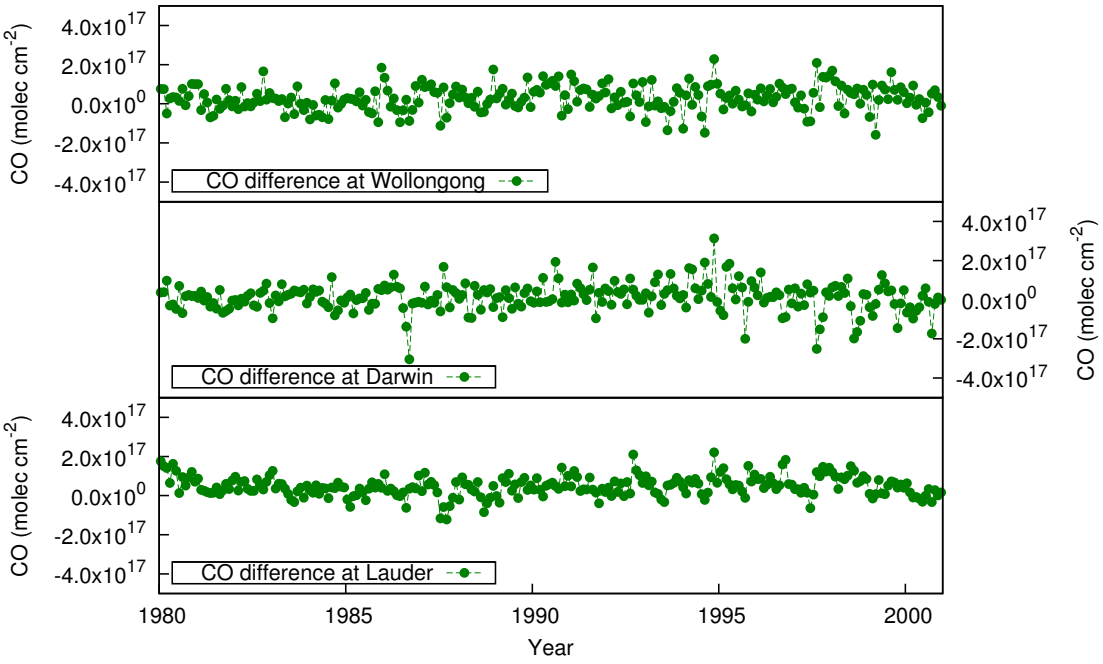

(a) Total column CO difference.

Figure 8.5.10: Timeseries of total column CO monthly differences between original and updated ACCESS simulations. Differences at Wollongong (top panel), Darwin (middle panel) and Lauder (bottom panel) are shown.

8.5.3 Summary and conclusions for stratospheric NO_2 study

A set of statistical parameters are collated in Table 8.5.1. Mean differences, and correlation coefficients between original and updated simulations, and average monthly standard deviation were used to understand and summarise the effect of altering stratospheric NO_2 within ACCESS.

Not surprisingly, changing ACCESS model NO_2 stratospheric boundary conditions had a significant effect on the NO_2 total column. Updated ACCESS column NO_2 significantly reduced compared to the original simulation and mean differences are outside the average monthly standard deviation at all sites. (Table 8.5.1). Additionally, NO_2 column values were uncorrelated between simulations, supporting the change in seasonality as previously observed (Figure 8.5.7). Surface NO_2 values are not significantly different between runs, which indicated the main source of surface NO_2 to be from emissions rather than from stratospheric intrusions. Although improved, updated ACCESS NO_2 column does not match Wollongong FTS measurements in magnitude or seasonal cycle. Well represented surface values by ACCESS indicated over-representation of

column NO_2 is likely due to remaining stratospheric biases.

Table 8.5.1: Summary of mean differences, average month standard deviation (σ), and correlation coefficients for trace gas total column and selected surface results from original and updated ACCESS simulations. Results are analysed at Wollongong (WOL), Lauder (LAU) and Darwin (DAR). Significant correlations are considered as coefficients > 0.70, values not reaching this criteria are in red. Statistically different means ($> 1\sigma$) are in green. Arrows visualise the mean difference as a shift either up or down in the updated ACCESS run relative to the original run.

Trace Gas		**Location**	**Mean Difference** (Original - Updated)		**Average Monthly σ**	**Correlation Coefficient**
NO_2	total column (molec cm^{-2})	WOL	*4.39×10^16*	↓	1.4×10^15	0.51
		DAR	*4.31×10^16*	↓	9.1×10^14	0.42
		LAU	*4.22×10^16*	↓	1.4×10^15	-0.25
	surface (mol mol^{-1})	WOL	2.4×10^−10	↓	6.7×10^−10	0.74
		DAR	5×10^−11	↓	1.3×10^−10	0.95
		LAU	1.2×10^−11	↓	4.5×10^−11	0.69
O_3	total column (molec cm^{-2})	WOL	*-7.14×10^17*	↑	3.7×10^16	0.87
		DAR	5.8×10^16	↓	5.5×10^16	0.93
		LAU	*-1.53×10^18*	↑	4.0×10^16	0.91
	surface (mol mol^{-1})	WOL	*-1.58×10^−8*	↑	1.2×10^−9	0.65
		DAR	*-5.83×10^−9*	↑	1.5×10^−9	0.88
		LAU	*-1.83×10^−8*	↑	1.1×10^−9	0.63
CO	total column (molec cm^{-2})	WOL	3.0×10^16	↓	4.8×10^16	0.92
		DAR	1.3×10^16	↓	4.8×10^16	0.93
		LAU	4.7×10^16	↓	3.3×10^16	0.95
H_2CO	total column (molec cm^{-2})	WOL	-6×10^13	↑	2.3×10^14	0.95
		DAR	-5×10^13	↑	2.6×10^14	0.86
		LAU	-5×10^13	↑	1.4×10^14	0.87
C_2H_6	total column (molec cm^{-2})	WOL	2.1×10^14	↓	6.15×10^14	0.91
		DAR	1.2×10^14	↓	6.48×10^14	0.90
		LAU	2.7×10^14	↓	4.49×10^14	0.94

ACCESS O_3 was significantly altered by a change in stratospheric NO_2 boundary conditions, both in total column and surface values. This reflects the close relationship of NO_2 and O_3 through atmospheric chemistry. In the statistical summary (Table 8.5.1), Wollongong and Lauder show significant increases in total column O_3 in the updated ACCESS simulation. In contrast to the other sites, Darwin total column shows no significant change in the updated simulation. The reason for no change at Darwin is likely related to being a tropical site, while the other sites are temperate. All sites show a significant increase in surface O_3. Low correlation coefficients for Lauder and Wollongong surface values indicate a possible change in surface O_3 annual cycle at these two locations between model runs.

CO, HCHO and C_2H_6 are not significantly altered between simulations, all showing high correlation coefficients between simulations. Additionally, all mean differences for all three trace gases and at all three sites are within one respective average monthly standard deviation. Although not significant, CO and C_2H_6 show a small consistent decrease in updated datasets (arrows in Table 8.5.1). This likely reflects an increase in oxidation of CO and C_2H_6 due to increased OH availability via increased O_3. In contrast, HCHO shows small consistent increases in the updated simulation, which suggest the increase in HCHO sources from higher VOC oxidation outweighed increased loss of HCHO via oxidation.

Stratospheric NO_2 within ACCESS will require further reduction due to the remaining mis-representation of NO_2 total column. Future stratospheric NO_2 reduction in ACCESS may influence other trace gases to a greater extent and in the same direction indicated by the arrows in Table 8.5.1, possibly altering composition to a significant level for CO, HCHO and C_2H_6. Therefore, if stratospheric NO_2 is again altered in ACCESS, the effect on O_3, CO, HCHO and C_2H_6 must be re-assessed. For the purposes of this study, it was determined that the analysis of CO, HCHO and C_2H_6 using original simulation results (presented in Sections 8.3 and 8.4) was robust to the change in modelled stratospheric NO_2 condition. Therefore, conclusions about CO, HCHO and C_2H_6 determined using data from the original ACCESS simulation remain valid.

Overall, investigation of NO_2 stratospheric boundary condition is an example of the interconnected nature of atmospheric composition. This study has demonstrated that a change in one trace gas species can greatly affect some species, while leaving other trace gases relatively unchanged. Quantifying and predicting connections is a key component to understanding atmospheric composition and change.

8.6 General conclusions

This chapter has evaluated output from the chemistry module of the new Earth System Model ACCESS. Comparisons of CO, HCHO and C_2H_6 total column values with measurements and results from the chemical transport model GEOS-Chem indicate that ACCESS still has some challenges in correctly representing atmospheric composition. CO, HCHO and C_2H_6 are all underestimated at the three stations studied here, Wollongong, Darwin and Lauder. Additionally total column CO and C_2H_6 seasonal cycles are early by one month. Table 8.6.1 summarises mis-matches between ACCESS and measurements with determined cause. Main reasons for mis-representation by ACCESS were found to be biases in direct emissions and lack of inclusion of isoprene and related chemistry. Dynamics was found to provide minimal contribution to the low bias seen in ACCESS columns. However, El Niño Southern Oscillation regimes were found to contribute to interannual variability. The NO_2 stratospheric boundary condition was found to not affect total column CO, HCHO and C_2H_6, although it produced an 80% reduction in NO_2 column.

Evaluation of ACCESS chemistry module output has lead to several recommended improvements to ACCESS:

- **Emissions:** Inventory biases, likely in biomass burning, are responsible for mistimed annual cycle peaks in total column CO and C_2H_6. Updated emissions are recommended based on IPCC Assessment Report 5.

- **Chemistry:** Lack of isoprene and related chemistry affected trace gases, CO, HCHO and C_2H_6. Future ACCESS simulations require implementation of the isoprene scheme (Zeng et al., 2008) to ensure correct representation of isoprene oxidation products. Additionally, study into atmospheric oxidation capacity through OH would help compare chemical loss mechanisms.

- **Meteorology:** Implementation of meteorological nudging would help confirm the insignificant role of meteorology in ACCESS misrepresentations.

- **Stratosphere:** NO_2 stratospheric conditions remain too high and produce incorrect seasonality in the NO_2 total column annual cycle. It is recommended to use an updated version of NO_2 stratospheric conditions from a more recent version of a stratospheric model, validated for the Southern Hemisphere.

Table 8.6.1: Summary of the comparison between ACCESS and measurements. Additional comparison with GEOS-Chem (not tabulated) helped lead to determined causes.

Trace Gas	**Mis-representation by ACCESS**	**Determined Cause**
CO	lower magnitude	Isoprene parameterisation biased low and possible missing higher order VOCs.
	annual cycle peaks early	CO emissions peak one month early for Australasia. Likely due to a non-representative biomass burning emissions inventory.
HCHO	lower magnitude	No account for HCHO from oxidation of isoprene.
	low variability	Isoprene oxidation drives HCHO annual cycle variability.
C_2H_6	lower magnitude	Lack of C_2H_6 parametrisation from oxidation of isoprene.
	annual cycle peaks early	C_2H_6 emissions peak one month early. Biomass burning emissions inventory is likely biased.
NO_2	total column too high	Stratospheric NO_2 biased high.
	incorrect annual cycle	Definition of stratospheric NO_2 from a dated 2D model, developed in the Northern Hemisphere.

Although not evaluated here, it would be valuable to compare OH fields between models, as this is the main loss mechanism for atmospheric CO, HCHO and C_2H_6. Differences in the amount of OH could therefore alter the rate and magnitude of loss of these chemical species, affecting atmospheric amounts. CSIRO had studied the CH_4 lifetime in ACCESS and indirectly determined that the modelled OH field is generally within expected magnitudes. ACCESS OH fields were not saved for the research presented in this thesis, and could not be directly studied. However, some differences between modelled total columns may be accounted for by OH differences, particularly as model results converge in future simulations. OH fields are therefore important for future study.

In addition to evaluating ACCESS, GEOS-Chem was found to have limitations representing HCHO and C_2H_6 columns. Summer mis-representation of HCHO at Wollongong and Lauder was determined due to isoprene emission biases. Significant over-representation of C_2H_6 at all three sites was most likely due to anthropogenic emission inventory bias in the Southern Hemisphere, found during this study. Loss mechanisms

or chemical sources may also contribute to GEOS-Chem bias, therefore overestimation of C_2H_6 by GEOS-Chem would benefit from future research.

Future research with ACCESS would benefit from comparisons with satellite data, such as CO from MOPITT or HCHO from the Ozone Monitoring Instrument (OMI). Using satellite data would extend the comparison to regions with limited ground-based measurements as well as present a spatial representation of ACCESS model validity. Additionally, performing a simulation using newly available GEOS-Chem meteorological fields and emission files from 1980 to 2000 would more appropriately overlap with ACCESS and remove the need for indirect comparisons. The climatological time period comparison with GEOS-Chem would also allow assessment of emission differences between El Niño and La Niña years. Nudging meteorological fields in ACCESS, that is relaxing meteorology towards real meteorological conditions, would aid in specifically evaluating the chemistry module, as modelled output would be able to be directly compared with observations for specific dates.

Analysing the validity of the Earth System model ACCESS has improved our understanding of seasonal variability and background concentrations of the target trace gases in the Australasian region. Comparison of the Earth System Model with the well established CTM, GEOS-Chem, and with measurements allows for insight into ACCESS modelling strengths, indicating processes accurately captured. Model processes identified as weaknesses have brought focus to areas requiring further development. This research has directly contributed to ACCESS model development and improved model simulations within the region.

Part IV

General Discussion

Chapter 9

Summary and Concluding Remarks

9.1 Summary of PhD outcomes

This thesis has presented a study on contemporary Southern Hemisphere atmospheric composition, with a focus on the Australasian region. A combination of analysis methods, using both models and measurements, took advantage of the complementary nature of combining theory and observation. A range of spatial and temporal scales were covered, leading to a deeper understanding of processes, sources and background concentrations of atmospheric trace gases in the Southern Hemisphere.

9.1.1 Outcomes of Part II - Measurements

The first ambient, semi-continuous, long-term record of CO, CO_2, CH_4, N_2O and $\delta^{13}C$ was measured at UOW using in situ FTIR instrumentation. Strict dataset preparation involving cross-sensitivity and calibration analysis was performed in order to produce a quality controlled record of atmospheric composition. This record at UOW provides atmospheric composition measurements relevant for a non-remote site.

Background analysis of the in situ record by constraining to wind directions from the ocean and applying REBS baseline analysis determined background properties of atmospheric composition at Wollongong. Although strongly influenced by urban pollution, it was found that air having close to global background composition arrived at Wollongong approximately 10% of the time. Background values were used to determine annual cycles for CO, CO_2 and CH_4, showing strong influence from Southern Hemi-

spheric biomass burning during Austral spring.

Preliminary trend analysis was completed for background values of CO, CO_2 and CH_4. Upward trends were found for CO_2 and CH_4, consistent with Cape Grim, Tasmania, and the global average from IPCC. These gases could be used to follow the trend in globally relevant, well-mixed background values. A downward trend resulted for CO, which was substantially more negative than the clean-air station of Cape Grim, and was attributed to the UOW site being closer to changing atmospheric sources of CO.

Analysis of daily cycles for the entire record confirmed strong local urban and industrial influence on the Wollongong atmosphere. Seasonal cluster analysis was performed on the in situ FTIR timeseries for CO to determine directional influences on atmospheric composition. Strong sources were found from the southern direction, most likely a combination of sources from the local urban and Port Kembla steel-making industrial area. High CO was also seen to be transported from the north/northwest in spring and summer, and from the northeast in winter, influences from local and Sydney pollution.

Subsequent within-cluster $\Delta O_3/\Delta CO$ correlation analysis allowed determination of tropospheric ozone production environments influencing the Wollongong atmosphere. Generally, the autumn and winter Wollongong atmosphere supports ozone destruction (negative correlations). In contrast, spring and summer show ozone production, indicated by positive correlations for air parcels arriving at UOW. Trajectory analysis helped determine that at UOW, ozone production environments are associated with slower moving, anticyclonic trajectories, while ozone destruction environments correspond with fast moving, direct trajectories.

Transported pollution was distinguished from local pollution by comparing ground based and satellite based remotely sensed total column CO. This used sensitivity differences between satellite and ground-based instruments to an advantage. Several anomalous CO events at Wollongong were identified for each instrument, and were further analysed by incorporating back trajectory analysis and MODIS fire count data. Long range transport from Southern Africa and South America biomass burning, as well as clean Antarctica air was observed to influence the atmosphere at Wollongong on several occasions. Also, regional transport events were identified from Northern Australia biomass burning. Finally, similar to the in situ record, anticyclonic episodes cycled urban outflow from Sydney, and retained local pollution over Wollongong to produce very high CO. Anomalies resulting from local pollution events were measured only by the ground-based FTS instrument.

9.1.2 Outcomes of Part III - Modelling

This research was the first to compare the Chemical Transport Model GEOS-Chem full chemistry simulation results with long-term timeseries of non-remote Australasian total column values of CO. Additionally, it is the first time total column amounts of, HCHO and C_2H_6 have been compared with GEOS-Chem full-chemistry runs in Australasia.

Generally, GEOS-Chem represented CO well at all sites with minimal differences, suggesting the processes for this trace gas are well understood. Modelled HCHO summer maximum was biased high at Wollongong and biased low at Lauder. GEOS-Chem significantly overrepresented total column C_2H_6, which was determined to be due to inadequately high modelled anthropogenic emissions for the Southern Hemisphere.

Australasian model-measurement mismatch was further studied for CO using MOPITT satellite-based measurements from 2008. Biases found between solar FTS and GEOS-Chem at Wollongong and Darwin FTS sites were generally representative of biases for wider local regions. The model overestimates tropical CO north of Darwin throughout the year. From April to December, a latitudinal band (20° S to 60° S) is biased low for the model, indicating a deficiency in transported CO. This was attributed to be most likely due to the use of GFED2 biomass burning inventory which underestimates burning in Africa.

Seasonal cycles of total column values were investigated for solar FTS, GEOS-Chem and the earth-system model ACCESS. Annual peak in CO and C_2H_6 at the three sites correlated with peak biomass burning season in the Southern Hemisphere (September-October), and biomass burning emissions were found to drive the variability in GEOS-Chem total CO and total C_2H_6 emissions. HCHO annual cycle maximum occurred during Austral summer (December-February) in the temperate regions of Wollongong and Lauder, corresponding with temperature dependent biogenic emissions. Annual maximum HCHO at Darwin coincided with biomass burning season, a reflection of this site being closer to biomass burning sources combined with the short lifetime of HCHO.

This work has also helped to develop the next-generation of earth-system models (ESMs), contributing to more accurate future simulations and ultimately a better understanding of climate-chemistry connections. Output from the ESM ACCESS was compared with both FTS measurements, for absolute accuracy, and output from GEOS-Chem, for missing processes. Recommendations developed from this research have been, or are in the process of being implemented and will directly improve the ACCESS model.

Specifically, it was recommended to update to a more recent emission inventory such as used for the IPCC AR5 due to annual cycle mis-matches in CO. Also, inclusion of the updated isoprene chemical mechanism was suggested to improve HCHO and C_2H_6 representation. Finally, correct NO_2 stratospheric boundary conditions were required to accurately represent Southern Hemisphere values.

9.1.3 Skills developed

In addition to scientific outcomes, extensive experience was gained in a variety of advanced techniques used to study atmospheric composition. Skills were gained in:

• Using complex instrumentation associated with FTIR measurements. As primary researcher in charge of the UOW in situ FTIR ambient record, responsibility included daily running procedures and instrument checks, as well as calibration and cross-sensitivity analysis. Experience was also gained with the daily collection of solar FTS spectra and respective retrieval analysis using GFIT. As a member of the solar FTS collection team, responsibilities included ensuring correct daily operation, cooling of detectors with liquid nitrogen, and performing end-of-days procedures.

• Installing and compiling the Chemical Transport Model GEOS-Chem on a high-performance computing system and subsequently performing extended GEOS-Chem simulations of full chemistry v8-03-01. This involved model-probing experiments to determine optimum set-up for modelling the Australasian region.

• Developing skills in computational programs used to analyse and interpret model output and measurements. Programs were written in the languages NCL, Perl, R and Igor. Analysis techniques involved handling large 3D datasets, such as during spatial comparison of satellite and model data. Additionally, algorithms were developed to smooth model data with relevant instrumental averaging kernels, required for accurate comparison.

• Attending various graduate courses, including a meteorology course at UNSW to gain knowledge of mathematical equations describing atmospheric and ocean dynamics; the European research course on Atmospheres (ERCA) to gain a breadth of knowledge in Atmospheric Science; and the online modelling chemistry-climate summer school at the University of Aveiro, Portugal to understand specific processes and challenges of the chemistry-climate system. I was also able to communicate research to peers via several national and international conference presentations.

Two first authored papers are being prepared from material within this thesis.

- **Chapter 4**: Buchholz, R. R., Paton–Walsh, C., Kubistin, D., Caldow, C., Cameron, M., Macatangay, R. C., Kettlewell, G. and Griffith, D. W. T., Using in situ carbon monoxide, methane and carbon dioxide to investigate the Southern Hemisphere site: Wollongong, Australia.
- **Chapter 7:** Buchholz, R. R., Paton–Walsh, C., Hurley, P., Jones, N. B., Kettlewell, G., Griffith, D. W. T., Zeng, G. and Smale, D., Total column CO and HCHO measurements compared with the Global Chemical Transport Model GEOS-Chem in Australasia.

Additionally, work completed during my PhD has contributed to several other studies, which are being written as co-authored publications:

- **Chapter 4:** Paton-Walsh, C., Guerétte, É-A., Humphries, R., Kubistin, D., Wilson, S., Griffith, D., Buchholz, R. *et* al., Overview of the MUMBA campaign: Measurements of Urban, Marine and Biogenic Air.
- **Chapter 5:** Edwards, D. P., Emmons, L. K., Jones, N. B., Paton-Walsh, C., Deutscher, N. M., Buchholz R. R., and Griffith, D. W. T., Satellite and ground-based remote sensing of carbon monoxide over Australasia: Linking global and local scales.
- **Chapter 7:** Velazco, V.A., Macatangay, R. C., Griffith, D. W. T., Deutscher, N. M., Jones, N. B., Paton-Walsh, C., Buchholz, R. R., Kettlewell, G. and Shi, X., Towards Pinpointing GHG & Pollution Hot Spots: Synergistic Use of High-Resolution Ground–Based Remote Sensing Measurements and a Lagrangian Transport Model.

9.2 Future directions

While delivering the outcomes listed in the previous section, this research has also provided avenues for further investigation relating to Australasian atmospheric composition. Some major opportunities for future research are highlighted below.

The in situ FTIR dataset at UOW, begun here, will continue to be recorded, creating a longer-term record. Trends determined here should be viewed with caution due to the short nature of the records. With extended measurements, robust trends in the background amounts of trace gases can be determined, a valuable addition to the global investigation of atmospheric composition and for interpreting future atmospheric change. Additionally, while CO is the main focus in this thesis, the other in situ trace gas datasets are prepared to a level for similar analysis using clustering techniques.

Backward Lagrangian and inverse modelling would support source attribution of trace gases both for the in situ and solar FTS records. In the case of in situ CO_2, which was suggested here to have influences from transported Northern Hemisphere sources, a local component may also be distinguished. Inverse modelling would also help update emissions in the Australasian region.

Another application for the in situ dataset is in comparison with total column FTS measurements, to help distinguish transported from local pollution. This would add to the study between FTS and satellite-based MOPITT column CO comparisons performed here. Request for the in situ CO record has been received from Paris, and in situ CO_2 has been earmarked for further study during an upcoming postdoctoral fellowship at UOW.

Comparison of GEOS-Chem with total column measurements of HCHO and C_2H_6 would benefit from additional solar FTS records of HCHO and C_2H_6 at Darwin, and updated HCHO at Lauder. During the writing of this thesis, HCHO at Lauder have become available. However, at this stage, HCHO and C_2H_6 at Darwin would require dedicated field campaigns due to the remote nature of the site, and high operator input required for recording of mid-infrared (MIR) measurements. A complete annual record of MIR measurements at Darwin would be very valuable to complete annual cycles of trace gases and to ascertain whether models are reproducing atmospheric composition in this area accurately.

Annual cycle analysis for model and measurement HCHO has highlighted a possible missing source for HCHO in models. Measurements of isoprene and HCHO in the oceanic PBL surrounding Lauder would help determine whether there is a missing model source as hypothesised. Comparison of HCHO with GEOS-Chem would also benefit by comparison with satellite measurements, such as those taken with the OMI instrument.

During the writing of this thesis, progress has been made on developing the ACCESS model at CSIRO. Emissions have been updated to the AR5 inventory, isoprene chemistry scheme implemented, lightning NO_X included and a meteorological nudging scheme implemented. Updated runs have been performed, and a current PhD student at UOW is using analysis code developed for the work in this thesis to perform comparisons for the updated ACCESS runs. Therefore, in addition to a reference comparison for the ACCESS model, the visualisation and analysis tools developed during this research has become a part of the UOW research team skill set.

Ideally, once the ESM configuration of ACCESS becomes operational, an ultimate aim is to project the Australasian atmosphere into the future based on IPCC emissions scenarios. Projections completed with ACCESS will include the feedback of chemistry into climate for each of the representative concentration pathways, allowing an assessment of air quality associated with different emission scenarios. A feature not currently included in earth-system models are human health outcomes. Linking atmospheric processes with social/health impact model will ultimately link climate, through atmospheric composition to an impact for human health.

References

1. Abad, G. G., Allen, N. D. C., Bernath, P. F., Boone, C. D., McLeod, S. D., Manney, G. L., Toon, G. C., Carouge, C., Wang, Y., Wu, S., Barkley, M. P., Palmer, P. I., Xiao, Y., & Fu, T. M. (2011). Ethane, ethyne and carbon monoxide concentrations in the upper troposphere and lower stratosphere from ACE and GEOS-Chem: a comparison study. *Atmospheric Chemistry and Physics 11* (18), 9927–9941.

2. Alexander, B., Park, R. J., Jacob, D. J., Li, Q. B., Yantosca, R. M., Savarino, J., Lee, C. C. W., & Thiemens, M. H. (2005). Sulfate formation in sea-salt aerosols: Constraints from oxygen isotopes. *Journal of Geophysical Research: Atmospheres 110* (D10), D10307.

3. Arellano, A. F. J., Kasibhatla, P. S., Giglio, L., van der Werf, G. R., Randerson, J. T., & Collatz, G. J. (2006). Time-dependent inversion estimates of global biomass-burning CO emissions using Measurement of Pollution in the Troposphere (MOPITT) measurements. *Journal of Geophysical Research: Atmospheres 111* (D9), D09303.

4. Arrhenius, S. (1896). On the Influence of Carbonic Acid in the Air upon the Temperature of the Ground. *Philosophical Magazine and Journal of Science 41* (Series 5), 237–276.

5. Atkinson, R. (2000). Atmospheric chemistry of VOCs and NOx. *Atmospheric Environment 34* (12-14), 2063–2101.

6. Aumann, H. H., Chahine, M. T., Gautier, C., Goldberg, M. D., Kalnay, E., McMillin, L. M., Revercomb, H., Rosenkranz, P., Smith, W. L., Staelin, D. H., Strow, L. L., & Susskind, J. (2003). AIRS/AMSU/HSB on the AQUA mission: design, science objectives, data products, and processing systems. *IEEE Transactions on Geoscience and Remote Sensing 41*, 253–264.

7. Australian Bureau of Meteorology (December 2010). Climate Information Services, New South Wales Climate Service Centre: wind direction and wind speeds for Illawarra stations. URL climate.nsw@bom.gov.au

8. Australian Bureau of Statistics (2011). Australian Census, 2011. URL http://www.censusdata.abs.gov.au/

9. Ayers, G., & Gillett, R. (1988). Isoprene emissions from vegetation and hydrocarbon emissions from bushfires in tropical Australia. *Journal of Atmospheric Chemistry 7*, 177–190.

10. Bacsik, Z., Mink, J., & Keresztury, G. (2004). FTIR spectroscopy of the atmosphere. I. Principles and methods. *Applied Spectroscopy Reviews 39* (3), 295–363.

11. Banwell, C. N., & McCash, E. M. (1994). *Fundamentals of molecular spectroscopy (4th ed.).* McGraw-Hill Book Company Europe, Berkshire, UK, Ch. 3: Infra-red Spectroscopy, pp. 55–99.

12. Barkley, M. P., De Smedt, I., Van Roozendael, M., Kurosu, T. P., Chance, K., Arneth, A., Hagberg, D., Guenther, A., Paulot, F., Marais, E., & Mao, J. (2013). Top-down isoprene emissions over tropical South America inferred from SCIAMACHY and OMI formaldehyde columns. *Journal of Geophysical Research: Atmospheres 118* (12), 6849–6868.

13. Barkley, M. P., Palmer, P. I., Ganzeveld, L., Arneth, A., Hagberg, D., Karl, T., Guenther, A., Paulot, F., Wennberg, P. O., Mao, J., Kurosu, T. P., Chance, K., Mueller, J. F., De Smedt, I., Van Roozendael, M., Chen, D., Wang, Y., & Yantosca, R. M. (2011). Can a "state of the art" chemistry transport model simulate Amazonian tropospheric chemistry? *Journal of Geophysical Research: Atmospheres 116* (D16), D16302.

14. Barkley, M. P., Palmer, P. I., Kuhn, U., Kesselmeier, J., Chance, K., Kurosu, T. P., Martin, R. V., Helmig, D., & Guenther, A. (2008). Net ecosystem fluxes of isoprene over tropical South America inferred from Global Ozone Monitoring Experiment (GOME) observations of HCHO columns. *Journal of Geophysical Research: Atmospheres 113* (D20), 6849–6868.

15. Beer, R. (2006). TES on the Aura mission: scientific objectives, measurements, and analysis overview. *IEEE Transactions on Geoscience and Remote Sensing 44*, 1102–1105.

16. Bey, I., Jacob, D. J., Yantosca, R. M., Logan, J. A., Field, B. D., Fiore, A. M., Li, Q. B., Liu, H. G. Y., Mickley, L. J., & Schultz, M. G. (2001). Global modeling of tropospheric chemistry with assimilated meteorology: Model description and evaluation. *Journal of Geophysical Research: Atmospheres 106* (D19), 23073–23095.

17. Bhaskaran, B., & Mulan, A. B. (2003). El Niño-related variations in the southern Pacific atmospheric circulation: model versus observations. *Climate Dynamics 20*, 229–239.

18. Bond, T. a. (2007). Historical emissions of black and organic carbon aerosol from energy-related combustion, 1850-2000. *Global Biogeochemical Cycles 21*, GB2018.

19. Bordi, F., Neeck, S., & Scolese, C. (1999). Contribution of EOS Terra to Earth science. *Proceedings of the Society of Photo-optical Instrumentation Engineers 3870*, 260–268.

20. Bouwman, A., Lee, D. S., Asman, W. A. H., Dentener, F. J., Van Der Hoek, K. W., & Olivier, J. G. J. (1997). A global high–resolution emission inventory for ammonia. *Global Biogeochemical Cycles 11*, 561–587.

21. Brune, W. (2007). Needs for Sampling on Short Time and Spatial Scales. In: Visconti, G., Di Carlo, P., Brune, W. H., Schoeberl, M. R., & Wahner, A. (Eds.), *Observing Systems for Atmospheric Composition.* Springer.

22. Bryant, E. A. (1982). Local Climate of the Illawarra. *Wollongong Studies in Geography, Department of Geography, University of Wollongong* (11).
URL http://ro.uow.edu.au/wollgeo/11

23. Burrows, J. P., Hölze, E., Goede, A. P. H., Visser, H., & Fricke, W. (1995). SCIAMACHY scanning imaging absorption spectrometer for atmospheric chartography. *Acta Astronautica 35* (7), 445–451.

24. Burrows, J. P., Platt, U., & Borrell, P. (2011). *The Remote Sensing of Tropospheric Composition from Space.* Springer Verlag, Heidelberg, Ch. 1: Tropospheric Remote Sensing from Space, pp. 1–61.

25. Calinski, R. B., & Harabasz, J. (1974). A Dendrite Method for Cluster Analysis. *Communications in Statistics 3*, 1–27.

26. Carslaw, D. C. (2013). The openair manual – open-source tools for analysing air pollution data. *Manual for version 0.8-0, King's College London.*

27. Carslaw, D. C., & Beevers, S. D. (2013). Characterising and understanding emission sources using bivariate polar plots and k-means clustering. *Environmental Modelling & Software 40* (0), 325–329.

28. Carslaw, D. C., & Ropkins, K. (2012). Openair – an R package for air quality data analysis. *Environmental Modelling & Software 27–28*, 52–61.

29. Ciais, P., Sabine, C., Bala, G., Bopp, L., Brovkin, V., Canadell, J., Chhabra, A., DeFries, R., Galloway, J., Heimann, M., Jones, C., Le Quéré, C., Myneni, R. B., Piao, S., & Thornton, P. (2013). Chapter 6: Carbon and other biogeochemical cycles. In: Stocker, T. F., Qin, D., Plattner, G. K., Tignor, M., Allen, S. K., Boschung, J., Nauels, A., Xia, Y., Bex, V., & Midgley, P. M. (Eds.), *Climate Change 2013: The Physical Science Basis. Contribution of Working Group I to the Fifth Assessment Report of the Intergovernmental Panel on Climate Change.* Cambridge University Press, Cambridge, United Kingdom and New York, NY, USA.
URL http://www.ipcc.ch/report/ar5/wg1/

30. Clerbaux, C., Boynard, A., Clarisse, L., George, M., Hadji-Lazaro, J., Herbin, H., Hurtmans, D., Pommier, M., Razavi, A., Turquety, S., Wespes, C., & Coheur, P. F. (2009). Monitoring of atmospheric composition using the thermal infrared IASI/MetOp sounder. *Atmospheric Chemistry and Physics 9*, 6041–6054.

31. Clerbaux, C., Coheur, P. F., Hurtmans, D., Barret, B., Carleer, M., Colin, R., Semeniuk, K., McConnell, J. C., Boone, C., & Bernath, P. (2005). Carbon monoxide distribution from the ACE-FTS solar occultation measurements. *Geophysical Research Letters 32*, 1–4.

32. Comiso, J. C., McClain, C. R., Sullivan, C. W., Ryan, J. P., & Leonard, C. L. (1993). Coastal zone color scanner pigment concentrations in the Southern Ocean and relationships to geophysical surface features. *Journal of Geophysical Research: Oceans 98* (C2), 2419–2451.

33. Craig, R., Heath, B., Raisbeck-Brown, N., Steber, M., J., M., & Smith, R. (2002). The distribution, extent and seasonality of large fires in Australia, April 1998-March 2000, as mapped from NOAA-AVHRR imagery. In: Russell-Smith, J., Craig, R., Gill, A. M., Smith, R., & Williams, J. (Eds.), *Australian fire regimes: contemporary patterns (April 1998 - March 2000) and changes since European settlement.* Australian Bureau of Meteorology and CSIRO Marine and Atmospheric Research., Department of the Environment and Heritage, Canberra.
URL http://www.ea.gov.au/soe/techpapers/index.html

34. Crutzen, P. J. (2002). Geology of mankind. *Nature 415* (6867), 23–23.

35. Crutzen, P. J., & Lelieveld, J. (2001). Human impacts on atmospheric chemisty. *Annual Review of Earth and Planetary Sciences 29*, 17–45.

36. CSIRO Marine and Atmospheric Research, & the Australian Bureau of Meteorology (July 2013a). Carbon Dioxide, Nitrous Oxide and Methane monthly data from Cape Grim Baseline Air Pollution Station.
URL http://www.csiro.au/greenhouse-gases/

37. CSIRO Marine and Atmospheric Research, & the Australian Bureau of Meteorology (July 2013b). Carbon Monoxide and δ^{13}C monthly data from Cape Grim Baseline Air Pollution Station via Global Atmospheric Watch World Data Centre for Greenhouse Gases.
URL http://ds.data.jma.go.jp/gmd/wdcgg/wdcgg.html

38. Dameris, M., & Jöckel, P. (2013). Numerical Modeling of Climate-Chemistry Connections: Recent Developments and Future Challenges. *Atmosphere 4*, 132–156.

39. Damian, V., Sandu, A., Damian, M., Potra, F., & R., C. G. (2002). The Kinetic PreProcessor KPP-A software environment for solving chemical kinetics. *Computers and Chemical Engineering 26* (11), 1567–1579.

40. Davies, D., Ilavajhala, S., Wong, M., & Justice, C. (2009). Fire Information for Resource Management System: Archiving and Distributing MODIS Active Fire Data. *IEEE Transactions on Geoscience and Remote Sensing 47* (1), 72–79.
URL http://firefly.geog.umd.edu/firemap/

41. Davies, D., Kumar, S., & Descloitres, J. (2004). Global fire monitoring using MODIS near-real-time satellite data. *GIM International 18* (4), 41–43.

42. Davies, T., Cullen, M. J. P., Malcolm, A. J., Mawson, M. H., Staniforth, A., White, A. A., & Wood, N. (2005). A new dynamical core for the Met Office's global and regional modelling of the atmosphere. *Quarterly Journal of the Royal Meteorological Society 131*, 1759–1782.

43. Davis, S. P., Abrams, M. C., & Brault, J. W. (2001). *Fourier Transform Spectrometry.* Academic Press, San Diego.

44. Deeter, M. N. (2011). MOPITT (Measurements of Pollution in the Troposphere) Version 5 Product. User's guide, MOPITT Algorithm Development Team, Atmospheric Chemistry Division, National Center for Atmospheric Research, Boulder, CO, USA.

45. Deeter, M. N. (2012). MOPITT Geolocation Bias Analysis and Corrections. Technical report, MOPITT Algorithm Development Team, Atmospheric Chemistry Division, National Center for Atmospheric Research, Boulder, CO, USA.

46. Deeter, M. N. (2013). MOPITT (Measurements of Pollution in the Troposphere) Version 6 Product. User's guide, MOPITT Algorithm Development Team, Atmospheric Chemistry Division, National Center for Atmospheric Research, Boulder, CO, USA.

47. Deeter, M. N., Edwards, D. P., Gille, J. C., Emmons, L. K., Francis, G., Ho, S. P., Mao, D., Masters, D., Worden, H., & Drummond, J. R.and Novelli, P. C. (2010). The MOPITT version 4 CO product: Algorithm enhancements, validation, and long-term stability. *Journal of Geophysical Research: Atmospheres 115*, D07306.

48. Deeter, M. N., Emmons, L. K., Francis, G. L., Edwards, D. P., Gille, J., Warner, J. X., Khattatov, B., Ziskin, D., Lamarque, J. F., Ho, S. P., Yudin, V., Attie, J. L., Packman, D., Chen, J., Mao, D., & Drummond, J. R. (2003). Operational carbon monoxide retrieval algorithm and selected results for the MOPITT instrument. *Journal of Geophysical Research: Atmospheres 108* (D14), 4399.

49. Deeter, M. N., Martinez-Alonso, S., Edwards, D. P., Emmons, L. K., Gille, J. C., Worden, H. M., Sweeney, C., Pittman, J. V., Daube, B. C., & Wofsy, S. C. (2014). The MOPITT Version 6 product: algorithm enhancements and validation. *Atmospheric Measurement Techniques 178*, 3623–3632.

50. Denmead, O. T., Macdonald, B. C. T., Bryant, G., Naylor, T., Wilson, S., Griffith, D. W. T., Wang, W. J., Salter, B., White, I., & Moody, P. W. (2010). Emissions of methane and nitrous oxide from Australian sugarcane soils. *Agricultural and Forest Meteorology 150*, 748–756.

51. Deutscher, N. M. (2009). Investigating greenhouse gases in Australia using atmospheric measurements with Fourier Transform Spectrometry and atmospheric modeling. Ph.D. thesis, School of Chemistry, University of Wollongong, Australia.

52. Deutscher, N. M., Griffith, D. W. T., Paton-Walsh, C., & Borah, R. (2010). Train-borne measurements of tropical methane enhancements from ephemeral wetlands in Australia. *Journal of Geophysical Research: Atmospheres 115* (D15304).

53. Drummond, J. R. (1992). Measurements of pollution in the troposphere (MOPITT). *Use of EOS for Studies of Atmospheric Physics*, 77–101.

54. Drummond, J. R., & Mand, G. S. (1996). The measurements of pollution in the troposphere (MOPITT) instrument: Overall performance and calibration requirements. *Journal of Atmospheric and Oceanic Technology 13* (2), 314–320.

55. Dufour, G., Szopa, S., Barkley, M. P., Boone, C. D., Perrin, A., Palmer, P. I., & Bernath, P. F. (2009). Global upper-tropospheric formaldehyde: seasonal cycles observed by the ACE-FTS satellite instrument. *Atmospheric Chemistry and Physics 9* (12), 3893–3910.

56. Duncan, B. N., Logan, J. A., Bey, I., Megretskaia, I. A., Yantosca, R. M., Novelli, P. C., Jones, N. B., & Rinsland, C. P. (2007). Global budget of CO, 1988-1997: Source estimates and validation with a global model. *Journal of Geophysical Research: Atmospheres 112* (D22), D22301.

57. Eamus, D., Hutley, L. B., & OGrady, A. P. (2001). Daily and seasonal patterns of carbon and water fluxes above a north Australian savanna. *Tree Physiology 21* (12-13), 977–988.

58. Edwards, D. P., Emmons, L. K., Gille, J. C., Chu, A., Attié, J. L., Giglio, L., Wood, S. W., Haywood, J., Deeter, M. N., Massie, S. T., Ziskin, D. C., & Drummond, J. R. (2006a). Satellite Observed Pollution From Southern Hemisphere Biomass Burning. *Journal of Geophysical Research: Atmospheres 111* (D14), D14312.

59. Edwards, D. P., Halvorson, C. M., & Gille, J. (1999). Radiative transfer modeling for the EOS Terra satellite Measurements of Pollution in the Troposphere (MOPITT) instrument. *Journal of Geophysical Research: Atmospheres 104* (D14), 16755–16775.

60. Edwards, D. P., Pétron, G., Novelli, P. C., Emmons, L. K., Gille, J. C., & Drummond, J. R. (2006b). Southern Hemisphere carbon monoxide interannual variability observed by Terra Measurement of Pollution in the Troposphere (MOPITT). *Journal of Geophysical Research: Atmospheres 111* (D16), D16303.

61. Edwards, J. M., & Slingo, A. (1996). Studies with a flexible new radiation code. 1. Choosing a configuration for a large-scale model. *Quarterly Journal of the Royal Meteorological Society 122* (531, Part a), 689–719.

62. Eller, P., Singh, K., Sandu, A., Bowman, K., Henze, D. K., & Lee, M. (2009). Implementation and Evaluation of an Array of Chemical Solvers in a Global Chemical Transport Model. *Geophysical Model Development 2*, 1–7.

63. Emmons, L. K., Walters, S., Hess, P. G., Lamarque, J. F., Pfister, G. G., Fillmore, D., Granier, C., Guenther, A., Kinnison, D., Laepple, T., J., O., Tie, X., Tyndall, G., Wiedinmyer, C., Baughcum, S. L., & Kloster, S. (2010). Description and evaluation of the Model for Ozone and Related chemical Tracers, version 4 (MOZART-4). *Geoscientific Model Development 3*, 43–67.

64. Esler, M. B., Griffith, D. W. T., Wilson, S. R., & Steele, L. P. (2000). Precision trace gas analysis by FT-IR spectroscopy, 1. Simultaneous analysis of CO_2, CH_4, N_2O and CO in air. *Analytical Chemistry 72*, 206–215.

65. Evans, M. J., & J., J. D. (2005). Impact of new laboratory studies of N_2O_5 hydrolysis on global model budgets of tropospheric nitrogen oxides, ozone and OH. *Geophysical Research Letters 32* (9), L09813.

66. Eyring, V., H. W. Kšhler, H. W., van Aardenne, J., & Lauer, A. (2005). Emissions from international shipping: 1. The last 50 years. *Journal of Geophysical Research: Atmospheres 110* (D17), D17305.

67. Fairlie, T. D., Jacob, D. J., & Park, R. J. (2007). The impact of transpacific transport of mineral dust in the United States. *Atmospheric Environment 41*, 1251–1266.

68. Fisher, J., Jacob, D. J., Wang, Q., Bahreini, R., Carouge, C. C., Cubison, M. J., Dibb, J. E., Diehl, T., Jimenez, J. L., Leibensperger, E. M., Meinders, M. B. J., Pye, H. O. T., Quinn, P. K., Sharma, S., van Donkelaar, A., & Yantosca, R. M. (2011). Sources, distribution, and acidity of sulfate-ammonium aerosol in the Arctic in winter-spring. *Atmospheric Environment 45*, 7301–7318.

69. Fishman, J., & Seiler, W. (1983). Correlative nature of ozone and carbon-monoxide in the troposphere - Implications for the tropospheric ozone budget. *Journal of Geophysical Research-Oceans 88* (C6), 3662–3670.

70. Fromm, M., Tupper, A., Rosenfeld, D., Servranckx, R., & McRae, R. (2006). Violent pyroconvective storm devastates australia's capital and pollutes the stratosphere. *Geophysical Research Letters 33* (5), 5815.

71. Fu, T. M., Jacob, D. J., Palmer, P. I., Chance, K., Wang, Y. X., Barletta, B., Blake, D. R., Stanton, J. C., & Pilling, M. J. (2007). Space-based formaldehyde measurements as constraints on volatile organic compound emissions in east and south Asia and implications for ozone. *Journal of Geophysical Research: Atmospheres 112* (D6), D06312.

72. Fu, T. M., Jacob, D. J., Wittrock, F., Burrows, J. P., Vrekoussis, M., & Henze, D. K. (2008). Global budgets of atmospheric glyoxal and methylglyoxal, and implications for formation of secondary organic aerosols. *Journal of Geophysical Research: Atmospheres 113* (D15), D15303.

73. Fung, I., John, J., Lerner, J., Matthews, E., Prather, M., Steele, L. P., & Fraser, P. J. (1991). Three-Dimensional Model Synthesis of the Global Methane Cycle. *Journal of Geophysical Research: Atmospheres 96* (D7), 13033–13065.

74. Ganzeveld, L., & Lelieveld, J. (1995). Dry deposition parameterization in a chemistry general-circulation model and its influence on the distribution of reactive trace gases. *Journal of Geophysical Research: Atmospheres 100* (D10), 20999–21012.

75. Giannakopoulos, C., Chipperfield, M. P., Law, K. S., & Pyle, J. A. (1999). Validation and intercomparison of wet and dry deposition schemes using ^{210}Pb in a global three- dimensional off-line chemistry model. *Journal of Geophysical Research: Atmospheres 104* (D19), 23761–23784.

76. Giglio, L., Descloitres, J., Justice, C. O., & Kaufman, Y. J. (2003). An enhanced contextual fire detection algorithm for MODIS. *Remote Sensing of Environment 87*, 273–282.

77. Gregory, D., & Rowntree, P. (1990). A mass flux convection scheme with representation of cloud ensemble characteristics and stability dependent closure. *Monthly Weather Review 118*, 1483–1506.

78. Griffin, D., Walker, K. A., Franklin, J. E., Parrington, M., Whaley, C., Hopper, J., Drummond, J. R., Palmer, P. I., Strong, K., Duck, T. J., Abboud, I., Bernath, P. F., Clerbaux, C., Coheur, P. F., Curry, K. R., Dan, L., Hyer, E., Kliever, J., Lesins, G., Maurice, M., Saha, A., Tereszchuk, K., & Weaver, D. (2013). Investigation of CO, C_2H_6 and aerosols in a boreal fire plume over eastern Canada during BORTAS 2011 using ground- and satellite-based observations and model simulations. *Atmospheric Chemistry and Physics 13* (20), 10227–10241.

79. Griffith, D., Deutscher, N., Krummel, P., Fraser, P., van der Schoot, M., & Allison, C. (2011). The UOW FTIR trace gas analyser: Comparison with LoFlo, AGAGE, and tank measurements at Cape Grim and GASLAB. In: Derek, N., & Krummel, P. B. (Eds.), *Baseline 2007–2008.* Australian Bureau of Meteorology and CSIRO Marine and Atmospheric Research., pp. 7–22.

80. Griffith, D. W. T. (1996). Synthetic Calibration and Quantitative Analysis of Gas-Phase infrared Spectra. *Applied Spectroscopy 50* (1), 59–70.

81. Griffith, D. W. T., Deutscher, N. M., Caldow, C. G. R., Kettlewell, G., Riggenbach, M., & Hammer, S. (2012). A Fourier transform infrared trace gas and isotope analyser for atmospheric applications. *Atmospheric Measurement Techniques 5* (10), 2481–2498.

82. Griffith, D. W. T. and Galle, B. (2000). Flux measurements of NH_3, N_2O and CO_2 using dual beam FTIR spectroscopy and the flux gradient technique. *Atmospheric Environment 34*, 1087–1098.

83. Griffith, D. W. T. and Jones, N. B. and Mathews, W. A. (1998). Interhemispheric ratio and annual cycle of carbonyl sulfide (OCS) total column from ground-based solar FTIR spectra. *Journal of Geophysical Research: Atmospheres 103* (D7), 8447–8454.

84. Griffiths, P. R., & de Haseth, J. A. (2007). *Fourier Transform Infrared Spectrometry, 2nd edition.* Wiley, New York.

85. Guenther, A., Hewitt, C. N., Erickson, D., Fall, R., Geron, C., Graedel, T., Harley, P., Klinger, L., Lerdau, M., McKay, W. A., Pierce, T., Scholes, B., Steinbrecher, R., Tallamraju, R., Taylor, J., & Zimmerman, P. (1995). A global model of natural volatile organic compound emissions. *Journal of Geophysical Research: Atmospheres 100* (D5), 8873–8892.

86. Guenther, A., Karl, T., Harley, P., Wiedinmyer, C., Palmer, P. I., & C., G. (2006). Estimates of global terrestrial isoprene emissions using MEGAN (Model of Emissions of Gases and Aerosols from Nature). *Atmospheric Chemistry and Physics 6*, 3181–3210.

87. Hammer, S., Griffith, D. W. T., Konrad, G., Vardag, S., Caldow, C., & Levin, I. (2012). Assessment of a multi-species in-situ FTIR for precise atmospheric greenhouse gas observations. *Atmospheric Measurement Techniques Discussions 5*, 3645–3692.

88. Hao, W. M., & Liu, M. H. (1994). Spatial and temporal distribution of tropical biomass burning. *Global Biogeochemical Cycles 8*, 495–503.

89. Hartmann, D. L., Klein Tank, A. M. G., Rusticucci, M., Alexander, L. V., Brönnimann, S., Charabi, Y., Dentener, F. J., Dlugokencky, E. J., Easterling, D. R., Kaplan, A., Soden, B. J., Thorne, P. W., Wild, M., & Zhai, P. M. (2013a). Chapter 2: Observations: Atmosphere and surface, supplementary material. In: Stocker, T. F., Qin, D., Plattner, G. K., Tignor, M., Allen, S. K., Boschung, J., Nauels, A., Xia, Y., Bex, V., & Midgley, P. M. (Eds.), *Climate Change 2013: The Physical Science Basis. Contribution of Working Group I to the Fifth Assessment Report of the Intergovernmental Panel on Climate Change.* online.
URL http://www.climatechange2013.org/report/full-report

90. Hartmann, D. L., Klein Tank, A. M. G., Rusticucci, M., Alexander, L. V., Brönnimann, S., Charabi, Y., Dentener, F. J., Dlugokencky, E. J., Easterling, D. R., Kaplan, A., Soden, B. J., Thorne, P. W., Wild, M., & Zhai, P. M. (2013b). Chapter 2: Observations: Atmosphere and surface. In: Stocker, T. F., Qin, D., Plattner, G. K., Tignor, M., Allen, S. K., Boschung, J., Nauels, A., Xia, Y., Bex, V., & Midgley, P. M. (Eds.), *Climate Change 2013: The Physical Science Basis. Contribution of Working Group I to the Fifth Assessment Report of the Intergovernmental Panel on Climate Change.* Cambridge University Press, Cambridge, United Kingdom and New York, NY, USA.
URL http://www.climatechange2013.org/report/full-report

91. Hase, F., Blumenstock, T., & Paton-Walsh, C. (1999). Analysis of the instrumental line shape of high-resolution Fourier transform IR spectrometers with gas cell measurements and new retrieval software. *Applied Optics 38* (15), 3417–3422.

92. Heald, C. L., Jacob, D. J., Fiore, A. M., Emmons, L. K., Gille, J. C., Deeter, M. N., Warner, J., Edwards, D. P., Crawford, J. H., Hamlin, A. J., Sachse, G. W., Browell, E. V., Avery, M. A., Vay, S. A., Westberg, D. J., Blake, D. R., Singh, H. B., Sandholm, S. T., Talbot,

R. W., & E., F. H. (2003). Asian outflow and trans-Pacific transport of carbon monoxide and ozone pollution: An integrated satellite, aircraft, and model perspective. *Journal of Geophysical Research: Atmospheres 108* (D24), 4804.

93. Henze, D. K., & Seinfeld, J. H. (2006). Global secondary organic aerosol from isoprene oxidation. *Geophysical Research Letters 33*, L09812.

94. Henze, D. K. a. (2008). Global modeling of secondary organic aerosol formation from aromatic hydrocarbons: High- vs. low-yield pathways. *Atmospheric Chemistry and Physics 8*, 2405–2420.

95. Hertel, O., Berkowicz, R., Christensen, J., , & Hov, O. (1993). Test of 2 numerical schemes for use in atmospheric transport-chemistry models. *Atmospheric Environment Part A-General Topics 27* (16), 2591–2611.

96. Herzberg, G. (1950). *Molecular spectra and molecular structure. I. Spectra of diatomic molecules. (2nd ed.)*. D. Van Nostrand Company, INC., Princeton, New Jersey.

97. Holloway, T., Levy, H. I., & Kasibhatla, P. (2000). Global distribution of carbon monoxide. *Journal of Geophysical Research: Atmospheres 105* (D10), 12123–12147.

98. Holtslag, A., & Boville, B. (1993). Local versus nonlocal boundary-layer diffusion in a global climate model. *Journal of Climate 6*, 1825.

99. Horowitz, L. W., Liang, J. Y., Gardner, G. M., & Jacob, D. J. (1998). Export of reactive nitrogen from North America during summertime: Sensitivity to hydrocarbon chemistry. *Journal of Geophysical Research: Atmospheres 103* (D11), 13451–13476.

100. Houghton, J. T., Taylor, F. W., & Rodgers, C. D. (1984). *Remote Sounding of Atmospheres.* Cambridge University Press.

101. Jacob, D. J. (1999). *Introduction to Atmospheric Chemsitry.* Princeton University Press.

102. Jacob, D. J. (2000). Heterogeneous chemistry and tropospheric ozone. *Atmospheric Environment 34* (12-14), 2131–2159.

103. Jiang, Z., Jones, D. B. A., Kopacz, M., Liu, J., Henze, D. K., , & C., H. (2011). Quantifying the impact of model errors on top?down estimates of carbon monoxide emissions using satellite observations. *Journal of Geophysical Research: Atmospheres 116* (D15), D15306.

104. Johns, T. C. a. (1997). The second Hadley Centre coupled ocean-atmosphere GCM: Model description, spinup and validation. *Climate Dynamics 13*, 103–134.

105. Jones, D. B. A., Bowman, K. W., Logan, J. A., Heald, C. L., Liu, J., Luo, M., Worden, J., & Drummond, J. (2009a). The zonal structure of tropical O3 and CO as observed by the Tropospheric Emission Spectrometer in November 2004 Part 1: Inverse modeling of CO emissions. *Atmospheric Chemistry and Physics 9*, 3547–3562.

106. Jones, N. B., Riedel, K., Allan, W., Wood, S., Palmer, P. I., Chance, K., & Notholt, J. (2009b). Long-term tropospheric formaldehyde concentrations deduced from ground-based fourier transform solar infrared measurements. *Atmospheric Chemistry and Physics 9* (18), 7131–7142.

107. Kajikawa, Y., Wang, B., & Yang, J. (2010). A multi-time scale Australian Monsoon index. *International Journal of Climatology 30*, 1114–1120.

108. Keeling, C. D., Bacastow, R. B., Bainbridge, A. E., Ekdahl, C. A., Guenther, P. R., & L.S. Waterman, L. S. (1976). Atmospheric carbon dioxide variations at Mauna Loa Observatory, Hawaii. *Tellus 28*, 538–551.

109. Keeling, R. F. (2008). Atmospheric science - Recording Earth's vital signs. *Science 319* (5871), 1771–1772.

110. Kim, P. S., Jacob, D. J., Liu, X., Warner, J. X., Yang, K., Chance, K., Thouret, V., & Nedelec, P. (2013). Global ozoneCO correlations from OMI and AIRS: constraints on tropospheric ozone sources. *Atmospheric Chemistry and Physics 13* (18), 9321–9335.

111. Kopacz, M., Jacob, D. J., Fisher, J. A., Logan, J. A., Zhang, L., Megretskaia, I. A., Yantosca, R. M., Singh, K., Henze, D. K., Burrows, J. P., Buchwitz, M., Khlystova, I., McMillan, W. W., Gille, J. C., Edwards, D. P., Eldering, A., Thouret, V., & Nedelec, P. (2010). Global estimates of CO sources with high resolution by adjoint inversion of multiple satellite datasets (MOPITT, AIRS, SCIAMACHY, TES). *Atmospheric Chemistry and Physics 10* (3), 855–876.

112. Kuhns, H., Green, M., & Etyemezian, V. (2003). Big Bend Regional Aerosol and Visibility Observational (BRAVO) Study Emissions Inventory. Report to BRAVO technical steering committee, Desert Research Institute, Las Vegas, USA.

113. Kumar, A., Wu, S., Weise, M. F., Honrath, R., Owen, R. C., Helmig, D., Kramer, L., Martin, M. V., & Li, Q. (2013). Free-troposphere ozone and carbon monoxide over the North Atlantic for 2001-2011. *Atmospheric Chemistry and Physics 13* (24), 12537–12547.

114. Lamarque, J.-F., Kiehl, J., Hess, P., Collins, W., Emmons, L., Ginoux, P., Luo, C., & Tie, X. (2005). Response of a coupled chemistry-climate model to changes in aerosol emissions: Global impact on the hydrological cycle and the tropospheric burdens of OH, ozone and NO_X. *Geophysical Research Letters 32*, L16809.

115. Langenfelds, R. L., Steele, L. P., Leist, M. A., Krummel, P. B., Spencer, D. A., & Howden, R. T. (2011). Atmospheric methane, carbon dioxide, hydrogen, carbon monoxide and nitrous oxide from cape grim flask air samples analysed by gas chromatography. In: Derek, N., & Krummel, P. B. (Eds.), *Baseline 2007–2008.* Australian Bureau of Meteorology and CSIRO Marine and Atmospheric Research., pp. 62–66.

116. Law, K. S., & Pyle, J. A. (1993). Modelling trace gas budgets in the troposphere. 1. ozone and odd nitrogen. *Journal of Geophysical Research: Atmospheres 98*, 18377–18400.

117. Le Treut, H., Somerville, R., Cubasch, U., Ding, Y., Mauritzen, C., Mokssit, A., Peterson, T., & Prather, M. (2007). Historical Overview of Climate Change. In: Solomon, S., Qin, D., Manning, M., Chen, Z., Marquis, M., Averyt, K. B., Tignor, M., & Miller, H. L. (Eds.), *Climate Change 2007: The Physical Science Basis. Contribution of Working Group I to the Fourth Assessment Report of the Intergovernmental Panel on Climate Change.* Cambridge University Press, Cambridge, United Kingdom and New York, NY, USA.

118. Leonard, B. P., Lock, A. P., & K., M. M. (1995). The NIRVANX scheme applied to one-dimensional advection. *International Journal of Numerical Methods for Heat & Fluid Flow 5*, 341–377.

119. Leue, C., Wenig, M., Wagner, T., Klimm, O., Platt, U., & Jahne, B. (2001). Quantitative analysis of NOx emissions from Global Ozone Monitoring Experiment satellite image sequences. *Journal of Geophysical Research: Atmospheres 106* (D6), 5493–5505.

120. Levelt, P. F., Hilsenrath, E., Leppelmeier, G. W., van den Oord, G. H. J., Bhartia, P. K., Tamminen, J., de Haan, J. F., & Veefkind, J. P. (2006). Science objectives of the Ozone Monitoring Instrument. *Ieee Transactions on Geoscience and Remote Sensing 44* (5), 1199–1208.

121. Levy, H. (1971). Normal Atmosphere: Large Radical and Formaldehyde Concentrations Predicted. *Science 173*, 141–143.

122. Levy, H. (1972). Photochemistry of the Lower Troposphere. *Planetary and Space Science 20*, 919–935.

123. Liang, Q., Jaegle, L., Hudman, R. C., Turquety, S., Jacob, D. J., Avery, M. A., Browell, E. V., Sachse, G. W., Blake, D. R., Brune, W., Ren, X., Cohen, R. C., Dibb, J. E., Fried, A., Fuelberg, H., Porter, M., Heikes, B. G., Huey, G., Singh, H. B., & Wennberg, P. O. (2007). Summertime influence of Asian pollution in the free troposphere over North America. *Journal of Geophysical Research: Atmospheres 112* (D12), D12S11.

124. Liao, H., Henze, D. K., Seinfeld, J. H., & Wu, S. Mickley, L. J. (2007). Biogenic Secondary Organic Aerosol over the United States: Comparison of Climatological Simulations with Observations. *Journal of Geophysical Research: Atmospheres 112* (D6), D06201.

125. Lin, J. T., & McElroy, M. (2010). Impacts of boundary layer mixing on pollutant vertical profiles in the lower troposphere: Implications to satellite remote sensing. *Atmospheric Environment 44* (14), 1726–1739.

126. Lin, S. J., & Rood, R. B. (1996). Multidimensional flux form semi-Lagrangian transport schemes. *Monthly Weather Review 124*, 2046–2070.

127. Liu, H. Y., Jacob, D. J., Bey, I., & Yantosca, R. M. (2001). Constraints from Pb-210 and Be-7 on wet deposition and transport in a global three-dimensional chemical tracer model driven by assimilated meteorological fields. *Journal of Geophysical Research: Atmospheres 106* (D11), 12109–12128.

128. Liu, J., Drummond, J. R., Jones, D. B. A., Cao, Z., Bremer, H., Kar, J., Zou, J., Nichitiu, F., & Gille, J. C. (2006). Large horizontal gradients in atmospheric CO at the synoptic scale as seen by spaceborne Measurements of Pollution in the Troposphere. *Journal of Geophysical Research: Atmospheres 111* (D2), D02306.

129. Liu, J., Logan, J. A., Jones, D. B. A., Livesey, N. J., Megretskaia, I., Carouge, C., & Nedelec, P. (2010). Analysis of CO in the tropical troposphere using Aura satellite data and the GEOS-Chem model: insights into transport characteristics of the GEOS meteorological products. *Atmospheric Chemistry and Physics 10* (24), 12207–12232.

130. Liu, J., Logan, J. A., Murray, L. T., Pumphrey, H. C., Schwartz, M. J., & Megretskaia, I. A. (2013). Transport analysis and source attribution of seasonal and interannual variability of CO in the tropical upper troposphere and lower stratosphere. *Atmospheric Chemistry and Physics 13*, 129–146.

131. Livesey, N. J., Filipiak, M. J., Froidevaux, L., Read, W. G., Lambert, A., Santee, M. L., Jiang, J. H., Pumphrey, H. C., Waters, J. W., Cofield, R. E., Cuddy, D. T., Daffer, W. H., Drouin, B. J., Fuller, R. A., Jarnot, R. F., Jiang, Y. B., Knosp, B. W., Li, Q. B., Perun, V. S., Schwartz, M. J., Snyder, W. V., Stek, P. C., Thurstans, R. P., Wagner, P. A., Avery, M., Browell, E. V., Cammas, J. P., Christensen, L. E., Diskin, G. S., Gao, R.-S., Jost, H. J., Loewenstein, M., Lopez, J. D., Nédélec, P., Osterman, G. B., Sachse, G. W., & Webster, C. R. (2008). Validation of Aura Microwave Limb Sounder O3 and CO observations in the upper troposphere and lower stratosphere. *Journal of Geophysical Research 113*, D15S02.

132. Lock, A. P., Brown, A. R., Bush, M. R., Martin, G. M., & Smith, R. N. B. (2000). A new boundary layer mixing scheme. Part I: Scheme description and single-column model tests. *Monthly Weather Review 128*, 3187–3199.

133. Mao, J., Jacob, D. J., Evans, M. J., Olson, J. R., Ren, X., Brune, W. H., St. Clair, J. M., Crounse, J. D., Spencer, K. M., Beaver, M. R., Wennberg, P. O., Cubison, M. J., Jimenez, J. L., Fried, A., Weibring, P., Walega, J. G., Hall, S. R., Weinheimer, A. J., Cohen, R. C., Chen, G., Crawford, J. H., Jaeglé, L., Fisher, J. A., Yantosca, R. M., Le Sager, P., & C., C. (2010). Chemistry of hydrogen oxide radicals (HOx) in the Arctic troposphere in spring. *Atmospheric Chemistry and Physics 10*, 5823–5838.

134. Mao, J., Paulot, F., Jacob, D. J., Cohen, R. C., Crounse, J. D., O., W. P., Keller, C. A., C., H. R., Barkley, P., & Horowitz, L. (2013). Ozone and organic nitrates over the eastern United States: Sensitivity to isoprene chemistry. *Journal of Geophysical Research: Atmospheres 118* (19), 11256–11268.

135. Marais, E. A., Jacob, D. J., Kurosu, T. P., Chance, K., Murphy, J. G., Reeves, C., Mills, G., Casadio, S., Millet, D. B., Barkley, M. P., Paulot, F., & Mao, J. (2012). Isoprene emissions in Africa inferred from OMI observations of formaldehyde columns. *Atmospheric Chemistry and Physics 12* (14), 6219–6235.

136. Mari, C., Jacob, D. J., & Bechtold, P. (2000). Transport and scavenging of soluble gases in a deep convective cloud. *Journal of Geophysical Research: Atmospheres 105* (D17), 22255–22267.

137. Marshall, J., & Plumb, R. A. (2008). *Atmosphere, Ocean, and Climate Dynamics: An Introductory Text.* Elsevier Inc.

138. Martin, G., Milton, S. F., Senior, C. A., Brooks, M., Ineson, S., Reichler, T., & Kim, J. (2010). Analysis and reduction of systematic errors through a seamless approach to modelling weather and climate. *Journal of Climate 23*, 5933–5957.

139. Martin, R., Jacob, D. J., Yantosca, R. M., Chin, M., & Ginoux, P. (2003). Global and Regional Decreases in Tropospheric Oxidants from Photochemical Effects of Aerosols. *Journal of Geophysical Research: Atmospheres 108* (D3), 4097.

140. McLinden, C. A., Olsen, S. C., Hannegan, B., Wild, O., Prather, M. J., & Sundet, J. (2000). Stratospheric ozone in 3-D models: A simple chemistry and the cross-tropopause flux. *Journal of Geophysical Research: Atmospheres 105* (D11), 14653–14665.

141. Meier, A., Goldman, A., Manning, P. S., Stephen, T. M., Curtis Rinsland, C. P., Jones, N. B., & Wood, S. W. (2004). Improvements to Air Mass Calculations for Ground-Based Infrared Measurements. *Journal of Quantitative Spectroscopy and Radiative 83* (1), 109–113.

142. Millet, D. B., Jacob, D. J., Boersma, K. F., Fu, T.-M., Kurosu, T. P., Chance, K., Heald, C. L., & Guenther, A. (2008). Spatial distribution of isoprene emissions from North America derived from formaldehyde column measurements by the OMI satellite sensor. *Journal of Geophysical Research: Atmospheres 113* (D2), D02307.

143. Miyazaki, K., Patra, P. K., Takigawa, M., Iwasaki, T., & Nakazawa, T. (2008). Global-scale transport of carbon dioxide in the troposphere. *Journal of Geophysical Research: Atmospheres 113* (D15), D15301.

144. MOPITT Science Team (2013). MOPITT/Terra Level 3 Gridded Monthly CO (on a latitude/longitude/pressure grid) derived from Near and Thermal Infrared Radiances, version 6, product short name MOP03JM.
URL https://eosweb.larc.nasa.gov/HPDOCS/datapool/

145. Murphy, D., & Fahey, D. (1994). An estimate of the flux of stratospheric reactive nitrogen and ozone into the troposphere. *Journal of Geophysical Research: Atmospheres 99* (D3), 5325–5332.

146. Myneni, R. B., Hoffman, S., Knyazikhin, Y., Privette, J. L., Glassy, J., Tian, Y., Wang, Y., Song, X., Zhang, Y., Smith, G. R., Lotsch, A., Friedl, M., Morisette, J. T., Votava, P., Nemani, R. R., & Running, S. W. (2002). Global products of vegetation leaf area and fraction absorbed PAR from year one of MODIS data. *Remote Sensing of Environment 83*, 214–231.

147. Myneni, R. B., Yang, W., Nemani, R. R., Huete, A. R., Dickinson, R. E., Knyazikhin, Y., Didan, K., Fu, R., Negrón Juárez, R. I., Saatchi, S. S., Hashimoto, H., Ichii, K., Shabanov, N. V., Tan, B., Ratana, P., Privette, J. L., Morisette, J. T., Vermote, E. F., Roy, D. P., Wolfe, R. E., Friedl, M. A., Running, S. W., Votava, P., El-Saleous, N., Devadiga, S., Su, Y., & V., S. V. (2007). Large seasonal swings in leaf area of Amazon rainforests. *Proceedings of the National Academy of Sciences 104* (12), 4820–4823.

148. Nakićenović, N., Alcamo, J., Davis, G., de Vries, B., Fenhann, J., Gaffin, S., Gregory, K., Grübler, A., Jung, T. Y., Kram, T., La Rovere, E. L., Michaelis, L., Mori, S., Morita, T., Pepper, W., Pitcher, H., Price, L., Riahi, K., Roehrl, A., Rogner, H.-H., Sankovski, A., Schlesinger, M., Shukla, P., Smith, S., Swart, R., van Rooijen, S., Victor, N., & Dadi, Z. (2000). *Special Report on Emission Scenarios: A special report of Working Group III of the Intergovernmental Panel on Climate Change.* Cambridge University Press, New York.

149. NCAS British Atmospheric Data Centre (December 2010). European Centre for Medium-Range Weather Forecasts, ECMWF Trajectories.
URL http://badc.nerc.ac.uk/view/badc.nerc.ac.uk__ATOM__dataent_ECMWF-TRJ

150. Notholt, J., Toon, G. C., Rinsland, C. P., Pougatchev, N. S., Jones, N. B., Connor, B. J., Weller, R., Gautrois, M., & Schrems, O. (2000). Latitudinal variations of trace gas concentrations in the free troposphere measured by solar absorption spectroscopy during a ship cruise. *Journal of Geophysical Research: Atmospheres 105* (D1), 1337–1349.

151. Novelli, P. C., Masarie, K. A., & Lang, P. M. (1998). Distributions and recent changes of carbon monoxide in the lower troposphere. *Journal of Geophysical Research: Atmospheres 103* (D15), 19015–19033.

152. Novelli, P. C., Masarie, K. A., Lang, P. M., Hall, B., Myers, R., & Elkins, J. (2003). Reanalysis of tropospheric CO trends: Effect of the 1997–1998 wilfires. *Journal of Geophysical Research 108*, 4464.

153. O'Connor, F. M., Johnson, C. E., Morgenstern, O., Abraham, N. L., Braesicke, P., Dalvi, M., A, F. G., Sanderson, M. G., Telford, P. J., Young, P. J., Zeng, G., Collins, W. J., & Pyle, J. (2013). Evaluation of the new UKCA climate-composition model – Part 2: The Troposphere. *Geoscientifc Model Development Discussions 6*, 1743–1857.

154. O'Doherty, S., Simmonds, P., Cunnold, D., Wang, H., Sturrock, G., Fraser, P., Ryall, D., Derwent, R., Weiss, R., Salameh, P., Miller, B., & Prinn, R. (2001). In situ chloroform measurements at Advanced Global Atmospheric Gases Experiment atmospheric research stations from 1994 to 1998. *Journal of Geophysical Research 106*, 20429–20444.

155. Office of Environment and Heritage (August 2011). Office of Environment and Heritage, Department of Premier and Cabinet, NSW. Hourly averaged air quality data of ozone, carbon monoxide and nitrogen dioxide 2005 to 2010, provided by David Salter.
URL http://www.environment.nsw.gov.au/aqms/aqi.htm

156. Office of Environment and Heritage (July 2013). Office of Environment and Heritage, Department of Premier and Cabinet, NSW. Hourly averaged and one minute averaged air quality data of ozone, carbon monoxide, nitrogen dioxide and sulphur dioxide 2011 to 2013, provided by David Salter.
URL http://www.environment.nsw.gov.au/aqms/aqi.htm

157. Olivier, J. G. J., van Aardenne, J. A., Dentener, F., Ganzeveld, L., & Peters, J. A. H. W. (2005). Recent trends in global greenhouse gas emissions: regional trends and spatial distribution of key sources in 2000. *Environmental Sciences 2* (2–3), 81–99.

158. Oltmans, S. J., Lefohn, A. S., Harris, J. M., Galbally, I., Scheel, H. E., Bodeker, G., Brunke, E., Claude, H., Tarasick, D., Johnson, B. J., Simmonds, P., Shadwick, D., Anlauf, K., Hayden, K., Schmidlin, F., Fujimoto, T., Akagi, K., Meyer, C., Nichol, S., Davies, J., Redondas, A., & Cuevas, E. (2006). Long-term changes in tropospheric ozone. *Atmospheric Environment 40* (17), 3156–3173.

159. Palmer, P. I., Abbot, D. S., Fu, T. M., Jacob, D. J., Chance, K., Kurosu, T. P., Guenther, A., Wiedinmyer, C., Stanton, J. C., Pilling, M. J., Pressley, S. N., Lamb, B., & Sumner, A. L. (2006). Quantifying the seasonal and interannual variability of North American isoprene emissions using satellite observations of the formaldehyde column. *Journal of Geophysical Research 111*, D12315.

160. Palmer, P. I., Jacob, D. J., Fiore, A. M., Martin, R. V., Chance, K., & Kurosu, T. P. (2003). Mapping isoprene emissions over North America using formaldehyde column observations from space. *Journal of Geophysical Research: Atmospheres 108* (D6), 4180.

161. Pan, L., Gille, J. C., Edwards, D. P., Bailey, P. L., & Rodgers, C. D. (1998). Retrieval of carbon monoxide for the MOPITT instrument. *Journal of Geophysical Research 103* (D24), 32277–32290.

162. Paton-Walsh, C., Deutscher, N. M., Griffith, D. W. T., Forgan, B. W., Wilson, S. R., Jones, N. B., & Edwards, D. P. (2010a). Trace gas emissions from savanna fires in northern Australia. *Journal of Geophysical Research: Atmospheres 115* (D16), D16314.

163. Paton-Walsh, C., Miller, C. C., Jones, N. B., Deutscher, N. M., & Griffith, D. W. T. (2010b). Trends in total column ethane measured over south eastern australia from 1996-2010. In: 11th International Global Atmospheric Chemistry Conference. Halifax, Canada, conference paper.

164. Paulot, F., Crounse, J. D., Kjaergaard, H. G., Kroll, J. H., Seinfeld, J. H., & Wennberg, P. O. (2009). Isoprene photooxidation: new insights into the production of acids and organic nitrates. *Atmospheric Chemistry and Physics 9*, 1479–1501.

165. Penner, J. E., Atherton, C. S., Dignon, J., Ghan, S. J., Walton, J. J., & Hameed, S. (1991). Tropospheric Nitrogen - A 3-Dimensional Study of Sources, Distributions, and Deposition. *Journal of Geophysical Research: Atmospheres 96* (D1), 959–990.

166. Pfister, G. G., Emmons, L. K., Hess, P. G., Lamarque, J.-F., Orlando, J. J., Walters, S., Guenther, A., Palmer, P. I., & Lawrence, P. J. (2008). Contribution of isoprene to chemical budgets: A model tracer study with the NCAR CTM MOZART-4. *Journal of Geophysical Research: Atmospheres 113* (D5), D05308.

167. Piccot, S., Watson, J. J., & Jones, J. W. (1992). A Global Inventory of Volatile Organic Compound Emissions From Anthropogenic Sources. *Journal of Geophysical Research: Atmospheres 97* (D9), 9897–9912.

168. Pougatchev, N. S., Connor, B. J., & Rinsland, C. P. (1995). Infrared measurements of the ozone vertical-distribution above Kitt Peak. *Journal of Geophysical Research: Atmospheres 100* (D8), 16689–16697.

169. Prather, M., Ehhalt, D., Dentener, F., Derwent, R., Dlugokencky, E., Holland, E., Isaksen, I., Katima, J., Kirchhoff, V., Matson, P., Midgley, P., Wang, M., Berntsen, T., Bey, I., Brasseur, G., Buja, L., Collins, W. J., Daniel, J., DeMore, W. B., Derek, N., Dickerson, R., Etheridge, D., Feichter, J., Fraser, P., Friedl, R., Fuglestvedt, J., Gauss, M., Grenfell, L., Grbler, A., Harris, N. andHauglustaine, D., Horowitz, L., Jackman, C., Jacob, D., Jaegl, L., Jain, A., Kanakidou, M., Karlsdottir, S., Ko, M., Kurylo, M., Lawrence, M., Logan, J. A., Manning, M., Mauzerall, D., McConnell, J., Mickley, L., Montzka, S., Mller, J. F., Olivier, J., Pickering, K., Pitari, G .and Roelofs, G. J., Rogers, H., Rognerud, B., Smith, S., Solomon, S., Staehelin, J., Steele, P., Stevenson, D., Sundet, J., Thompson, A., van Weele, M., von Kuhlmann, R., Wang, Y., Weisenstein, D., Wigley, T., Wild, O., Wuebbles, D., & Yantosca, R. (2001). *Climate Change 2001: The Scientific Basis.* Cambridge University Press, Ch. 4: Atmospheric chemistry and greenhouse gases., pp. 239–287.

170. Press, W. H., Teukolsky, S. a., Vetterling, W. T., & Flannery, B. P. (1992). *Numerical Recipes.* Cambridge University Press, Cambridge.

171. Price, C., & Rind, D. (1994). Modelling global lightning distributions in a general circulation model. *Monthly Weather Review 122*, 1930–1939.

172. Puri, K. (30 June 2005). Blueprint for ACCESS. *Personal Communication.*

173. R Core Team (2012). *R: A Language and Environment for Statistical Computing.* R Foundation for Statistical Computing, Vienna, Austria, ISBN 3-900051-07-0.
URL http://www.R-project.org/

174. Rastigejev, Y., Park, R., Brenner, M. P., & Jacob, D. J. (2010). Resolving intercontinental pollution plumes in global models of atmospheric transport. *Journal of Geophysical Research: Atmospheres 115* (D2), D02302.

175. Ridder, T., Gerbig, C., Notholt, J., Rex, M., Schrems, O., Warneke, T., & Zhang, L. (2012). Ship-borne FTIR measurements of CO and O_3 in the Western Pacific from 43° N to 35° S: an evaluation of the sources. *Atmospheric Chemistry and Physics 12*, 815–828.

176. Rienecker, M. M., Suarez, M. J., Todling, R., Bacmeister, J., Takacs, L., Liu, H. C., Gu, W., Sienkiewicz, M., Koster, R. D., Gelaro, R., Stajner, I., & Nielsen, J. E. (2008). The GEOS-5 Data Assimilation System - Documentation of Versions 5.0.1, 5.1.0, and 5.2.0. Technical report series on global modeling and data assimilation, 27, NASA, USA.

177. Rinsland, C. P., Jones, N. B., Connor, B. J., Logan, J. A., Pougatchev, N. S., Goldman, A., Murcray, F. J., Stephen, T. M., Pine, A. S., Zander, R., Mahieu, E., & Demoulin, P. (1998). Northern and southern hemisphere ground-based infrared spectroscopic measurements of tropospheric carbon monoxide and ethane. *Journal of Geophysical Research: Atmospheres 103* (D21), 28197–28217.

178. Rodgers, C. D. (2000). *Inverse Methods for Atmospheric Sounding, Theory and Practice.* World Scientific Publishing Co. Ptd. Ltd, New Jersey.

179. Rodgers, C. D., & Connor, B. J. (2003). Intercomparison of remote sounding instruments. *Journal of Geophysical Research: Atmospheres 108* (D3), 4116.

180. Rothman, L. S., Gordon, I., Babikov, Y., Barbe, A., Benner, D. C., Bernath, P. F., Birk, M., Bizzocchi, L., Boudon, V., Brown, L. R., Campargue, A., Chance, K., Cohen, E. A., Coudert, L. H., Devi, V. M., Drouin, B. J., Fayt, A., Flaud, J.-M., Gamache, R. R., Harrison, J. J., Hartmann, J. M., Hill, C., Hodges, J. T., Jacquemart, D., Jolly, A., Lamouroux, J., Le Roy, R. J., Li, G., Long, D. A., Lyulin, O. M., Mackie, C. J., Massie, S. T., Mikhailenko, S., Müller, H. S. P., Naumenko, O. V., Nikitin, A. V., J., O., Perevalov, V. I., Perrin, A., Polovtseva, E. R., Richard, C., Smith, M. A. H., Starikova, E., Sung, K., Tashkun, S., Tennyson, J., Toon, G. C., Tyuterev, V. G., & Wagner, G. (2013). The HITRAN 2012 molecular spectroscopic database. *Journal of Quantitative Spectroscopy & Radiative Transfer 130*, 4–50.

181. Rothman, L. S., Gordon, I., Barbe, A., Benner, D. C., Bernath, P. F., Birk, M., Boudon, V., Brown, L. R., Campargue, A., Champion, J.-P., Chance, K., Coudert, L. H., Dana, V., Devi, V. M., Fally, S., Flaud, J.-M., Gamache, R. R., Goldman, I. A., Jacquemart, D.,

Kleiner, I., Lacome, N., Lafferty, W. J., Mandin, J. Y., Massie, S. T., Mikhailenko, S. N., Miller, C. E., Moazzen-Ahmadi, N., Naumenko, O. V., Nikitin, A. V., J., O., Perevalov, V. I., Perrin, A., Predoi-Cross, A., Rinsland, C. P., Rotger, M., Šimečková, M., Smith, M. A. H., Sung, K., Tashkun, S., Tennyson, J., Toth, R., Vandaele, A., & Vander Auwera, J. (2009). The HITRAN 2008 molecular spectroscopic database. *Journal of Quantitative Spectroscopy & Radiative Transfer 110*, 533–572.

182. Ruckstuhl, A., Henne, S., Steinbacher, M., Vollmer, M. K., O'Doherty, A., Buchmann, B., & Hueglin, C. (2012). Robust extraction of baseline signal of atmospheric trace species using local regression. *Atmospheric Measurement Techniques 5*, 2613–2624.

183. Ruckstuhl, A. F., Jacobson, M. P., Field, R. W., & Dodd, J. A. (2001). Baseline Subtraction Using Robust Local Regression Estimation. *Journal of Quantitative Spectroscopy and Radiative Transfer 68*, 179–193.

184. Ruckstuhl, A. F., Unternaehrer, T., & Locher, R. (2009). IDPmisc: Utilities of Institute of Data Analyses and Progress Design.
URL http://CRAN.R-projects.org/package=IDPmisc

185. Rudolph, J. (1995). The tropospheric distribution and budget of ethane. *Journal of Geophysical Research: Atmospheres 100* (D6), 11369–11381.

186. Russell-Smith, J., Yates, C. P., Whitehead, P. J., Smith, R., Craig, R., Allan, G. E., Thackway, R., Frakes, I., Cridland, S., Meyer, M. C. P., & Gill, M. A. (2007). Bushfires 'down under': patterns and implications of contemporary Australian landscape burning. *International Journal of Wildland Fire 16*, 361–377.

187. Sakulyanontvittaya, T., Duhl, T., Wiedinmyer, C., Helmig, D., Matsunaga, S., Potosnak, M., Milford, J., & Guenther, A. (2008). Monoterpene and Sesquiterpene Emission Estimates for the United States. *Environmental Science & Technology 42* (5), 1623.

188. Salau, O. R., Warneke, T., Notholt, J., Shim, C., Li, Q., & Xiao, Y. (2009). Tropospheric trace gases at Bremen measured with FTIR spectrometry. *Journal of Environmental Monitoring 11* (8), 1529–1534.

189. Sander, R., & Crutzen, P. (1996). Model study indicating halogen activation and ozone destruction in polluted air masses transported to the sea. *Journal of Geophysical Research: Atmospheres 101* (D4), 9121–9138.

190. Sauvage, B., Martin, R. V., van Donkelaar, A., Liu, X., Chance, K., Jaegle, L., Palmer, P. I., Wu, S., & Fu, T. M. (2007). Remote sensed and in situ constraints on processes affecting tropical tropospheric ozone. *Atmospheric Chemistry and Physics 7*, 815–838.

191. Seco, R., Penuelas, J., & Filella, I. (2007). Short-chain oxygenated VOCs: Emission and uptake by plants and atmospheric sources, sinks, and concentrations. *Atmospheric Environment 41* (12), 2477–2499.

192. Seinfeld, J. H., & Pandis, S. N. (2006a). *Atmospheric Chemistry and Physics. From Air Pollution to Climate Change. Second Edition.* John Wiley & Sons Inc., Ch. 6: Chemistry of the Troposphere, pp. 204–283.

193. Seinfeld, J. H., & Pandis, S. N. (2006b). *Atmospheric Chemistry and Physics. From Air Pollution to Climate Change. Second Edition.* John Wiley & Sons Inc., Ch. 25: Atmospheric Chemical Transport Models, pp. 1092– 1135.

194. Seinfeld, J. H., & Pandis, S. N. (2006c). *Atmospheric Chemistry and Physics. From Air Pollution to Climate Change. Second Edition.* John Wiley & Sons Inc., Ch. 2: Atmospheric Trace Constituents, pp. 22–27.

195. Sen, P. K. (1968). Estimates of regression coefficient based on Kendall's tau. *Journal of the American Statistical Association 63* (324).

196. Sharkey, T., & F., L. (1993). Water stress, temperature and light effects on the capacity for isoprene emission and photosynthesis of kudzu leaves. *Oecologia 95*, 328–333.

197. Shaw, S. L., Gantt, B., & Meskhidze, N. (2010). Production and Emissions of Marine Isoprene and Monoterpenes: A Review. *Advances in Meteorology 2010*, 408696.

198. Shim, C., Wang, Y. H., Choi, Y., Palmer, P. I., Abbot, D. S., & Chance, K. (2005). Constraining global isoprene emissions with Global Ozone Monitoring Experiment (GOME) formaldehyde column measurements. *Journal of Geophysical Research: Atmospheres 110* (D24), D24301.

199. Stavrakou, T., Mueller, J.-F., De Smedt, I., Van Roozendael, M., van der Werf, G. R., Giglio, L., & Guenther, A. (2009). Global emissions of non-methane hydrocarbons deduced from SCIAMACHY formaldehyde columns through 2003-2006. *Atmospheric Chemistry and Physics 9* (11), 3663–3679.

200. Stevenson, D. S., Dentener, F. J., Schultz, M. G., Ellingsen, K., van Noije, T. P. C., Wild, O., Zeng, G., Amann, M., Atherton, C. S., Bell, N., Bergmann, D. J., Bey, I., Butler, T., Cofala, J., Collins, W. J., Derwent, R. G., Doherty, R. M., Drevet, J., Eskes, H. J., Fiore, A. M., Gauss, M., Hauglustaine, D. A., Horowitz, L. W., Isaksen, I. S. A., Krol, M. C., Lamarque, J. F., Lawrence, M. G., Montanaro, V., Müller, J. F., Pitari, G., Prather, M. J., Pyle, J. A., S. Rast, S., Rodriguez, J. M., Sanderson, M. G., Savage, N. H., Shindell, D. T., Strahan, S. E., Sudo, K., & Szopa, S. (2006). Multimodel ensemble simulations of present-day and near-future tropospheric ozone. *Journal of Geophysical Research: Atmospheres 111* (D8), D08301.

201. Streets, D. G., Bond, T. C., Carmichael, G. R., Fernandes, S. D., Fu, Q., Klimont, Z., Nelson, S. M., Tsai, N. Y., Wang, M. Q., Woo, J. H., & F., Y. K. (2003). An inventory of gaseous and primary aerosol emissions in Asia in the year 2000. *Journal of Geophysical Research: Atmospheres 108* (D21), 8809.

202. Streets, D. G., Zhang, Q., Wang, L., He, K., Hao, J., Wu, Y., Tang, Y., & C., C. G. (2006). Revisiting China's CO emissions after the Transport and Chemical Evolution over the Pacific (TRACE-P) mission: Synthesis of inventories, atmospheric modeling, and observations. *Journal of Geophysical Research: Atmospheres 111* (D14), D14306.

203. Sverdrup, H. U., Johnson, M. W., & Fleming, R. H. (1942). *The Oceans, Their Physics, Chemistry, and General Biology.* Prentice-Hall, New York, Ch. 2: The Earth and the Ocean Basins.
URL http://ark.cdlib.org/ark:/13030/kt167nb66r/

204. Tans, P., & Keeling, R. (accessed June 2014). Trends in Atmospheric Carbon Dioxide. URL www.esrl.noaa.gov/gmd/ccgg/trends/

205. Theil, H. (1950). A rank invariant method of linear and polynomial regression analysis, i, ii, iii. *Proceedings of the Koninklijke Nederlandse Akademie Wetenschappen, Series A–Mathematical Sciences 53*, 386–392, 521–525, 1397–1412.

206. Thoning, K., Tans, P., & Komhyr, W. (1989). Atmospheric Carbon Dioxide at Mauna Loa Observatory. 2. Analysis of the NOAA GMCC Data, 1974–1985. *Journal of Geophysical Research 94*, 8549–8565.

207. UCAR (2013). The NCAR Command Language, NCL. [Software]. URL http://dx.doi.org/10.5065/D6WD3XH5

208. United Nations (2012). World Urbanization Prospects: The 2011 Revision. Report, United Nations, Department of Economic and Social Affairs, Population Division, 2 United Nations Plaza, New York, NY 10017 USA. URL http://esa.un.org/unup/index.html

209. United States Geological Survey (USGS) (July 2013). Landsat true color scene, courtesy of the U.S. Geological Survey. URL http://www.usgs.gov

210. United States Geological Survey (USGS) (February 2014). MODIS product: Land Cover Type Yearly L3 Global 0.05Deg CMG, product short name MCD12C1. URL https://lpdaac.usgs.gov/data_access/data_pool

211. van der A, R. J., Eskes, H. J., Boersma, K. F., van Noije, T. P. C., Van Roozendael, M., De Smedt, I., Peters, D., & Meijer, E. W. (2008). Trends, seasonal variability and dominant NO_X source derived from a ten year record of NO_2 measured from space. *Journal of Geophysical Research: Atmospheres 113* (D4), 12.

212. van der Werf, G. R., Morton, D. C., DeFries, R. S., Giglio, L., Randerson, J. T., Collatz, G. J., & Kasibhatla, P. S. (2009). Estimates of fire emissions from an active deforestation region in the southern Amazon based on satellite data and biogeochemical modelling. *Biogeosciences 6* (2), 235–249.

213. van Donkelaar, A., Martin, R. V., Leaitch, W. R., Macdonald, A. M., Walker, T. W., Streets, D. G., Zhang, Q., Dunlea, E. J., Jimenez, J. L., Dibb, J. E., Huey, L. G., Weber, R., & O., A. M. (2008). Analysis of Aircraft and Satellite Measurements from the Intercontinental Chemical Transport Experiment (INTEX-B) to Quantify Long-Range Transport of East Asian Sulfur to Canada. *Atmospheric Chemistry and Physics 8*, 2999–3014.

214. Vestreng, V., Mareckova, K., Kakareka, S., Malchykhina, A., & Kukharchyk, T. (2007). Inventory Review 2007; Emission Data reported to LRTAP Convention and NEC Directive. MSC-W technical report 1/2007, Norwegian Meteorological Institute, Oslo Norway.

215. Vicente-Serrano, S. M., López-Moreno, J. I., Gimeno, L., Nieto, R., Morán-Tejeda, E., Lorenzo-Lacruz, J., Begueria, S., & Azorin-Molina, C. (2011). A multiscalar global evaluation of the impact of ENSO on droughts. *Journal of Geophysical Research: Atmospheres 116* (D20), D20109.

216. Vigouroux, C., Stavrakou, T., Whaley, C., Dils, B., Duflot, V., Hermans, C., Kumps, N., Metzger, J. M., Scolas, F., Vanhaelewyn, G., Müller, J. F., Jones, D. B. A., Li, Q., & De Mazière, M. (2012). FTIR time-series of biomass burning products (HCN, C_2H_6, C_2H_2, CH_3OH and HCOOH) at Reunion Island (21° S, 55° E) and comparisons with model data. *Atmospheric Chemistry and Physics 12*, 10367–10385.

217. Voulgarakis, A., Telford, P. J., Aghedo, A. M., Braesicke, P., Faluvegi, G., Abraham, N. L., Bowman, K. W., Pyle, J. A., & Shindell, D. T. (2011). Global multi-year O_3-CO correlation patterns from models and TES satellite observations. *Atmospheric Chemistry and Physics 11*, 5819–5838.

218. Wang, Y., Jacob, D. J., & Logan, J. A. (1998). Global simulation of tropospheric O_3-NO_x-hydrocarbon chemistry, 1. Model Formation. *Journal of Geophysical Research: Atmospheres 103* (D9), 10713–10726.

219. Wang, Y., & Zeng, T. (2004). On tracer correlations in the troposphere: The case of ethane and propane. *Journal of Geophysical Research: Atmospheres 109* (D24), D24306.

220. Warneck, P., & Williams, J. (2012). *The Atmospheric Chemist's Companion. Numerical Data for Use in the Atmospheric Sciences*. Springer, Ch. 4: Trace Gases, pp. 69–125.

221. Warner, J., Carminati, F., Wei, Z., Lahoz, W., & Attié, J.-L. (2013). Tropospheric carbon monoxide variability from AIRS under clear and cloudy conditions *13* (24), 12469–12479.

222. Warner, J., Gille, J., Edwards, D. P., Ziskin, D., Smith, M., Bailey, P., & Rokke, L. (2001). Cloud detection and clearing for the Earth observing system Terra satellite Measurements of Pollution in the Troposphere (MOPITT) experiment. *Applied Optics 40*, 1269–1284.

223. Washenfelder, R. A., Toon, G. C., Blavier, J. F., Yang, Z., Allen, N. T., Wennberg, P. O., Vay, S. A., Matross, D. M., & Daube, B. C. (2006). Carbon dioxide column abundances at the Wisconsin Tall Tower site. *Journal of Geophysical Research: Atmospheres 111* (D22), D22305.

224. WaveMetrics (2012). Igor Pro.
URL http://www.wavemetrics.com/

225. Wayne, R. P. (2000). *Chemistry of Atmospheres.*, 3rd Edition. Oxford University Press.

226. Wesely, M. L. (1989). Parameterization of surface resistances to gaseous dry deposition in regional-scale numerical models. *Atmospheric Environment 23* (6), 1293–1304.

227. White, J. (1942). Long Optical Paths of Large Aperture. *Journal of the Optical Society of America 32* (4), 285.

228. Wild, O., Zhu, X., & M.J., P. (2000). Fast-J: Accurate simulation of in- and below-cloud photolysis in tropospheric chemical models. *Journal of Atmospheric Chemistry 37* (3), 245–282.

229. Worden, H. M., Deeter, M. N., Frankenberg, C., George, M., Nichitiu, F., Worden, J., Aben, I., Bowman, K. W., Clerbaux, C., Coheur, P. F., de Laat, A. T. J., Detweiler, R., Drummond, J. R., Edwards, D. P., Gille, J. C., Hurtmans, D., Luo, M., Martinez-Alonso, S., Massie, S., Pfister, G., & Warner, J. X. (2013a). Decadal record of satellite carbon monoxide observations. *Atmospheric Chemistry and Physics 13*, 837–850.

230. Worden, J., Wecht, K., Frankenberg1, C., Alvarado, M., Bowman, K., Kort, E., Kulawik, S., Lee, M., Payne, V., & Worden, H. (2013b). CH_4 and CO distributions over tropical fires during October 2006 as observed by the Aura TES satellite instrument and modeled by GEOS-Chem. *Atmospheric Chemistry and Physics 13*, 3679–3692.

231. World Health Organization (2013). World Health Statistics 2013. Report, World Health Organization, 1211 Geneva 27, Switzerland.
URL http://www.who.int/gho/publications/world_health_statistics/en/

232. World Health Organization (2014). Burden of disease from Ambient Air Pollution for 2012. Report, World Health Organization, 1211 Geneva 27, Switzerland.
URL http://www.who.int/phe/health_topics/outdoorair/databases/en/

233. World Meteorological Organization (2011). Report of the 15th WMO/IAEA meeting of experts on carbon dioxide, other greenhouse gases, and related tracers measurement techniques, 7–10 September 2009. Gaw report no. 194, wmo td no. 1553, WMO, Jena, Germany, 2009.
URL http://www.wmo.int/pages/prog/arep/gaw/documents/GAW_194_WMO_TD_No_1553_web_low_resol.pdf

234. Wu, S., Mickley, L. J., Jacob, D. J., Logan, J. A., & Yantosca, R. M. (2007). Why are there large differences between models in global budgets of tropospheric ozone? *Journal of Geophysical Research: Atmospheres 112* (D5), D05302.

235. Wunch, D., Toon, G. C., Wennberg, P. O., Wofsy, S. C., Stephens, B. B., Fischer, M. L., Uchino, O., Abshire, J. B., Bernath, P., Biraud, S. C., Blavier, J. F. L., Boone, C., Bowman, K. P., Browell, E. V. Campos, T., Conner, B. J., Daube, B. C., Deutscher, N. M., Diao, M., Elkins, J. W., Gerbig, C., Gottlieb, E., Griffith, D. W. T., Hurst, D. F., Jiménez, R., Keppel-Aleks, G., Kort, E. A., Macatangay, R., Machida, T., Matsueda, H., Moore, F., Morino, I., Park, S., Robinson, J., Roehl, C. M., Sawa, Y., Sherlock, V., Sweeney, C., Tanaka, T., & Zondlo, M. A. (2010). Calibration of the total carbon column observing network using aircraft profile data. *Atmosphere Measurement Techniques 3* (5), 1351–1362.

236. Xiao, Y., Logan, J. A., Jacob, D. J., Hudman, R. C., Yantosca, R., & Blake, D. R. (2008). Global budget of ethane and regional constraints on U.S. sources. *Journal of Geophysical Research: Atmospheres 113* (D21), D21306.

237. Yashiro, H., Sugawara, S., Sudo, K., Aoki, S., & Nakazawa, T. (2009). Temporal and spatial variations of carbon monoxide over the western part of the Pacific Ocean. *Journal of Geophysical Research: Atmospheres 114* (D8), D08305.

238. Yevich, R., & Logan, J. A. (2003). An assesment of biofuel use and burning of agricultural waste in the developing world. *Global Biogeochem. Cycles 17* (4), 1095.

239. Yienger, J. J., & Levy, H. (1995). Empirical model of global soil-biogenic NOx emissions. *Journal of Geophysical Research: Atmospheres 100* (D6), 11447–11464.

240. Young, P. J., Archibald, A. T., Bowman, K. W., Lamarque, J. F., Naik, V., Stevenson, D. S., Tilmes, S., Voulgarakis, A., Wild, O., Bergmann, D., Cameron-Smith, P., Cionni, I., Collins, W. J., Dalsoren, S. B., Doherty, R. M., Eyring, V., Faluvegi, G., Horowitz, L. W., Josse, B., Lee, Y. H., MacKenzie, I. A., Nagashima, T., Plummer, D. A., Righi,

M., Rumbold, S. T., Skeie, R. B., Shindell, D. T., Strode, S. A., Sudo, K., Szopa, S., & Zeng, G. (2013). Pre-industrial to end 21st century projections of tropospheric ozone from the Atmospheric Chemistry and Climate Model Intercomparison Project (ACCMIP). *Atmospheric Chemistry and Physics 13*, 2063–2090.

241. Zeng, G., & Pyle, J. A. (2003). Changes in Tropospheric ozone between 2000 and 2100 modeled in a chemistry-climate model. *Geophysical Research Letters 30* (7), 1392.

242. Zeng, G., Pyle, J. A., & Young, P. J. (2008). Impact of climate change on tropospheric ozone and its global budgets. *Atmospheric Chemistry and Physics 8*, 369–387.

243. Zeng, G., Wood, S. W., Morgenstern, O., Jones, N. B., Robinson, J., & Smale, D. (2012). Trends and variations in CO, C_2H_6, and HCN in the Southern Hemisphere point to the declining anthropogenic emissions of CO and C_2H_6. *Atmospheric Chemistry and Physics 12*, 7543–7555.

244. Zhang, L., Li, Q. B., Jin, J., Liu, H., Livesey, N., Jiang, J. H., Mao, Y., Chen, D., Luo, M., & Chen, Y. (2011). Impacts of 2006 Indonesian fires and dynamics on tropical upper tropospheric carbon monoxide and ozone. *Atmospheric Chemistry and Physics 11*, 10929–10946.

245. Zhang, Q., Streets, D. G., Carmichael, G. R., He, K. B., Huo, H., Kannari, A., Klimont, Z., Park, I. S., Reddy, S., Fu, J. S., Chen, D., Duan, L., Lei, Y., Wang, L. T., , & Yao, Z. L. (2009). Asian emissions in 2006 for the NASA INTEX-B mission. *Atmospheric Chemistry and Physics 9*, 5131–5153.

Glossary of Abbreviations and Terms

Abbreviation/Term	Definition
a posteriori	from the latter - hypotheses are the result of observation or data with derived relationships
a priori	from the former - hypothesis for example the hypothesised trace gas profile
CTM	Chemical Transport Model
diel	daily - 24 hour periods
diurnal	daily - 12 hour periods
ECMWF	European Centre for Medium-range Weather Forecasts
ENVISAT	ESA's ENVIronmental SATellite
EOS	Earth Observing System – a group of satellites administered by NASA
ESA	European Space Agency
ESM	Earth System Model
FORTRAN	FORmula TRANslation - computational coding language
FTS	Fourier Transform infrared Spectrophotometer
GAMAP	Global Atmospheric Modelling (output) Analysis Package – IDL program package to analyse GEOS-Chem output
GCM	Global Circulation Model
GEOS	Goddard Earth Observing System – a system of models for support of NASA's earth science research
GEOS-Chem	Global 3-D CTM developed at Harvard and available at http://www.geos-chem.org
GFIT	Program used to retrieve total column values from ground based FTS.

Continued on next page –

– continued from previous page

Abbreviation/Term	Definition
GMAO	NASA's Global Modelling & Assimilation Office
HOx	H + OH + HO_2 + H_2O + H_2O_2
IDL	Interactive Data Language
in situ	In relation to measurements: direct sampling of ambient air
IPCC	Intergovernmental Panel on Climate Change
limb	Satellite viewing geometry – measure attenuated solar radiation through the Earth's limb
MERRA	Modern–Era Retrospective analysis for Research Applications
molecules cm^{-2}	Vertical column density or total column: A way to describe atmospheric composition
MLS	Microwave Limb Sounder – instrument aboard the EOS-AURA satellite
MOPITT	Measurements Of Pollution In The Troposphere: a satellite based infrared radiometer aboard NASA's EOS Terra spacecraft
nadir	Satellite viewing geometry - directly below a particular location
NASA	National Aeronautics and Space Administration (USA)
NCAR	National Center for Atmospheric Research (USA)
NCEP	National Centers for Environmental Prediction
NCL	NCAR command Language - used to visualise and process large datasets.
NDACC	Network for the Detection of Atmospheric Composition Change – 70 global remote-sensing research stations
NMHC	Non-methane hydrocarbons, a subset of VOCs (Le Treut et al., 2007)
NOAA	National Oceanic and Space Administration (USA)
NO_X	The chemical family of NO and NO_2
NO_Y	The chemical family of NO_X, also including other sources of NO_X such as N_2O_5, HNO_3, HNO_4, $ClONO_2$ and PAN
OMI	Ozone Monitoring Instrument – aboard the EOS-AURA satellite
O_X	$O(^3P)$ + $O(^1D)$ + O_3
PBL	Planetary Boundary Layer, an area of highly turbulent atmosphere which extends from ground level to 0.5–2km during the day and less at night.

Continued on next page –

– continued from previous page

Abbreviation/Term	Definition
ppmv or ppm	Parts per million by volume: 1 ppmv = 1×10^{-6} v/v, or the mole fraction μmol mol^{-1}
ppbv or ppb	Parts per billion by volume: 1 ppbv = 1×10^{-9} v/v, or the mole fraction ηmol mol^{-1}
SCIAMACHY	SCanning Imaging Absorption SpectroMeter for Atmospheric CHartographY - an imaging spectrometer aboard ENVISAT
SFIT-2	Software tool to analyse ground-based solar FTS spectra
SST	Sea Surface Temperature
TES	Tropospheric Emission Spectrometer – instrument aboard the EOS-AURA satellite
TCCON	Total Column Carbon Observing Network - a network of ground-based Fourier Transform Spectrometers recording direct solar spectra in the near-infrared spectral region
tcol	total column value (in molecules cm^{-2})
vmr	Volume mixing ratio: defined as relative proportion of gas to total volume of air molecules $\left[\frac{\text{volume of target gas}}{\text{volume of air+gas in sample}}\right]$
UOW	University of Wollongong
VOC	Volatile organic compound
WMO-GAW	World Meteorological Organization - Global Atmosphere Watch

Appendices

Appendix A

Scripting

Brief descriptions of coding developed during this PhD are given below. For a copy of any code, please contact the author: r.r.buchholz@gmail.com.

Perl scripts

Table A.0.1: Perl scripts developed for research presented in this thesis.

Script filename	Brief description
apriori-pcol	Calculates a selected pcol for GFIT apriori formatted files.
avker-average	Calculate and average representative averaging kernel..
collate-pixels	Combines fractions of annual cycles for surrounding pixels with a centre pixel. Set up for ACCESS output.
correlation	Pearson's product-moment correlation coefficient calculation using means and standard deviations. Used for FTS, GEOS-Chem and ACCESS. Two files to correlate require the same date format.
difference-access	Calculates difference between output from two ACCESS runs (or between pixels).
difference-gc	Calculates difference between output from two GEOS-Chem runs.
percent-diff	Calculates percentage differences between two files of annual cycle data.
plot	User definitions determine variables and select data to be used in plotting. Uses GNUPlot to create plots. For profiles, total and partial column plotting. Choose monthly or daily averaged timeseries, daily cycles, annual cycles.

Continued on next page –

Table A.0.1 – continued from previous page

Script filename	Brief description
plot-surf	User definitions determine variables and select data to be used in plotting. Uses GNUPlot to create plots. For surface values.
monthavg	Calculates month averages from daily averages.
readandplotaccess	Converts .csv formatted ACCESS output into total column or partial column results. Options to: extract surface layer; create average annual cycles data over selected years; plot results.
seasonal	Seasonally averages single column in files.
separate-enso	Separate values in files to La Nina and El Nino months.
std-dev	Calculates standard deviation for annual cycles for FTS, GEOS-Chem or ACCESS. Requires a previously created file with average values (such as created from using the seasonal script) to compare with.
vmr2moleccm2	Transforms mole fractions into total column values.
vmrseasonal-access	Calculates monthly averaged trace gas profiles for ACCESS output.

NCL scripts

Table A.0.2: NCAR Command Language (NCL) scripts developed for research presented in this thesis.

Script filename	Brief description
apply_ak_access.ncl	Applies satellite or ground based solar FTS averaging kernels to ACCESS output prior to computing total column values.
apply_ak_geoschem.ncl	Applies satellite or ground based solar FTS averaging kernels to GEOS-Chem output prior to computing total column values.
BADCtrajplot	Plots back trajectories from British Atmospheric Data Centre (BADC) runs, downloaded in NASA Ames (.na) format. Enables visualisation of the evolution of trajectory height.
calc_emissions	Calculate emissions from ACCESS output.

Continued on next page –

Table A.0.2 – continued from previous page

Script filename	Brief description
compare_mopitt	Creates difference plots between MOPITT and GEOS-Chem over selected area. Includes averaging kernel convolution.
correlate_mopitt	Correlates MOPITT and GEOS-Chem over selected area. Includes averaging kernel convolution.
mapWgrid	Plots a map of choice overlayed with a user defined grid. Selected gridboxes may be coloured. Zoom in on locations with ACCESS grid overlayed with equivalent GEOS-Chem gridbox.
mopitt_avker.ncl	Plots MOPITT averaging kernel matrix.
plot_ak.ncl	Plots FTS averaging kernel vector.
vegland.ncl	Extracts MODIS land surface IGBP types and plots over selected regions.

Shell and PBS scripts

Table A.0.3: Shell and batch scripts developed for research presented in this thesis.

Script filename	Brief description
changedate(.pl)	perl script to use with run_geos
met-dwld(.pl)	perl script for use with run_copy
run_copy	Sets up a PBS job to copy met files from a remote location to the local machine and upload to a mass store. Requires met-dwld.pl to determine wget commands.
run_copymet	Copies met files (such as GEOS5 or MERRA) from mass store to local machine in order to run GEOS-Chem. Submits run_geos after met files have been downloaded to local machine.
run_geos	Sets PBS variables and sends the GEOS-Chem to queue. Daisy chains with run_copyment using shell environment variables. Requires changedate.pl to change GEOS-Chem input file.

Appendix B

Calinski-Harabasz method to determine optimal clusters

In all clustering techniques, there is a fundamental question of how to determine the optimal number of clusters. It is acknowledged to be a rather heuristic task and any method chosen is complemented by external verification. For this study, the optimal number of clusters was determined using the Calinski–Harabasz (C–H) index (Calinski & Harabasz, 1974). The C–H index calculates the ratio of between group variance to within group variance (Equation B.0.1). In clustering, the aim is to maximise between group variance and minimise within group variance, thereby maximising the C-H index.

$$C-H = \frac{\left[\frac{\sum_{i=1}^{g}(\bar{y}_i-\bar{y})^2}{g-1}\right]}{\left[\frac{\sum_{i=1}^{g}\sum_{j=1}^{n_i}(y_{ij}-\bar{y}_i)^2}{n-g}\right]} \tag{B.0.1}$$

Where:
n = number of points in entire dataset
$\bar{y}$ = entire dataset mean
g = number of cluster groups
n_i = number of points in cluster group i
$\bar{y}_i$ = mean of cluster group i
y_{ij} = value of point j in group i

Here, the trace gas dataset was clustered to differing degrees, ranging the number of clusters from 1 to 15. Subsequently for each clustering scenario, the C–H index was determined. A plot of C–H against number of clusters indicates maximum C–H value, and associated optimum number of clusters. An example of using C–H values is shown in Figure B.0.1, undertaken for trajectory clustering. If the plot of C–H versus number of clusters displays decreasing

values with no obvious peak, the C–H technique is inconclusive. In these cases, the first large change for within group variance was used to determine optimal clustering. For example, for autumn trajectory clustering there was an 8 % reduction in within group variance increasing clustering from 4 to 5 groups. Elsewhere for autumn, between other degrees of clustering only saw less than 1% improvements. Therefore, in autumn, 5 clusters are retained.

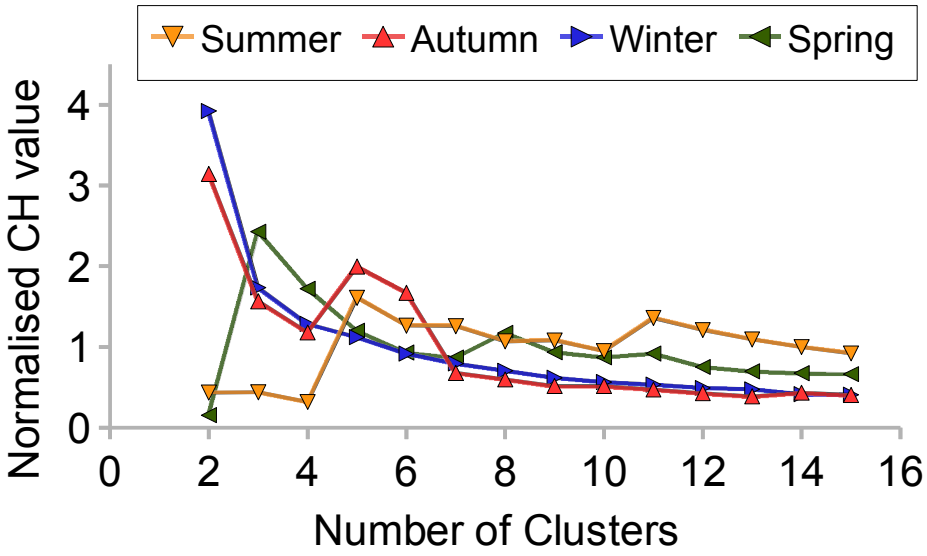

Figure B.0.1: Calinski-Harabasz (C-H) index values associated with different clustering regimes per season in the UOW dataset. Maximum C-H index in each season indicates the optimum number of clusters.

Appendix C

Case Study: Comparison at two Wollongong sites

For the timeperiod December 13, 2012 to February 23, 2013, Sandpit was located approximately 3 km northeast from UOW, at a site within the urban extent and located closer to the ocean. Sandpit was deployed as one of the instruments for the MUMBA (Measurements of Urban, Marine and Biogenic Atmosphere) campaign. The site shall be herein referred to as the MUMBA site. The MUMBA site, being closer to the ocean, would capture less local influence from University related pollution, which was particularly important for measuring other shorter-lived trace gases with instruments other than the *in situ* FTIR, involved in MUMBA. Concurrently, Eddy remained measuring ambient air at UOW with the aim of comparing trace gas composition between locations in Wollongong. The appropriateness of UOW as a receptor site for the Wollongong region was then able to be determined.

Correlation plots between UOW and MUMBA records were prepared filtering for wind speeds above 0.4 ms^{-1}. Correlations between trace gases were investigated over increasing time averaging periods, for 10 minute, 3 hour and 12 hour timeseries. The range of correlations is shown for CO in Figure C.0.1. As the averaging time increases, datasets move towards the 1:1 line, indicating that differences between sites are reducing. This is a reflection of increased atmospheric mixing time, meaning relative location of pollution sources becomes less important, that is, sources are diluted into a regional signal. Additionally, increasing averaging times increases the probability of including more wind directions in the average value, therefore producing more comparable average values.

Variations between sites may be accounted for by differences in wind direction, which include different local sources depending upon site. For example, roads close to the University will have a large influence on the UOW record, but a lower influence on the MUMBA site record. Bivariate polar pollution plots of CO at the two sites show two sources of higher CO values for the sites, namely northwest and southwest of both the MUMBA and UOW sites (Figure C.0.2). Similar results to CO were found for other trace gases, but in the interest of brevity, are not included here.

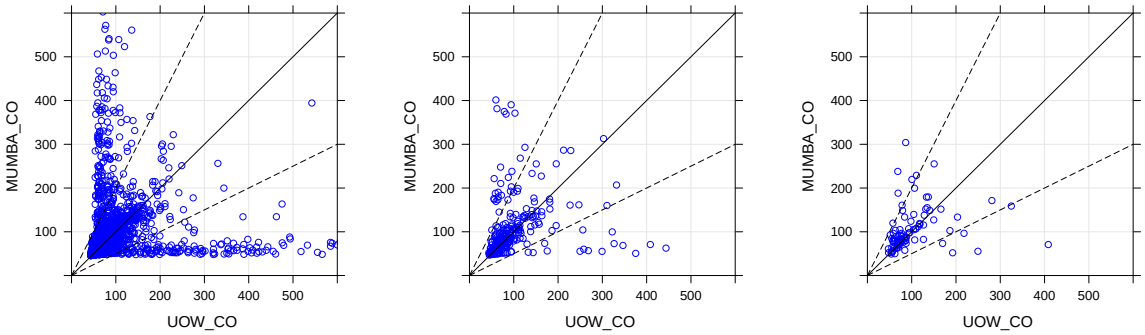

(a) 10 minute (RMA = 0.21) (b) 3 hour (RMA = 0.49) (c) 12 hour (RMA = 1.16)

Figure C.0.1: MUMBA CO compared with UOW CO over different averaging periods. Wind speeds were filter to be above 0.4 ms^{-1}. Solid line is 1:1, 0.5:1 and 2:1 dashed lines are also shown for comparison. Linear regression slope results using the reduced major axis (RMA) method are recorded below plots.

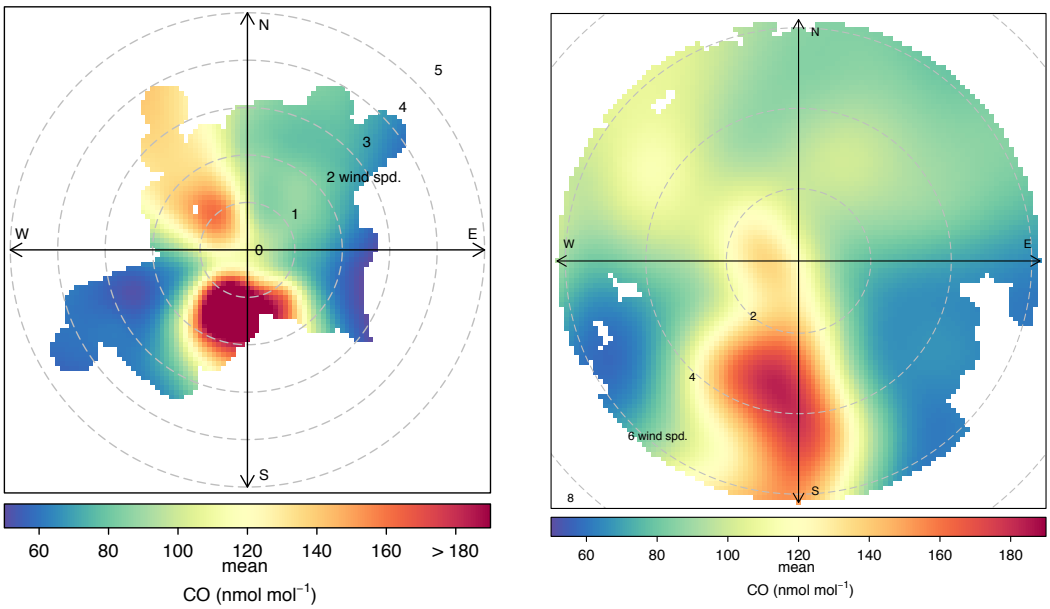

(a) UOW (b) MUMBA site

Figure C.0.2: Bivariate polar plots of CO during the MUMBA campaign at (a) UOW and (b) MUMBA site.

Overall, it is concluded that UOW may be used as a representative site in Wollongong for data which satisfies the conditions of wind speeds greater than 0.4 ms^{-1}. Regional representativeness increases with increasing averaging times. Therefore, monthly and yearly conclusions determined from the UOW dataset are expected to be remain robust for the region. Conclusions made on smaller averaging timescales remain useful, but must be combined with the knowledge of the UOW location within the Wollongong region, to give meaningful insights. Further comparisons at other sites within the Wollongong region would be useful to validate results found here. The comparison between sites would also benefit from lagged correlation analysis.

Appendix D

Converting mole fraction to total column

In model environments, the atmosphere is simplified into discrete vertical layers. Within each level the mole fractions or volume mixing ratios are constant. Often we are interested in the total column value and need to transform mole fraction into molecules$\cdot cm^{-2}$. The process of conversion is described below.

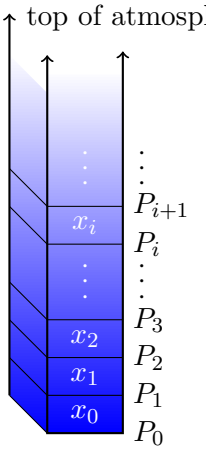

Where
x_i = volume mixing ratio (or mole fraction)
P_i = pressure edges

The first step is to calculate masses within layers. Pressure is a force per unit area, shown below as Pa.

$$P = \frac{N}{m^2} = \frac{M \cdot \phi}{m^2} \tag{D.0.1}$$

Where
N = Newtons $\frac{kg \cdot m}{s^2}$
M = mass in kg
ϕ = graviation $\frac{m}{s^2}$ (can be a function)

Therefore the mass above a unit area of a metre squared at layer i is:

$$\frac{M_i}{m^2} = \frac{P_i}{\phi \cdot m^2} \tag{D.0.2}$$

For example, substituting gravity $\phi = 9.8ms^{-2}$, at the Earth's surface the mass above a unit area of one m^2 is

$$\frac{101325}{9.8 \cdot m^2} \approx 1.03 \times 10^4 kg/m^2$$

Assuming gravity is constant, $\phi = 9.8ms^{-2}$, converting to $g \cdot cm^{-2}$ and using pressure given in hPa:

$$M_i = \frac{P_i}{9.8} \cdot \frac{1kg \cdot \frac{1000g}{kg} \cdot 1hPa \frac{100Pa}{hPa}}{1m^2 \cdot \frac{10{,}000cm^2}{m^2}} \tag{D.0.3}$$

$$= \frac{10 \cdot P_i}{9.8} \frac{g}{cm^2} \tag{D.0.4}$$

Converting mass of air into number of molecules (c_i) follows two calculations. Firstly, number of moles of the trace gas within each layer is calculated. The mass of air above a layer is converted to number of moles (n_i) using the molecular weight of air (MW_{air}). Here, MW_{air} is taken as the constant molecular mass of dry air: 28.9 $g \cdot mol^{-1}$. However, MW_{air} can also be a function that includes a variable component of water vapour.

$$n_i = \frac{M_i}{MW_{air}} \tag{D.0.5}$$

$$= \frac{10 \cdot P_i}{9.8 \cdot 28.9} \frac{g}{cm^2 \cdot \frac{g}{mol}} \tag{D.0.6}$$

$$= \frac{10 \cdot P_i(hPa)}{9.8 \cdot 28.9} \frac{mol}{cm^2} \tag{D.0.7}$$

The number of moles of air within a layer is then:

$$n_i - n_{i+1} = \frac{10 \cdot P_i - P_{i+1}}{9.8 \cdot 28.9} \frac{mol}{cm^2} \tag{D.0.8}$$

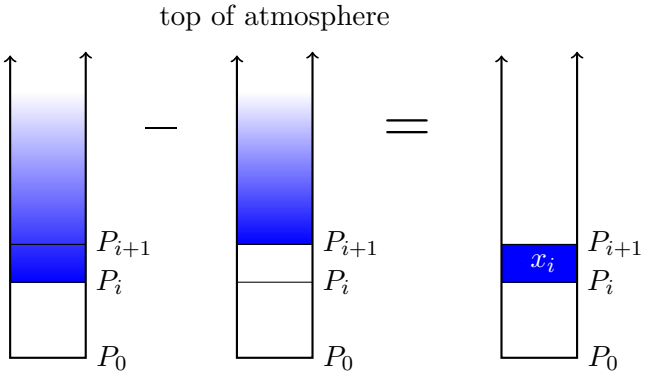

The mole fraction (x_i) may then be used to determine the the number of moles of trace gas in layer i.

$$n_{gas} = x_i \cdot (n_i - n_{i+1}) \tag{D.0.9}$$

$$= x_i \cdot \frac{10 \cdot P_i - P_{i+1}}{9.8 \cdot 28.9} \frac{mol}{cm^2} \tag{D.0.10}$$

Once the number of moles of trace gas is calculted, Avogadro's number ($N_A = 6.022 \times 10^{23} \frac{molecules}{mol}$) is used to convert from number of moles to number of molecules.

$$c_i = x_i \cdot (n_i - n_{i+1}) \cdot N_A \tag{D.0.11}$$

$$= x_i \cdot \frac{10 \cdot P_i - P_{i+1}}{9.8 \cdot 28.9} \cdot 6.022 \times 10^{23} \frac{\cancel{mol}}{cm^2} \frac{molecules}{\cancel{mol}} \tag{D.0.12}$$

Total column is calculated by summing the number of molecules in each layer, to the top of the atmosphere.

$$\sum c_i = \sum x_i \cdot \frac{10 \cdot P_i - P_{i+1}}{9.8 \cdot 28.9} \cdot 6.022 \times 10^{28} \frac{molecules}{cm^2} \tag{D.0.13}$$

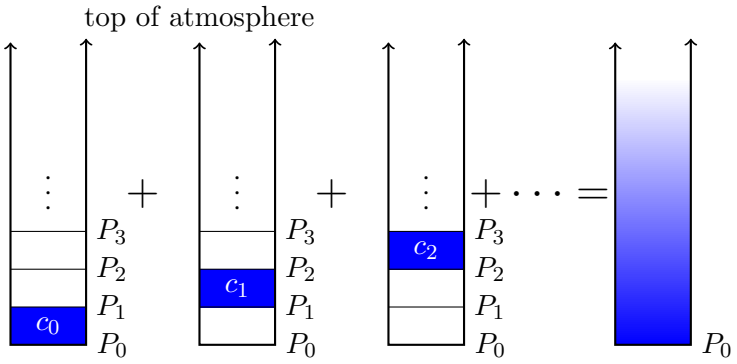

Below is shown both the discrete layer form and the continuous form of converting to total column.

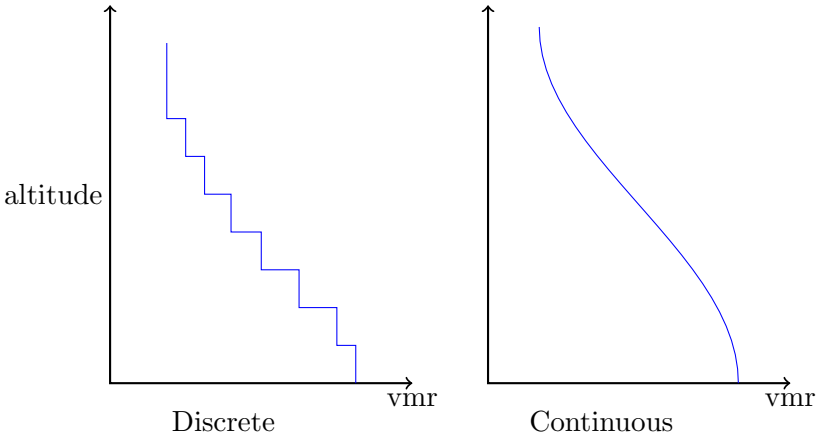

XX

Discrete-layer form:

$$VC_G = \sum x_i \cdot \frac{10 \cdot \Delta P}{\phi \cdot MW_{air}} \cdot N_{Av} \frac{molecules}{cm^2} \tag{D.0.14}$$

Where:
VC_G = vertical column value for a gas G
$\Delta P = P_i - P_{i+1}$
$\phi = \phi(z, lat)$, gravitational function
$MW_{air} = m_{air}^{dry}[1 + x_{H_2O}^{dry}(p) \cdot (m_{H_2O}/m_{air}^{dry})]$

As $\Delta P \to 0$, the VC_G sum becomes an integral and $\Delta P = dp$. Additionally, functions for gravity and mass of air are incorporated.

Continuous form (Wunch et al., 2010):

$$VC_G = \int_0^{P_s} \frac{x(p)^{dry}}{\phi(z, lat) m_{air}^{dry}[1 + x_{H_2O}^{dry}(p) \cdot (m_{H_2O}/m_{air}^{dry})]} dp \tag{D.0.15}$$

Where:
$m_{air}^{dry}, m_{H_2O}^{dry}$ have units of $\frac{}{N_{Av}} \frac{kg}{molecule}$

Appendix E

Additional Plots

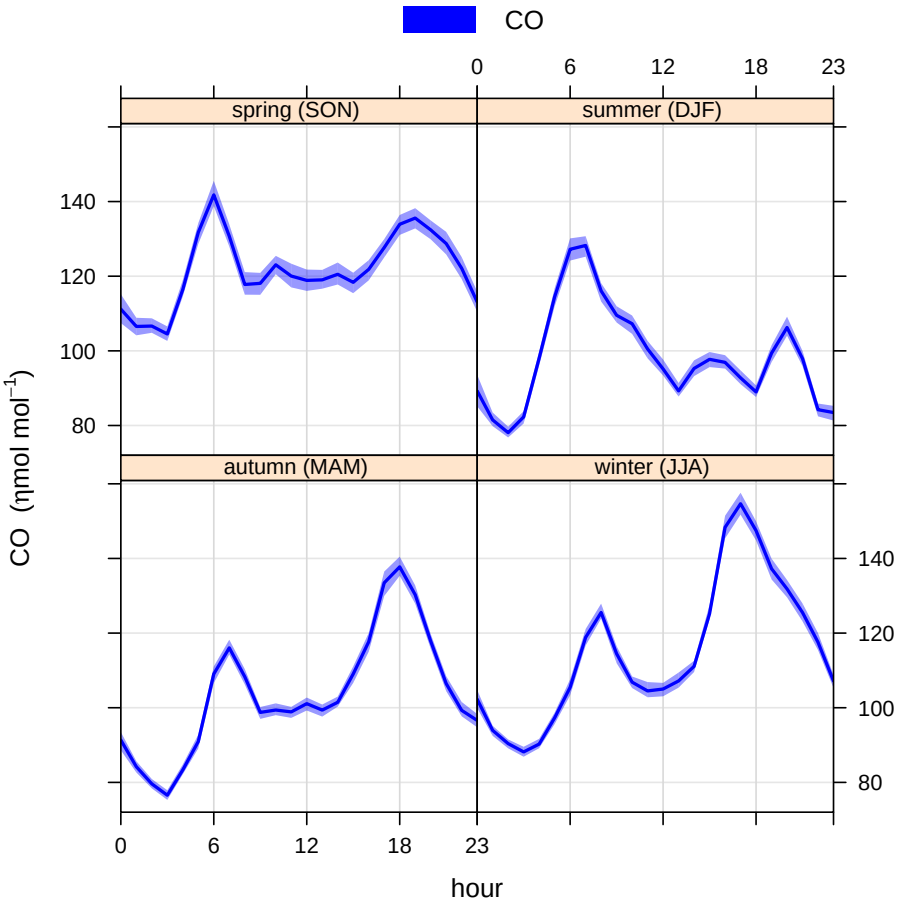

Figure E.0.1: Daily cycles of CO at UOW for the entire data record, split up by season.

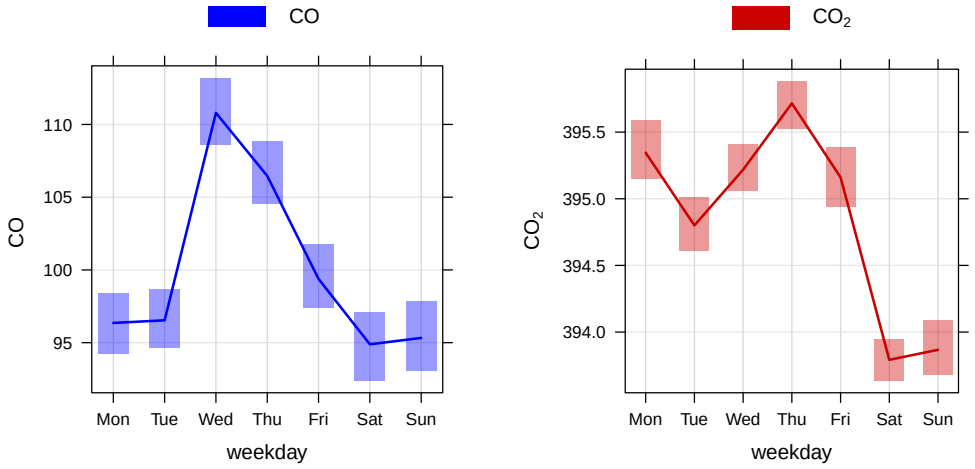

(a) CO

(b) CO_2

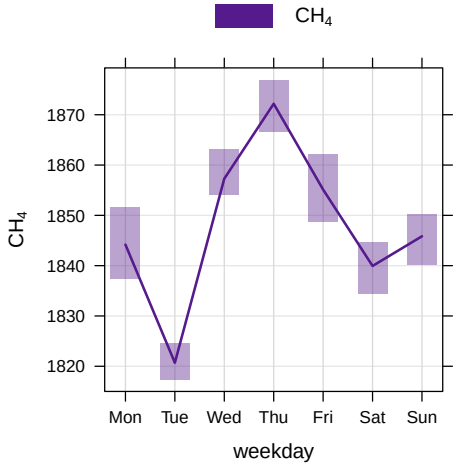

(c) CH_4

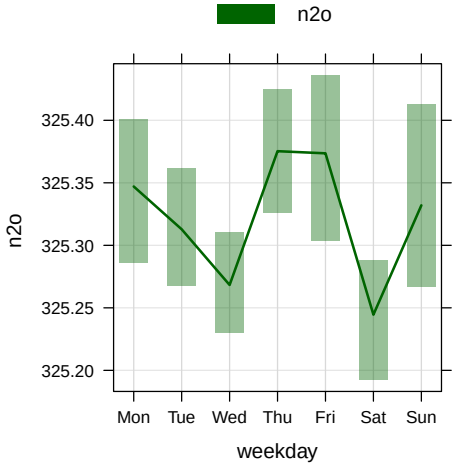

(d) N_2O

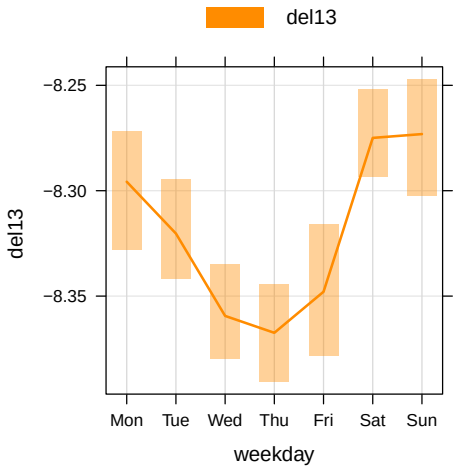

(e) $\delta^{13}C$

Figure E.0.2: Average weekly cycles in the *in situ* FTIR measurements at UOW, 2011 to 2013. Shaded areas indicate 95% confidence intervals, calculated using bootstrap simulations.

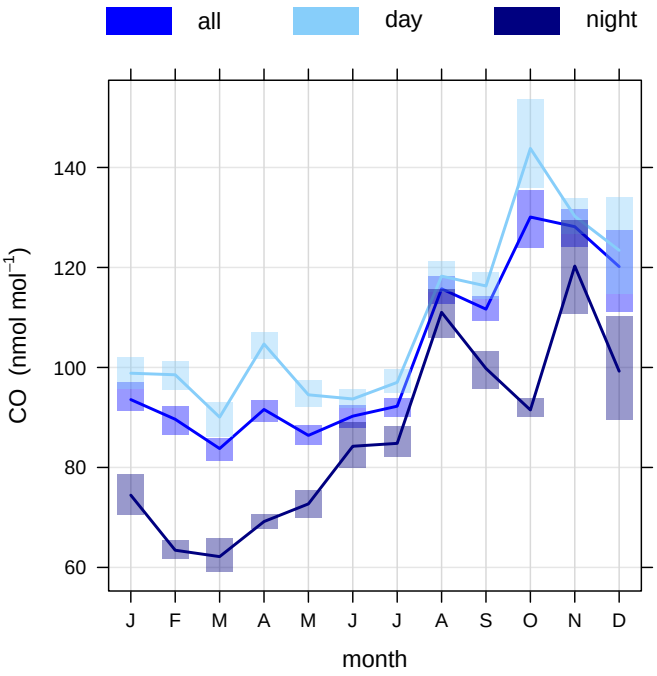

Figure E.0.3: Monthly cycles split up by day (6:00 to 21:00) and night (22:00 to 5:00).

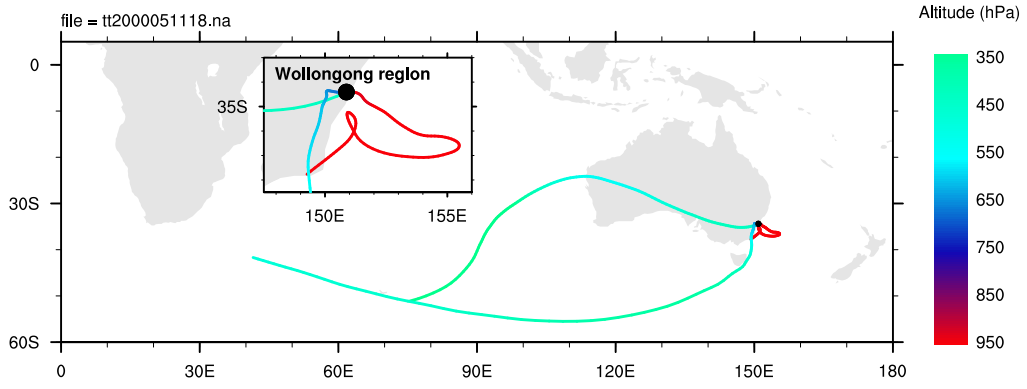

Figure E.0.4: BADC Back trajectory examples for events of type II showing indirect transported pollution. Slow moving swirling trajectory at 950 hPa (inset) traps and re-circulates local pollution. Other trajectories are fast moving and remain at higher altitudes, so are expected to have relatively low CO content (event **a**).

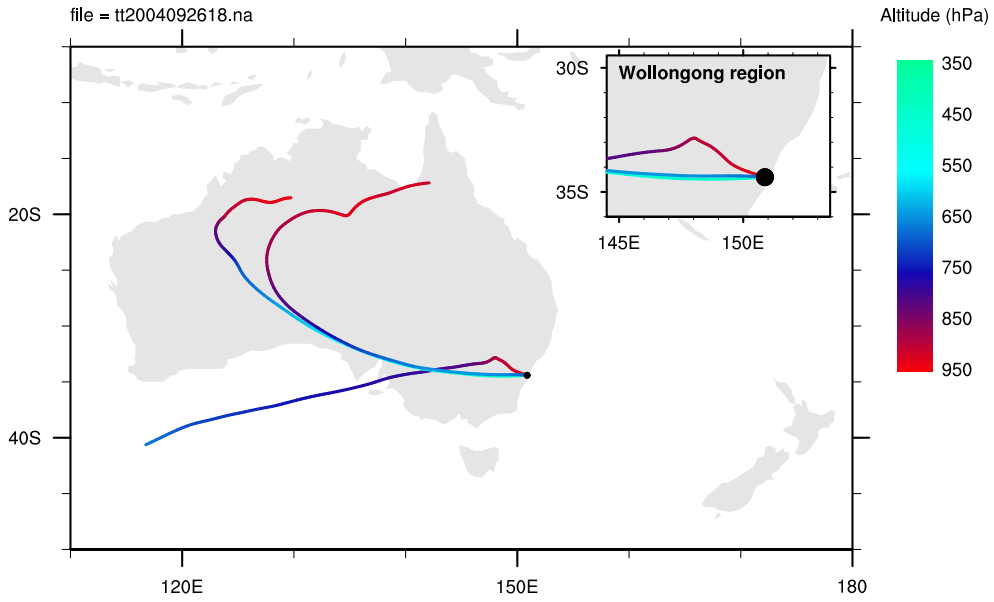

(a) Back trajectory plot (5-days), 26 September, 2004

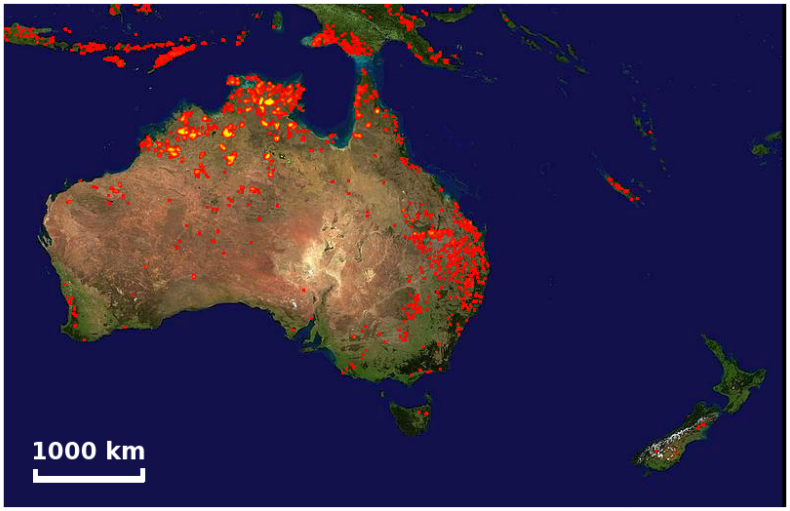

(b) MODIS fire count 17 to 26 September, 2004 (Giglio et al., 2003; Davies et al., 2004)

Figure E.0.5: Medium–range transport of surface air from Western Australia and the Northern Territory to higher altitudes over Wollongong on 26 September, 2004 (event **o**).

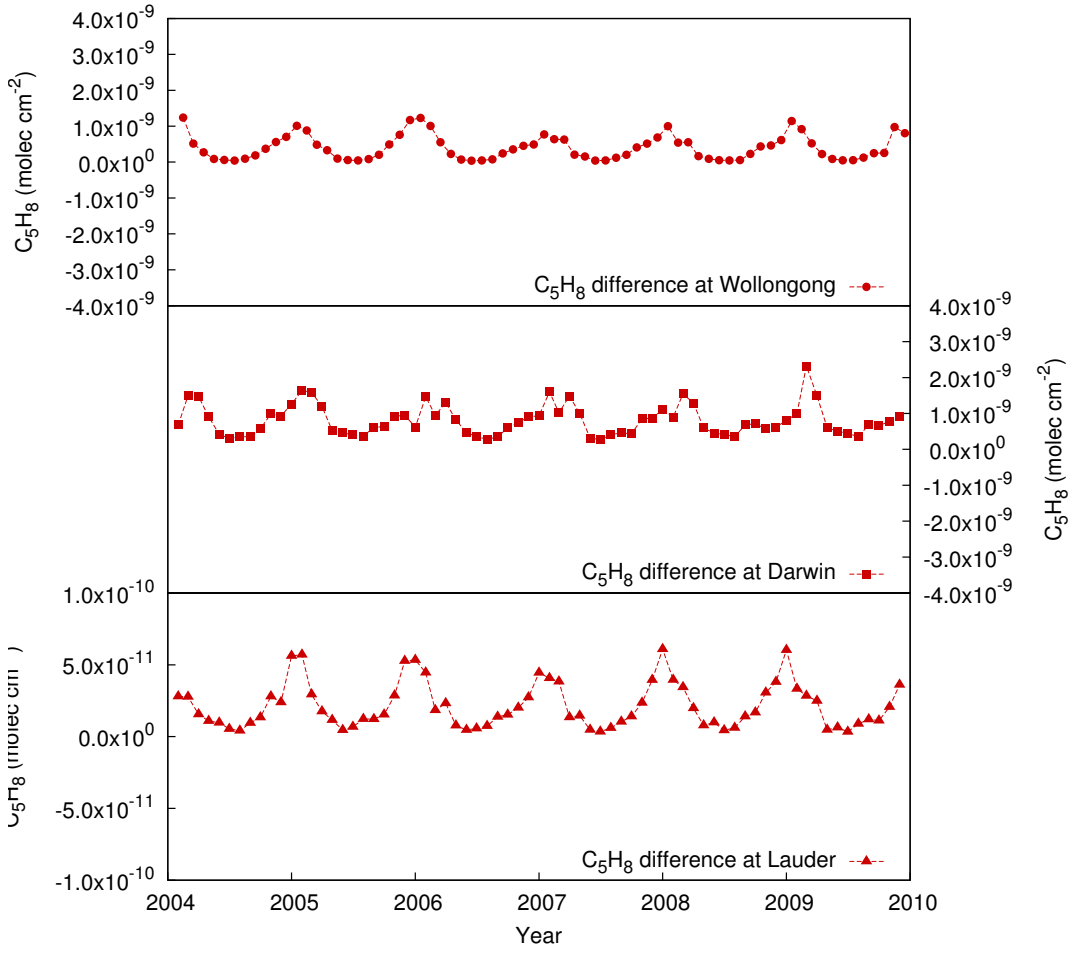

Figure E.0.6: Isoprene monthly surface mole fraction differences between standard and Caltech isoprene scheme simulations.

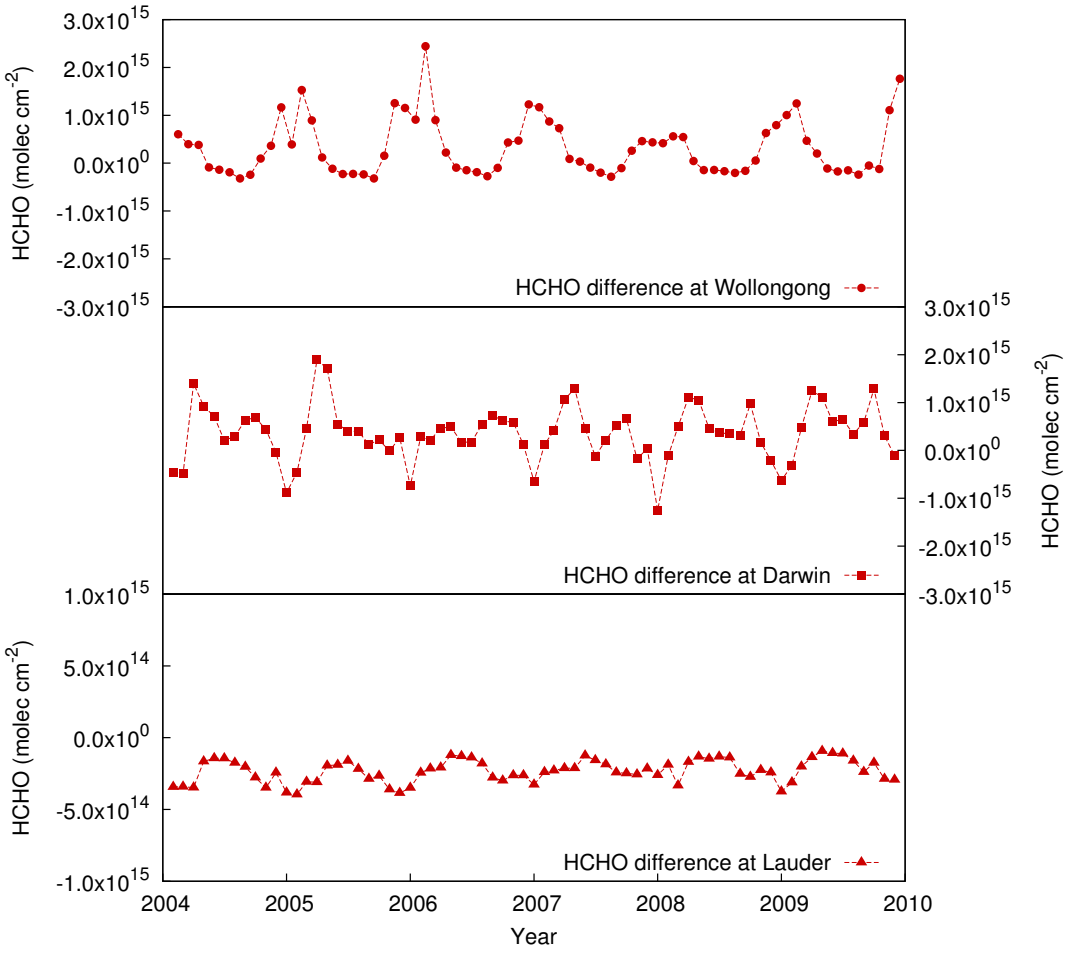

Figure E.0.7: Formaldehyde monthly total column differences between standard and Caltech isoprene scheme simulations.

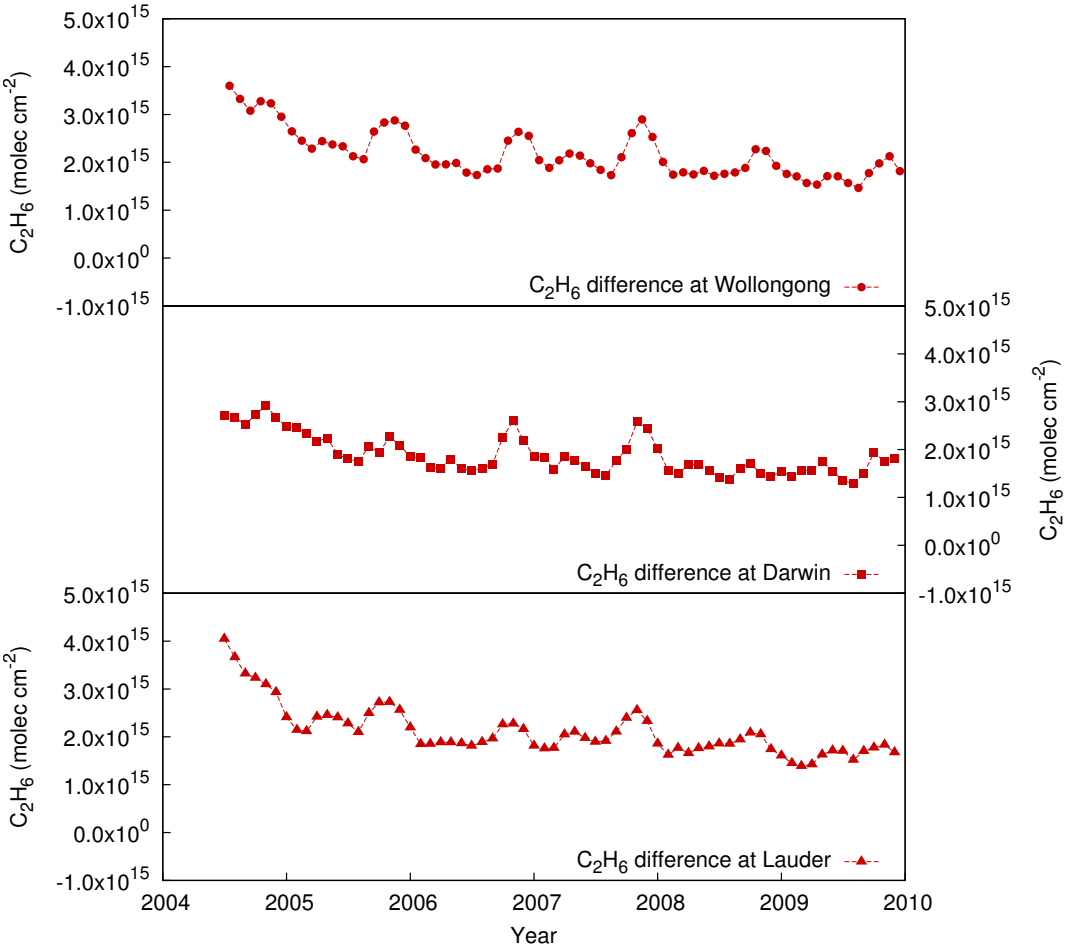

Figure E.0.8: Ethane monthly total column differences between standard and Caltech isoprene scheme simulations.

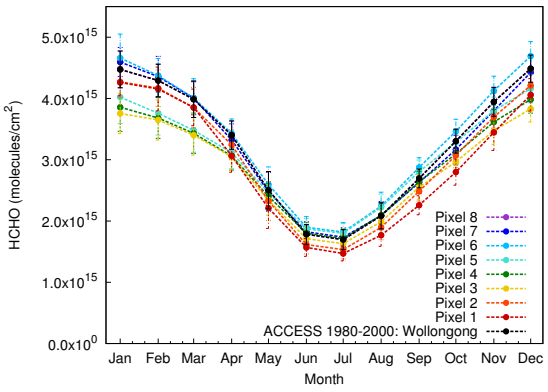

(a) Wollongong total column HCHO by grid-box

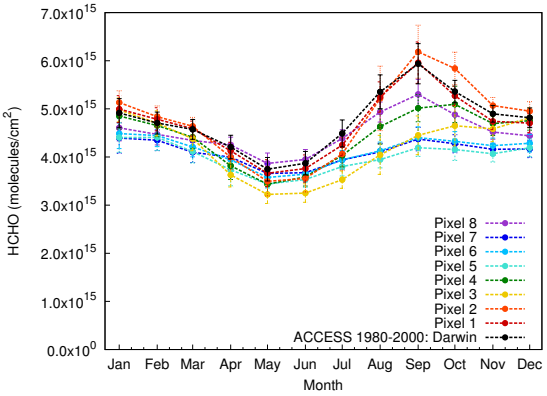

(b) Darwin total column HCHO by grid-box

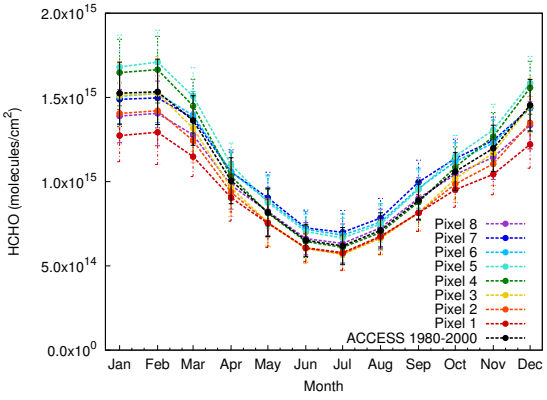

(c) Lauder total column HCHO by grid-box

Figure E.0.9: HCHO annual cycles

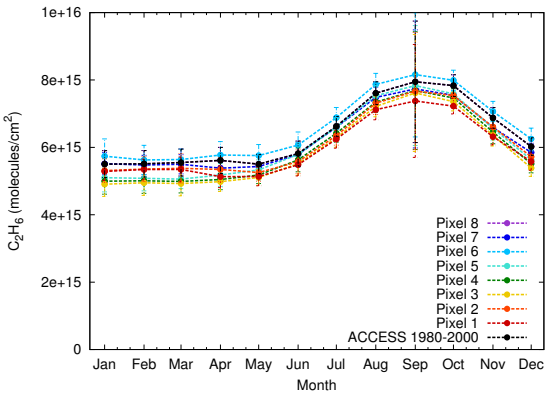

(a) Wollongong total column C_2H_6 by grid-box

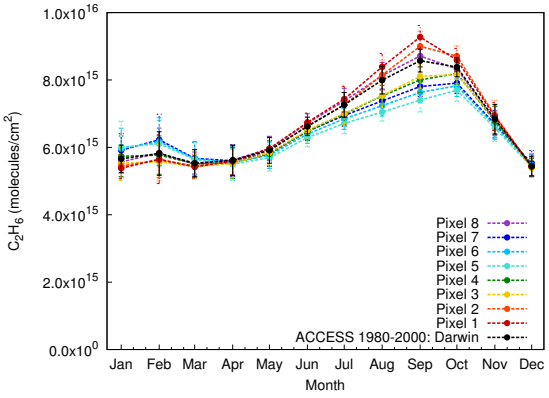

(b) Darwin total column C_2H_6 by grid-box

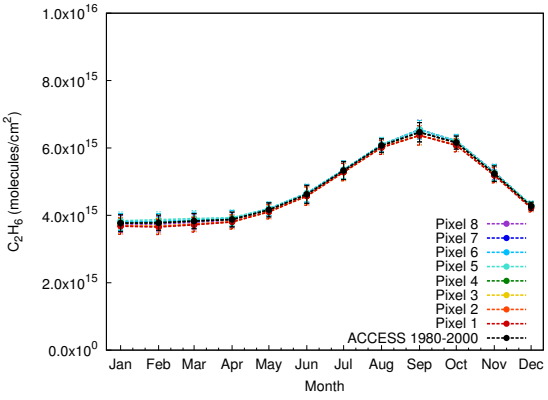

(c) Lauder total column C_2H_6 by grid-box

Figure E.0.10: C_2H_6 annual cycles

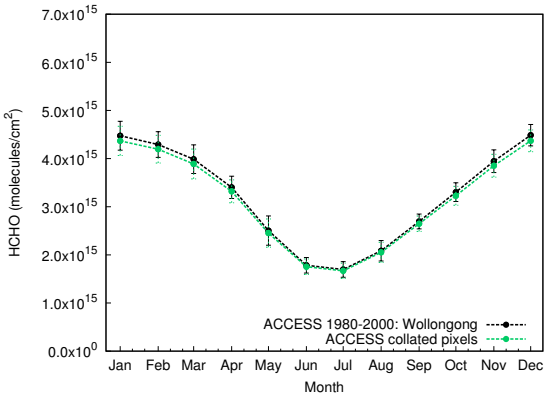

(a) Resolution effect on Wollongong total column HCHO

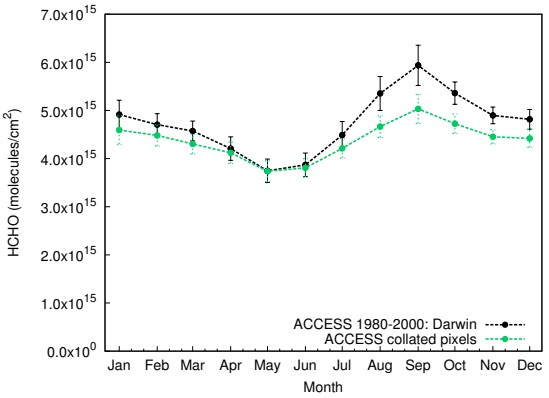

(b) Resolution effect on Darwin total column HCHO

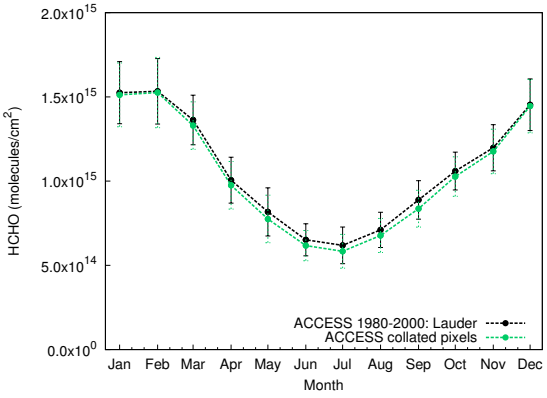

(c) Resolution effect on Lauder total column HCHO

Figure E.0.11: ACCESS total column HCHO annual cycle for the central grid-box against the combined lower resolution ACCESS product at each location (a) Wollongong, (b) Darwin and (c) Lauder.

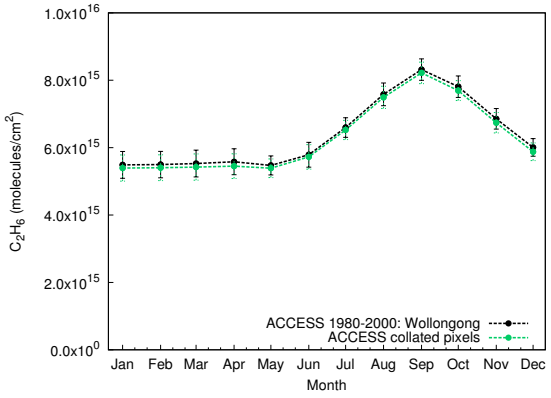

(a) Resolution effect on Wollongong total column C_2H_6

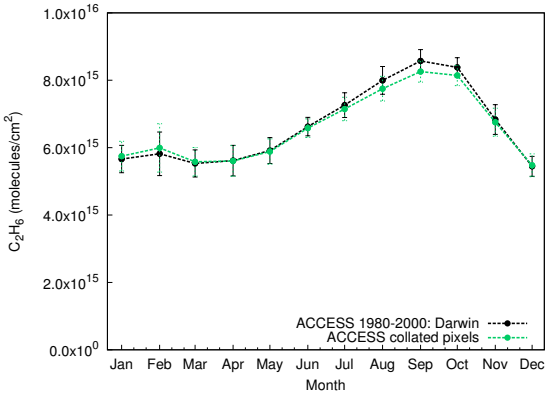

(b) Resolution effect on Darwin total column C_2H_6

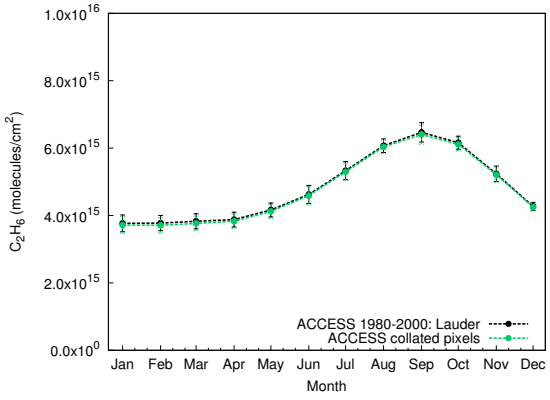

(c) Resolution effect on Lauder total column C_2H_6

Figure E.0.12: ACCESS total column C_2H_6 annual cycle for the central grid-box against the combined lower resolution ACCESS product at each location (a) Wollongong, (b) Darwin and (c) Lauder.

Figure E.0.13: ACCESS NO_2 profiles at Darwin and Lauder

(a) New Darwin NO_2 profile

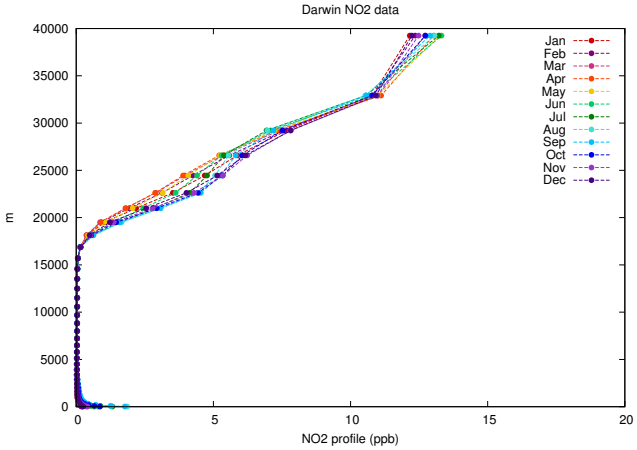

(b) Old Darwin NO_2 profile

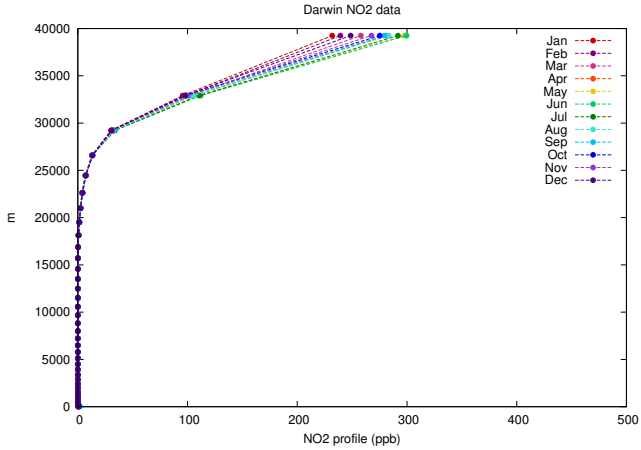

(c) New Lauder NO_2 profile

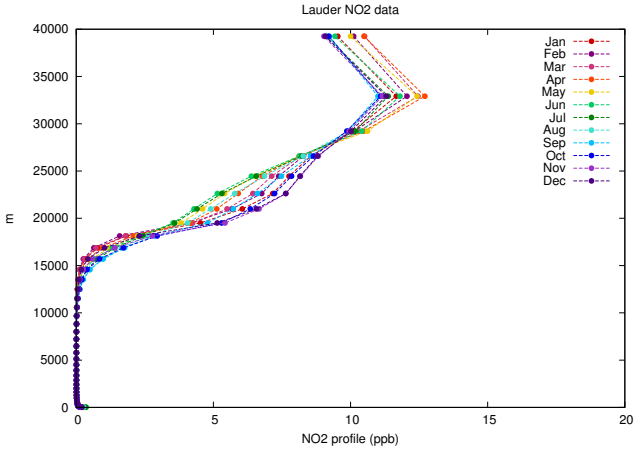

(d) Old Lauder NO_2 profile

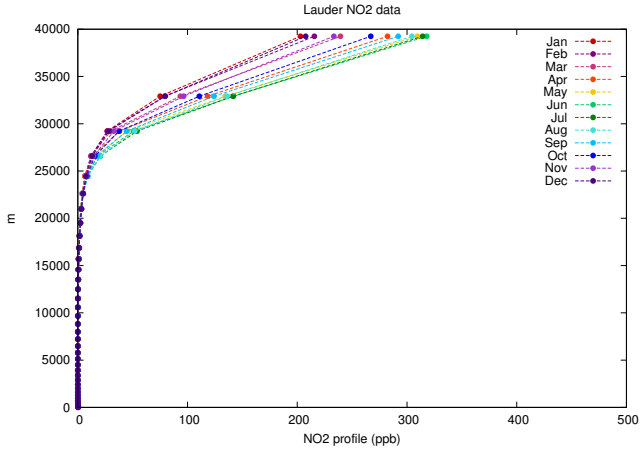

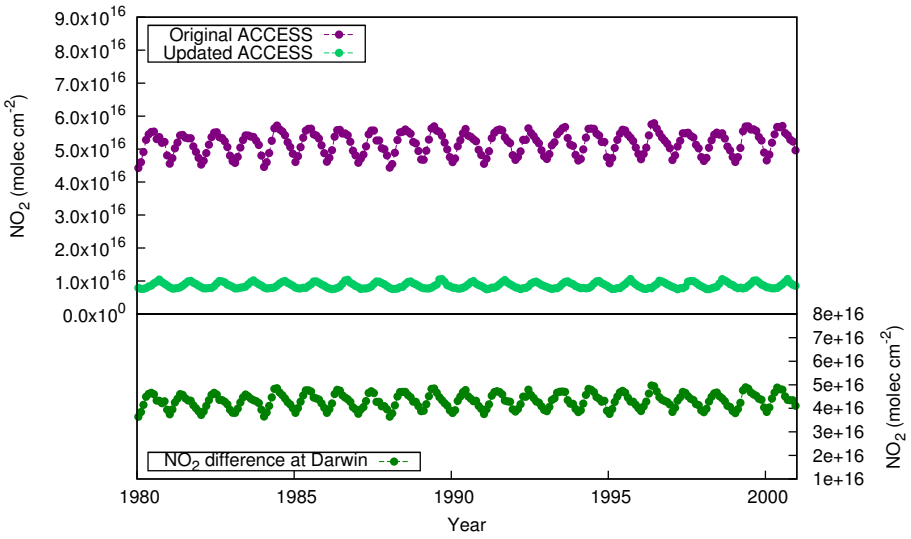

Figure E.0.14: ACCESS NO_2 original (purple) and updated (light green) simulations at Darwin. Lower panel plots the difference between original and updated NO_2.

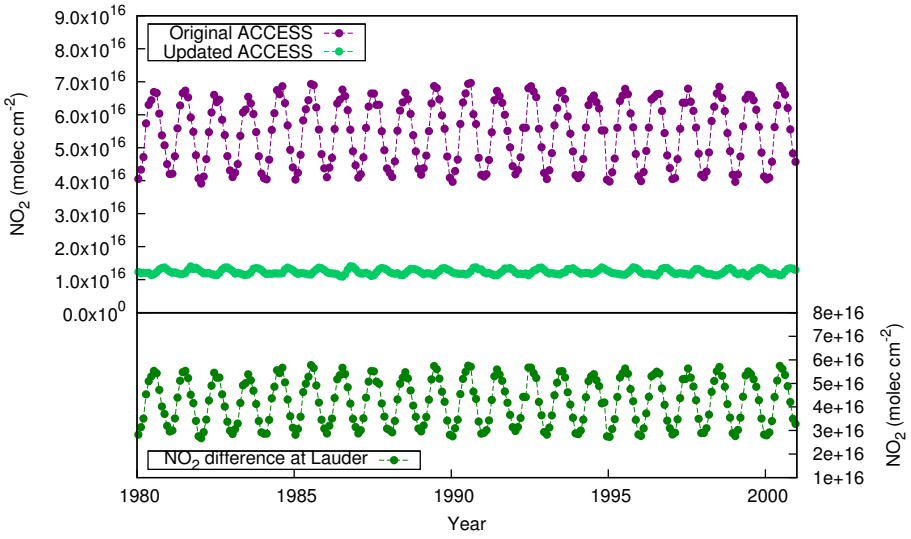

Figure E.0.15: ACCESS NO_2 original (purple) and updated (light green) simulations at Lauder. Lower panel plots the difference between original and updated NO_2.

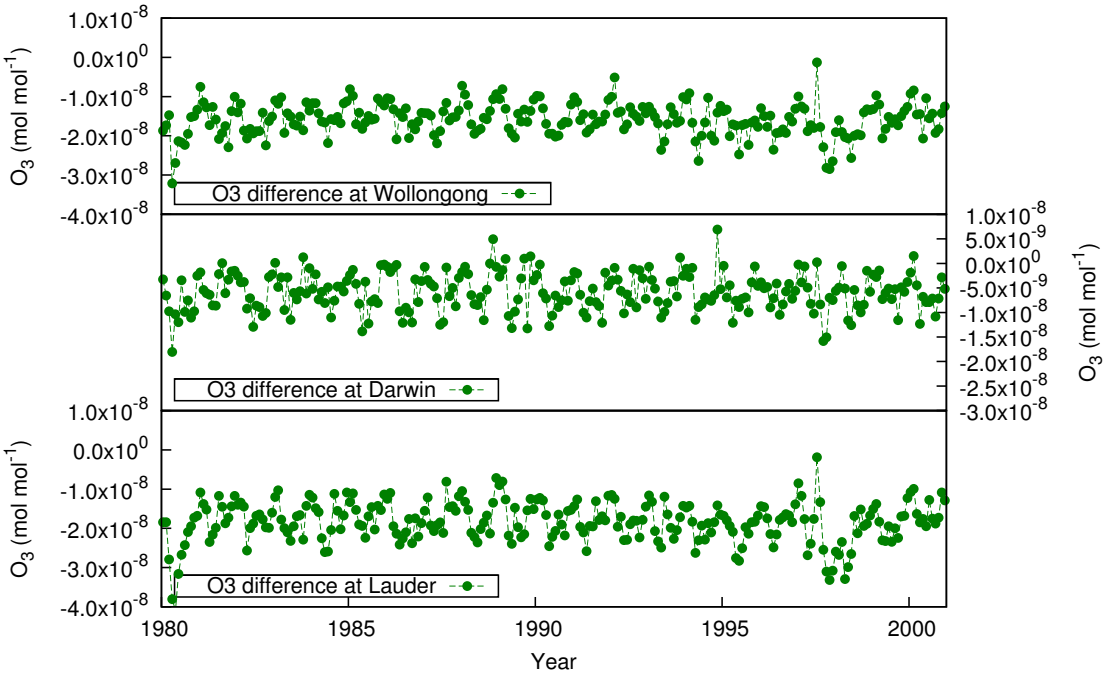

Figure E.0.16: Timeseries of monthly surface mole fraction O_3 differences between original and updated ACCESS simulations. Differences are plotted for Wollongong (top panel), Darwin (middle panel) and Lauder (bottom panel).

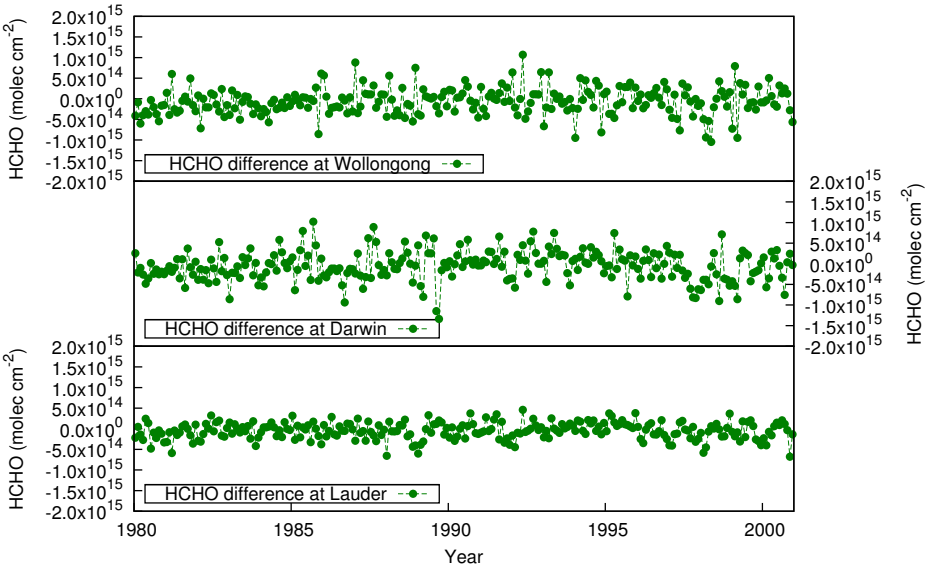

(a) Total column HCHO difference.

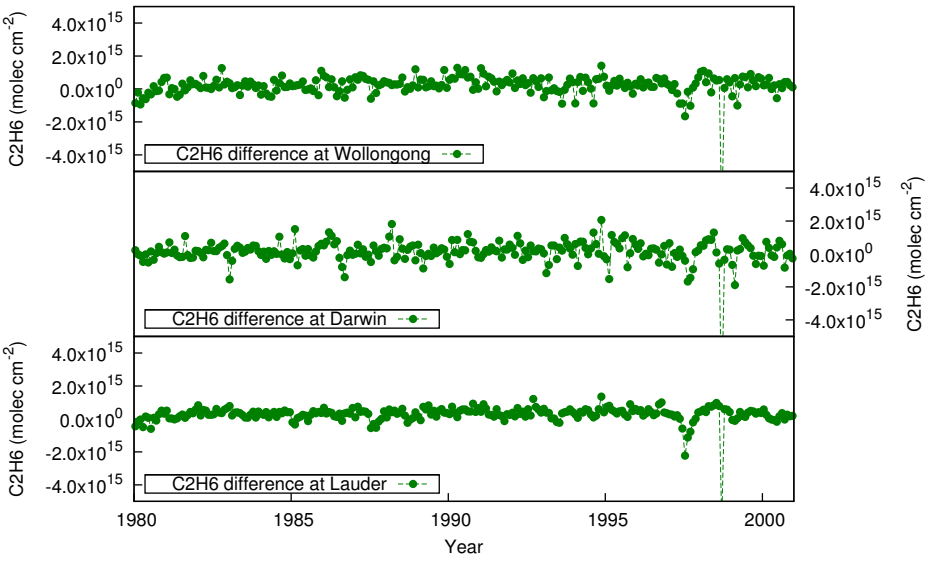

(b) Total column C_2H_6 difference.

Figure E.0.17: Timeseries of total column monthly differences between original and updated ACCESS simulations for (a) HCHO and (b) C_2H_6. For each trace gas differences at Wollongong (top panel), Darwin (middle panel) and Lauder (bottom panel) are shown.

Figure E.0.18: ACCESS NO_2 Darwin and Lauder: Monthly averaged total column. Note the different y-axis scales between plots for old and new simulations.

(a) New monthly averaged NO_2.

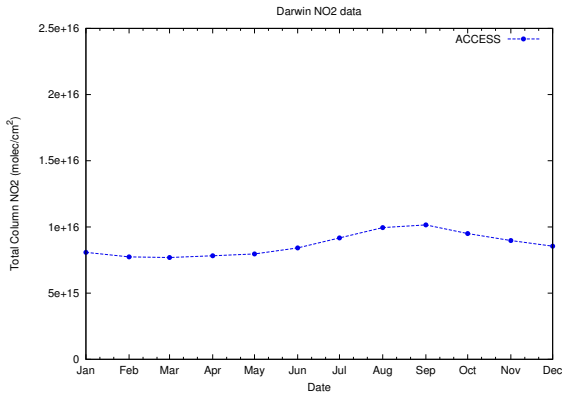

(b) Old monthly averaged NO_2.

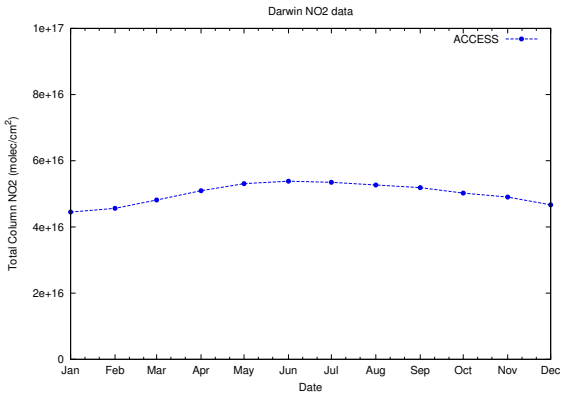

(c) New monthly averaged NO_2.

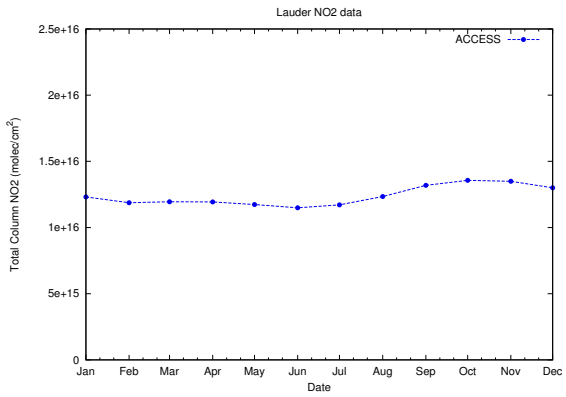

(d) Old monthly averaged NO_2.